



**HAL**  
open science

# Development of transparent electrodes by vacuum-free and low cost deposition methods for photovoltaic applications

Viet Huong Nguyen

► **To cite this version:**

Viet Huong Nguyen. Development of transparent electrodes by vacuum-free and low cost deposition methods for photovoltaic applications. Electric power. Université Grenoble Alpes, 2018. English. NNT : 2018GREAI072 . tel-01992223

**HAL Id: tel-01992223**

**<https://theses.hal.science/tel-01992223>**

Submitted on 24 Jan 2019

**HAL** is a multi-disciplinary open access archive for the deposit and dissemination of scientific research documents, whether they are published or not. The documents may come from teaching and research institutions in France or abroad, or from public or private research centers.

L'archive ouverte pluridisciplinaire **HAL**, est destinée au dépôt et à la diffusion de documents scientifiques de niveau recherche, publiés ou non, émanant des établissements d'enseignement et de recherche français ou étrangers, des laboratoires publics ou privés.

## THÈSE

Pour obtenir le grade de

**Docteur de la Communauté Université Grenoble Alpes**

Spécialité : **Matériaux, Mécanique, Génie Civil, Electrochimie**

Arrêté ministériel : 25 mai 2016

Présenté par

**Viet Huong NGUYEN**

Thèse dirigée par **David MUÑOZ-ROJAS** et **Daniel BELLET**

Co-encadrée par **Delfina MUÑOZ**

Préparée au sein du **Laboratoire des Matériaux et du génie Physique (LMGP)**

et du **Laboratoire de cellules à hétérojonction (LHET)** du **Département de Technologies Solaires (DTS)** du **CEA à l'Institut National de l'énergie Solaire (INES)**

Dans **l'École Doctorale I-MEP2**

**Développement d'électrodes transparentes par méthodes de dépôt à pression atmosphérique et bas coût pour applications photovoltaïques**

**Development of transparent electrodes by vacuum-free and low-cost deposition methods for photovoltaic applications**

Thèse soutenue publiquement le **08 Octobre 2018**

Devant le jury composé de

**M. Daniel LINCOT**

Directeur de Recherche, Institut Photovoltaïque Ile de France (IPVF),  
(Rapporteur)

**M. Cristobal VOZ**

Professeur, Universitat Politècnica de Catalunya, (Rapporteur)

**M. Christophe VALLÉE**

Professeur, Laboratoire des Technologies de la Microélectronique,  
(Président)

**Mme. Elisabeth BLANQUET**

Directrice de Recherche, Laboratoire de Science et Ingénierie des Matériaux  
et Procédés, (Examinatrice)

**M. George KIRIAKIDIS**

Professeur, University of Crete, (Examineur)

**M. Mario MAGLIONE**

Directeur de Recherche, Institut de Chimie de la Matière Condensée  
de Bordeaux, (Examineur)





## Acknowledgements

Writing acknowledgments reminds me of the first days into my PhD, when I had plenty of ideas but I did not know what to start with and how to organize my time. I have passed through both exciting moments and stressful periods, but at this moment I feel so grateful for those people who walked with me through the last three years of PhD.

First of all, I would like to express my deepest gratitude to my two main supervisors, Dr. David Muñoz-Rojas and Prof. Daniel Bellet, for their excellent guidance, constant support, and encouragements. I am very thankful to you for opening me to the door of LMGP and for providing me an excellent atmosphere for doing research. Thank you for giving me a lot of opportunities to visit different laboratories and to attend several international conferences over the world. Those were extremely useful for me to train myself, extend my vision to a wider research community and to build collaboration with several research groups. I feel very lucky to have supervisors who always try to find available time to help me overcome all the difficulties, both in experimental work and in writing papers and dissertation. Both of you always showed an extraordinary positive attitude, and it was really a great pleasure to work under your supervision. Besides my direct two supervisors, I would like to specially thank Dr. Delfina Muñoz as co-supervisor in CEA-INES, for the support during these last three years, the insightful comments and encouragement. I am very grateful for sharing her knowledge on solar cells with me and the proofreading.

I would like to thank Dr. Daniel Lincot and Prof. Cristobal Voz for the honor they gave me by accepting to evaluate my work. I also want to thank Prof. Christophe Vallée, Dr. Elisabeth Blanquet, Prof. George Kiriakidis and Dr. Mario Maglione for accepting to be the members of my PhD examination committee. Thanks a lot for your suggestions which greatly contributed to improving the quality of this manuscript.

This work would not have been possible without the financial support, I would like to acknowledge the ARC Energies Auvergne-Rhône Alpes, the Agence Nationale de Recherche via several projects, the Carnot Energies du Futur and the Marie Curie Actions for this reason.

I would like to express my gratitude to Serge Quessada, Matthieu Jouvert, Mikhail Anikin, Michèle San Martin, Josiane Viboud, Virginie Charrière for the administrative and technical help. I would particularly like to thank Dr. Carmen Jiménez and Dr. Dominique De Barros

for their help in developing the experimental system and for their invaluable suggestions and comments. My first days in PhD were dedicated to the construction of the SALD deposition system by doing 'small' things such as soldering electric cables, bending iron pipes to make a nice gas panel, learning how to do a leakage test or performing a doping recipe on new software. And I have learned, with their instruction, how to perform those 'small' things in an attentive and nice way, which actually greatly influences the research result. Without them, I was not able to proceed my work efficiently.

I would like to acknowledge Odette Chaix, Hervé Roussel, Laetitia Rapenne, Isabelle Gélard and Etienne Pernot for support with the characterization techniques and consequent scientific consultations. I want also to thank Martine Gri, Irène Peck, Xavier Mescot and Anne Kaminski from IMEP-LAHC; Anthony Valla, Perrine Carroy, Elise Bruhat, Médéric Descazeaux and Félix Gérenton from CEA-INES and Prof. Bruno Masenelli from INL for your generous support and constructive comments, without you this thesis would not have been complete. I would like to thank Prof. Judith Driscoll and her PhD student, Ravi Raninga, from the Device Materials Group, University of Cambridge for providing training on AP-SALD, with support from the HERALD.

I am particularly grateful for the invaluable assistance of Dr. Ulrich Gottlieb, who, although no longer with us. The meticulous discussion with Ulrich about the quantum tunneling phenomenon at grain boundaries in polycrystalline TCOs was very helpful and has truly inspired me to develop a better, numerical solution for describing the electron mobility limiting by grain boundary scattering. Also, I want to thank Kissan Mistry, a great PhD student from University of Waterloo, for the fruitful discussion.

My sincere gratitude goes to my LMGP colleagues, João, Thomas, Klaasjan, Hongjun, César, Sara, Dorina, Antalya, Morgane, Fanny, Max, Thuy, Long, Raquel, Mirasbek, Eugene, Getnet, Caroline, Damir, Pierre, Clément, Lukas, Guillaume, Soraya, Monica... with whom I have been sharing both difficult and amazing time. You truly made my lab life enjoyable and unforgettable. I would like to thank my best friends, Phong, Huy, Hau, and Tai, for their constant support, encouragement and for all joyful moments, memorable trips that we share together.

I express my deepest gratitude to my family for encouraging me in all of my pursuits and inspiring me to follow my dreams. I am especially grateful to my parents, who made countless sacrifices to ensure the best education to me and my brothers, thanks dad for teaching me how to face and overcome difficulties in life.

Finally, I owe thanks to a very special person, my girlfriend, Bông, for her continued and unfailing love, support and understanding during my pursuit of PhD degree. Thank you for everything!

## Abstract

The thesis work involves the study of Indium-free Transparent Conductive Materials (TCMs), which constitute key components of many optoelectronic devices, using Atmospheric Pressure Spatial Atomic Layer Deposition (AP-SALD). This new approach shares the main advantages of conventional ALD but allows open-air, very fast deposition of high-quality nanometer-thick materials over large surfaces. We focused on the optimization of the electrical properties of Aluminum doped Zinc Oxide (ZnO:Al) films, one of the most studied Transparent Conductive Oxides (TCOs). The effect of several experimental parameters on the physical properties of the deposited films has been evaluated. The carrier transport mechanism limited by grain boundaries was identified to be tunneling rather than thermionic emission in highly doped ZnO, thanks to a new model we have developed using the Airy Function Transfer Matrix Method. Accordingly, the electron trap density at grain boundaries for ZnO:Al samples (carrier concentration of  $2.2 \times 10^{20} \text{ cm}^{-3}$ ) prepared by AP-SALD was estimated to be about  $7.6 \times 10^{13} \text{ cm}^{-2}$ . Our model shows that grain boundary scattering is the dominant scattering mechanism in our films. We found that UV assisted annealing ( $\sim 200 \text{ }^\circ\text{C}$ ) under mild vacuum was an efficient method to reduce grain boundary traps, resulting in an improvement of mobility from  $1 \text{ cm}^2\text{V}^{-1}\text{s}^{-1}$  to  $24 \text{ cm}^2\text{V}^{-1}\text{s}^{-1}$  for ZnO and to  $6 \text{ cm}^2\text{V}^{-1}\text{s}^{-1}$  for ZnO:Al. We have also used AP-SALD to fabricate high-performance, stable and flexible TCMs based on metallic nanowire network. For that, we developed composite electrodes by coating silver/copper nanowires (AgNWs/CuNWs) with ZnO,  $\text{Al}_2\text{O}_3$ , or ZnO:Al. A thin conformal ZnO coating deposited by AP-SALD technique enhanced drastically the thermal/electrical stability of the AgNWs network. High optoelectronic properties (sheet resistance of about  $7 \text{ } \Omega/\text{sq}$ , transmittance of about 83 %) of the AgNW/ZnO:Al composite make them very appropriate for application as transparent electrodes, especially for flexible devices. Finally, as a soft deposition technique, AP-SALD is completely compatible to the silicon heterojunction (SHJ) solar cell technology in terms of interface passivation. The integration of ZnO:Al films to SHJ solar cell has been briefly explored.



# Résumé

Le travail de thèse comprend l'étude de matériaux conducteurs transparents sans indium, qui constituent des composants clés de nombreux dispositifs optoélectroniques, utilisant le dépôt de couche atomique à pression atmosphérique (AP-SALD). Cette nouvelle technique partage les principaux avantages de l'ALD classique, mais permet de déposer à l'air libre et avec de grande vitesse des matériaux de haute qualité, d'une épaisseur de l'ordre du nanomètre et sur de grandes surfaces. Nous nous sommes concentrés sur l'optimisation des propriétés électriques des films d'oxyde de zinc (ZnO:Al) dopés à l'aluminium, l'un des oxydes conducteurs transparents (TCOs) les plus étudiés. L'effet des paramètres expérimentaux différents sur les propriétés physiques des films déposés a été évalué. Le mécanisme de transport des porteurs libres limité par les joints de grains dans ZnO fortement dopé a été identifié comme étant un phénomène de tunneling quantique plutôt que d'émission thermoionique, grâce à un nouveau modèle que nous avons développé dans le cadre de cette thèse en utilisant la méthode Airy Function Transfer Matrix (AFTMM). En conséquence, la densité des pièges à électrons aux joints de grains pour les échantillons de ZnO: Al (concentration des porteurs de  $2.2 \times 10^{20} \text{ cm}^{-3}$ ) préparée par AP-SALD a été estimée à environ  $7.6 \times 10^{13} \text{ cm}^{-2}$ . Notre modèle montre que la diffusion aux joints de grains est le mécanisme de diffusion dominant dans nos films déposés à l'air libre. Nous avons constaté que le recuit assisté par UV ( $\sim 200 \text{ }^\circ\text{C}$ ) sous vide doux était une méthode efficace pour réduire les pièges aux joints de grains, entraînant une amélioration de la mobilité de  $1 \text{ cm}^2\text{V}^{-1}\text{s}^{-1}$  à  $24 \text{ cm}^2\text{V}^{-1}\text{s}^{-1}$  pour ZnO et à  $6 \text{ cm}^2\text{V}^{-1}\text{s}^{-1}$  pour ZnO: Al. Nous avons également utilisé AP-SALD pour la fabrication des matériaux transparents conducteurs (TCMs) de hautes performances, stables et flexibles, basés sur un réseau de nanofils métalliques. Pour cela, nous avons développé des électrodes composites en enrobant des nanofils argent/cuivre (AgNWs/CuNWs) avec du ZnO,  $\text{Al}_2\text{O}_3$  ou ZnO:Al. Un revêtement mince et conforme de ZnO déposé par la technique AP-SALD a considérablement amélioré la stabilité thermique et électrique du réseau des AgNWs. Les propriétés optoélectroniques remarquables (résistance carrée d'environ  $7 \text{ } \Omega/\text{sq}$  et transmittance dans le visible d'environ 83%) du composite AgNW/ZnO:Al les rendent très appropriées pour les applications des électrodes transparentes, en particulier pour les dispositifs flexibles. Enfin, en tant que technique

de dépôt souple, AP-SALD est totalement compatible avec la technologie des cellules solaires de silicium à hétérojonction (SHJ) en termes de passivation d'interface. L'intégration des films de ZnO: Al dans la cellule solaire SHJ a été brièvement explorée.

# Contents

<b>Abstract</b>	<b>v</b>
<b>Contents</b>	<b>ix</b>
<b>List of Figures</b>	<b>xiii</b>
<b>List of Tables</b>	<b>xxv</b>
<b>1 Introduction</b>	<b>1</b>
1.1 General context . . . . .	1
1.2 Towards high performance TCOs based on ZnO . . . . .	5
1.2.1 ZnO: fundamentals and physical properties . . . . .	5
1.2.2 ZnO:Al thin films . . . . .	11
1.3 Solar cells: from fundamentals to advanced concepts . . . . .	13
1.3.1 Working principle of a solar cell . . . . .	13
1.3.2 Silicon heterojunction solar cells . . . . .	19
1.4 Aim and outline of this work . . . . .	21
<b>2 Growth and Characterization techniques</b>	<b>23</b>
2.1 Thin film growth by AP-SALD . . . . .	23
2.1.1 Overview about AP-SALD . . . . .	23
2.1.2 Description of the AP-SALD system at LMGP . . . . .	26
2.2 Characterization techniques . . . . .	29
2.2.1 Electrical measurements . . . . .	29
2.2.2 Structural and optical measurements . . . . .	32
2.3 Conclusion . . . . .	33
<b>3 Optimization of ZnO and ZnO:Al film growth</b>	<b>35</b>
3.1 Optimization of ZnO thin film deposition . . . . .	38

---

3.1.1	Effect of deposition temperature . . . . .	38
3.1.2	Effect of gas flows . . . . .	43
3.1.3	Effect of substrate velocity . . . . .	51
3.1.4	Effect of the injector-substrate distance . . . . .	55
3.2	Optimization of ZnO:Al thin film deposition . . . . .	59
3.2.1	Tuning aluminum content in ZnO:Al films . . . . .	59
3.2.2	Influence of doping on physical properties . . . . .	64
3.2.2.1	Structural properties . . . . .	64
3.2.2.2	Electrical properties . . . . .	69
3.3	Application of ZnO:Al films deposited by AP-SALD to SHJ solar cells . . . . .	71
3.4	Conclusion . . . . .	74
<b>4</b>	<b>Carrier transport in ZnO:Al thin film</b> . . . . .	<b>77</b>
4.1	Degeneracy and nonparabolicity in TCOs . . . . .	78
4.1.1	Non-degenerate semiconductors . . . . .	79
4.1.2	Degenerate semiconductors . . . . .	79
4.2	Scattering mechanisms in ZnO:Al . . . . .	81
4.2.1	Phonon - electron scatterings . . . . .	82
4.2.1.1	Optical mode scattering . . . . .	82
4.2.1.2	Acoustical mode scattering . . . . .	84
4.2.1.3	Piezoelectric mode scattering . . . . .	84
4.2.1.4	Comparison of phonon-electron scattering mechanisms . . . . .	85
4.2.2	Dislocation scattering . . . . .	86
4.2.3	Ionized impurity scattering . . . . .	87
4.2.4	Grain boundary scattering . . . . .	88
4.2.4.1	Analytical approach: SPM model . . . . .	92
4.2.4.2	Airy Function Transfer Matrix Method: a new approach . . . . .	96
4.3	Application of AFTMM model . . . . .	101
4.3.1	Illustration of the AFTMM model in comparison with the analytical model . . . . .	103
4.3.2	Model application to experimental data . . . . .	107
4.4	Effect of UV post-deposition treatment . . . . .	113
4.4.1	Experimental section . . . . .	113
4.4.2	Theoretical model . . . . .	114
4.4.3	Effect of doping concentration . . . . .	116
4.4.4	Effect of temperature during the UV treatment . . . . .	118
4.4.5	Model application to experimental data . . . . .	119

---

4.4.6	Oxygen readsorption after the UV treatment . . . . .	121
4.5	Conclusion . . . . .	123
<b>5</b>	<b>Metal oxide/AgNW composites: high performance flexible TCMs</b>	<b>127</b>
5.1	Thin conformal ZnO coating as a protective layer for AgNWs . . . . .	128
5.1.1	Experimental section . . . . .	129
5.1.2	Effect of ZnO coating on adhesion and transparency of AgNW networks	130
5.1.3	Effect of the ZnO coating on the electrical and thermal stability of AgNW networks . . . . .	133
5.1.4	Rationalization of the effect of the ZnO coating on the stability of AgNW networks . . . . .	136
5.1.5	Evaluation of the performance of transparent heaters based on ZnO coated AgNWs . . . . .	139
5.2	ZnO:Al/AgNW nanocomposites . . . . .	141
5.2.1	Model of two parallel resistances . . . . .	143
5.2.2	Model considering the presence of local percolating AgNW clusters below the network percolation threshold . . . . .	145
5.3	Quantitative assessment of the effects of the ZnO coating on AgNW networks	154
5.4	Conclusion . . . . .	156
	<b>Bibliography</b>	<b>159</b>
	<b>List of related publications</b>	<b>180</b>



# List of Figures

1.1	Worldwide installed capacity (MW) of solar PV power plants from 2007 to 2017, data extracted from <a href="http://irena.org/solar">http://irena.org/solar</a> . . . . .	2
1.2	Evolution of the number of publications related to ALD, between 1980 and 2018 (data extracted from <a href="#">Web of Science</a> , Figure performed in 05/2018) . . .	4
1.3	Wurtzite structure of ZnO with Zn cations and O anions highlighted in dark color and light color, respectively. (from Wikipedia) . . . . .	6
1.4	(left) ZnO single crystal Ingot, produced through hydrothermal process, (right) ZnO wafers ( $10 \times 10 \times 0.5 \text{mm}^3$ ). (by Mineral Ltd, Russia) . . . . .	8
1.5	Formation energies versus Fermi level of some native point defects in ZnO, calculated using an extrapolation scheme based on LDA and LDA+U calculations. Results are shown for Zn-rich (left graph) and O-rich (right graph) conditions. The zero level of Fermi energy corresponds to the top of valence band (extracted from [1]: A. Jannotti & C.G. Van de Walle, 2007). . . . .	9
1.6	Solar spectrum AM1.5 plotted versus wavelength (Data extracted from <a href="http://pv-lighthouse.com.au">pv-lighthouse.com.au</a> ). The red area illustrates the fraction that can be used with a silicon solar cell . . . . .	14
1.7	Schematic representation of bandgap energies in metal, intrinsic semiconductor and insulator at 300 K. Red and white dots represent electrons and holes, respectively. . . . .	14
1.8	Absorption coefficient in a variety of semiconductor materials at 300 K as function of incident light wavelength ( <a href="https://www.pveducation.org">https://www.pveducation.org</a> ). . . . .	16
1.9	Schematic representation of a pn junction in the dark and under illumination. . . . .	17
1.10	JV curves under dark and illumination conditions, and electrical power density of a standard solar cell as function of external voltage . . . . .	18
1.11	Sketch of a front emitter (pn junction in on the front side) SHJ solar cell including its band diagram. . . . .	20

2.1	Simple schematic representations of: a) CVD and b) ALD processes, respectively; simple schematic representations of films deposited by: c) CVD and d) ALD, respectively. The SEM images shown in c) and d) are SiO <sub>2</sub> deposited on Silicon by Plasma Enhanced CVD ( <a href="https://www.corial.com">https://www.corial.com</a> ) and alternating layers of Ta <sub>2</sub> O <sub>3</sub> /Al <sub>2</sub> O <sub>3</sub> deposited on Silicon by ALD ( <a href="http://lotusat.com">http://lotusat.com</a> ), respectively. . . . .	24
2.2	Schematic representation of a SALD process. Precursors are continuously supplied at different locations, while spatially separated thanks to inert gas barriers located alternatively between the precursor flows. The substrate moves from one location to another in order to reproduce the ALD cycles. . . . .	25
2.3	Images of the AP-SALD system used in this work: a) a global view of the system, b) a side view showing the motor, the substrate holder, as well as the mechanical system allowing to adjust the distance between the substrate and the gas injector, c) a close view of the gas injector and the substrate. . . . .	27
2.4	A simple schematic representation of the gas delivery system of our AP-SALD system for the case of ZnO deposition. The precursors are stored in the metallic bubblers in the liquid form (DEZ: diethylzinc, TMA: trimethylaluminum and H <sub>2</sub> O: water) and carried to the gas injector via a pure nitrogen bubbling flow and a nitrogen dilution flow. Green valves refer to the opening state, while the red one refer to the close state. . . . .	28
2.5	a) scheme of the cross-section view of AP-SALD gas injection head and a substrate at a distance of 150 μm from the head. Exhaust channels alternatively located in between each gas output inlet are not represented in this scheme, b) a view from the bottom of our AP-SALD gas injector showing 21 parallel gas channels. . . . .	29
2.6	a) A sample of arbitrary shape with four small contacts at arbitrary places along the perimeter, b) schematic representation of a thin film sample of square shape used for Van Der Pauw measurements in our work, the corners of the film are contacted with silver paste. . . . .	31
2.7	Schematic representation of the Hall effect. . . . .	32
3.1	Number of publications having the key words: ZnO, AZO or ZnO:Al in the title versus publication year for a variety of fabrication technique. Data extracted from Web of Science. . . . .	36
3.2	A summary of different parameters affecting the ALD growth, both for conventional ALD and AP-SALD. . . . .	37

3.3	Temperature dependence of the growth rate in nm per cycle of ZnO thin films deposited at different pressures. The gas pulse conditions used for depositions are identical. Data extracted from Mousa et al.'s work.[2] . . . . .	38
3.4	Growth rate in nm per cycle of ZnO thin films deposited on glass at different temperatures with our AP-SALD system. The number of cycles was kept at 200 for all samples. . . . .	39
3.5	Mass density of ZnO thin films deposited on glass versus substrate temperature with our AP-SALD system. The number of cycles was kept at 200 for all samples. . . . .	39
3.6	Total transmittance of ZnO thin films deposited at different temperatures. The number of cycles was kept at 200 for all samples. . . . .	40
3.7	Optical band gap calculated using Tauc plot (inset image) of ZnO thin films deposited at different temperatures. The number of cycles was kept at 200 for all samples. . . . .	40
3.8	A 2D-model representation of density of states in the conduction and valence bands of a) crystalline semiconductors and b) amorphous semiconductors. The region of localized states are shaded. $E_C$ , $E_V$ denote the bottom of the conduction band and the top of the valence band, respectively. $E_A$ and $E_B$ denote the optical absorption edges, which are related to the optical band gap in an amorphous material.[3] . . . . .	41
3.9	X-Ray Diffraction patterns for ZnO films prepared at different temperatures. The number of cycles was fixed at 800 for all samples. . . . .	41
3.10	Room temperature resistivity, electron mobility and electron concentration as a function of deposition temperature, measured by Hall effect (for the more resistive samples prepared at lower temperatures, measurement results were not reliable). The number of cycles was fixed at 800 for all samples. . . . .	42
3.11	Growth per cycle as a function of nitrogen bubbling flow through water. . . . .	44
3.12	Refractive index of films as a function of nitrogen bubbling flow through water. . . . .	44
3.13	X-Ray Diffraction patterns for ZnO films prepared with different nitrogen bubbling flows through H <sub>2</sub> O. . . . .	44
3.14	SEM images of ZnO films prepared with different nitrogen bubbling flows through H <sub>2</sub> O. . . . .	45
3.15	Growth per cycle as a function of N <sub>2</sub> bubbling flow through DEZ (sccm). The fit using the theory of Langmuir adsorption kinetics is shown in red line for N <sub>2</sub> bubbling flow through DEZ in the range of [0 sccm, 30 sccm]. . . . .	47

---

3.16	X-ray diffraction patterns of ZnO samples deposited with different DEZ bubbling flows (from 5 sccm to 35 sccm). . . . .	47
3.17	Growth per cycle and refractive index of ZnO films prepared by using various nitrogen barrier flows. . . . .	49
3.18	X-Ray Diffraction patterns for ZnO films prepared at different nitrogen barrier flows. . . . .	49
3.19	SEM images of ZnO films prepared at different nitrogen barrier flows. . . . .	50
3.20	A schematic zoom of the cross-section view of the gas injector. . . . .	51
3.21	The results extracted from COMSOL Multiphysics simulation of: a) precursor velocity, b) precursor concentration spatially distributed above the substrate. Gas flows, temperature, as well as the distance between the injector and the substrate were kept constant, as in reality. Here, only the cross-section views including a DEZ inlet and two exhaust inlets are shown. The blue color corresponds to low velocity or low precursor concentration (in volume fraction), while red or yellow color correspond to high velocity or high precursor concentration. . . . .	52
3.22	Critical width on the substrate that is exposed to a precursor concentration corresponding to 80 % of the precursor concentration at the input DEZ channel. . . . .	53
3.23	Experimental values of the growth per cycle of ZnO films as a function of the substrate velocity, and DEZ bubbling flows, and the associated fits using eq. 3.6. . . . .	54
3.24	The effect of the injector-substrate distance to the precursor concentration, illustrated using COMSOL Multiphysics simulation. For this illustration, only one part of the injector is shown. Red color corresponds to the precursor concentration at the input inlet level, while blue color corresponds to pure nitrogen. . . . .	55
3.25	Precursor concentration profile at the interface gas/substrate as a function of the position on the substrate for the case of an injector-substrate distance of 70 microns. . . . .	56
3.26	Precursor concentration profile at the interface gas/substrate as a function of the position on the substrate for the case of an injector-substrate distance of 230 microns. . . . .	56
3.27	Growth per cycle of ZnO films as a function of the distance between the injector and the substrate. . . . .	56
3.28	The effect of the injector-substrate distance on the gas velocity, illustrated using COMSOL Multiphysics simulation. For this illustration, only one part of the injector is shown. . . . .	57

3.29	X-ray diffraction patterns of ZnO samples deposited with different injector/substrate distances (from 70 $\mu\text{m}$ to 270 $\mu\text{m}$ ). . . . .	58
3.30	Schematic view of the close-proximity AP-SALD system used for ZnO:Al deposition. The Al precursor (TMA) is mixed with the Zn precursor (DEZ) before injecting the mixture onto the substrate. . . . .	59
3.31	Schematic representation of nitrogen bubbling flows through DEZ and TMA bubblers as a function of time. . . . .	60
3.32	The aluminum content estimated by EDS analysis of the samples having the same deposition parameters during the saturation period of TMA in TMA/DEZ mixture. After 12 times of repeating exactly the same deposition parameters, the concentration of TMA in TMA/DEZ mixture is stable. . . . .	61
3.33	Total transmittance with optical bandgap calculated from Tauc plot of the ZnO:Al samples having the same deposition parameters during the saturation period of TMA in TMA/DEZ mixture. . . . .	61
3.34	a) The Al content (%) estimated by EDX analysis and the resulting carrier concentration versus TMA pulse time used during AP-SALD deposition; b) the total transmittance of ZnO:Al films deposited with different TMA pulse time, varying from 500 ms to 900 ms while the other deposition parameters were fixed. . . . .	62
3.35	Influence of Al content on the Zn content and the total metal content in ZnO:Al films. The data was measured with X-ray micro-analysis technique. . . . .	62
3.36	X ray diffraction spectra of ZnO:Al samples with different Al doping concentrations. Left: full spectra, right: a zoom on the (100) and (002) reflections. . . . .	65
3.37	ZnO unit cell, as well as (002) and (100) crystallographic planes. . . . .	65
3.38	SEM images of ZnO:Al samples with different Al doping concentrations, along with a cross-section view scheme of different types of morphology for different crystallographic orientations. . . . .	66
3.39	AFM images of ZnO:Al films with various thicknesses deposited by AP-SALD at 200 °C. The inset images show corresponding top-view AFM images. . . . .	67
3.40	a) Mean grain size measured with AFM and b) X-Ray Diffraction patterns of ZnO:Al films with various thicknesses deposited by AP-SALD at 200 °C. . . . .	68
3.41	a) SEM micrographs of ZnO:Al films with various thicknesses deposited by AP-SALD at 200 °C. b) Dark-field TEM image, c-d) high-resolution TEM images of 500nm-thick ZnO:Al film deposited by AP-SALD on Silicon substrate at 200 °C. . . . .	68

3.42	a) sheet resistance, b) carrier concentration and c) carrier mobility measured by Hall effect measurement of ZnO:Al samples having different Al doping concentrations. All the films are 185 nm thick. . . . .	69
3.43	Implied open-circuit voltage at 1-sun of a SHJ-like structure before and after ZnO deposition by AP-SALD versus deposition temperature. . . . .	72
3.44	J-V curves in the dark (a) and under illumination (b) of SHJ solar cells with ITO (reference cell, size of 14.44 cm <sup>2</sup> ) and ZnO:Al as transparent electrodes on both sides, respectively. The results for ZnO:Al were an average of 4 cells of the same size of 24.9 cm <sup>2</sup> . . . . .	73
4.1	Simulation curves of temperature-dependent Fermi-Dirac distribution of a non-degenerate ZnO sample having Fermi level at 0.1 eV below the minimum of the conduction band. The density of states in the conduction band is also presented on the right axis . . . . .	80
4.2	Simulation curves of temperature-dependent electron density in the conduction band of a non-degenerate ZnO sample having Fermi energy level at 0.1 eV below the minimum of the conduction band. . . . .	80
4.3	Simulation of electron density in the conduction band of a degenerately doped ZnO sample, where the Fermi energy level is found at 0.25 eV above the minimum of the conduction band. . . . .	80
4.4	Simulation of temperature-dependent electron density of degenerate and non-degenerate ZnO samples. The Fermi energies used in the simulation are measured with respect to the minimum of the conduction band. . . . .	80
4.5	Scheme of scattering phenomenon of an electron when an electric field is applied	83
4.6	Simulated curves of temperature-dependent mobilities induced by acoustic/optical/piezoelectric mode scatterings in non-degenerate ZnO. . . . .	86
4.7	Simulated curves of temperature-dependent mobilities induced by acoustic/optical/piezoelectric mode scatterings in degenerate ZnO. . . . .	86
4.8	Schematic of the band energy at the vicinity of a grain boundary, for the case of n-type degenerate semiconductors such as ZnO:Al films . . . . .	90
4.9	Scheme of tunneling through a constant potential barrier, showing a change in wave function of electron before, during and after tunneling through a square potential barrier. $E_1$ , $E_2$ are two electron energy levels in the conduction band ( $E_1 < E_2$ ), $\phi_0$ represents the potential barrier. . . . .	92
4.10	Simulation of a grain boundary potential barrier in the case of ZnO:Al along with the electron distribution in the conduction band. . . . .	95

4.11 Simulation of tunneling probability versus electron energy using Seager and Pike's model. . . . .	95
4.12 Illustration of Airy functions $Ai$ and $Bi$ used for calculation of the electron tunneling probability through an arbitrary potential barrier.[4] . . . . .	97
4.13 A parabolic potential barrier is segmented into $N$ linear potentials. For this illustration, we used $n = 2 \times 10^{20} \text{ cm}^{-3}$ , $N_t = 6 \times 10^{13} \text{ cm}^{-2}$ , $L = 20 \text{ nm}$ . . .	98
4.14 Schematic of the incident, reflected and transmitted electron waves in the conduction band at the $j^{\text{th}}$ grain boundary. . . . .	98
4.15 Tunneling probability, and associated Matlab running time calculated for electrons at the Fermi level as function of the number of segments used for the discretization of the grain boundary potential barrier. For this evaluation, we used $n = 2 \times 10^{20} \text{ cm}^{-3}$ , $N_t = 6 \times 10^{13} \text{ cm}^{-2}$ , $L = 20 \text{ nm}$ . . . . .	102
4.16 Spatial variation of potential plotted for different trap densities in the vicinity of the grain boundary. . . . .	103
4.17 The tunneling probability calculated from the Seager Pike modified (SPM) and the AFTMM models. . . . .	103
4.18 Supply function and tunneling probability from the AFTMM model versus electron energy for different applied voltage ( $V_a = 0.1 \text{ V}$ , $0.2 \text{ V}$ ). . . . .	104
4.19 Potential barrier at grain boundary (on left) and the associated tunneling current through the barrier as function of electron energy in the conduction band. . . . .	104
4.20 Contribution of different scattering mechanisms to the electron mobility, the contribution from grain boundary scattering has been calculated with the AFTMM model. For this illustration, we used $L = 20 \text{ nm}$ , $C = 0.5$ , $K = 0.12$ , $N_t = 6 \times 10^{13} \text{ cm}^{-2}$ , $n = 1.5 \times 10^{20} \text{ cm}^{-3}$ . . . . .	105
4.21 Total electron mobility as function of substrate temperature, calculated using three different models: Seager-Pike, SPM and AFTMM with different grain boundary trap densities from $N_t = 3 \times 10^{13} \text{ cm}^{-2}$ to $6 \times 10^{13} \text{ cm}^{-2}$ , and the other parameters used for this simulation: $L = 20 \text{ nm}$ , $C = 0.5$ , $K = 0.12$ , $n = 1.5 \times 10^{20} \text{ cm}^{-3}$ . . . . .	106
4.22 Three types of temperature-dependent mobility with corresponding dominant scattering mechanisms in the case of highly doped ZnO. $\mu_{TI}$ : temperature independent contributions (ionized impurity and dislocation scattering); $\mu_{TD}$ : temperature-dependent contributions (acoustical and optical phonons scattering); $\mu_{GB}$ : grain boundary scattering contribution. . . . .	107

- 
- 4.23 Electron mobility as a function of carrier concentration, calculated with the AFTMM model with different grain boundary trap densities ( $L = 20 \text{ nm}$ ,  $C = 0.5$ ,  $K = 0.12$ ). The dotted lines represent the limits of two regions where grain boundaries and ionized impurity scattering dominate the mobility. . . . 108
- 4.24 The trap density calculated by fitting the temperature-dependent Hall mobility with the model AFTMM as a function of carrier concentration. The samples have a thickness of around 200 nm, grown by AP-SALD at 200 °C (with UV assisted annealing at 200 °C under vacuum as the post-deposition treatment, see section 4.4 below), ALD and DC sputtering. . . . . 109
- 4.25 Experimental (points) and fitted (dashed lines) mobility as a function of the temperature for the ZnO:Al samples grown at 200 °C by AP-SALD, ALD, and DC sputtering, and two sets of extracted data from the paper of Ellmer and Mientus (samples prepared by RF sputtering). . . . . 110
- 4.26 Schematic image of the oxygen desorption mechanisms at grain boundaries of ZnO:Al.  $E_F$ ,  $E_C$  and  $E_V$  refer respectively to the Fermi level, the minimum of the conduction level and the top of the valence band. . . . . 115
- 4.27 Electrical properties of ZnO films deposited by AP-SALD with different Al doping levels before and after the UV treatment at 200 °C under vacuum: a) sheet resistance, b) Hall carrier concentration, c) Hall carrier mobility. The insets show the variations of the conductance, carrier concentration and mobility before and after the UV treatment, respectively. All the films are 185 nm thick. . . . . 117
- 4.28 a) Total transmittance of ZnO:Al films with different doping concentrations, the inset image zooms into the UV range of [320 nm, 420 nm] and b) The photoluminescence spectrum around 365 nm of ZnO and ZnO:Al with different doping levels, the emissions were recorded at 20 K using an excitation energy of 4.66 eV. . . . . 118
- 4.29 Influence of the substrate temperature during UV treatment on the electric properties of undoped and doped ZnO films; a) sheet resistance, b) Hall carrier concentration and c) Hall carrier mobility as a function of substrate temperature. All the films have the same thickness of 220 nm. . . . . 119
- 4.30 The variation of resistance ( $R/R_{\text{initial}}$ ) during UV treatment under vacuum for undoped ZnO and two ZnO:Al samples. The substrate temperature was maintained at 70 °C. A high fitting quality of experimental data with the two presented models is observed, as shown by the solid red lines. . . . . 120

- 
- 4.31 The relative variation of resistance ( $\Delta R/R_{\text{initial}}$ ) of two 200 nm thick ZnO:Al samples, with and without 15 nm of  $\text{Al}_2\text{O}_3$  protection layer, as a function of time when the samples were maintained at 150 °C in the open air. . . . . 122
- 4.32 The variation of resistance ( $R/R_{\text{initial}}$ ) of 25 nm - thick ZnO sample as a function of time when alternatively illuminating the samples with the 365 nm UV light. The samples were maintained at 130 °C and 200 °C, respectively, in the open air. . . . . 123
- 5.1 (a) Scanning electron microscopy (SEM) image of the AgNW network deposited by spin coating and annealed at 250 °C for 30 minutes to sinter the junctions, (b) SEM image of AgNW networks coated with 30 nm of ZnO deposited with AP-SALD. (c) Transmission electron microscopy (TEM) image of a 30 nm thick ZnO coated AgNW, (d) Back scattered SEM image of a coated AgNW (allowing to highlight the elemental contrast) showing the usual fivefold symmetry twinning of AgNWs surrounded by a uniform 30 nm thick ZnO layer. . . . . 131
- 5.2 (a-b) Optical microscope images of the bare and the AgNW network coated by a thin layer (30 nm) of ZnO, respectively, showing the effect of the scotch tape test. The upper (lower) half is the region where tape was (not) applied; (c) Transmittance of AgNW networks at 550 nm (after subtraction of the glass substrate transmittance) versus the ZnO coating thickness deposited by AP-SALD. Increase in thickness of the ZnO coating results in a linear decrease of the transmittance. . . . . 132
- 5.3 a) Variation of electrical resistance ( $R/R_0$ ) of bare and ZnO coated AgNW networks measured during thermal ramps from room temperature to 500 °C with a heating/cooling rate of 2 °C/min. (b) Ratio between final and initial resistances of AgNW networks, respectively, after and before the thermal ramp up to 500 °C. Increasing the thickness of the ZnO coating increases the thermal stability, and thus the electrical resistance reversibility. (c) Relative variation of resistance of bare and ZnO coated AgNW networks measured at constant temperature of 320 °C versus time. . . . . 134

- 5.4 (a) Variation of electrical resistance for bare and ZnO coated AgNW networks subjected to voltage ramps of 0.1 V/min. The bare AgNW network shows failure at around 9 V, while the stability of ZnO coated AgNW networks increases with increasing ZnO coating thickness reaching up to 18 V for 30 nm of ZnO coating. (b) Failure voltage limit dependence versus ZnO coating thickness. A clear, nonlinear increase of the failure voltage versus ZnO layer thickness is observed (the line is a guide to the eye). . . . . 135
- 5.5 Schematic representation of a junction between two adjacent AgNWs for a) as-deposited junction, while b) shows a local sintering and c) the beginning of the deterioration of the junction that will eventually (if the thermal or electrical load continues) lead to the deterioration of the network. d) SEM image of a junction within a AgNW network after thermal or electrical load just before the failure point. e) A very thin and conformal ZnO coating (of thickness  $L_{\text{ZnO}}$ ) over a junction is schematically represented. f) SEM image of an intact junction coated with ZnO. g) Dependence of the experimental failure voltage versus the ZnO coating thickness, measured during a voltage ramp, as well as the calculated values using eq. 5.3, showing a good agreement (the rate of voltage increase,  $\dot{V}$ , is 0.1 V/min). h) Resistance versus voltage for voltage ramps with different  $\dot{V}$  values for ZnO coated samples (25 nm in all cases). i) Dependence of the experimental network failure voltage versus the product of  $\dot{V}$  and  $(L_{\text{ZnO}})^2$ , as well as the theoretical values from eq. 5.3, again showing a good agreement. . . . . 137
- 5.6 (a) Electrical resistance of AgNW networks measured versus time during voltage plateaus of 1, 3, 5 and 7 V applied to the bare and ZnO coated networks. Each plateau was 45 minutes long, and the whole series then reversed. (b) Dependence of electrical resistance versus temperature measured during voltage plateaus of 1-3-5-7-5-3-1 V for both bare and ZnO coated (25 nm) networks. A much better stability is observed for the ZnO coated network. . . . . 140
- 5.7 Measured temperature versus voltage during a voltage ramp of 0.1 V/min for bare and coated AgNW networks, the latter being associated to a 25 nm thick ZnO coating. The bare AgNW network exhibits an electrical failure at about 8 volts while the coated AgNW network can undergo a voltage up to 14 volts and can therefore remain a transparent heater at much higher temperature. . . 140

- 5.8 SEM images of a bare AgNW network (left) and a ZnO:Al/AgNW nanocomposite (right, with 100 nm thick ZnO:Al film) under electron beam having an acceleration voltage of 10 kV. The charge effect in the gaps between AgNWs can be clearly observed in the case of bare AgNWs. The inset image on the right illustrates the similar ZnO:Al morphology obtained on glass and on AgNWs. . . . . 142
- 5.9 Experimental electrical resistance of AgNW network measured during this work versus areal mass density ( $amd$ ) for a network deposited on glass (blue symbols) and for a 100 nm thick ZnO:Al layer grown by AP-SALD deposited above a similar AgNW network (green symbols). The resistance of 100 nm thick ZnO:Al film on glass was 800  $\Omega$ . The fitting curves use eq. 5.6 and eq. 5.7 for the AgNW deposited on glass (black dashed curve) and for the AgNW/AZO nanocomposite (red dashed curve), respectively. . . . . 144
- 5.10 a) Illustration of the probability density function (denoted  $pdf^{\overline{amd}}$ , left axis) and the cumulative density function (denoted  $cdf^{\overline{amd}}$ , right axis) as a function of areal mass density ( $amd$ ), the shaded area corresponds to a probability of 79 % of obtaining an  $amd$  in between [35, 55] ( $\text{mg}/\text{m}^2$ ) (for this **simulation**,  $\overline{amd} = 45$ ,  $\sigma_{amd} = 8$  were used); b) Optical microscope image of a AgNW network deposited on glass by spin-coating (image credit to A. Khan). . . . . 146
- 5.11 Illustration of the numbers of clusters having an  $amd > amd_C$  when increasing the average network density  $\overline{amd}$  from 35 to 45 ( $\text{mg}/\text{m}^2$ ) ( $\sigma_{amd}$  was fixed at 8  $\text{mg}/\text{m}^2$  for this **simulation**). Black regions refer to the non-percolating part of the network, bright regions refer to the percolating clusters. . . . . 147
- 5.12 A simple equivalent electrical circuit of the ZnO:Al/AgNW nanocomposite.  $R_{ZnO:Al}^S$  is a resistance related to the fraction of the ZnO:Al film covering the non-percolating AgNW network (the black part in Figure 5.11),  $R_{ZnO:Al}^P$  is a resistance related to the fraction of the ZnO:Al film covering the percolating clusters, which is in parallel with the  $R_{clusters}^P$  (the total resistance of the clusters). 147
- 5.13 Density of percolation probability ( $pdf$ ) as a function of  $amd$  for the case of a sample having an average  $\overline{amd} = 35$ , and the percolation threshold  $amd_C = 45$ . The surface of the red shaded area refers to the probability of having percolating clusters, and can be calculated as  $\left(1 - cdf^{\overline{amd}}(amd_C)\right)$ . . . . . 148
- 5.14 Effect of a)  $R_{ZnO:Al}$  and b)  $K$  on the resistance of the nanocomposites. These **simulation** results were obtained by using  $amd_C = 45$ ,  $\sigma_{\overline{amd}} = 5$ ,  $\alpha = 1.2$  for both figures, then  $K = 9.5 \times 10^{10}$  for a) and  $R_{ZnO:Al} = 800$  for b). . . . . 151

- 5.15 Effect of a)  $\alpha$  and b)  $\overline{\sigma_{amd}}$  on the resistance of the nanocomposites. These **simulation** results were obtained by using  $amd_C = 45$ ,  $K = 9.5 \times 10^{10}$ ,  $R_{ZnO:Al} = 800$  for both figures, then  $\overline{\sigma_{amd}} = 5$  for a) and  $\alpha = 1.2$  for b). . . . . 151
- 5.16 Experimental electrical resistance of AgNW network measured during this work versus areal mass density ( $amd$ ) for a network deposited on glass (blue symbols) and for a 100 nm thick ZnO:Al layer grown by AP-SALD deposited above a similar AgNW network (green symbols). The resistance of 100 nm thick ZnO:Al film on glass was 800  $\Omega$ . The fitting curves use eq. 5.10 and eq. 5.15 for the AgNW deposited on glass (black dashed curve,  $\overline{amd_C} = 45$ ) and for the AgNW/AZO nanocomposite (red dashed curve,  $\overline{amd_C} = 39$ ).  $\overline{\sigma_{amd}} = 5$ ,  $\alpha = 1.2$  and  $K = 9.5 \times 10^{10}$  were used. . . . . 152
- 5.17 a) Variation of the sheet resistance and the total transmittance of a 110 nm thick ZnO:Al/AgNW nanocomposite as a function of the spray coating cycle, i.e. AgNW network density; b) the dependence of the diffuse transmittance of the ZnO:Al/AgNW nanocomposite on the AgNW network density. . . . . 153
- 5.18 The ratio of FoM, the coated network's FoM divided by the bare network's FoM, as a function of ZnO coating thickness. . . . . 155

# List of Tables

1.1	Physical properties of ZnO in comparison to indium oxide ( $\text{In}_2\text{O}_3$ ), tin dioxide ( $\text{SnO}_2$ ) and Silicon (Si). Abundance of the metal in the earth's crust (approximate % by weight, <a href="http://periodictable.com">periodictable.com</a> ), crystal structure and lattice parameters,[5] $\parallel$ and $\perp$ denote parallel and perpendicular to c-axis, respectively; $\kappa$ : thermal conductivity, $\alpha$ : thermal expansion coefficient, $P_{\perp}$ : piezoelectric coupling coefficient, $\epsilon_s$ and $\epsilon_{\infty}$ : static and optical dielectric constants, $T_m$ : melting temperature, $\Delta H_f$ : heat of formation per formula unit. . . . .	7
1.2	List of donors with corresponding binding energy level and ionic radius. $E_C$ and $E_D$ refer to the minimum of the conduction band and the donor defect energy level with respect to $E_C$ . . . . .	10
1.3	A summary of factors, with impact on the electrical conductivity of a semiconductor material. The words highlighted in <i>italic</i> refer to external impacts. . . . .	11
1.4	Comparison of physical properties of commercially available ZnO single crystals and some ZnO:Al thin films prepared by different deposition techniques, s-CVT (seeded chemical vapour transport), HT (hydrothermal), PLD, ALD and AP-SALD. $\rho$ ( $\Omega\text{cm}$ ), $n$ ( $\text{cm}^{-3}$ ), $\mu$ ( $\text{cm}^2\text{V}^{-1}\text{s}^{-1}$ ) denote resistivity, carrier concentration and carrier mobility, respectively. . . . .	12
1.5	Bandgap energies of different materials ( <a href="http://www.ioffe.ru">http://www.ioffe.ru</a> ). . . . .	15
3.1	Extracted parameters from the fits shown in Figure 3.23. . . . .	54
3.2	Variation of (002) peak position and of the mean crystallite size oriented along [002] direction versus percentage of aluminum in ZnO:Al films; for this calculation the value of Scherrer constant was set at 0.9 as a typical value. . . . .	65
3.3	The electrical properties of as-deposited ZnO:Al films prepared by different deposition methods (MSD, ALD and AP-SALD) in comparison with ITO prepared by MSD. The oxygen partial pressure during the deposition and the film thickness are also shown. The data related to ITO and to ZnO:Al by MSD was extracted from the work of Carroy et al.[6] . . . . .	70

3.4	IV parameters of SHJ cells with ZnO:Al as transparent electrode(s) (average of 4 cells). Data extracted from the work of Carroy et al. (2015).[6] . . . . .	71
3.5	IV parameters of SHJ cells with ITO deposited by MSD and ZnO:Al deposited by AP-SALD as transparent electrodes on both sides. . . . .	73
4.1	Material parameters of ZnO:Al used for the simulation. . . . .	102
4.2	Parameters used for and extracted from the fits in Fig. 4.25 of the temperature-dependent Hall mobility of selected ZnO:Al films grown by AP-SALD, ALD, and DC sputtering and two samples from the literature.[7] The Fermi level is also represented along the barrier height calculated from the AFTMM model. . . . .	111
4.3	Results of fitting the experimental curves shown in Figure 4.30 with the SPM and AFTMM models. $N_{t_0}$ denotes the initial grain boundary trap density, $A$ and $t_0$ are two constants related to the initial desorption rate and the time constant of the desorption kinetics, respectively. . . . .	121
5.1	Parameters used for the simulation of the resistance of ZnO:Al/AgNW nanocomposites. . . . .	150

# Chapter 1

## Introduction

### Contents

---

<b>1.1</b>	<b>General context</b>	<b>1</b>
<b>1.2</b>	<b>Towards high performance TCOs based on ZnO</b>	<b>5</b>
1.2.1	ZnO: fundamentals and physical properties	5
1.2.2	ZnO:Al thin films	11
<b>1.3</b>	<b>Solar cells: from fundamentals to advanced concepts</b>	<b>13</b>
1.3.1	Working principle of a solar cell	13
1.3.2	Silicon heterojunction solar cells	19
<b>1.4</b>	<b>Aim and outline of this work</b>	<b>21</b>

---

### 1.1 General context

An energy crisis and climate change are two major challenges that humankind has to face in the twenty-first century. While our modern life is essentially powered by electricity, there is currently still more than 80 % of electric energy produced by burning carbon fuels such as coal, oil or natural gas. However, this traditional form of electricity generation is not sustainable because of finite fossil resources and greenhouse gas emissions, which are widely believed to cause climate change. An uneven distribution of these resources is also at the origin of inequalities and conflicts. Also, as the world population is continuously growing (with predictions to reach 10 billion inhabitants in 2050), the global energy demand will increase as well. In order to reduce the dependence on fossil fuels and their environmental associated challenges, renewable energy sources and new technologies for electricity generation should

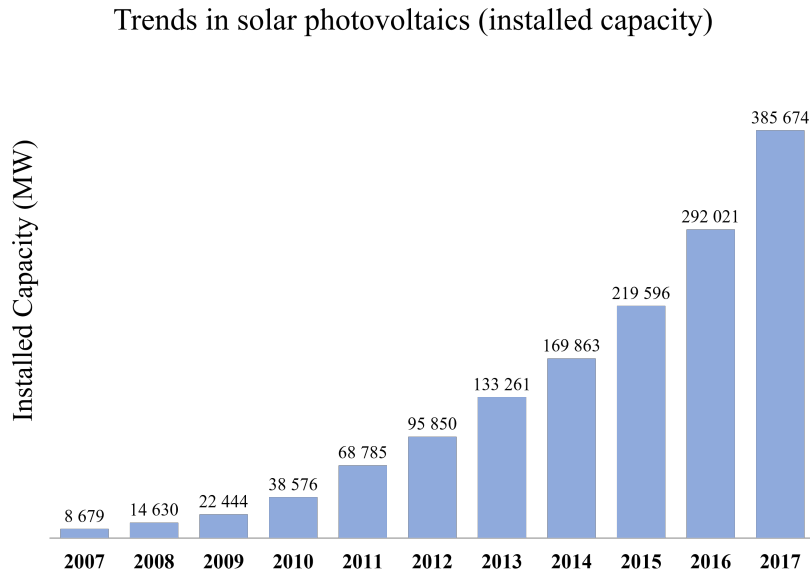


Figure 1.1: Worldwide installed capacity (MW) of solar PV power plants from 2007 to 2017, data extracted from <http://irena.org/solar>.

be developed. Today, solar photovoltaic (PV) power is one of the most rapidly growing technology, and it is expected to play a major role in the future global electricity generation mix. According to the International Renewable Energy Agency (IRENA)<sup>1</sup>, solar PV power generation has exponentially increased from less than 9 gigawatt (GW) in 2007 to about 300 GW worldwide in 2017, as shown in Figure 1.1. Until now, solar PV only contributes less than 3 % of the total energy required to power the whole planet, which is estimated at 14000 GW (total energy consumption rate). The main problems preventing solar energy from becoming the most used energy source are the still non-competitive cost with respect to fossil fuels and the intermittency of electricity production. In order to harvest more of this inexhaustible energy, developing high performance, cost-effective materials with efficient production techniques, together with solving the problem of storing energy, are key success factors towards a pollution-free, sustainable energy production for the future.

The primary element in a solar cell is a semiconductor which absorbs light to produce free carriers of electrical charge. These carriers can then be separated by an internal electric field and extracted out of the semiconductor to produce an electrical current. In order to maximize light absorption and charge extraction efficiency, a transparent conductive material (TCM) is used in most of types of solar cell. Indeed, such a layer should collect the photo-generated carriers (it should be conductive) without absorbing much the visible light (it should then be

---

<sup>1</sup><http://www.irena.org/>

transparent). TCMs are key components not only in photovoltaic devices but are also very important in other optoelectronic devices, such as Light-Emitting Diodes (LEDs), flat-panel displays or smart windows.[8] Therefore, the development of TCMs using low-cost and easily scalable fabrication methods is of immense interest. To date, Indium Tin Oxide (ITO) is still the most used TCM thanks to its excellent optoelectronic properties (resistivity in the range of  $\sim 10^{-4} \Omega cm$ , optical transmittance above 80% in visible range).[9] However, this material is facing several challenges for a long-term use in the PV industry, such as Indium scarcity, brittleness and requirement of vacuum-processing. The substitution of ITO by alternative materials is required for a sustainable development in the photovoltaic industry. Over the years, research on alternative TCMs has been developed, going from TCMs with reduced amounts of In, including ZnO-In<sub>2</sub>O<sub>3</sub>, In<sub>2</sub>O<sub>3</sub>-SnO<sub>2</sub> or Zn-In-Sn-O, to In-free ones, including Al, Ga, or Cl doped ZnO (ZnO:Al, ZnO:Ga and ZnO:Cl [10]), conductive polymers, carbon nanotubes, graphene or Ag nanowires.[11–13] Taking into account the resource availability and environmental points of view, Aluminum doped Zinc Oxide (ZnO:Al) is one of the best candidates due to its advantages, namely earth-abundant elements and non-toxicity compared to Indium based TCO films.[14, 15] ZnO:Al films have been deposited using a wide variety of thin-film deposition techniques, both through physical vapour deposition (PVD) methods such as evaporation, magnetron sputtering deposition (MSD), molecular beam epitaxy (MBE) and pulsed laser deposition (PLD), and through chemical vapour deposition (CVD) techniques such as high-temperature CVD, metal–organic CVD (MOCVD), atomic layer deposition (ALD) and a range of other chemical methods, including electrochemistry, spin coating and the sol-gel method. After decades of research, ZnO:Al films with similar optoelectronic performance as ITO were only successfully deposited by using physical deposition techniques, such as MSD[16] or PLD.[17, 18] However, these techniques require vacuum-processing and a fairly complex set-up, increasing investment cost and limiting scalability. Therefore, thin film fabrication techniques should be low-cost, high-throughput and easily scalable in order to meet the industrial requirements.

To date, many thin film deposition techniques have been developed and widely used at both laboratory and industry scales, such as DC/RF magnetron sputtering, electron beam evaporator, molecular beam epitaxy (MBE), spin coating, electrochemistry, CVD, ALD... Over the past ten years, the field of ALD has experienced a dramatic increase. The Web of Science reveals that more than 3000 publications in 2017 and over 22000 publications since 2007 had “atomic layer deposition” in their abstracts or key words, as shown in Figure 1.2. What makes ALD a very interesting nanofabrication technology is its ability to achieve conformal and atomic layer controlled deposition thanks to the sequential exposures of gaseous precursors to the substrate and the self-limiting surface chemistry. These characteristics have

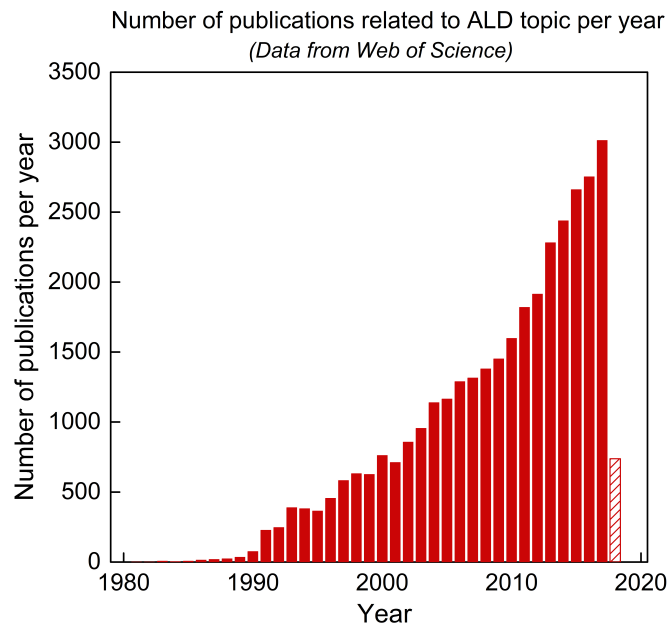


Figure 1.2: Evolution of the number of publications related to ALD, between 1980 and 2018 (data extracted from [Web of Science](#), Figure performed in 05/2018)

been well known since their introduction by Suntola in the early 1970s.[19, 20] In ALD, the separation sequence of half surface reactions by a purging step is the key point to achieve high-quality materials, but also this leads to the main drawback of ALD: being too slow to become widely used in industry. In recent years, an alternative approach to conventional ALD, namely Atmospheric Pressure Spatial Atomic Layer Deposition (AP-SALD), has received much attention.[21–24] In this novel concept, the precursors are injected continuously in different locations of the injection head that are separated by a region of inert gas. By alternatively exposing the substrate to the regions contains the different precursors, the ALD chemistry is replicated. SALD shares the same unique assets of ALD, but the main advantages are that it is orders of magnitudes faster than ALD since no purge is required, and that it can be performed at atmospheric pressure and even in the open air, i.e. without using a deposition chamber.

In the next sections of the introduction, we will present a bibliography summary on ZnO and related materials for transparent electrode applications. Then, the basic working principle of a solar cell and one type of high-efficiency solar cells, i.e. silicon heterojunction (SHJ), will be briefly recalled. At the end of the introduction, the aim and the outline of this work will be stated.

## 1.2 Towards high performance TCOs based on ZnO

Zinc oxide (ZnO) is a II-VI compound semiconductor with direct bandgap energy ( $E_g = 3.4$  eV at 300 K), which belongs to the class of transparent conductive oxides (TCO) like indium oxide ( $\text{In}_2\text{O}_3$ ) and tin oxide ( $\text{SnO}_2$ ). Over decades, ZnO has been attracting the research community because of having several advantages such as bio-compatibility, earth-abundance and non-toxicity, resulting in a potentially lower cost for ZnO-based devices.[25–27] In addition, its large exciton binding energy of 60 meV is very interesting for potential applications in laser diodes and light emitting diodes (LEDs).[28] The most commonly used ZnO-based transparent electrodes (i.e. Aluminum doped ZnO - ZnO:Al) is already commercially available for applications as the front contact for solar cells or liquid crystal displays (LCD).[29] In this sub-section, the fundamentals of ZnO and ZnO:Al, as well as their physical properties with emphasis on the electrical conductivity, will be briefly summarized.

### 1.2.1 ZnO: fundamentals and physical properties

Zinc Oxide exists naturally as the mineral zincite, usually colored red or orange by manganese impurities. Today, most of the ZnO produced worldwide is consumed in the powder form (in white color), and used in non-electronic applications such as for rubber production, chemicals, paints, in agriculture and for ceramics.<sup>2</sup> At ambient conditions, ZnO crystallizes in the hexagonal wurtzite structure  $P6_3mc$ , as shown in Figure 1.3. Besides the hexagonal wurtzite phase, ZnO has also two other allotropes, namely cubic rocksalt and cubic zinc-blende. The rocksalt structure is a metastable cubic phase, which can be observed at high pressure (wurtzite-rocksalt phase transition occurs at about 6 GPa at 300 K), while the cubic zinc-blende can be stabilized only by growth on cubic substrates.[5, 30]

Table 1.1 summarizes a number of physical properties of ZnO in comparison to indium oxide ( $\text{In}_2\text{O}_3$ ), tin dioxide ( $\text{SnO}_2$ ), and to silicon (Si). The data is extracted from the book of K. Ellmer et al. 2008.[5] From this summary, we can see that, in terms of the availability in the earth's crust, Zn and Sn are 400 times more abundant than Indium, which is one of the reasons for developing Indium-free TCOs.

In Table 1.1, ZnO is the only material exhibiting a piezoelectric property, i.e. the generation of a local electric field when subjected to a mechanical deformation. This is caused by the noncentrosymmetric characteristic of the ZnO crystal, i.e.lack of inversion center. The melting temperature of ZnO is very high ( $\simeq 1975$  °C). However, ZnO can decompose into the elements at temperatures as low as 1000 °C if the oxygen/zinc partial pressures are too low.[31, 32] Another important point when comparing ZnO to  $\text{In}_2\text{O}_3$  and  $\text{SnO}_2$  is their for-

<sup>2</sup><https://minerals.usgs.gov/minerals/pubs/commodity/zinc/>

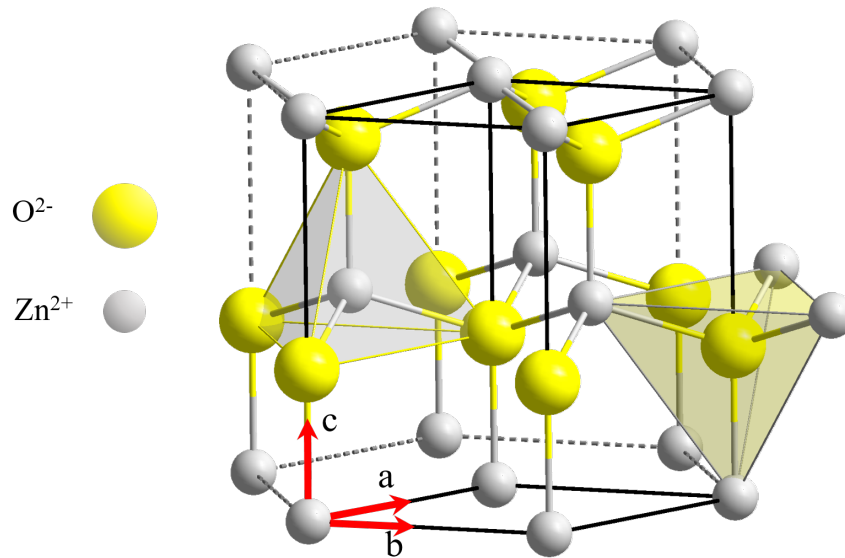


Figure 1.3: Wurtzite structure of ZnO with Zn cations and O anions highlighted in dark color and light color, respectively. (from Wikipedia)

mation energies (3.6 eV for ZnO, 4.8 eV for  $\text{In}_2\text{O}_3$  and 6 eV for  $\text{SnO}_2$ ), which explains the increase of their thermodynamic stability going from ZnO to  $\text{SnO}_2$ .

ZnO single crystals were successfully grown in the 1930s. Today, single crystalline ZnO can be grown by three main methods: hydrothermal growth (HT),<sup>[33, 34]</sup> seeded chemical vapour transport (s-CVT)<sup>[35]</sup> and from melts of salts ( $\text{ZnBr}_2$ ).<sup>[36]</sup> Figure 1.4 shows photographs of ZnO single crystal ingots (left) and wafers (right) produced through the hydrothermal process by the company Mineral Ltd in Russia.<sup>3</sup> In addition, the growth of thin ZnO crystal can be also performed by epitaxy on a monocrystalline substrate, for example  $\text{Al}_2\text{O}_3$ ,<sup>[37]</sup> diamond,<sup>[38]</sup> SiC<sup>[39]</sup> or GaAs.<sup>[40]</sup> In an ideal ZnO crystal, there should not be any free electron in the conduction band due to very large bandgap, however, free electron concentration up to  $1 \times 10^{17} \text{ (cm}^{-3}\text{)}$  is observed in ZnO single crystals, which confirms the n-type nature of as-grown ZnO single crystals.<sup>[35]</sup> Actually, there are always point defects such as vacancies, interstitials... or unintentionally doped impurities during processing, which may act as electron donors. Since the density and the nature of point defects in ZnO (or more generally, in any semiconductor material) are directly related to the material's physical properties, knowing and being able to control them in order to adapt the deposition conditions is the key success factor towards high-quality materials. A summary of intrinsic and extrinsic defects in ZnO

<sup>3</sup><https://gemmakorea.wordpress.com/2015/07/27/we-provide-zno-material/>

Parameter	Unit	ZnO	In <sub>2</sub> O <sub>3</sub>	SnO <sub>2</sub>	Si
Abundance	%	$7.8 \times 10^{-3}$	$1.6 \times 10^{-5}$	$2.2 \times 10^{-4}$	27.7
Eg (@300 K)	eV	3.4 (D)	3.6 (D)	3.6 (D)	1.12 (I)
Lattice		Hexagonal	Cubic	Tetragonal	Cubic
Structure		Wurtzite	Bixbyite	Rutile	Diamond
Space group		P6 <sub>3</sub> mc	Ia3	P4 <sub>2</sub> /nm	Fd3m
Lattice constants	Å	a=3.25; c=5.21	10.12	a=4.74; c=3.19	5.43
Density	$g \cdot cm^{-3}$	5.67	7.12	6.99	2.33
$\kappa$	$Wm^{-1}K^{-1}$	69 <sub>  </sub> ; 60 <sub>⊥</sub>		98 <sub>  </sub> ; 55 <sub>⊥</sub>	150
$\alpha$	$10^{-6}/K$	2.92 <sub>  </sub> ; 4.75 <sub>⊥</sub>	6.7	3.7 <sub>  </sub> ; 4 <sub>⊥</sub>	2.59
$P_{\perp}$		0.21			
$\epsilon_s$		8.75 <sub>  </sub> ; 7.8 <sub>⊥</sub>	8.9	9.58 <sub>  </sub> ; 13.5 <sub>⊥</sub>	11.9
$\epsilon_{\infty}$		3.75 <sub>  </sub> ; 3.7 <sub>⊥</sub>	4.6	4.17 <sub>  </sub> ; 3.78 <sub>⊥</sub>	
$T_m$	°C	1 975	1 910	1 620	1 410
$\Delta H_f$	eV	3.6	4.8	6.0	

Table 1.1: Physical properties of ZnO in comparison to indium oxide (In<sub>2</sub>O<sub>3</sub>), tin dioxide (SnO<sub>2</sub>) and Silicon (Si). Abundance of the metal in the earth's crust (approximate % by weight, [periodictable.com](http://periodictable.com)), crystal structure and lattice parameters,[5] || and ⊥ denote parallel and perpendicular to c-axis, respectively;  $\kappa$ : thermal conductivity,  $\alpha$ : thermal expansion coefficient,  $P_{\perp}$ : piezoelectric coupling coefficient,  $\epsilon_s$  and  $\epsilon_{\infty}$ : static and optical dielectric constants,  $T_m$ : melting temperature,  $\Delta H_f$ : heat of formation per formula unit.

will be briefly described below.

Of all the TCO materials, native defects have been studied most extensively in ZnO.[25, 41–43] By definition, intrinsic point defects are any displacement, replacement or removal of lattice atoms. Some popular types of intrinsic defects that can be found in ZnO are listed below:

- Vacancy: absence of an atom in the crystal structure;  $V_{Zn}$ ,  $V_O$  denote zinc and oxygen vacancies, respectively.
- Interstitial: insertion of an atom in the crystal structure at which there is usually not an atom;  $Zn_i$ ,  $O_i$  denote zinc and oxygen interstitials, respectively.
- Antisite: replacement of a zinc atom in the crystal structure by an oxygen atom or conversely, replacement of an oxygen atom by a zinc atom;  $Zn_O$ ,  $O_{Zn}$  denote antisite zinc and oxygen, respectively

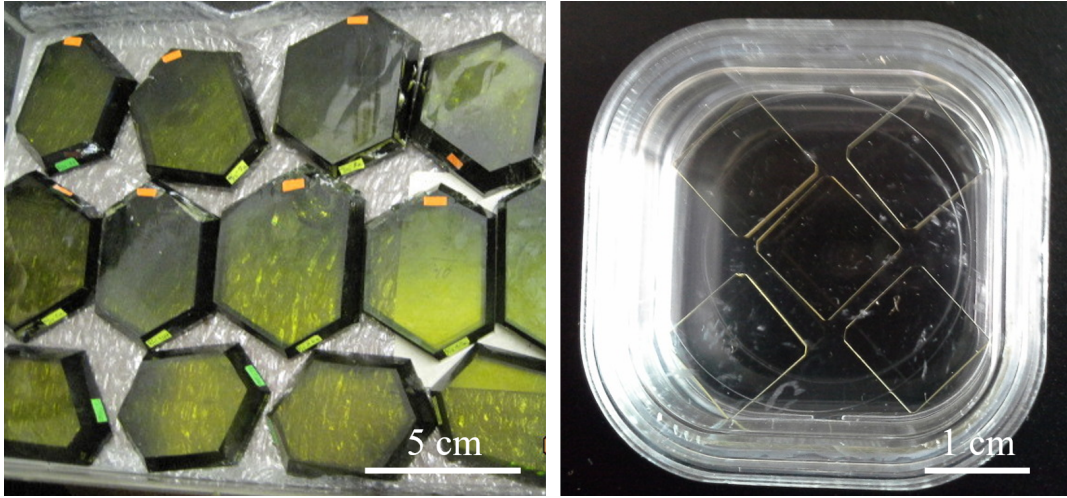


Figure 1.4: (left) ZnO single crystal ingot, produced through hydrothermal process, (right) ZnO wafers ( $10 \times 10 \times 0.5 \text{ mm}^3$ ). (by Mineral Ltd, Russia)

- Defect complexes: Schottky (cation and anion vacancy) or Frenkel (cation vacancy and cation interstitial). In ionic crystal such as ZnO, the cation ( $\text{Zn}^{2+}$ ) is smaller than the anion ( $\text{O}^{2-}$ ), which means that the formation of Frenkel defects for cations is much more favorable than for anions

An important aspect of intrinsic defects in ZnO is their formation energies. At thermodynamic equilibrium, the concentration of a defect can be written as follows:[1]

$$N_D = N \cdot \exp\left(-\frac{E^f}{k_B T}\right) \quad (1.1)$$

where  $N$ ,  $E^f$ ,  $k_B$ ,  $T$  are the available sites per volume in the lattice where the defect type can be incorporated, the formation energy per defect, the Boltzmann constant and temperature, respectively. In their review, A. Jannotti and C.G. Van de Walle performed a comprehensive first-principles investigation of native point defects in ZnO based on density functional theory (DFT).[44] Accordingly, Figure 1.5 shows a summary of a number of common types of point defects usually found in ZnO for both Zn-rich (left) and O-rich (right) conditions. A point defect can be neutral, which corresponds to a constant  $E^f$ , or charged, which correspond to either ionized donors (with positive slope) or ionized acceptors (with negative slope). For example, in the case of a zinc vacancy in ZnO, the formation energy is given by:

$$E^f(V_{\text{Zn}}^q) = E_{\text{tot}}(V_{\text{Zn}}^q) - E_{\text{tot}}(\text{ZnO}) + \mu_{\text{Zn}} + q(E_F) \quad (1.2)$$

where  $E_{\text{tot}}(V_{\text{Zn}}^q)$  is the total energy of a supercell containing the zinc vacancy in the charge state  $q$ ,  $E_{\text{tot}}(\text{ZnO})$  is the total energy of a ZnO perfect crystal in the same supercell,  $\mu_{\text{Zn}}$  is

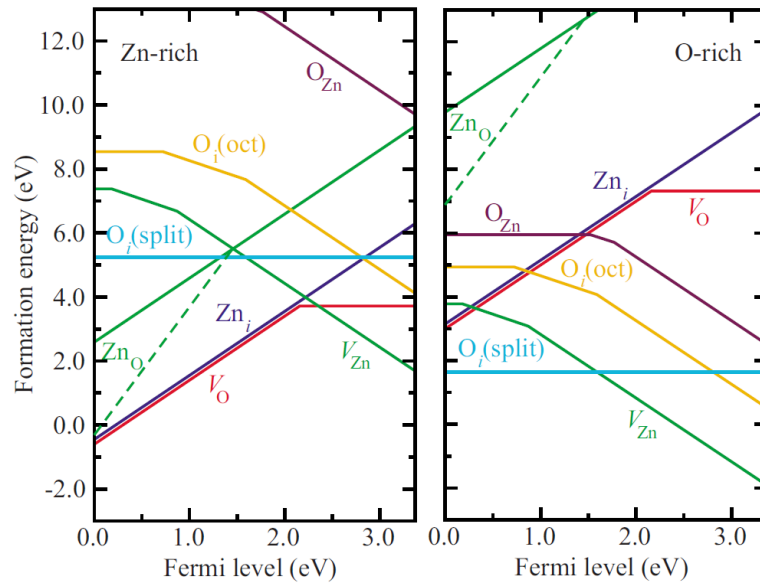


Figure 1.5: Formation energies versus Fermi level of some native point defects in ZnO, calculated using an extrapolation scheme based on LDA and LDA+U calculations. Results are shown for Zn-rich (left graph) and O-rich (right graph) conditions. The zero level of Fermi energy corresponds to the top of valence band (extracted from [1]: A. Jannotti & C.G. Van de Walle, 2007).

the zinc chemical potential and  $E_F$  is the Fermi level. As can be seen, the formation energy of a charged defect directly depends on the Fermi level, which is the chemical potential of electrons, and is not constant but depends on growth conditions and post-deposition conditions. For example, in the case of O-rich conditions, a lowering of  $E^f$  for defect formation energies concerning the addition of oxygen or the removal of Zn ( $O_i$ ,  $V_{Zn}$ ) and vice versa is observed.[5] Concerning the donor-type defects, the oxygen vacancies had been commonly assumed to be sources of n-type conductivity in ZnO because it has the lowest formation energy. However, several DFT calculations revealed that oxygen vacancies are rather deep donors, with the  $[0/2+]$  transition level lying well below the minimum of the conduction band. Therefore, these cannot be the origin of n-type behavior in ZnO. Other suggestions to explain the n-type nature of ZnO are hydrogen impurities, which have been identified as a shallow donor, or defects complexes such as oxygen vacancy and zinc interstitial, Zn-interstitial with a nitrogen impurity on the oxygen site...[42, 43, 45, 46] It should be also noted that the formation energy of native defects in ZnO is mainly drawn from the framework of DFT calculations, which are strictly valid at 0 K. Conversely, ZnO growth usually occurs at high temperature, and not always in an equilibrium process. Therefore, the real formation energy should be evaluated within these conditions. Consequently, a complete explanation for n-type nature of as-grown intrinsic ZnO is still pending. Concerning the acceptor-type defects, the zinc vacancy  $V_{Zn}$

Element	Structure	Energy ( $E_C - E_D$ ) (meV)	Ionic radius (pm) ( $Zn^{2+} = 74$ pm)	Source
B	$B_{Zn}$	–	41	[15]
Al	$Al_{Zn}$	53	53	[5]
Ga	$Ga_{Zn}$	54.5	62	[5]
In	$In_{Zn}$	63.2	80	[5]
H	$H_i$	46	–	[49]
O	$V_O$	300	–	[49]

Table 1.2: List of donors with corresponding binding energy level and ionic radius.  $E_C$  and  $E_D$  refer to the minimum of the conduction band and the donor defect energy level with respect to  $E_C$ .

has the lowest formation energy, therefore, the most favorable acceptor in ZnO. Moreover, the formation energy of acceptor-type defects decreases with increasing Fermi level.  $V_{Zn}$  can thus more easily form in n-type samples. The presence of  $V_{Zn}$  in n-type ZnO has been identified by positron annihilation experiments.[47, 48] In highly doped ZnO, the free electron injected from appropriate donors to the conduction band is partly trapped by the acceptors, lowering the effective carrier concentration and thus, the electrical conductivity. This so-called self-compensation effect is originated from the tendency of a crystalline semiconductor material to lower its free energy by forming point defects to compensate the effects of dopants. In doped ZnO materials, this effect becomes more important in O-rich conditions such as in the case of films prepared in open atmosphere, as in the case of the present work, or undergoing an annealing in oxygen rich condition.

Since undoped ZnO is not conductive nor stable enough (with temperature, atmosphere) for applications, extrinsic doping with group-III elements such as Boron (B), Aluminum (Al), Gallium (Ga) or Indium (In) has been studied to fabricate controlled n-type doped ZnO. Table 1.2 summaries these donor elements, along with hydrogen interstitial and oxygen vacancy discussed in the previous section, in ZnO with corresponding ionization energy of the donor level in the ZnO bandgap. The ion radius of B, Al, Ga and In are also listed in comparison with the one of zinc (74 pm). Boron has the smallest ion radius, it can act as either interstitial or substituted boron in the ZnO lattice. Also, the big difference between the radius sizes of boron and zinc ions can degrade the crystal quality of deposited film. In term of doping efficiency, Al and Ga have been studied and known as the two most efficient dopant elements for ZnO. However, using Al is much cheaper and easier to handle during processing than Ga, making Al the most attractive dopant element for ZnO. In the next part, the state-of-the-art of ZnO:Al development will be briefly discussed.

<b>Main factors affecting carrier concentration and mobility</b>		
<u>Carrier concentration <math>n</math></u>		<u>Carrier mobility <math>\mu</math></u>
Intrinsic defects (vacancies, interstitials...)		Phonon-electron scattering ( <i>temperature</i> )
Extrinsic dopants (H, B, Al, Ga, In...)	Concentration	Intrinsic defect scattering (in-grain crystallographic defects)
	Activation efficiency	
<i>Temperature</i>		Impurity scattering (ionized impurities)
<i>Light</i>		Grain boundary scattering ( <i>temperature</i> )

Table 1.3: A summary of factors, with impact on the electrical conductivity of a semiconductor material. The words highlighted in *italic* refer to external impacts.

### 1.2.2 ZnO:Al thin films

The essential requirements for a transparent electrode (TE) are high transparency, high conductivity, as well as a tailored interfaces between the TE and the active electronic material. In the case of ZnO:Al, its large optical bandgaps ( $> 3.3$  eV) is responsible for high transparency ( $\geq 85$  %) in the NIR-visible range (360 nm - 1100 nm). A drop of transparency in the IR range is usually observed due to the plasmonic effect, i.e. interaction between the electric field of incident light and electrons in the conduction band. Concerning the electrical properties, ZnO:Al films with a high conductivity  $\sigma$  should have a high carrier concentration  $n$  (electrons in n-type case or holes in p-type case) and a high carrier mobility  $\mu$ . Since  $\sigma = nq\mu$ , all experimental efforts towards a high conductivity should be improving the carrier concentration, as well as keeping a sufficiently high carrier mobility. Now, it is interesting to look back to a fundamental question: which factors impact  $n$  and  $\mu$ ? so that these parameters can be tuned in order to reach a high performance material.

Table 1.3 summarizes a number of factors that impact the electrical conductivity of a semiconductor material in general, which is also valid for ZnO:Al films. Accordingly, the carrier concentration is mainly attributed to the density of shallow extrinsic donors, as well as the activated fraction of these defects that contribute to electrical conduction. As well, the carrier concentration is strongly affected by the compensation effect, or by the post-deposition treatment. Look et al. studied and showed the evidence of the compensation effect for the case of ZnO:Ga films deposited by PLD, with carrier concentration in the range  $[8 \times 10^{20}; 1.5 \times 10^{21}]$  ( $cm^{-3}$ ).<sup>[50]</sup> Two years later, Thienprasert et al. used Synchrotron X-Ray Absorption Spectroscopy (XAS) to demonstrate that the compensation effect in ZnO:Al films becomes more important when the sample deposition is carried out in an oxygen-rich atmosphere, which promotes the formation of  $V_{Zn}$ .<sup>[51]</sup> Another example to show the importance of post-deposition

treatment was reported by B.-Y. Oh et al, who showed that annealing ZnO:Al sample in hydrogen atmosphere can increase free carrier concentration from  $2.11 \times 10^{20}$  up to  $8.86 \times 10^{20}$  ( $cm^{-3}$ ), which originated from electron release during the desorption of the negatively charged oxygen species from the grain boundary interfaces by the hydrogen treatment.[52]

Sample	Method	$T(^{\circ}C)$	$P(Pa)$	$\rho (\Omega cm)$	$n (cm^{-3})$	$\mu$ (300 K)	Ref
Single crystal	s-CVT	1100		0.3	$1 \times 10^{17}$	209	[35]
Single crystal	HT	300-400	$10^8$	390	$8 \times 10^{13}$	200	[33]
ZnO:Al Film	PLD	230	$10^{-4}$	$8.5 \times 10^{-5}$	$1.5 \times 10^{21}$	47.6	[53]
ZnO:Al Film	Sputtering	100	0.3	$3.7 \times 10^{-4}$	$5.9 \times 10^{20}$	28	[54]
ZnO:Al Film	ALD	125	$10^3$	$1.4 \times 10^{-3}$	$2.2 \times 10^{20}$	19.7	[55]
ZnO:Al Film	AP-SALD	200	$10^3$	$2 \times 10^{-3}$	$5 \times 10^{20}$	5	[56]

Table 1.4: Comparison of physical properties of commercially available ZnO single crystals and some ZnO:Al thin films prepared by different deposition techniques, s-CVT (seeded chemical vapour transport), HT (hydrothermal), PLD, ALD and AP-SALD.  $\rho (\Omega cm)$ ,  $n(cm^{-3})$ ,  $\mu(cm^2V^{-1}s^{-1})$  denote resistivity, carrier concentration and carrier mobility, respectively.

The carrier mobility is limited by several scattering mechanisms including phonon-electron interactions, scattering by defects or by grain boundaries in the case of polycrystalline films. In practice, it is very difficult to increase the carrier density without affecting their mobility, as well the crystallinity of the base material. While ZnO single crystal exhibits a relatively high electron mobility of about  $200 cm^2V^{-1}s^{-1}$ , the highly doped ZnO thin films required for transparent electrode applications have a much lower carrier mobility ( $< 60 cm^2V^{-1}s^{-1}$ ), which are mainly attributed to grain boundary and impurity scatterings. Table 1.4 presents a summary of electrical properties of some undoped ZnO single crystal and doped ZnO thin films, along with their preparation methods and experimental parameters. The reported electrical properties for ZnO:Al films are very different, with the record conductivity associated to films deposited by pulsed laser deposition (PLD). This observation suggests a limit of physical properties of as-deposited films related to the fabrication method itself. However, it is always interesting to compare different methods over different aspects than only the optoelectronic properties, such as cost, applicability in large scale, thickness uniformity, possibility to deposit films at low temperature on polymeric substrate, compatibility with vacuum-free processing, etc. The key challenge at present is thus to develop chemical routes with a focus on the parameters just cited and capable of yielding high performance ZnO:Al films.

## 1.3 Solar cells: from fundamentals to advanced concepts

As mentioned previously, solar energy is one of the renewable energy sources with the highest potential, one of the main applications of TCMs. In this section, we present an overview on the working principles of solar cells, then an attractive new generation silicon-based technology, namely silicon heterojunction (SHJ) solar cells.

### 1.3.1 Working principle of a solar cell

The fundamental principle of a solar cell is the photovoltaic effect, i.e. the generation of voltage and electric current via the interaction between a junction of two different materials, namely n-type and p-type semiconductors, and the electromagnetic radiation received from the sun. Three physical processes occur during the operation of conventional solar cells:

- Absorption of incident photons by the semiconductor material resulting in photo-generated carriers of two types of charges: electron and hole
- Separation of the carriers thanks to an electric field created by a p-n junction between the two semiconductors
- Transport and collection of the carriers at the output electrodes

The starting question concerns the criteria to select optimal materials to absorb as much as possible of the solar spectrum. The visible light that we see everyday is only a fraction of the total solar radiation incident on the earth. In the PV sector, the so-called AM1.5 Global solar spectrum is used as standard reference, which has an integrated power of about  $1000 \text{ W/m}^2$ . The whole AM1.5 spectrum exhibits a wide range of wavelengths, from the ultraviolet to the infrared range, as shown in Figure 1.6. However, there is no ideal material that can absorb the entire solar spectrum: only the photons having energy higher than a threshold value, i.e. the bandgap energy  $E_g$  of the semiconductor material, can be absorbed.

In addition, each photon of sufficient energy ( $> E_g$ ) can only create one electron-hole pair, the exceeding energy being transferred to heat via thermalization phenomena (creation of phonons). Figure 1.6 shows the maximum fraction of the solar spectrum that could be converted into electricity by using a single junction silicon solar cell. The mentioned term 'bandgap' refers to the energy difference between the top of the valence band (which is a filled band at least at low temperature and without any doping) and the bottom of the conduction band (empty band). In other words, it is the minimum amount of energy required for an electron to break free of its bound state through the absorption of a photon with equal or higher energy, resulting in the creation an electron-hole pair. The bandgap concept is fundamental to

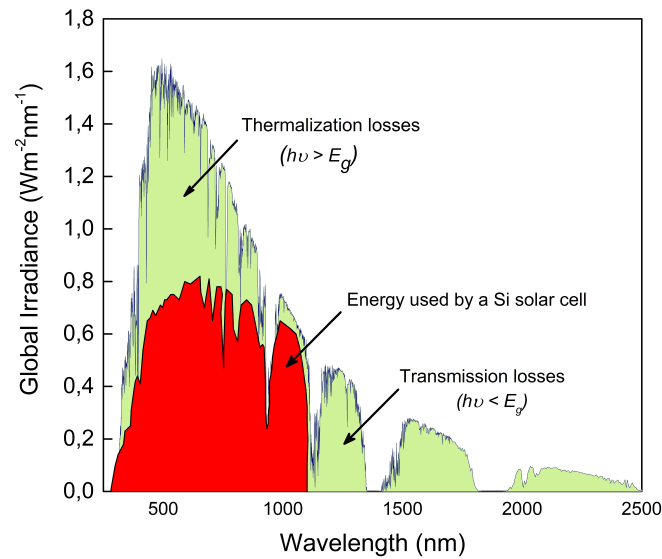


Figure 1.6: Solar spectrum AM1.5 plotted versus wavelength (Data extracted from [pvlighthouse.com.au](http://pvlighthouse.com.au)). The red area illustrates the fraction that can be used with a silicon solar cell

the understanding of the operation of solar cells. Figure 1.7 shows a schematic representation of bandgap energies in metal, semiconductor and insulator materials, respectively.

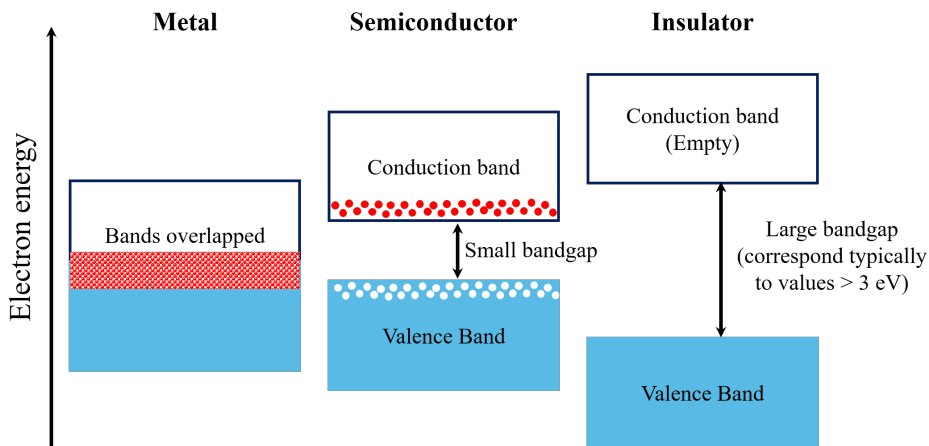


Figure 1.7: Schematic representation of bandgap energies in metal, intrinsic semiconductor and insulator at 300 K. Red and white dots represent electrons and holes, respectively.

In metals, the valence and conduction bands overlap or are partially filled. Therefore, electron states and available energy states are intermixed within the bands, in which a large number of electrons can freely move under an applied electric field or a gradient temperature: this is at the origin of the very good thermal and electrical conductivity of metals. In insulators, the large bandgap energy, usually greater than 3 eV, is insurmountable for electrons in the

Material	Symbol	Bandgap energy (eV) @ 300 K	Nature of bandgap
Gallium arsenide	GaAs	1.43	Direct
Germanium	Ge	0.66	Indirect
Silicon	Si	1.12	Indirect
Indium phosphide	InP	1.35	Direct
Cadmium telluride	CdTe	1.49	Direct
Cadmium sulfide	CdS	2.42	Direct
Amorphous silicon	a-Si	~ 1.8	Indirect

Table 1.5: Bandgap energies of different materials (<http://www.ioffe.ru>).

valence band to be excited into the conduction band. In the case of an intrinsic semiconductor, the bandgap energy is small enough so that even at room temperature some electrons (depicted by red dots) can be thermally excited from the valence band to the conduction band and leaving some positive charges in the valence band, namely, holes (depicted by white dots), as shown in Figure 1.7.

The light absorption efficiency of a semiconductor is related not only to its bandgap energy but also its bandgap nature, i.e. direct or indirect. Table 1.5 shows bandgap energies and natures of different semiconductors used in photovoltaics. In reality, the valence and conduction bands of a semiconductor material are not flat but depend on the  $k$ -vector, which describes the momentum of electrons in the material. The direct bandgap refers to the case when the maximum of the valence band and the minimum of the conduction band are both situated at the same  $k$ -vector. The situation is opposite for an indirect bandgap semiconductor. Consequently, an electron in a direct bandgap semiconductor can get excited from the valence band to the conduction without changing its momentum, which results in a higher absorption coefficient. Conversely, the absorption of a photon by an indirect bandgap semiconductor layer would require the interaction with a third quasiparticle (phonon) which drastically lowers the occurrence probability, resulting in a lower absorption coefficient. Figure 1.8 shows the absorption coefficient of typical semiconductor materials used in photovoltaics at 300 K as function of incident light wavelength.

It is clear that low bandgap materials such as germanium (0.66 eV) show a very high absorption coefficient. The most popular solar cell material, silicon, has a bandgap energy of 1.12 eV, which is comparable with gallium arsenide (1.42 eV), indium phosphide (1.35 eV) or cadmium telluride (1.44 eV). However, Silicon has an indirect bandgap, therefore the photon absorption is less efficient than in the case of direct bandgap materials. This is the reason why in crystalline Silicon photovoltaic technologies, the substrate is usually much thicker than III-V material technologies (GaAs, InP or CdTe). The appropriate semiconductor to be used in photovoltaics should absorb as much as possible of the solar spectrum, hence, a low bandgap

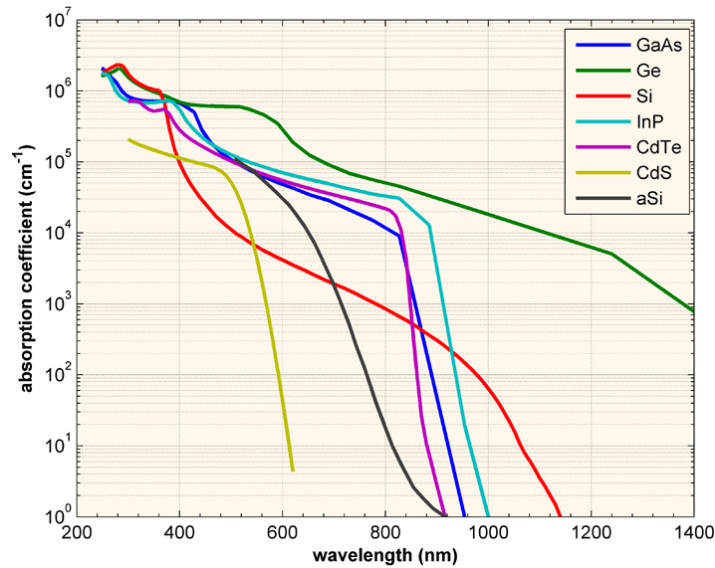


Figure 1.8: Absorption coefficient in a variety of semiconductor materials at 300 K as function of incident light wavelength (<https://www.pveducation.org>).

material seems desirable. However, if the bandgap is too low, as in the case of Germanium, a high degree of thermalization occurs, as explained above. In addition, the bandgap energy of absorbing material determines the output potential difference, which is directly related to the device performance. Therefore, the compromise between the absorption efficiency and the energy lost in the form of heat leads to an optimum bandgap range in between 1 eV and 1.7 eV.[57]

PN junctions are the key to numerous electronic devices. In a solar cell, after generation of electron-hole pairs by photon absorption, electrons in the p-type materials and holes in the n-type materials are not stable and only exist during a short time, called the minority carrier lifetime, before they recombine. The role of the electric field at the pn junction is to spatially separate the photo-generated electrons and holes (electrons driven to n-type side, holes driven to p-type side), thus preventing the photo-generated carriers from recombining. Figure 1.9 shows schematic representations of a pn junction and corresponding band diagrams under dark and illumination conditions.

In the dark, the electron diffusion current (from n-type to p-type side) and the electron drift current (electrons thermally generated in p-type side are swept across the junction to n-type side by the electric field) exactly balance out. As a result, the net current is zero. Under illumination condition, the electron-hole pairs photo-generated in the junction area can be very efficiently separated without recombination losses. In the other regions, the minority photo-generated carriers, which are represented by red dots for electrons in the p-type zone

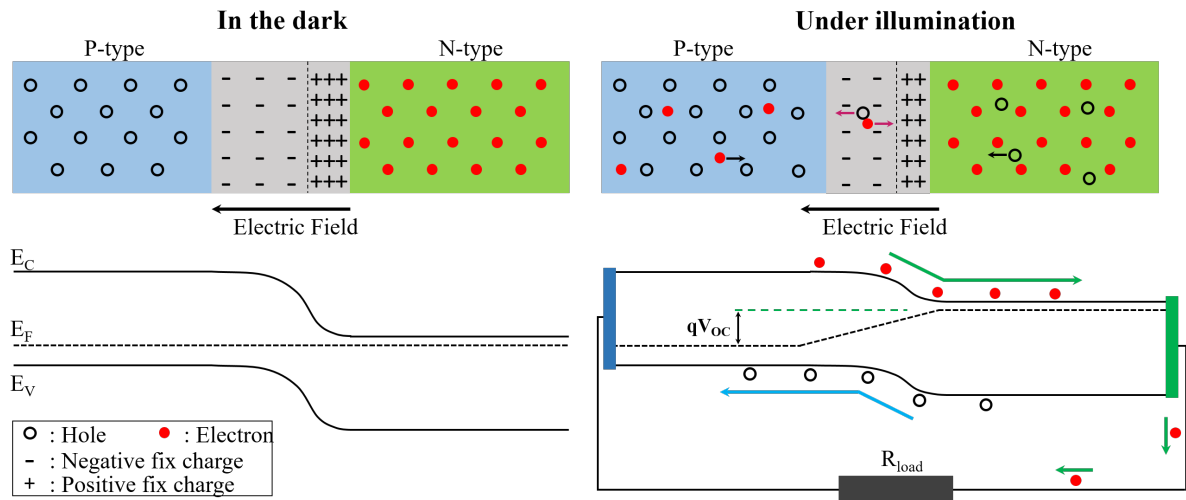


Figure 1.9: Schematic representation of a pn junction in the dark and under illumination.

and blank cycles for holes in the n-type zone, have to diffuse to the space charge region before they recombine. Then they are separated by the built-in electric field. Finally, these photo-generated free carriers can be collected at two electrodes connected to a suitable external load.

For solar characterization, the current voltage JV curve is an important characteristic which allows to evaluate the performance of solar cells. In Figure 1.10, the current density  $J$  and the power density  $P$  as function of voltage  $V$  of a standard solar cell are illustrated. This JV characteristic can be simply described by the one-diode model as follows:

$$J(V) = J_0 \left( \exp \left( \frac{q(V - |J \cdot R_s|)}{n \cdot k_B \cdot T} \right) - 1 \right) + \frac{V - |J \cdot R_s|}{R_{sh}} - J_{ph} \quad (1.3)$$

where  $J_0$  is the dark saturation current density,  $q$  the elementary charge,  $k_B$  the Boltzmann's constant,  $T$  the temperature,  $n$  the ideality factor describing the quality of the diode,  $R_s$  the series resistance,  $R_{sh}$  the shunt resistance and  $J_{ph}$  the photogeneration current density. In the dark, the solar cell behaves as a normal diode, as shown in first term of eq. 1.3. The illuminated JV curve has the same form as the dark JV one, but shifted down by adding the photo-generated current density  $J_{ph}$ . The open-circuit voltage  $V_{oc}$  and the short-circuit current density  $J_{sc}$  are the intersection points of the JV curve with the voltage and current axes, respectively. The JV curve also allows to calculate the maximum electrical power generated from the solar cell  $P_m$ , which corresponds to a product of a current density  $J_m$  and a voltage  $V_m$ . Another important parameter is the so-called fill-factor  $FF$ , which is the ratio  $P_m$  to the product of  $V_{oc}$  and  $J_{sc}$ . Finally, the energy conversion efficiency  $\eta$  is the ratio of maximum

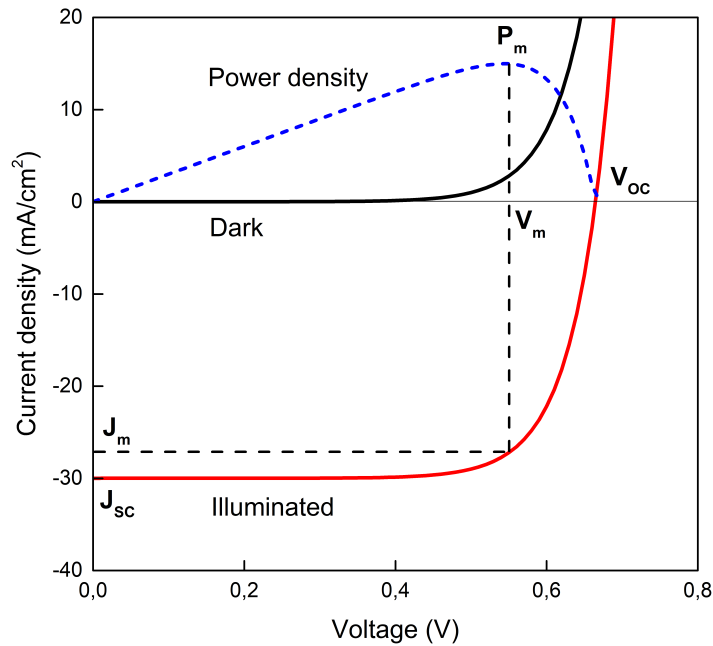


Figure 1.10: JV curves under dark and illumination conditions, and electrical power density of a standard solar cell as function of external voltage

obtainable power to the incident solar power  $P_{in}$ , and can be expressed as follows:

$$\eta = \frac{P_m}{P_{in}} = \frac{J_{sc} \cdot V_{oc} \cdot FF}{P_{in}} \quad (1.4)$$

According to the Shockley–Queisser limit,[58] the maximum solar conversion efficiency is around 33.7% for a single p-n junction photovoltaic cell and for a material having an optimal bandgap energy of 1.34 eV. In the case of Silicon, this limit value is about 29 %. In order to achieve high energy conversion efficiency in silicon solar cells, some following strategies are usually considered:

- Maximize the light absorption by texturing the front surface, applying transparent conductive layers... (which mainly affects  $J_{sc}$ )
- Reduce recombination losses by passivating surfaces, either by field effect passivation or chemical passivation
- Reduce electrical losses due to series and shunt resistances (which mainly affects  $FF$ )

### 1.3.2 Silicon heterojunction solar cells

The first crystalline Si (c-Si) solar cell had an energy conversion efficiency of 6 % using diffused p-n junctions.[59] Since its discovery, c-Si is still by far the most used PV material, with a current share of more than 80%. The first factor that makes c-Si such a popular PV material is its non-toxicity, abundance as well as the well controlled and known physical properties and fabrication methods. The second factor is that c-Si has been widely used with extraordinary success in the microelectronics industry, from which the PV community profited greatly from its expertise.[60] After several decades of research, the energy conversion efficiency of c-Si solar cells have been improving continuously and reached more than 24 % in 2014,[61, 62] and the current world-record 26.6 % in 2017,[63] which approaches the theoretical limit of c-Si solar cell efficiency. One of the most important efforts made to achieve high efficiency is reducing the minority carrier losses via recombination. This can occur both in c-Si bulk due to improved crystalline quality of substrate or at the interfaces where exists a high density of defects due to the abrupt ending of the crystal lattice. Using a high quality of c-Si substrate certainly enhances the device performance via a great reduction of bulk recombination, however, this solution is not cost-effective. Another solution, which just requires low-cost, low temperature processing, is to reduce the interface recombination by using a thin passivation layer. In a c-Si heterojunction (SHJ) structure, thin hydrogenated amorphous silicon (a-Si:H) layers deposited on the c-Si wafer allow decreasing greatly the recombination losses at the interfaces a-Si:H/c-Si. Actually, the current world-record c-Si solar cell with efficiency of 26.7 % is based on this type of approach.[63, 64] The key success factors of SHJ solar cells includes: a) the great interface passivation quality between c-Si substrate and a-Si:H thin films; b) the metal contacts, which are highly recombination active in traditional, diffused-junction cells, are electronically separated from the c-Si absorber by inserting a wider bandgap material: a-Si layer ( $E_g \sim 1.6 \text{ eV} - 1.9 \text{ eV}$ ). Figure 1.11 shows is a scheme of today's standard SHJ cell layer stack including its band diagram. This simple structure can provide a high conversion efficiency with no complicated structural techniques, such as partly heavy doping or a partial oxidation method. The band diagram illustrates how electrons and holes can be selectively transported through the  $n^+$  and  $p^+$  sides, respectively, thanks to the high bandgap and appropriate doping of a-Si:H layers.

A surface passivation can be achieved by two methods: the field effect passivation and the chemical passivation. The field effect passivation consists of producing a band bending at the c-Si surface, thus creating an electric field. This electric field will prevent one type of carriers to reach the surface defect center. Therefore, two types of carriers cannot be present at the same time at the surface defects to recombine, the recombination rate thus being strongly reduced. Concerning the chemical passivation, it aims to reduce the surface defects by saturat-

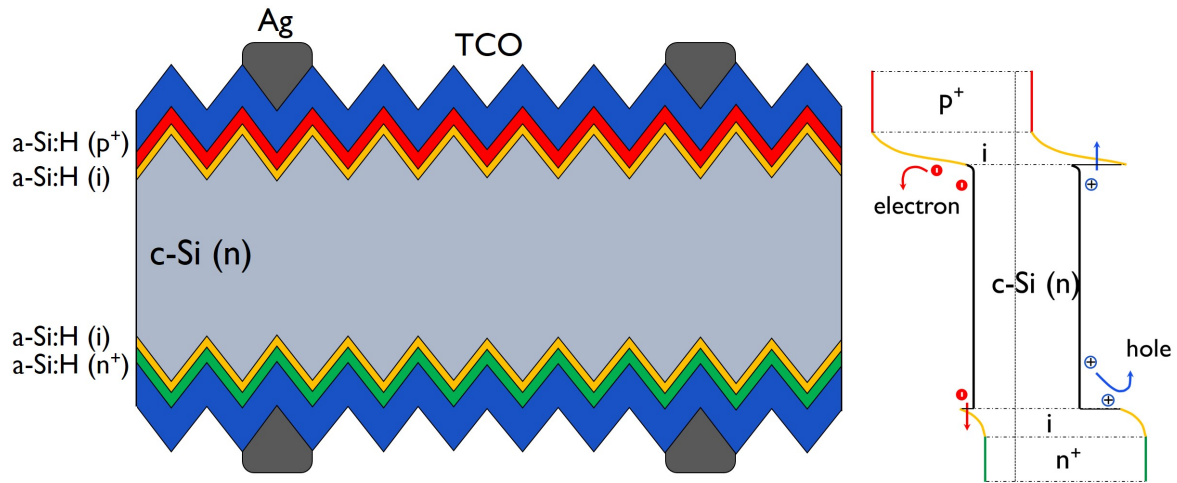


Figure 1.11: Sketch of a front emitter (pn junction in on the front side) SHJ solar cell including its band diagram.

ing the silicon dangling bonds. In the case of c-Si/a-Si:H interfaces, both type of passivations play important role. The hydrogen added during the a-Si:H layer deposition allows to saturate the silicon dangling bonds, while the band bending between c-Si and highly doped a-Si:H is responsible of field effect passivation, as shown in Figure 1.11.

The a-Si:H layers are deposited by Plasma Enhanced Chemical vapour Deposition (PECVD) at temperatures as low as 200 °C to ensure the amorphous nature of the layers. The light absorption in a-Si:H layers cannot be converted into free carriers, therefore, the a-Si:H films used in SHJ solar cells are often very thin (less than 20 nm). Moreover, the a-Si:H layers are very resistive, which makes the charge collection not efficient. A transparent conductive material (TCM) layer, usually a transparent conductive oxide (TCO), is thus necessary in this case. It helps to collect charges from a-Si:H layers, to make a better contact with metal contacts, as well as to act as an antireflective layer. In order to reach a high-performance SHJ solar cell, some requirements concerning the physical properties of TCO layers are listed below:

- High transparency, particularly in the visible range ( $> 85\%$ )
- High conductivity ( $> 10^3 S/cm$ )
- Low contact resistance with a-Si:H layers, allowing to extract efficiently charge carriers
- Low contact resistance with metal grid

The performances of SHJ solar cells depend not only on the properties of the TCO layer itself but also on its deposition technique, which affects the bottom layers. Therefore, some particular conditions for deposition technique are required:

- Low temperature ( $\leq 200$  °C), in order to preserve the electrical properties of the active layers, mainly the amorphous state of silicon, as well as the possibility to use low-cost substrate.
- Low-damage deposition, allowing to keep high-quality of interface passivation
- High uniformity and conformality of deposited layers
- Low-cost and easy to scale up

To date, the most used TCOs in SHJ solar cell is still ITO, deposited by sputtering. The company IDTechEx estimates that 1 m<sup>2</sup> of 50 nm thick ITO layer, which is a lower bound to what is used in SHJ solar cells, costs around 30 €. Considering a solar cell efficiency of 20 %, this means that the ITO amounts for 0.15 € per peak Watt: this is about 12 % of the price of the photovoltaic energy. When analyzing the cost of the different components of a heterojunction solar cell produced at LABFAB (pilot line at CEA-INES): the cost share of ITO also represents 12% of the global price, making TCO the second most expensive element in such a solar cell (after silicon wafer and silver). Because of the high cost and perceived scarcity of Indium, replacement of ITO with alternative materials thus has a high commercial potential.

## 1.4 Aim and outline of this work

As stated in the previous sections, high performance TCMs produced by low-cost chemical approaches are required for application in attractive new generation solar cell technologies. The aim of this thesis is thus to develop low-cost TCMs based on ZnO:Al thin film for photovoltaic applications by using a new and attractive deposition method, i.e. AP-SALD. For this purpose, the optimization of the TCMs, which is crucial for the improvement of the solar cells, was realized in several steps, which are described in this work as follows:

Chapter 2 presents the deposition technique used in this work, i.e. AP-SALD, including the description of both its working principle and the technical details of the set-up developed at LMGP. The main characterization techniques used in this thesis work are also presented.

Chapter 3 focuses on the study of the effect of different experimental parameters including the deposition temperature, gas flows, and the substrate/precursor injector distance on the growth rate, the crystallinity, the electrical properties and the nanostructure of the deposited films. For that, both experimental characterization techniques and Comsol Multiphysics simulation were used. At the end of the chapter, the integration of ZnO:Al films in SHJ solar cell is presented.

With the aim of understanding the main limiting factors to the conductivity of the films studied in order to further improve the conductivity of the deposited ZnO:Al films, Chapter 4 presents a full theoretical study on the scattering mechanisms limiting the electron transport in ZnO:Al films, with an emphasis on the effects of grain boundary on carrier mobility. Thanks to a new physical model based on Airy Function Transfer Matrix Method, and by analyzing in depth Hall data at varying temperatures, the limiting factors for electron mobility in different scenarios can be determined. In the second part of this chapter, a simple post-deposition treatment technique based on UV illumination under vacuum and at low temperature (< 220 °C) is also presented: it clearly improves the physical properties of ZnO and ZnO:Al thin layers.

Towards high-performance and flexible TCMs beyond standard ZnO:Al, Chapter 5 presents the development of TCMs based on AgNW networks and ZnO or ZnO:Al thin films. The effect of a thin conformal ZnO coating deposited by our AP-SALD system on the electrical and thermal stabilities of the AgNW networks is discussed first. Then, for the sake of improving both the stability and the conductivity, nanocomposites based on ZnO:Al thin film and AgNW are presented, including both theoretical and experimental studies of the electrical properties of the nanocomposites.

Finally, this work is summarized in a conclusion section, with the main contributions to the research field and providing further perspectives.

# Chapter 2

## Growth and Characterization techniques

### Contents

---

<b>2.1 Thin film growth by AP-SALD</b> . . . . .	<b>23</b>
2.1.1 Overview about AP-SALD . . . . .	23
2.1.2 Description of the AP-SALD system at LMGP . . . . .	26
<b>2.2 Characterization techniques</b> . . . . .	<b>29</b>
2.2.1 Electrical measurements . . . . .	29
2.2.2 Structural and optical measurements . . . . .	32
<b>2.3 Conclusion</b> . . . . .	<b>33</b>

---

In this chapter, the deposition technique used in this work, i.e. Atmospheric Pressure Spatial Atomic Layer Deposition - AP-SALD, is introduced. Both the working principle and the technical details of the set-up used will be discussed. Subsequently, the characterization techniques employed for the analysis of the electrical, optical and structural properties of the undoped ZnO and ZnO:Al films will be briefly reviewed.

## 2.1 Thin film growth by AP-SALD

### 2.1.1 Overview about AP-SALD

AP-SALD is actually a particular case of ALD, which is in turn a particular case of CVD. In CVD, the reactive gases, usually called precursors, are mixed in the gas phase, and the chemical reaction between the precursors is activated at the substrate (most commonly thermally or using plasma).[65] CVD allows deposition of high quality thin films, but because it is a process controlled by diffusion of species, homogeneity over large areas or on high aspect ratio

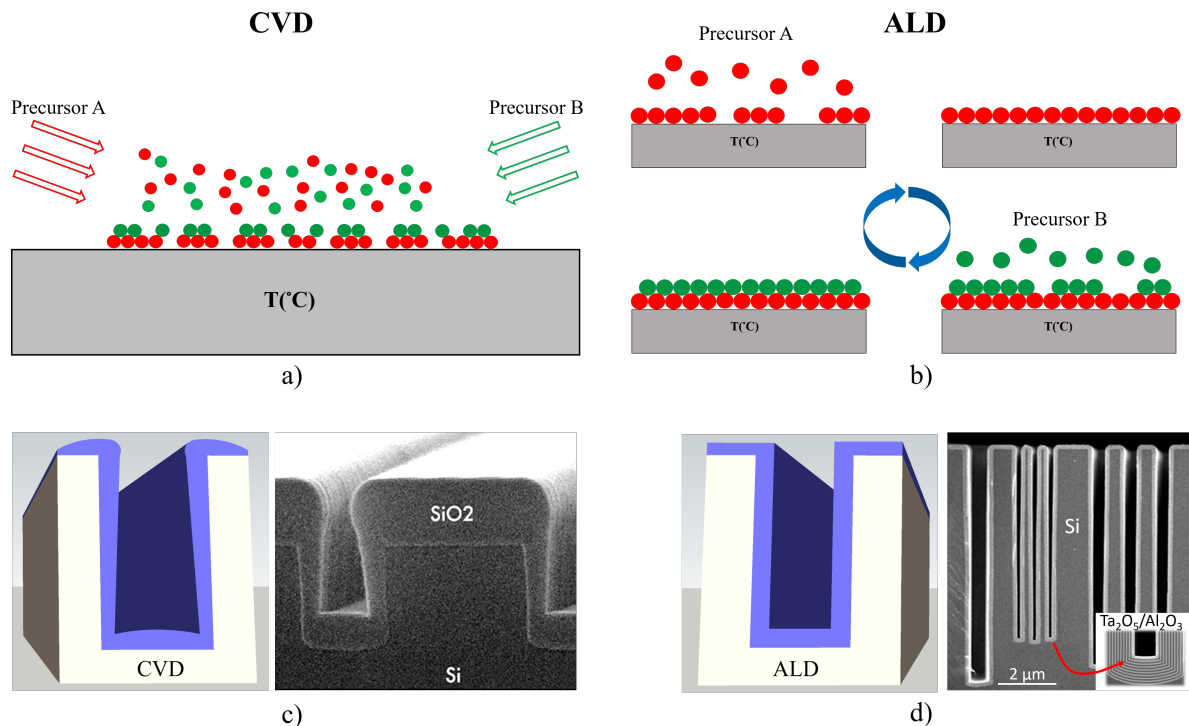


Figure 2.1: Simple schematic representations of: a) CVD and b) ALD processes, respectively; simple schematic representations of films deposited by: c) CVD and d) ALD, respectively. The SEM images shown in c) and d) are SiO<sub>2</sub> deposited on Silicon by Plasma Enhanced CVD (<https://www.corial.com>) and alternating layers of Ta<sub>2</sub>O<sub>3</sub>/Al<sub>2</sub>O<sub>3</sub> deposited on Silicon by ALD (<http://lotusat.com>), respectively.

or complex substrates is an issue. In ALD, precursors are injected sequentially, reacting one at a time with active sites on the substrate surface. The injection of precursors is separated by a purge step in order to prevent mixing and reaction of precursors in the gas phase. Simple schematic representations of the CVD and ALD processes are shown in Figure 2.1a and 2.1b, respectively. The key feature of ALD, the self-limiting film growth, relies on saturative self-terminating surface reactions between precursors and the substrate surface. For this, the requirements for ALD precursors should include high volatility, no self-decomposition, fast and complete surface reactions. Thanks to its surface controlled nature, ALD allows depositing homogeneous and pinhole-free films with excellent conformality. Figure 2.1c and 2.1d show two simple schematic representations of the films deposited by CVD and ALD on a high aspect ratio surface, along with two examples of SiO<sub>2</sub> layer and Ta<sub>2</sub>O<sub>3</sub>/Al<sub>2</sub>O<sub>3</sub> superlayer deposited on Silicon by PECVD and ALD, respectively.

The ALD technique was patented in 1977 by Suntola.[19] In this first patent, both the temporal and spatial approaches were already proposed. In the former, precursors are injected in

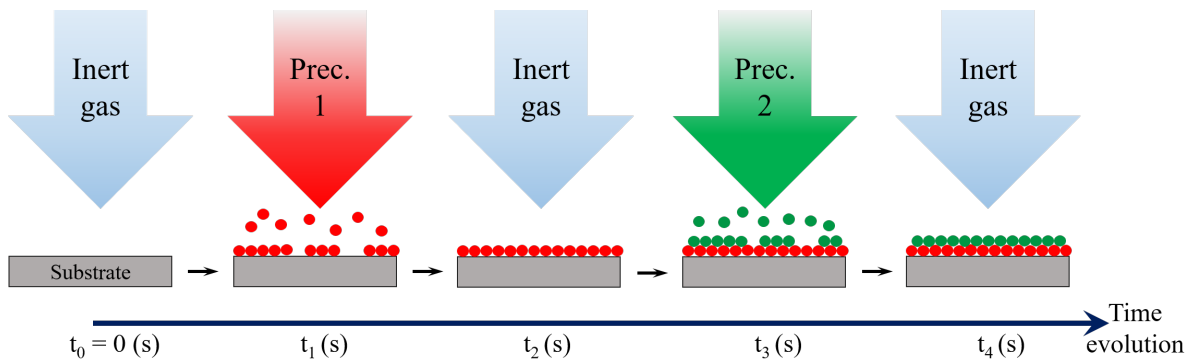


Figure 2.2: Schematic representation of a SALD process. Precursors are continuously supplied at different locations, while spatially separated thanks to inert gas barriers located alternatively between the precursor flows. The substrate moves from one location to another in order to reproduce the ALD cycles.

consecutive pulses separated by purge steps (and thus separated in time, as shown in Figure 2.1b). In the later, precursors are continuously supplied in different locations, which are separated by regions containing an inert gas, and it is the substrate which moves from one location to another (thus separated in space, as shown in Figure 2.2).

AP-SALD is thus equivalent to ALD from the chemical point of view, and thus surface controlled, self-limiting reactions take place. This ensures a very precise growth per cycle, the conformal coating of high aspect ratio features, and the deposition of high quality films at low temperatures (below 300 °C). But in addition to retaining the unique assets of ALD, AP-SALD can be up to two orders of magnitude faster. Particularly, the possibility to perform ALD at atmospheric pressure makes AP-SALD cheaper and easier to scale up since complex and expensive vacuum processing is not required. Despite being patented in 1983, it was not until 2008 that the first scientific article on AP-SALD was published.[66] Since this publication interest around AP-SALD has grown, with the associated increase in the number of publications involving AP-SALD (both concerning development and applications), reaching more than 65 at present (according to Web of Science). In addition, and due to the suitability of the AP-SALD approach for industrial applications, many patents have been filled since 1983. The first one by Levy (Kodak) dates from 2008,[67] and in a rather quick time, the technique has indeed reached industrial commercialization and there are currently several companies developing, fabricating and/or selling AP-SALD equipment, both for laboratory use and for industrial production. The spatial approach has proven to be a very versatile one from the engineering point of view since many reactors have been reported to date.[23, 68]

In Kodak's initial patent and papers, a very neat approach to AP-SALD was proposed based on an open-air close-proximity reactor.[66] In their approach, a gas injector was de-

signed in which the different precursors were supplied along parallel channels kept away by adjacent inert gas flow channels. By placing the substrate close enough to the deposition head, precursor separation is achieved with reasonable gas flows (a few hundred sccm). As a result, the system is completely atmospheric and operates in the open-air, without the use of a deposition chamber. In the initial Kodak model, the injector head was placed on top of the substrate. In a second model, the head was placed at the bottom with the outlets facing upwards and the substrate is oscillated on top of the head. Afterwards, other groups, including our group, Laboratoire des Matériaux et du Génie Physique (LMGP) in Grenoble, have developed similar "close-proximity" approaches.[68–71] Yersak et al. for example have taken advantage of the open air environment offered by this AP-SALD approach to implement the in-situ monitoring of film thickness. In that case, a web is scanned below the injection module and a reflectometer is placed in series to monitor film thickness.[72] In the next section, we will briefly describe the AP-SALD system developed in our group.

### 2.1.2 Description of the AP-SALD system at LMGP

Figure 2.3a shows a global view of the AP-SALD system. Figure 2.3b shows a view with the motor, the substrate holder, as well as the mechanical system allowing to adjust the distance between the substrate and the gas injector. And Figure 2.3c shows a closer view of the gas injector and the substrate from the user working space. The description of the AP-SALD system used in this work can be divided into 3 main parts:

1. The gas delivery system, including precursor containers, gas panels, valves, mass-flow controllers, as well as the gas injector
2. The substrate holder system, including the heater, the vacuum pump to fix the substrate on the hot plate, the motor allowing to control the oscillation of the substrate under the gas injector
3. The interface between the gas delivery system and the substrate, which is the mechanical system allowing maintaining the small distance ( $\sim 100 \mu m$ ) between the gas injector and the substrate.

#### Gas delivery system

Figure 2.4 shows a simple schematic representation of the gas delivery system of our AP-SALD system for the case of ZnO and ZnO:Al deposition. The precursors are stored in metallic bubblers in the liquid form and kept at room temperature (DEZ: diethylzinc, TMA:

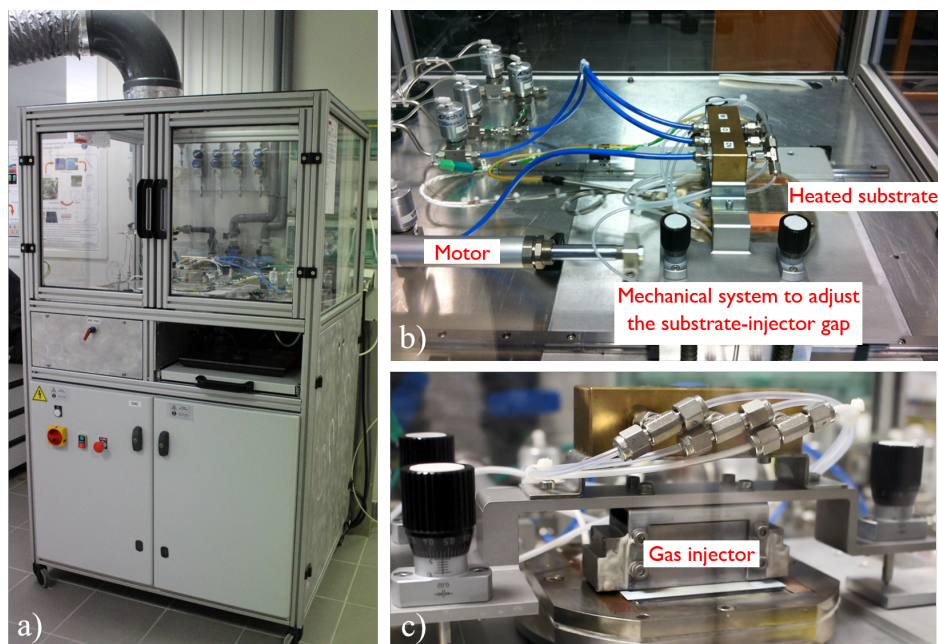


Figure 2.3: Images of the AP-SALD system used in this work: a) a global view of the system, b) a side view showing the motor, the substrate holder, as well as the mechanical system allowing to adjust the distance between the substrate and the gas injector, c) a close view of the gas injector and the substrate.

trimethylaluminum and  $\text{H}_2\text{O}$ : water). They are transported to the gas injector by bubbling a pure nitrogen flow through the liquid precursors. Then at the output of the bubblers, another nitrogen flow, usually called dilution flow, is used in order to adjust the precursor concentration in the gas phase before sending to the substrate. All these flows are controlled by mass-flow controllers with a relative error of about 1 % of the set value.

Figure 2.5a shows the scheme of our AP-SALD gas injector with 3 big input gas channels for  $\text{H}_2\text{O}$ ,  $\text{N}_2$  and DEZ, respectively. From these 3 channels, the gas will be then distributed to 2 metal precursor outlets, 3 water vapour outlets and 6 nitrogen purging outlets. Figure 2.5b shows a view from the bottom of our AP-SALD gas injector with 21 parallel gas channels (11 gas outlets, 10 exhaust inlets alternatively located in between 11 outlets). In this work, the values of gas flows discussed in the chapter 3 refer to the total amount of gas entering to the inputs of the distribution head. As a rule of thumb, the total gas flow in each input channel will be balanced in order to keep a constant flow per outlet.

In order to achieve a film deposited in ALD condition, the two half surface reactions between oxidant/metal precursor and the substrate surface should reach the saturation state during the time the substrate is exposed to the gases.. This requires a sufficient/stable precursor concentration in the gas phase at the injector outlets, an efficient nitrogen purging flow, as

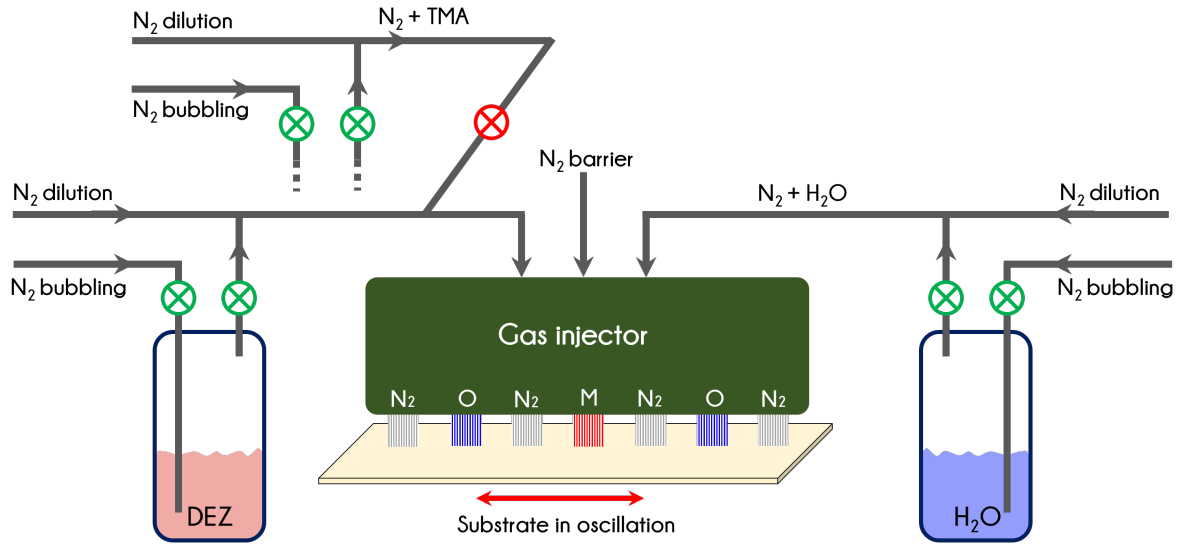


Figure 2.4: A simple schematic representation of the gas delivery system of our AP-SALD system for the case of ZnO deposition. The precursors are stored in the metallic bubblers in the liquid form (DEZ: diethylzinc, TMA: trimethylaluminum and  $\text{H}_2\text{O}$ : water) and carried to the gas injector via a pure nitrogen bubbling flow and a nitrogen dilution flow. Green valves refer to the opening state, while the red one refer to the close state.

well as a sufficient interaction time between the precursor and the moving substrate. The two first conditions can be optimized via the gas flows, while the last one is directly related to the substrate velocity. In practice, to determine whether the precursor concentration at the injector outlets is constant or not, several saturation depositions must be performed until reaching a constant growth rate. The time to reach the steady state depends on the nitrogen bubbling flows through the precursor bubblers. With flows used in our work, the saturation time is less than 30 mins for TMA, DEZ and  $\text{H}_2\text{O}$ .

### Substrate holder system and distance injector/substrate

Our home-made AP-SALD system allows to deposit thin films over a maximum area of  $5\text{ cm} \times 5\text{ cm}$ . The substrate temperature is controlled via a temperature controller, and can be adjusted between RT and up to  $400\text{ }^\circ\text{C}$ . However, we only used low a temperature range (RT -  $220\text{ }^\circ\text{C}$ ) in this work due to the low temperature interest in future applications, as well as some restrictions related to the electrical properties of the deposited films. The substrate velocity is controlled by a cylinder-type motor with a maximum speed of  $50\text{ cm/s}$ . In this work, we studied the effect of substrate velocity only in the low range of  $[0\text{ cm/s}, 10\text{ cm/s}]$ . A critical parameter in the AP-SALD system is the gap between the gas injector and the substrate, which influences directly the quality of the deposited films such as homogeneity, crystallinity and

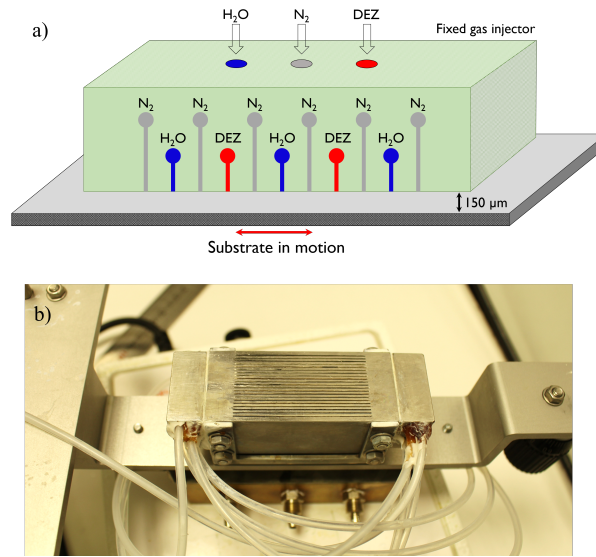


Figure 2.5: a) scheme of the cross-section view of AP-SALD gas injection head and a substrate at a distance of  $150\ \mu\text{m}$  from the head. Exhaust channels alternatively located in between each gas output inlet are not represented in this scheme, b) a view from the bottom of our AP-SALD gas injector showing 21 parallel gas channels.

electrical properties. This distance can be tuned via a system of three micro-screws with a graduation of  $20\ \mu\text{m}$ . The effect of the substrate temperature and velocity, as well as the injector/substrate distance will be discussed in details in the next chapter.

## 2.2 Characterization techniques

### 2.2.1 Electrical measurements

In this work, we have used the Van Der Pauw method to determine the specific resistivity of the films and the Hall effect measurement to determine the carrier concentration and mobility. Also, temperature-dependent Hall effect measurements were performed, which has permitted to study the degeneracy of the doping in the films, as well as the different scattering mechanisms.

#### Resistivity measurement

In 1958, Van Der Pauw showed that the specific resistivity of a flat sample of arbitrary shape can be measured without knowing the current pattern if the following conditions are fulfilled:[73]

- The contacts are at the circumference of the sample

- The contacts are sufficiently small
- The sample is homogeneous in thickness
- The surface of the sample is continuous, i.e., the sample does not have isolated holes

Figure 2.6a shows a sample of arbitrary shape with four small contacts at arbitrary places along the circumference, and if the listed conditions above are fulfilled, the following formula, namely the Van Der Pauw formula, holds:

$$\exp\left(-\pi\frac{R_{AB,CD}}{R_{\square}}\right) + \exp\left(-\pi\frac{R_{BC,DA}}{R_{\square}}\right) = 1 \quad (2.1)$$

where  $R_{\square}$  is the sheet resistance of the sample, which is given by:  $\frac{\rho}{t}$  ( $\rho$  is the film resistivity and  $t$  is the film thickness);  $R_{AB,CD}$  is a resistance defined as the potential difference  $V_D - V_C$  between the contacts D and C per unit current through the contacts A and B, and similarly for  $R_{BC,DA}$ . The reciprocity theorem tells us that:  $R_{AB,CD} = R_{CD,AB}$ , therefore, in practice, a more precise value for the resistances  $R_{AB,CD}$  and  $R_{BC,DA}$  can be obtained by making additional measurements of their reciprocal values, as well as by reversing the polarity of the measurement voltages applied. Hence, eq. 2.1 is rewritten as:

$$\exp\left(-\pi\frac{R_I}{R_{\square}}\right) + \exp\left(-\pi\frac{R_{II}}{R_{\square}}\right) = 1 \quad (2.2)$$

$$R_I = \frac{R_{AB,CD} + R_{CD,AB} + R_{BA,DC} + R_{DC,BA}}{4} \quad (2.3)$$

$$R_{II} = \frac{R_{BC,DA} + R_{DA,BC} + R_{CB,AD} + R_{AD,CB}}{4} \quad (2.4)$$

Finally, the sheet resistance of the film with an arbitrary shape is given as follows:

$$R_{\square} = \frac{\pi}{\ln 2} \frac{R_I + R_{II}}{2} f\left(\frac{R_I}{R_{II}}\right) \quad (2.5)$$

where  $f$  is a function of the ratio  $\frac{R_I}{R_{II}}$  only and satisfies the relation:

$$\frac{R_I - R_{II}}{R_I + R_{II}} = f \operatorname{arccosh} \left[ \frac{\exp(\ln 2 / f)}{2} \right] \quad (2.6)$$

In the case of a perfectly square shape sample (as shown in Figure 2.6b), the function  $f$  defined in the eq. 2.6 takes the value of unity and two resistance  $R_I$  and  $R_{II}$  are identical,

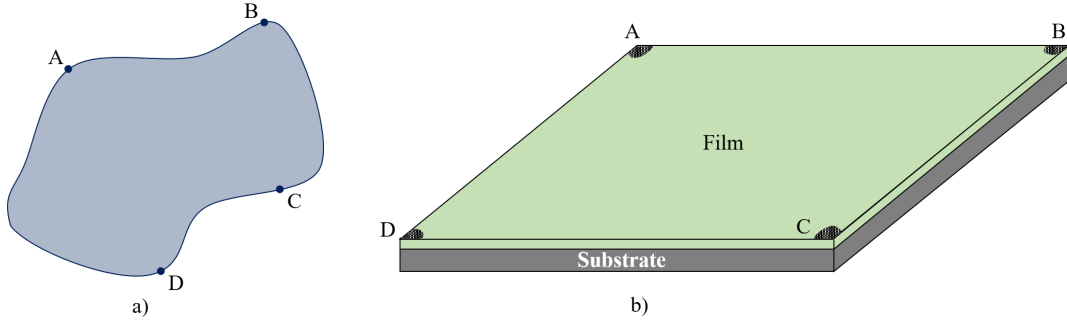


Figure 2.6: a) A sample of arbitrary shape with four small contacts at arbitrary places along the perimeter, b) schematic representation of a thin film sample of square shape used for Van Der Pauw measurements in our work, the corners of the film are contacted with silver paste.

which leads to a very simple formula of the sheet resistance:

$$R_{\square} = \frac{\pi}{\ln 2} R_I \quad (2.7)$$

In the case of samples deposited via AP-SALD, the samples are homogeneous in thickness and pinhole-free, therefore, the accuracy of the sheet resistance obtained by the Van Der Pauw method depends mainly on the quality of the contacts. In our case since the samples used for the Van Der Pauw measurement have a size of  $10 \text{ mm} \times 10 \text{ mm}$ , while the contacts taken by silver paste have a size of about  $1 \text{ mm}$ , therefore the effect of the contacts may not be negligible.

### Hall effect measurement

Figure 2.7 illustrates a simple schematic representation of the Hall effect, in which a magnetic field  $\vec{B}_z$  is applied perpendicular to the surface of a piece of semiconducting material (along the  $\vec{z}$  direction), while an electrical current  $I_x$  flows through the materials (along  $\vec{x}$  direction). As we know, when a moving charged particle, such as an electron or a hole, is placed in a magnetic field, it undergoes a Lorentz force proportional to the strength of the magnetic field ( $\vec{B}_z$ ) and the velocity ( $\vec{v}$ ):  $q_e \vec{v} \wedge \vec{B}_z$ ,  $q$  refers to the charge of the particle. At equilibrium, this Lorentz force induces a charge accumulation at the surface perpendicular to the  $\vec{y}$  direction, which creates an electric field, namely  $\vec{E}_{Hall}$ , in order to balance the effect of the Lorentz force:

$$q \vec{v} \wedge \vec{B}_z + q \vec{E}_{Hall} = 0 \quad (2.8)$$

Since the charge carrier velocity at equilibrium  $\vec{v}$  can be expressed as a function of the

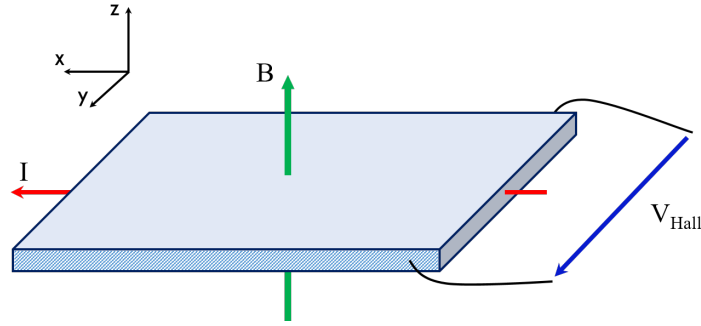


Figure 2.7: Schematic representation of the Hall effect.

electrical current  $\vec{I}_x$ :  $\vec{v} = \vec{I}_x / (nqA)$ , with  $n$  being the carrier density ( $cm^{-3}$ ) and  $A$  being the sample section where the current is injected, we can easily obtain:

$$V_{Hall} = \frac{I_x B_z}{nqt} = R_{Hall} \frac{I_x B_z}{t} \quad (2.9)$$

where  $V_{Hall}$  is the Hall voltage measured in between two surfaces of the sample perpendicular to the  $\vec{y}$  direction,  $R_{Hall}$  is Hall coefficient given by  $1/(nq)$ . Consequently, by measuring the Hall voltage, the carrier concentration  $n$  can be determined, thus the carrier mobility can be deduced as well. Noting that the sign of the Hall voltage indicates the type of semiconducting material, positive for p-type materials and negative for n-type material.

In this work, all electrical measurement results including Hall carrier concentration and mobility were obtained by using the Van Der Pauw geometric configuration, as shown in Figure 2.6b. For that, two home-made systems were used for Van Der Pauw and Hall effect measurements (built by Xavier Mescot and Martine Gri in the laboratory IMEP-LAHC). The first system allows the room temperature measurement and in open-air, while the second system was dedicated for the temperature-dependent Hall effect measurement under a low pressure of 0.003 mbar. For that, a Helium cryostat system was used, which allows controlling the temperature between 325 K and 20 K. The contacts for low temperature Hall effect measurement were performed via the wire bonding technique (using Ni-Al alloy wires with diameter of about  $20 \mu m$ ).

## 2.2.2 Structural and optical measurements

In this work, the surface morphology of the different films was analyzed by scanning electron microscopy (SEM-FEG Environmental FEI QUANTA 250) and atomic force microscopy (AFM Digital Instruments Dimension 3100). Atomic structure and crystallinity were studied by X-ray diffraction (XRD, Bruker D8 Advance) in Bragg-Brentano configuration; using Cu-

$K\alpha$  radiation ( $\lambda = 0.15406$  nm) in the  $2\theta$  range of  $20^\circ$ – $80^\circ$  ( $0.011^\circ/\text{step}$ ,  $2$  s/step). The density and the thickness of the ZnO and ZnO:Al films was also determined via the X-ray reflectometry technique in some cases. Transmission electron microscopy (TEM) images were obtained using a JEOL JEM-2010 microscope operating at 200 kV. The optical properties, such as total/diffuse transmittances and reflectances, were studied using a Perkin Elmer Lambda 950 UV/Vis/NIR spectrophotometer in the wavelength range of [250 nm; 2500 nm]. The photoluminescence measurement has been carried out with a continuous laser excitation at 266 nm (1.2 mW, Crylas FQCW 266-10). The emission from the ZnO and ZnO:Al samples was collected by an optic fiber located close to the samples, dispersed by a spectrometer (iHR Triax 320 Jobin-Yvon) and detected by a liquid-nitrogen cooled Si CCD detector.

## 2.3 Conclusion

In summary, we have presented and discussed the deposition technique used in this work, i.e. AP-SALD, including both the working principle and the technical details of the set-up developed. As said above, AP-SALD is equivalent to ALD from the chemical point of view, and thus surface controlled, self-limiting reactions which take place, which allows the deposition high quality films at low temperatures. But additionally, AP-SALD can be up to two orders of magnitude faster, and particularly, the possibility to perform ALD at atmospheric pressure and in the open air, i.e. without any deposition chamber, makes AP-SALD cheaper and easier to scale up. The AP-SALD system used in this work has a close-proximity reactor with precursors supplied along parallel channels. The precursors for zinc, aluminum and oxygen were DEZ, TMA and  $\text{H}_2\text{O}$ , respectively. This home-made system allows depositing ZnO,  $\text{Al}_2\text{O}_3$  and ZnO:Al thin films in open-air, low temperature ( $<220$  °C) over an area of  $5\text{ cm} \times 5\text{ cm}$  with a high growth rate up to about 30 nm/min. The main characterization techniques used in this thesis work were also presented with a focus on the electrical characterization techniques, i.e. Van Der Pauw method and Hall effect measurement technique.



# Chapter 3

## Optimization of ZnO and ZnO:Al film growth

### Contents

---

<b>3.1 Optimization of ZnO thin film deposition . . . . .</b>	<b>38</b>
3.1.1 Effect of deposition temperature . . . . .	38
3.1.2 Effect of gas flows . . . . .	43
3.1.3 Effect of substrate velocity . . . . .	51
3.1.4 Effect of the injector-substrate distance . . . . .	55
<b>3.2 Optimization of ZnO:Al thin film deposition . . . . .</b>	<b>59</b>
3.2.1 Tuning aluminum content in ZnO:Al films . . . . .	59
3.2.2 Influence of doping on physical properties . . . . .	64
<b>3.3 Application of ZnO:Al films deposited by AP-SALD to SHJ solar cells .</b>	<b>71</b>
<b>3.4 Conclusion . . . . .</b>	<b>74</b>

---

Literature shows that ZnO and ZnO:Al films have been deposited using a wide variety of thin-film deposition techniques, both through physical vapour deposition (PVD) methods such as evaporation, magnetron sputtering, molecular beam epitaxy and pulsed laser deposition, and through chemical vapour deposition (CVD) techniques such as high-temperature CVD, metal–organic CVD (MOCVD), atomic layer deposition and a range of other chemical methods, including spin coating, the sol-gel and the electrodeposition methods. Figure 3.1 shows a comparison of the number of publications related to ZnO and ZnO:Al film deposition using different techniques. The data was extracted from the Web of Science in July

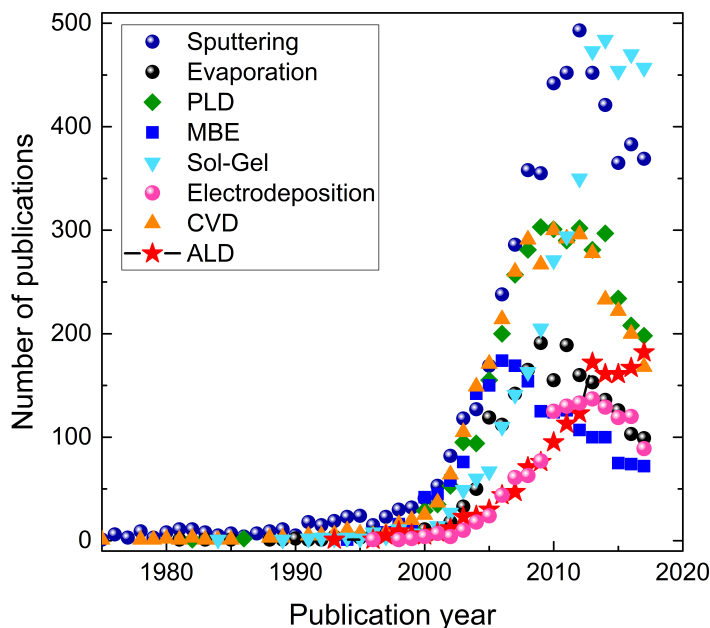


Figure 3.1: Number of publications having the key words: ZnO, AZO or ZnO:Al in the title versus publication year for a variety of fabrication technique. Data extracted from Web of Science.

2018.<sup>1</sup> Accordingly, the first ZnO films were fabricated in 1975 by both sputtering and CVD techniques.[74, 75] As can be seen, the most used techniques are still vacuum-based PVD methods, however, they started decreasing in 2010. The ALD and sol-gel methods are the two only techniques that keep showing a non-decreasing number of publications per year. While ALD is a unique technique allowing the deposition of high-quality nanometer-thick films with excellent uniformity and conformality, other vacuum-free techniques such as sol-gel method have been attracting the research community thanks to their low-cost and high potential to scale up. AP-SALD is actually a promising combination since it combines vacuum-free, high-throughput depositions with the unique properties related to ALD. As a result, AP-SALD has shown an increasing interest which is expected to continue rising in the coming years. While ZnO based films deposited by PVD techniques have been optimized and rather well understood after several decades of research, the first ZnO based films prepared by AP-SALD were just fabricated in 2009-2014.[76–81] Therefore, the understanding of both the AP-SALD technique, and the deposited materials still needs to be deepened.

In this chapter, the effect of various experimental parameters on the physical properties of ZnO and ZnO:Al films are discussed. Figure 3.2 summarizes various parameters affecting the ALD growth of the films. Some parameters are technique-independent, such as the choice

<sup>1</sup>[webofknowledge.com](http://webofknowledge.com)

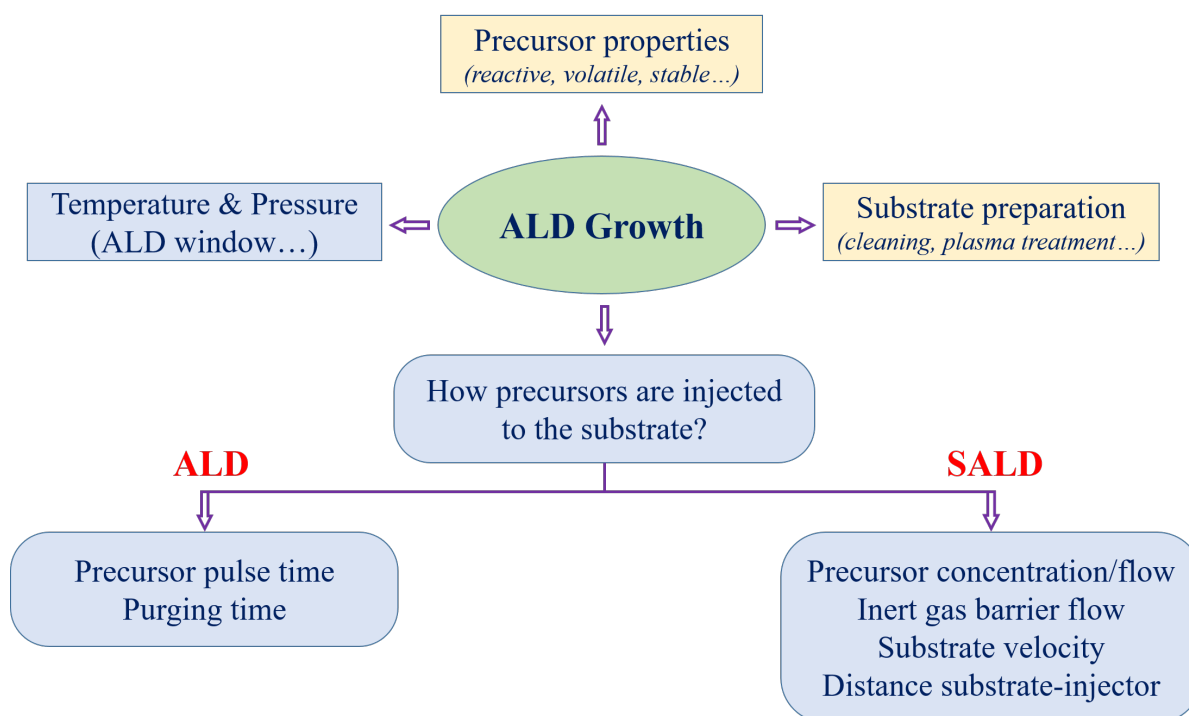


Figure 3.2: A summary of different parameters affecting the ALD growth, both for conventional ALD and AP-SALD.

of precursors or substrate preparation. The deposition pressure can be tuned in the case of a conventional ALD set-up, but it is fixed in the case of atmospheric pressure SALD, where in turn precursor flow and partial pressure can be adjusted. The optimization of the deposition temperature is fairly similar in both ALD and AP-SALD. The essential difference between these two approaches is on how precursors are delivered to the substrate. In the case of ALD for which the exposures of the precursors to the substrate are sequentially separated by purging steps, it is fairly easy to optimize separately each step with just a limited number of parameters, including the pulse time of precursors and the purging time. Conversely, in the case of AP-SALD, several parameters need to be optimized at the same time, including the precursor and barrier gas flows, the substrate velocity, or the distance between the injector and the substrate as in our case of close proximity gas injector. In any case, the essential objectives are not only to achieve a controllable ALD growth through the optimization of the experimental parameters, but also to achieve high-quality material, i.e. with high crystallinity, transparency, conductivity, via the understanding of the relationship between the deposition/post-treatment conditions and the physical properties of the films.

For that, firstly, the effect of different experimental parameters including the deposition temperature, the gas flows, and the substrate/precursor injector distance on the growth rate,

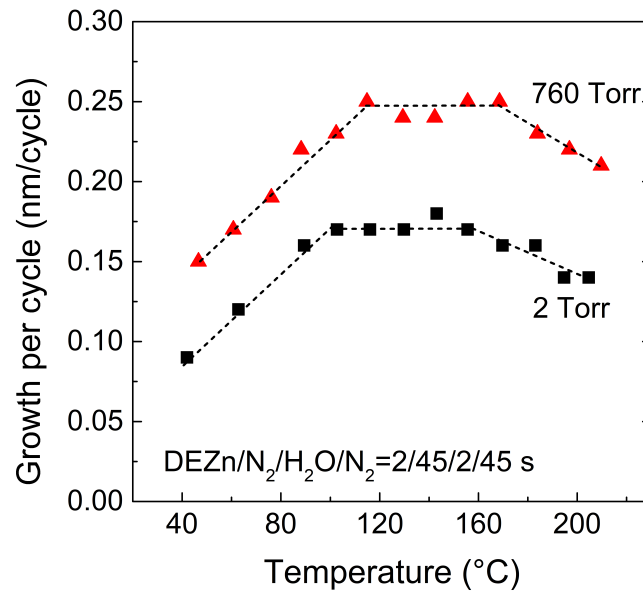


Figure 3.3: Temperature dependence of the growth rate in nm per cycle of ZnO thin films deposited at different pressures. The gas pulse conditions used for depositions are identical. Data extracted from Mousa et al.'s work.[2]

the crystallinity, as well as the nanostructure of the deposited films will be discussed. Then, the second part will be dedicated to study the effect of the aluminum doping on the growth of ZnO:Al films, as well as on their physical properties.

## 3.1 Optimization of ZnO thin film deposition

### 3.1.1 Effect of deposition temperature

The deposition temperature is one of the most important parameters in chemical vapour growth, especially in the case of atomic layer deposition where the growth rate is constant if the deposition temperature used lays within the so-called ALD window. In literature, the ALD growth rate for ZnO is found to vary from below 0.1 nm/cycle up to 0.25 nm/cycle, depending on the reactor pressure. Figure 3.3 shows the dependence of the growth rate of ZnO with pressure and temperature, data extracted and re-drawn from Mousa et al.'s work.[2]) As shown, the growth rate increases for increasing the reactor pressure. Indeed, this is due to a change of the adsorption/desorption kinetics of the precursors on the surface of the sample. Concerning the dependence of the growth rate with deposition temperature, the low growth rate obtained at low temperature range is related to the unsaturated surface reactions due to a low thermal energy, which is not enough to efficiently decompose the precursors, while for high tempera-

tures ( $> 170\text{ }^{\circ}\text{C}$ ), the precursor desorption rate from the substrate is too high, also leading to low growth rates.

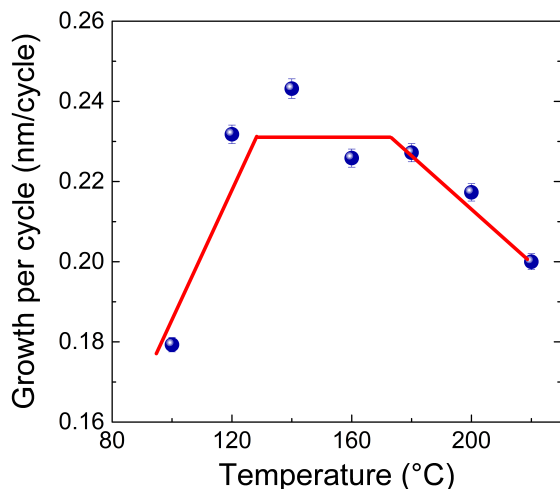


Figure 3.4: Growth rate in nm per cycle of ZnO thin films deposited on glass at different temperatures with our AP-SALD system. The number of cycles was kept at 200 for all samples.

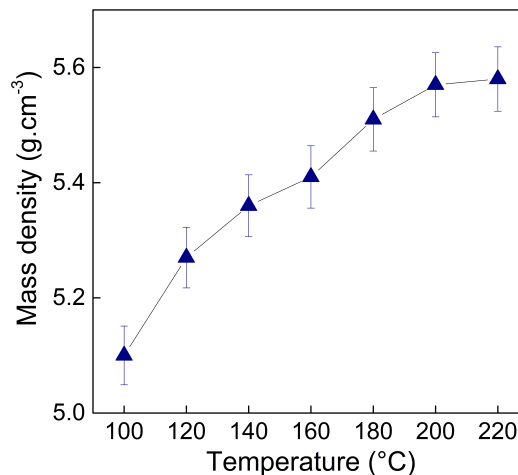


Figure 3.5: Mass density of ZnO thin films deposited on glass versus substrate temperature with our AP-SALD system. The number of cycles was kept at 200 for all samples.

Figure 3.4 shows the growth rate in nm per cycle of ZnO thin films deposited on glass at different temperatures with our AP-SALD system. For this study, the bubbling and dilution flows were respectively 30 and 270 sccm for DEZn, 150 and 300 sccm for H<sub>2</sub>O; the N<sub>2</sub> flow was fixed at 1000 sccm; the distance between the gas injector and the substrate was kept at 150  $\mu\text{m}$ ; the substrate velocity was at 6.5 cm/s, and the number of cycles was kept at 200 for all samples, which corresponds to about 40 nm thick films. At low temperatures ( $< 120\text{ }^{\circ}\text{C}$ ), the condensation of precursors, especially H<sub>2</sub>O, on the substrate surface makes the growth more CVD type than ALD type due to the high sticky coefficient of water which prevents a complete purge of unreacted water while going through the inert gas. The growth rate is pretty stable over a large range from 130  $^{\circ}\text{C}$  to 180  $^{\circ}\text{C}$  and equal to 0.23 nm/cycle, then it decreases when increasing the substrate temperature higher than 180  $^{\circ}\text{C}$ . This can be explained by an increase of the precursor desorption rate at high temperature. Therefore, in our case, the ALD window and the deposition rate are observed to be similar to the ones found in literature.[2] Figure 3.5 shows the temperature-dependent mass density of ZnO thin films deposited on glass by AP-SALD (data obtained from X-ray Reflectivity measurement). The mass density increases with the deposition temperature, which can be related to an improvement of the crystallinity. For high deposition temperatures (200  $^{\circ}\text{C}$  - 220  $^{\circ}\text{C}$ ), the mass density approaches the one of monocrystalline ZnO (5.61 g/cm<sup>3</sup>).

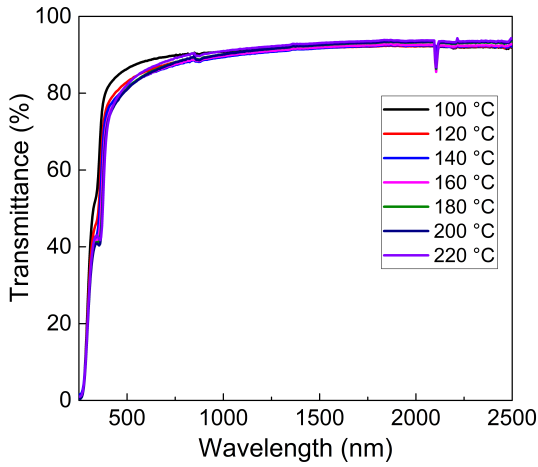


Figure 3.6: Total transmittance of ZnO thin films deposited at different temperatures. The number of cycles was kept at 200 for all samples.

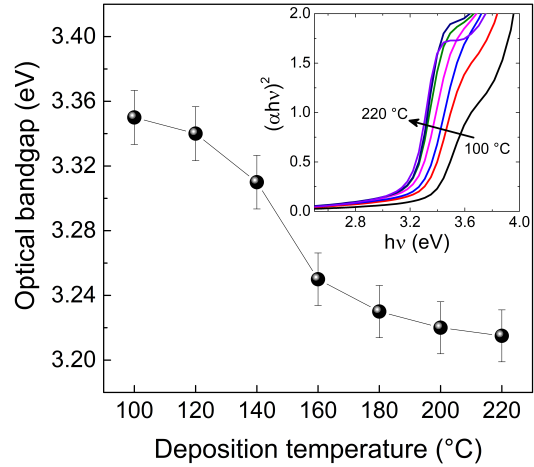


Figure 3.7: Optical band gap calculated using Tauc plot (inset image) of ZnO thin films deposited at different temperatures. The number of cycles was kept at 200 for all samples.

The total optical transmittance and optical band gap calculated using the Tauc plot [82] of ZnO thin films deposited at different temperatures are shown in Figure 3.6 and Figure 3.7, respectively. Interestingly, the optical band gap of ZnO films varies from 3.35 eV to 3.21 eV when the deposition temperature increases from 100 °C to 220 °C (see Figure 3.7). This can be explained by an increase of the crystallinity with deposition temperatures, which is supported by the XRD patterns of ZnO films deposited at different temperature, as shown below in Figure 3.9. The broadening of the optical bandgap in the amorphous semiconducting material compared with the crystalline materials has been studied by several researchers, in most cases applied to amorphous silicon.[83–85] The theory behind is the notion of the electron localization in amorphous materials, which was first introduced by Anderson (1958),[83]. In the case of a crystalline material with a long-range order, the electronic structure is well defined with very sharp band edges ( $E_C$  and  $E_V$ ), as shown in Figure 3.8a.

Conversely, in the case of an amorphous material with a short-range order, there exists localized energy states, which broadens the band edges into tails of localized states, as shown in Figure 3.8b. The energy values separating the localized from the extended states (in which electrons can freely move in the whole system) are called mobility edges (similar to  $E_C$  and  $E_V$  in a crystalline material). When an amorphous material interacts with a photon, the localized-to-extended states transitions are actually possible via a hopping mechanism,[3] which leads to an optical bandgap  $E_{opt}$ , as shown in Figure 3.8b. This optical bandgap increases when increasing the disorder in the material, which can explained the result obtained in Figure 3.7.

For X-ray diffraction and electrical measurement studies, thicker films (800 cycles instead

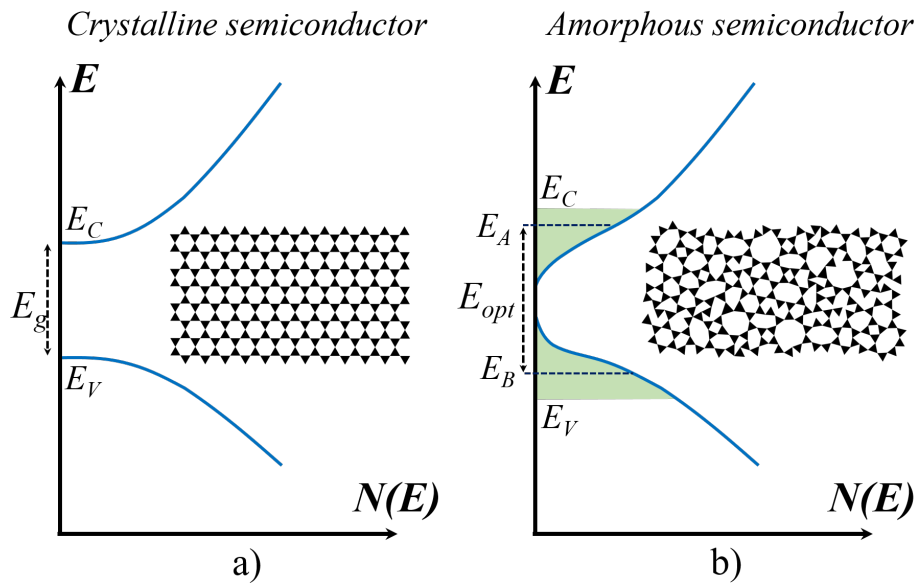


Figure 3.8: A 2D-model representation of density of states in the conduction and valence bands of a) crystalline semiconductors and b) amorphous semiconductors. The region of localized states are shaded.  $E_C$ ,  $E_V$  denote the bottom of the conduction band and the top of the valence band, respectively.  $E_A$  and  $E_B$  denote the optical absorption edges, which are related to the optical band gap in an amorphous material.[3]

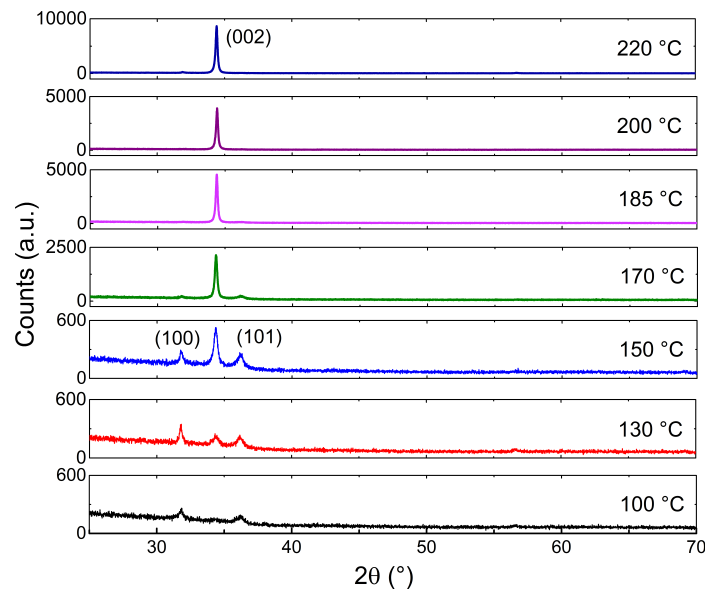


Figure 3.9: X-Ray Diffraction patterns for ZnO films prepared at different temperatures. The number of cycles was fixed at 800 for all samples.

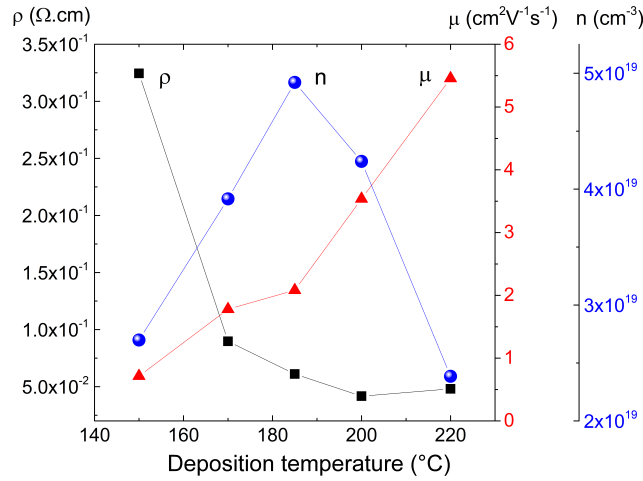


Figure 3.10: Room temperature resistivity, electron mobility and electron concentration as a function of deposition temperature, measured by Hall effect (for the more resistive samples prepared at lower temperatures, measurement results were not reliable). The number of cycles was fixed at 800 for all samples.

of 200 cycles previously) were deposited. The peak intensity increases with the deposition temperature (note that different scales are used in the XRD patterns in Figure 3.9) and the preferential growth orientation evolves from [100] (for the films deposited at 100 °C and 130 °C) to [002] at higher temperatures. The mean crystallite size oriented in the [002] direction, calculated with the Scherrer equation, increases from 22 nm to 49 nm when the deposition temperature increases from 130 °C to 220 °C. The possibility to tune the bandgap, as well as the band alignment, in ZnO by just varying deposition temperature can be very interesting for some applications such as heterojunction solar cells ( $\text{Cu}_2\text{O}/\text{ZnO}$ ) or buffer layer in organic solar cells.

To study the electronic properties of ZnO films deposited by AP-SALD, the carrier concentration, mobility and the resistivity were investigated by Hall Effect and are shown in Figure 3.10. Because of high resistivity, the ZnO films prepared at low temperatures (100 °C, 130 °C) cannot be measured with our Hall Effect measurement setup, we used instead 4 probes measurement, which gives a resistivity of  $1.5 \times 10^4$  ( $\Omega \text{cm}$ ). The mobility tends to increase from 0.5 to 5.5 ( $\text{cm}^2 \text{V}^{-1} \text{s}^{-1}$ ) when the deposition temperature increases, which is attributed to the improvement of crystalline quality with temperature. The carrier concentration reaches a maximum value of  $5 \times 10^{19}$  ( $\text{cm}^{-3}$ ) for the films deposited at 185 °C, which is a remarkable value for carrier concentration in intrinsic ZnO films. The drop of the carrier concentration may be explained by an increase of oxygen adsorption rate by ZnO grain boundaries when increasing temperature. Actually, we will see in the chapter 4 that oxygen in atmosphere can act as electron traps at the grain boundaries, leading to the drop of both carrier mobility and

concentration. The trade-off between the carrier mobility and carrier concentration gives an optimum resistivity value of  $4.17 \times 10^{-2}$  ( $\Omega cm$ ) for the films deposited at 200 °C. In the next section, the deposition temperature for ZnO:Al will be fixed at 200 °C, since it provides the best compromise between crystallinity, electrical conductivity and the compatibility with most of polymeric substrates, as well as with the amorphous silicon layer in silicon heterojunction solar cell as mentioned previously in the introduction part.

### 3.1.2 Effect of gas flows

In conventional ALD, at a given temperature, the pulse duration of each precursor and the purging time will determine the growth rate. Since ALD is based on the self-limiting surface reaction between precursors and active sites on the surface of the substrate, the ALD condition corresponding to a constant growth rate is achieved when enough precursor is supplied during the injection pulse to saturate all active sites on the surface. However, longer injection pulses lead to a longer deposition time and precursor waste. As well, the purging time in ALD process should be long enough to prevent the CVD contribution due to cross-talk between the two precursors. In the case of AP-SALD, the key factor towards a controllable growth is similar to the conventional ALD case, i.e. obtaining a saturated reaction between precursors and substrate, while being able to purge the excess precursor away by nitrogen.

#### Effect of H<sub>2</sub>O flow

In general, purging properly the excess amount of H<sub>2</sub>O from the surface to keep only a monolayer is more difficult than purging the metal precursor, since this last one is usually very volatile and has high auto-limiting reaction activity. In order to study the effect of H<sub>2</sub>O supplied to the ALD reaction, we varied the N<sub>2</sub> bubbling flow through H<sub>2</sub>O from 50 sccm to 200 sccm, while balancing the H<sub>2</sub>O dilution flow to have the same flow in each output gas channel. The number of cycles was kept at 400 for all samples. The substrate moved under the gas injector at 5 cm/s, while the diethylzinc (DEZ) bubbling, dilution, and the nitrogen barrier flow were kept at 35 sccm, 265 sccm and 900 sccm, respectively (in order to have 150 sccm in each outlet).

Figure 3.11 and Figure 3.12 show respectively the growth per cycle and refractive index of ZnO films as a function of nitrogen bubbling flow through H<sub>2</sub>O (film thicknesses extracted from the fits of transmittance spectrum to the Swanepoel's model with the Sellmeier dispersion relation used for the refractive index [86]). Interestingly, by supplying less H<sub>2</sub>O (50 sccm and 75 sccm), the deposited film becomes thicker with a growth rate of about 0.35 nm/cycle, compared to 0.31 nm/cycle for higher H<sub>2</sub>O flows. Conversely the refractive index is observed

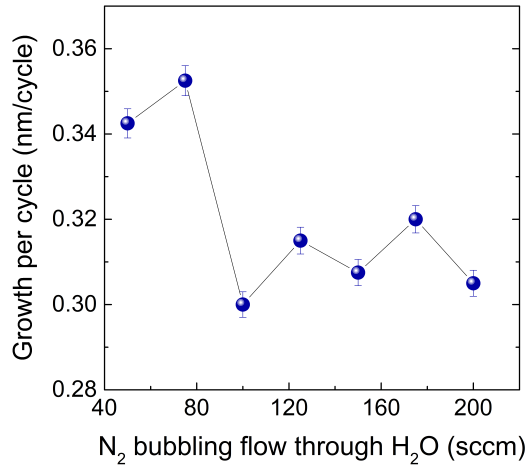


Figure 3.11: Growth per cycle as a function of nitrogen bubbling flow through water.

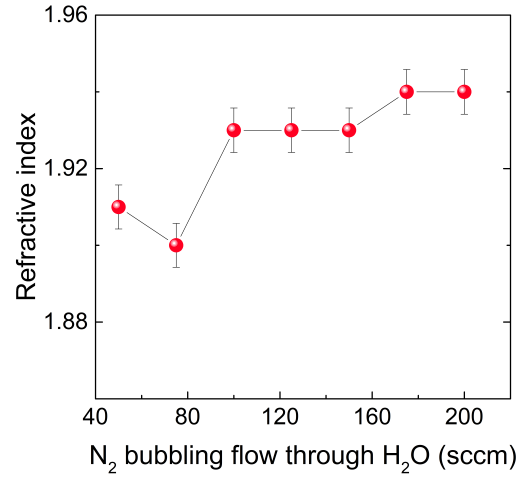


Figure 3.12: Refractive index of films as a function of nitrogen bubbling flow through water.

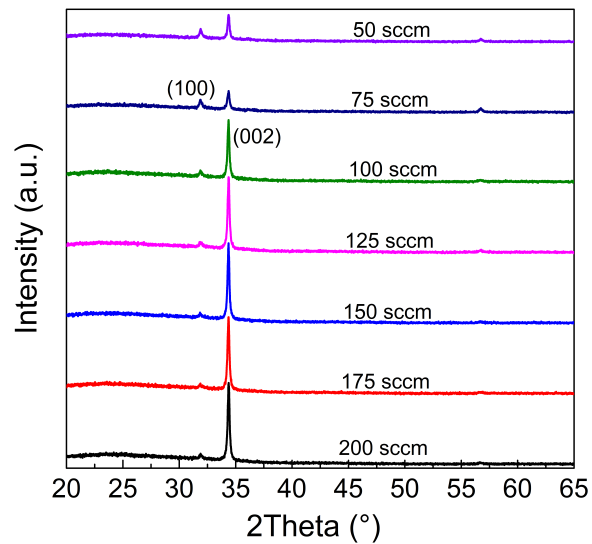


Figure 3.13: X-Ray Diffraction patterns for ZnO films prepared with different nitrogen bubbling flows through H<sub>2</sub>O.

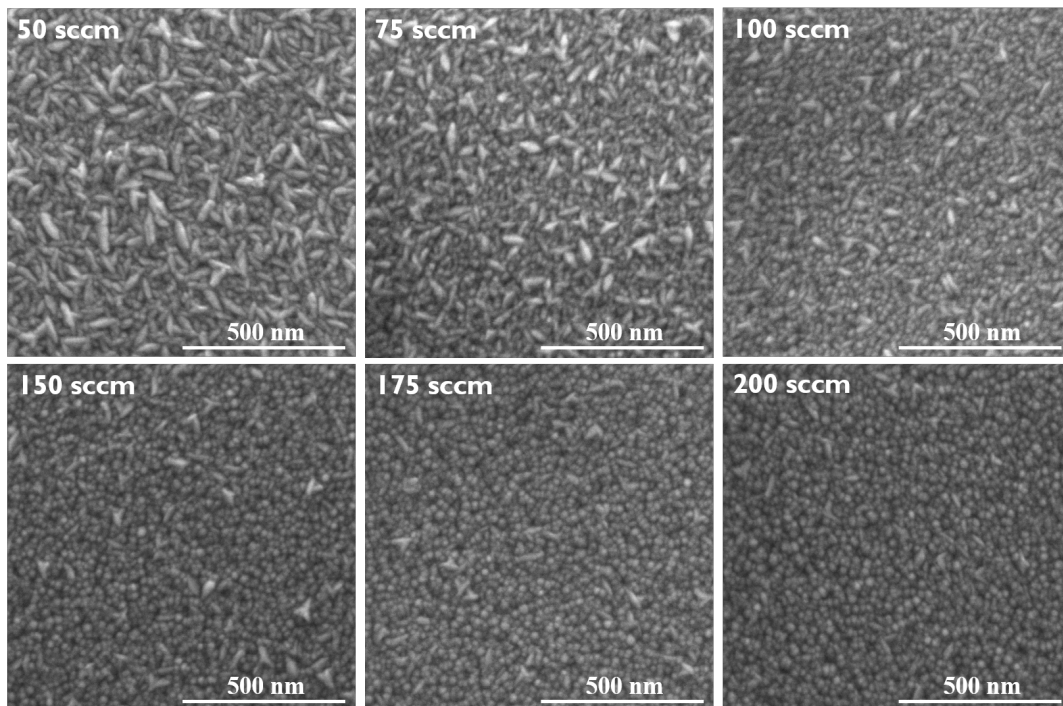


Figure 3.14: SEM images of ZnO films prepared with different nitrogen bubbling flows through H<sub>2</sub>O.

to be lower than in the case of high N<sub>2</sub> bubbling through H<sub>2</sub>O, which may relate to a change in porosity or crystallinity of the deposited films.

Figure 3.13 shows X-ray diffraction patterns of these ZnO samples, in which we observe a decrease of the intensity of the [002] reflections accompanied by an increase of the [100] reflection when lowering the H<sub>2</sub>O supply. In the same way, a change in the ZnO morphology versus H<sub>2</sub>O supply can be as well observed in SEM images, as shown in Figure 3.14. It is worth to notice that the grain size observed in the SEM images seems larger for the case of low H<sub>2</sub>O supply, but the corresponding low refractive index, as well as lower reflection peaks indicate that those films are less crystalline. Another important remark drawn from this observation is that the grain sizes estimated with SEM images are not comparable if the texture of the films is not identical. To summarize, the N<sub>2</sub> bubbling flow through H<sub>2</sub>O should be higher than 125 sccm in order to obtain high-crystallinity, dense films. As described, the ZnO film structure can be tuned from [002] to [100] just by decreasing the H<sub>2</sub>O supply in the ALD reaction.

### Effect of DEZ flow

An ideal ALD process should provide a single monolayer of precursor after each exposure. However, when molecules from the gas phase impinge on a surface and begin to stick, a complete (100%) monolayer may not be formed if the pressure or concentration of precursor in the gas phase is not enough.[87] In order to study the effect of DEZ flow, H<sub>2</sub>O was supplied in enough amount (150 sccm) in order to ensure a surface saturation. The DEZ bubbling flow was then varied to study the effect of DEZ concentration on the growth rate of ZnO films.

Using the simple model based on Langmuir isotherm adsorption and desorption, the growth rate of ZnO at a constant temperature can be theoretically calculated. Let  $\theta(t)$  be the fraction of surface covered at the time  $t$ , the variation of this quantity is just the difference between the adsorption and desorption rates, expressed as follows:

$$\frac{d\theta(t)}{dt} = k_a [DEZ] (1 - \theta(t)) - k_d \theta(t) \quad (3.1)$$

where  $k_a$ ,  $k_d$  and  $[DEZ]$  refer to the constant rate for the adsorption and desorption processes, respectively, and the gas phase concentration of the molecular species (in this case is zinc precursor, DEZ). This equation can be easily solved, which leads to the expression of the fraction of surface covered expressed as follows:

$$\theta(t) = \frac{k_a [DEZ]}{k_a [DEZ] + k_d} \left[ 1 - e^{-(k_a [DEZ] + k_d)t} \right] \quad (3.2)$$

Since the deposition temperature is rather low and the AP-SALD is a high-pressure process, as a first approximation, we assumed that the desorption rate is small compared to the adsorption rate during saturation period. The eq. 3.2 can be rewritten:

$$\theta(t) = 1 - e^{-k_a [DEZ]t} \quad (3.3)$$

Because the growth per cycle depends on how completely the surface is saturated after each exposure of precursor, which corresponds to an exposure time calculated from the substrate velocity, we assume that the growth per cycle is proportional to the fraction of surface covered  $\theta$ . Also, the gas phase concentration of the molecular species  $[DEZ]$  is assumed to be proportional to the nitrogen bubbling flow through DEZ, denoted  $f_{DEZ}$ . Therefore, the expression for growth per cycle can be expressed as follows:

$$GPC(f_{DEZ}) = X \left[ 1 - e^{-Y \cdot f_{DEZ}} \right] \quad (3.4)$$

here X and Y are two constants. X corresponds to the growth rate when having the surface saturated. Y depends on the substrate velocity and the adsorption coefficient  $k_a$ .

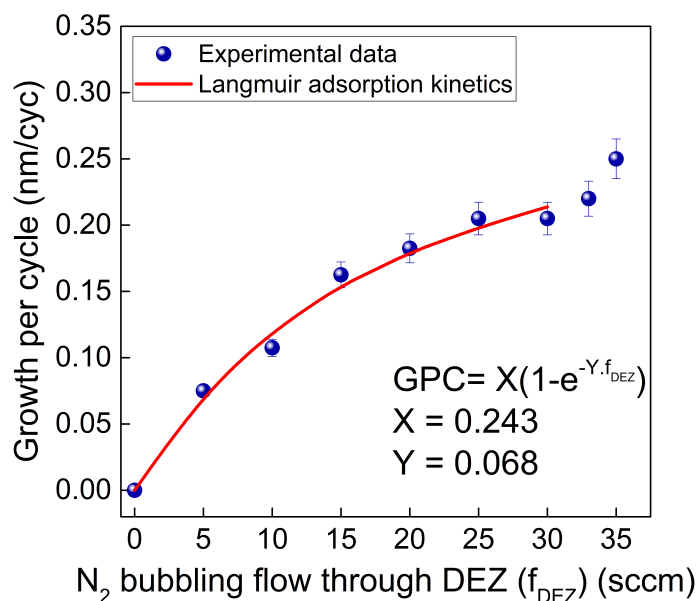


Figure 3.15: Growth per cycle as a function of  $N_2$  bubbling flow through DEZ (sccm). The fit using the theory of Langmuir adsorption kinetics is shown in red line for  $N_2$  bubbling flow through DEZ in the range of [0 sccm, 30 sccm].

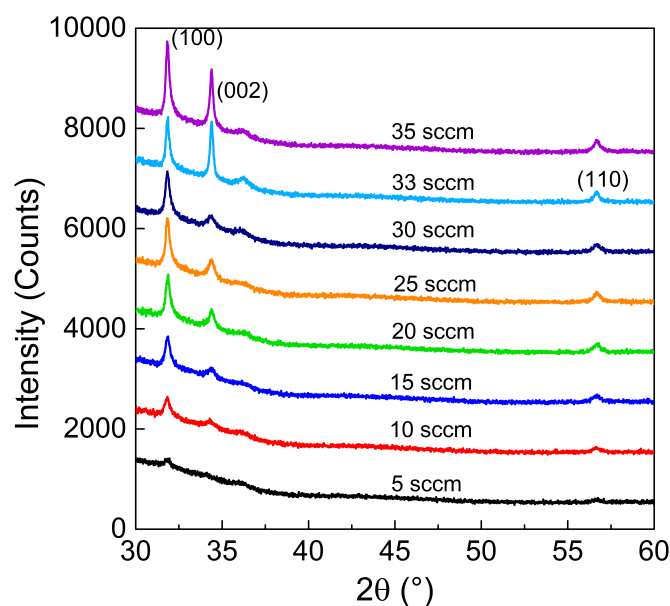


Figure 3.16: X-ray diffraction patterns of ZnO samples deposited with different DEZ bubbling flows (from 5 sccm to 35 sccm).

Figure 3.15 shows the growth per cycle of ZnO films deposited at 200 °C, and the theoretical fit using eq. 3.4 as a function of the nitrogen flow bubbling through DEZ, also called the DEZ bubbling flow. In this study, the other parameters ( $H_2O$  bubbling and dilution flows

(150/300 sccm), N<sub>2</sub> barrier flow (1000 sccm), scanning speed (6.25 cm/s) and number of cycles (400) were kept constant, while the dilution flow for DEZ line was balanced to have the same flow in each output gas channel. A constant growth rate of 0.2 nm/cycle is observed for the DEZ bubbling flows in between [25 sccm; 30 sccm]. The lower growth rate for small DEZ bubbling flows (< 20 sccm) can be explained by the unsaturated DEZ/substrate reaction. The experimental data is coherently fitted by the model described in eq.3.4. Then, when we keep supplying more DEZ (> 30 sccm), the growth per cycle increases up to 0.25 nm/cycle, which seems not coherent with ALD theory, i.e. the self-limiting surface reaction between DEZ and substrate. However, this could be explained by an enhanced contribution of CVD component due to diffusion of DEZ through the nitrogen barrier. The dependence of growth rate on the DEZ flow will be reduced with a new design of the gas injector, in which some improvements should be developed: a) the precursor channels should be more spatially separated to prevent any spatial inter-diffusing; b) the exhaust channels are efficient enough to pump out all residual precursors and products.

Figure 3.16 shows the X-ray diffraction patterns of ZnO samples deposited with different DEZ bubbling flows (from 5 sccm to 35 sccm). The results revealed that all samples with a DEZ bubbling flows  $\leq 30$  sccm exhibit a growth following the preferential direction of [100]. However, For the samples having the DEZ bubbling flows of 33 sccm and 35 sccm, two dominant XRD peaks were identified, [100] and [002].

### Effect of N<sub>2</sub> barrier flow

As mentioned previously, film growth in ALD conditions can only be achieved with a perfect separation of reactant exposures to the substrate. In this part, the N<sub>2</sub> barrier flows was studied in the range of [500 sccm, 1500 sccm] to study the effect of the precursor seshow respectively the XRD patterns and SEM imageseparation on the film properties. The other parameters remained unchanged (deposition cycles: 400, substrate velocity: 5 cm/s, DEZ and H<sub>2</sub>O bubbling flows: 30 sccm and 100 sccm, DEZ and H<sub>2</sub>O dilution flows: 270 sccm and 350 sccm, respectively). The balance of gas flows at the output inlets of the injector can be achieved with a N<sub>2</sub> barrier flow of 900 sccm. Figure 3.17 shows the growth rate and refractive index of ZnO films as a function of nitrogen barrier flow, as measured by ellipsometry. The growth rate seems stable in the range [900 sccm, 1100 sccm], corresponding to highest refractive index (~ 1.94). For very low nitrogen barrier flows (500 sccm and 700 sccm), the precursors can easily inter-diffuse to react in the gas phase (CVD condition). Coherently, the deposited films are observed to be thicker, and have pretty low refractive index (~ 1.87). Also, if the nitrogen flows are too high compared with the precursor flows, the deposited films are as well observed to be non-homogeneous and thicker, while the refractive index decreases. This can be explained by the turbulent regime of gas flows occurring under the injector due to the confined space between the injector and the substrate.

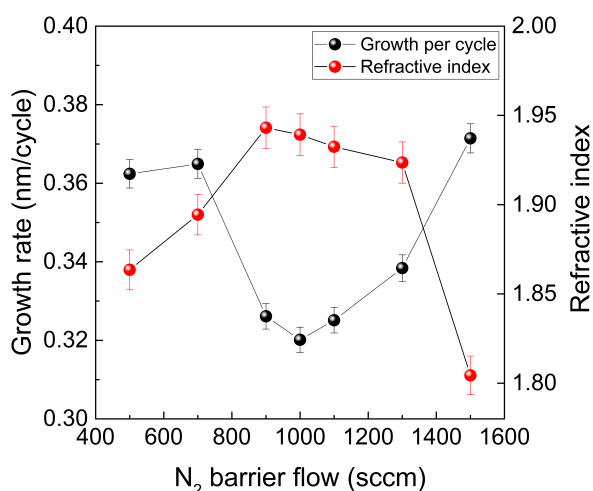


Figure 3.17: Growth per cycle and refractive index of ZnO films prepared by using various nitrogen barrier flows.

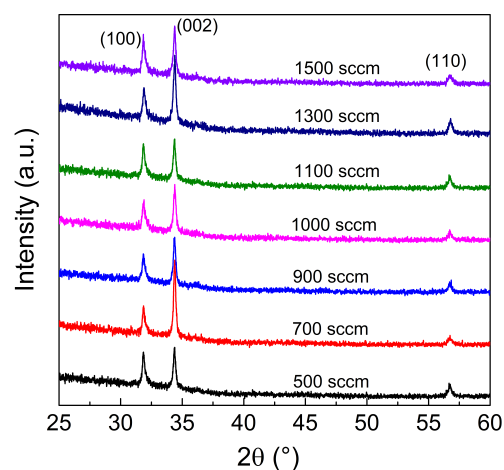


Figure 3.18: X-Ray Diffraction patterns for ZnO films prepared at different nitrogen barrier flows.

Figures 3.18 and 3.19 show respectively the XRD patterns and SEM images of ZnO films prepared with different nitrogen barrier flows. The microstructure of the films is similar for all samples with the preferential orientation of [002]. Lowest intensity of the peak (002)

corresponds to two extreme values of  $N_2$  barrier flows (500 sccm and 1500 sccm). Via the SEM observation, it can be seen that the samples prepared by using  $N_2$  barrier flows of [900 sccm, 1100 sccm] have the bigger grain size, although their thicknesses are smaller compared to the sample prepared by using  $N_2$  barrier flows of 500 sccm or 1500 sccm. As described, high film quality with bigger grain size, high refractive index can thus be prepared for  $N_2$  barrier flow in the range of [900 sccm, 1100 sccm].

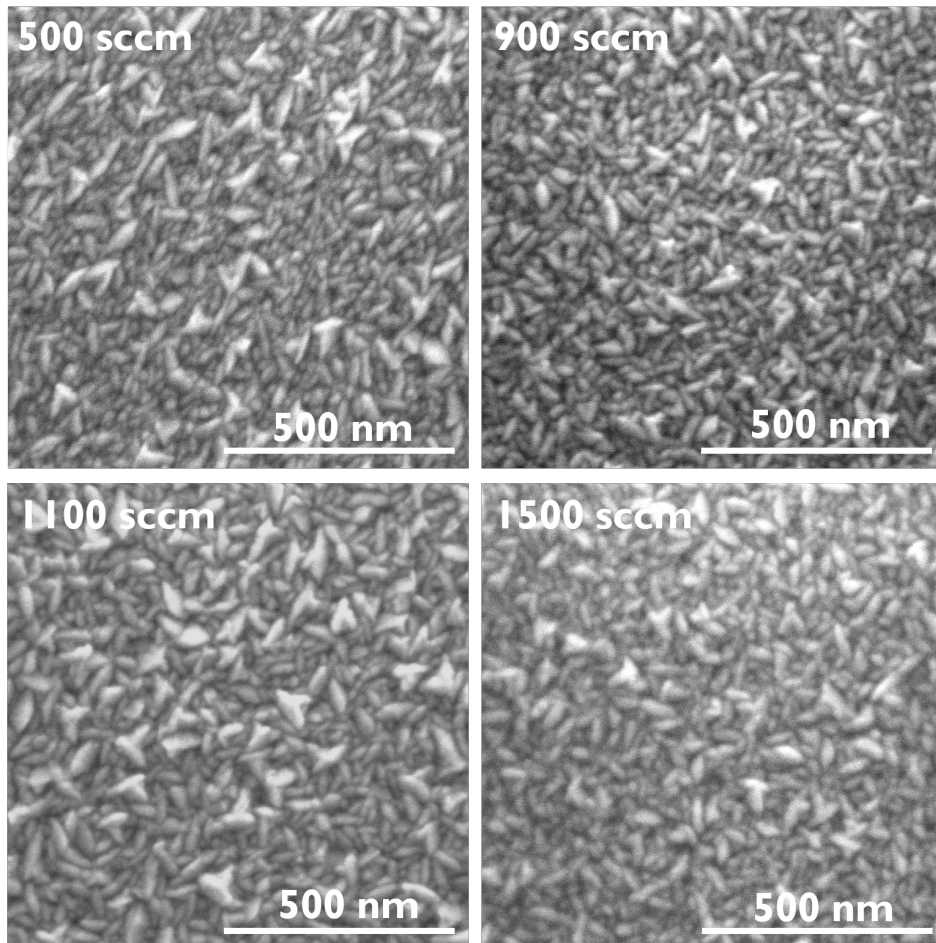


Figure 3.19: SEM images of ZnO films prepared at different nitrogen barrier flows.

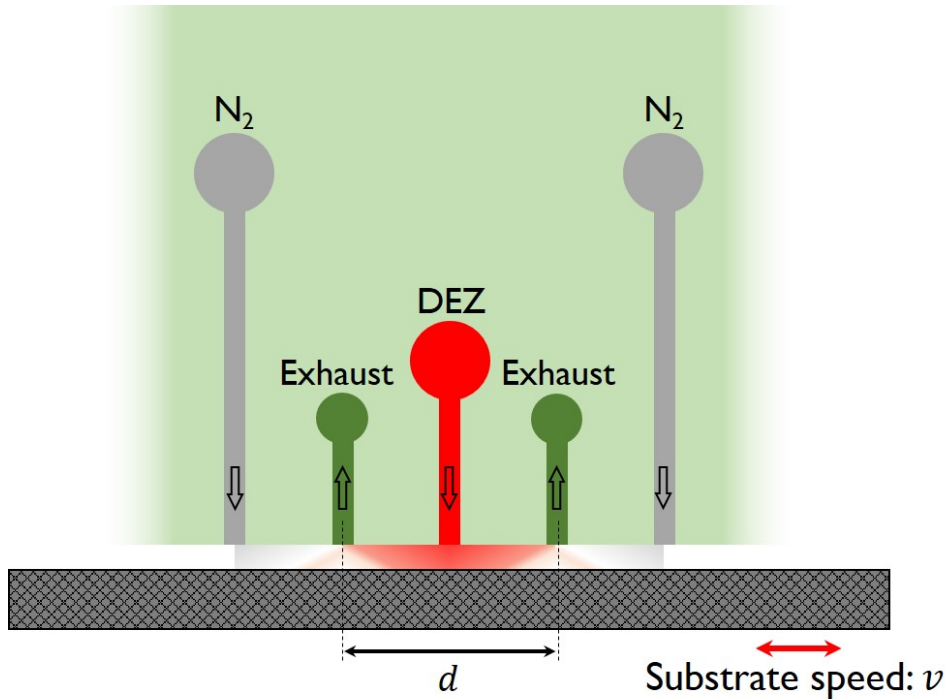


Figure 3.20: A schematic zoom of the cross-section view of the gas injector.

### 3.1.3 Effect of substrate velocity

In AP-SALD, the substrate velocity is directly related to the exposure time, or the residence time, of a precursor on the substrate. This is indeed equivalent to the duration of a pulse in the case of conventional ALD. Figure 3.20 shows a schematic zoom of the cross-section view of a fraction of the AP-SALD gas injector. When the substrate moves with a speed  $v$  (cm/s), any point on the substrate will be exposed to the precursor during a time  $t_{res} = \frac{d}{v}$ , with  $d$  is the distance between two consecutive exhaust channels next to the precursor channel (= 2.5 mm). Depending on the substrate/precursor reaction kinetics, there should be a critical residence time, which corresponds to the time required to saturate the surface. This critical value depends not only on the substrate velocity but also on the precursor concentration injected onto the substrate.

To study the effect of substrate velocity, we fixed H<sub>2</sub>O bubbling and dilution flows at 150 sccm/300 sccm, N<sub>2</sub> barrier flow at 900 sccm and the temperature at 200 °C. This sets a flow per channel of 150 sccm, which corresponds to a gas speed of 5 cm/s. The experiments were repeated for three values of the DEZ bubbling flows: 15 sccm, 30 sccm and 50 sccm, which corresponds to an increase of the DEZ concentration in gas phase. The growth per cycle (*GPC*)

versus substrate velocity ( $v$ ) can be expressed as follows:

$$GPC(v) = X \left[ 1 - e^{-\frac{k_a[A]d}{v}} \right] = X \left[ 1 - e^{-\frac{Y}{v}} \right] \quad (3.5)$$

where  $X$  and  $Y (= k_a[A]d)$  are two constants. However, while this so-called Langmuir model was appropriate to study the effect of precursor flow, it does not fit properly the data obtained from various substrate velocities. Indeed, the flow of the precursor injected onto the substrate is significantly affected by the substrate velocity, which modifies the gas speed and the spatial distribution of the precursor above the substrate. Figure 3.21 shows a COMSOL multiphysics simulation of the spatial distribution of precursor velocity (Fig 3.21.a) and precursor concentration (Fig 3.21.b) above the substrate.

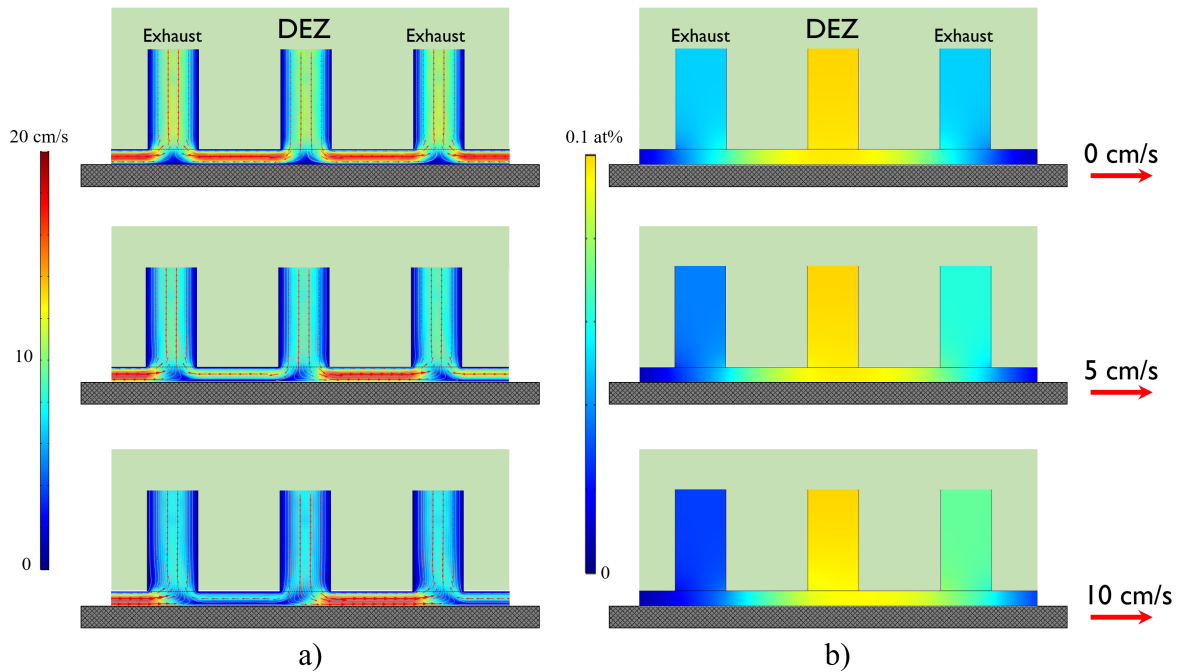


Figure 3.21: The results extracted from COMSOL Multiphysics simulation of: a) precursor velocity, b) precursor concentration spatially distributed above the substrate. Gas flows, temperature, as well as the distance between the injector and the substrate were kept constant, as in reality. Here, only the cross-section views including a DEZ inlet and two exhaust inlets are shown. The blue color corresponds to low velocity or low precursor concentration (in volume fraction), while red or yellow color correspond to high velocity or high precursor concentration.

Results are shown for three substrate velocities (0, 5 and 10 cm/s). When the substrate is immobile, the gas velocity and concentration are symmetrically distributed over the distance  $d$ , which corresponds to the distance between two exhausts. When the substrate velocity

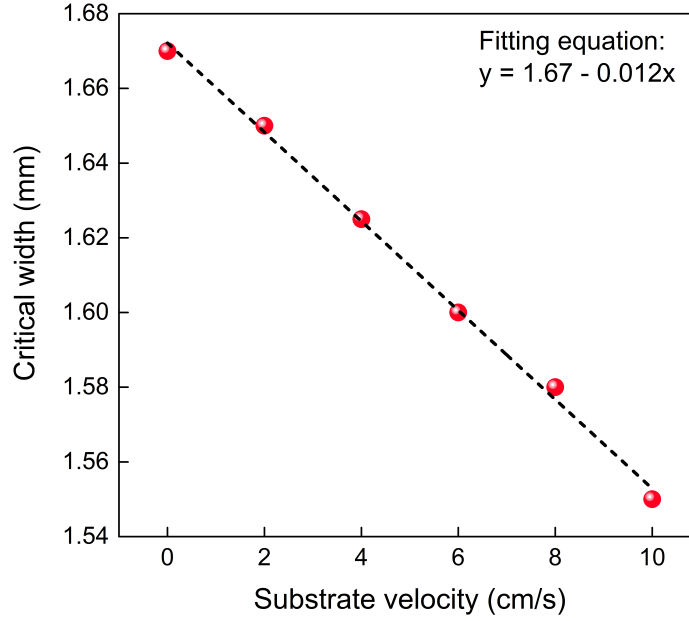


Figure 3.22: Critical width on the substrate that is exposed to a precursor concentration corresponding to 80 % of the precursor concentration at the input DEZ channel.

increases, the gas molecules at the gas/substrate boundary layer will be entrained with the same speed. Due to the interaction between gas molecules in the gas phase, the gas speed increases in the direction of the substrate motion. Moreover, it can be observed that the precursor concentration profile shifts to the right, i.e. the moving direction of the substrate. Now, the question will be how this concentration profile shift modifies the film growth. We have defined a critical distance  $d_c$  on the substrate which is exposed to a precursor concentration corresponding to 80 % of the precursor concentration at the input DEZ channel. Figure 3.22 summarizes the critical distance  $d_c$  as a function of the substrate velocity (result obtained via COMSOL multiphysics simulation). As a first approximation, a linear relationship is observed between  $d_c$  and the substrate velocity  $v$ .

Therefore, we can assume that the effective residence time has the following expression:  $t_{res} = \frac{d_c}{v} = \frac{d - k_{ss}v}{v}$ , with  $k_{ss}$  is a constant related to the substrate speed dependence. The modified model is thus written:

$$GPC(v) = X \left[ 1 - e^{-\frac{k_a[A]d}{v} + k_a[A]k_{ss}} \right] = X \left[ 1 - e^{-\frac{Y_1}{v} + Y_2} \right] \quad (3.6)$$

where  $Y_1 = k_a[A]d$  and  $Y_2 = k_a[A]k_{ss}$  are two new constants.

Figure 3.23 shows the growth per cycle of ZnO films deposited at 200 °C as a function of substrate velocity. The fits from our modified model are represented in black dashed curves.

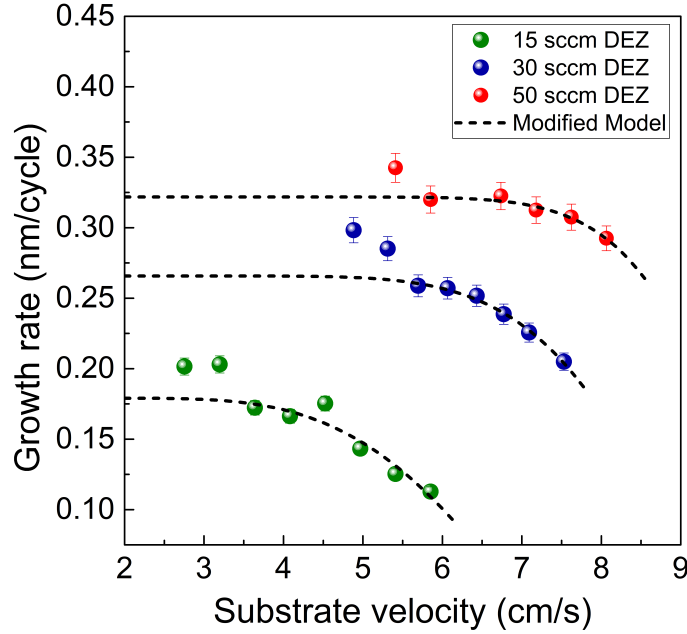


Figure 3.23: Experimental values of the growth per cycle of ZnO films as a function of the substrate velocity, and DEZ bubbling flows, and the associated fits using eq. 3.6.

DEZ bubbling flow	$X$ (nm/cycle)	$Y_1$ (m/s)	$Y_2$	$k_{ss}$ (s)
15 sccm	0.18	0.27	3.7	0.0184
30 sccm	0.27	0.58	6.2	0.0178
50 sccm	0.32	0.86	9.5	0.0229

Table 3.1: Extracted parameters from the fits shown in Figure 3.23.

Interestingly, for three values of the DEZ bubbling flows, our model properly fits the data of the high and intermediate substrate velocities, which experimentally validates the existence of a critical distance  $d_c$ , as discussed above. The summary of the parameters extracted from the fits is shown in Table 3.1. We observed an increasing trend in the static growth rate (parameter  $X$ ) as a function of the DEZ bubbling flows, which corresponds to an increase of the precursor concentration  $[A]$  in the gas phase. This is supported by the same trend observed for  $Y_1$  and  $Y_2$ , which is actually proportional to  $[A]$ . Additionally, from two constants  $Y_2$  and  $Y_1$ , the value of  $k_{ss}$  can also be evaluated ( $\sim 0.02 \pm 0.003$  (s)). Comparing with the  $k_{ss}$  value extracted from Figure 3.22 ( $\sim 0.012$  (s)), this value is slightly higher.

For very low substrate speeds, higher growth rates are observed, which can be explained by the fact that one part of the DEZ can diffuse through the  $N_2$  barrier flow resulting in an important CVD component, which adds to the total growth rate.

### 3.1.4 Effect of the injector-substrate distance

The distance between the gas injector and the moving substrate is a specific parameter existing only in the case of close-proximity SALD set-up. As mentioned in the previous chapter, the substrate is usually kept at a small distance ( $\sim 150 \mu\text{m}$ ) from the injector. In this part, we will justify the choice of this value and study the effect of the injector-substrate distance on the film growth. Figure 3.24 illustrates the precursor concentration on the substrate for two values of the injector-substrate distance ( $70$  and  $230 \mu\text{m}$ ).

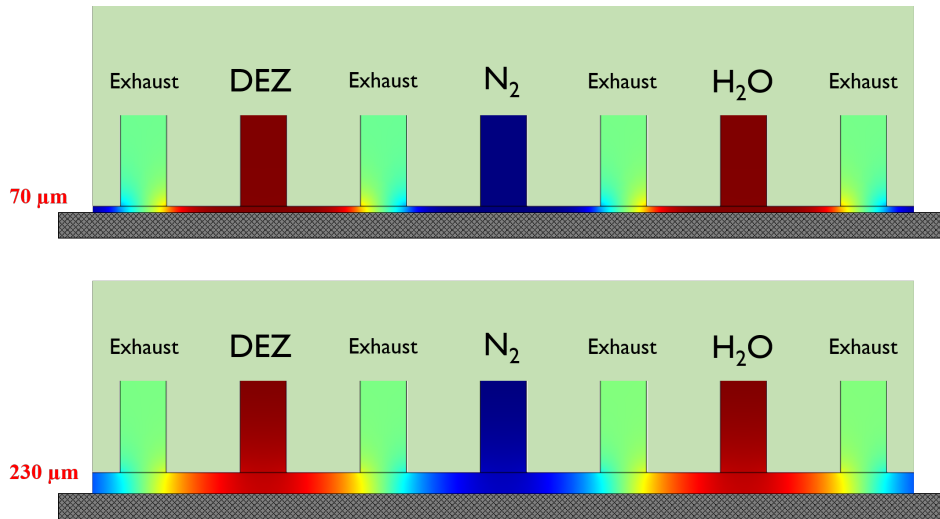


Figure 3.24: The effect of the injector-substrate distance to the precursor concentration, illustrated using COMSOL Multiphysics simulation. For this illustration, only one part of the injector is shown. Red color corresponds to the precursor concentration at the input inlet level, while blue color corresponds to pure nitrogen.

For the smaller distance case ( $70 \mu\text{m}$ ), the precursor concentrations are homogeneous under the injection channels, while the nitrogen barrier is fairly efficient to prevent the precursors from mixing. For the higher distance case ( $230 \mu\text{m}$ ), the precursor concentration tends to extend its profile due to the diffusion phenomenon. Figures 3.25 and 3.26 represent the precursor concentration in the gas phase above the substrate as a function of the position on the substrate, for two injector-substrate distances:  $70$  and  $230 \mu\text{m}$ , respectively. For the later, an overlap between two precursor concentration profiles can be observed, which means that the CVD component cannot be neglected in the case of the higher distance.

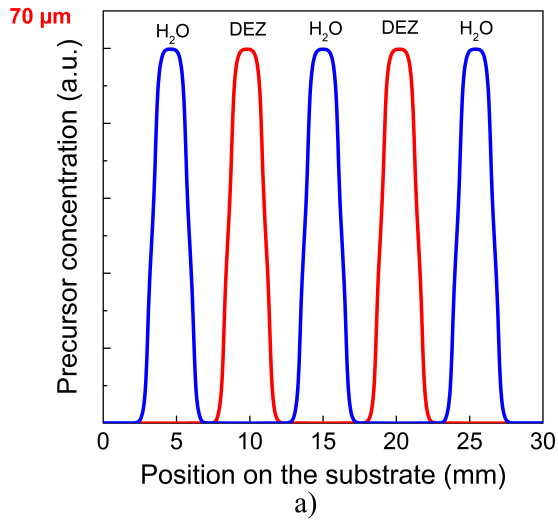


Figure 3.25: Precursor concentration profile at the interface gas/substrate as a function of the position on the substrate for the case of an injector-substrate distance of 70 microns.

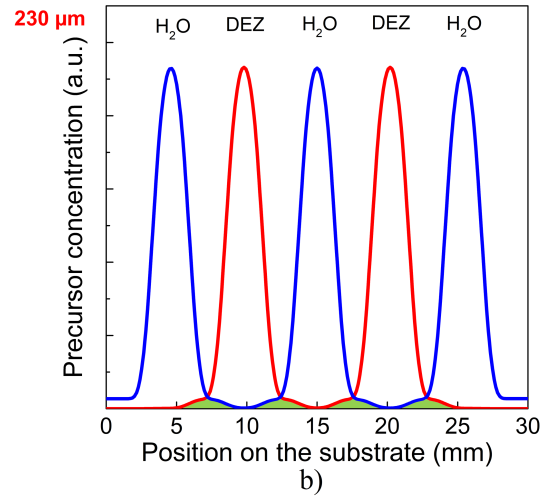


Figure 3.26: Precursor concentration profile at the interface gas/substrate as a function of the position on the substrate for the case of an injector-substrate distance of 230 microns.

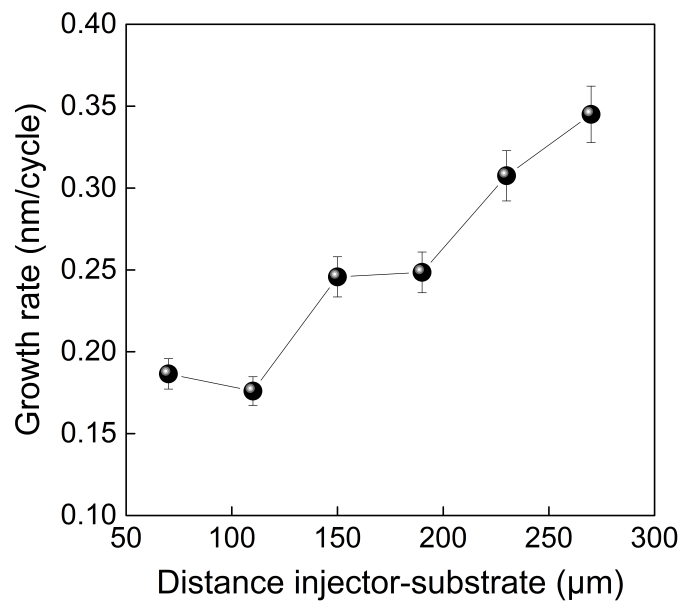


Figure 3.27: Growth per cycle of ZnO films as a function of the distance between the injector and the substrate.

Figure 3.27 shows the experimental result of the growth rate as a function of the injector-substrate distance. The high distances leads to the higher growth rates due to the CVD component, as discussed in the previous paragraph. The growth per cycle is rather stable at 0.25

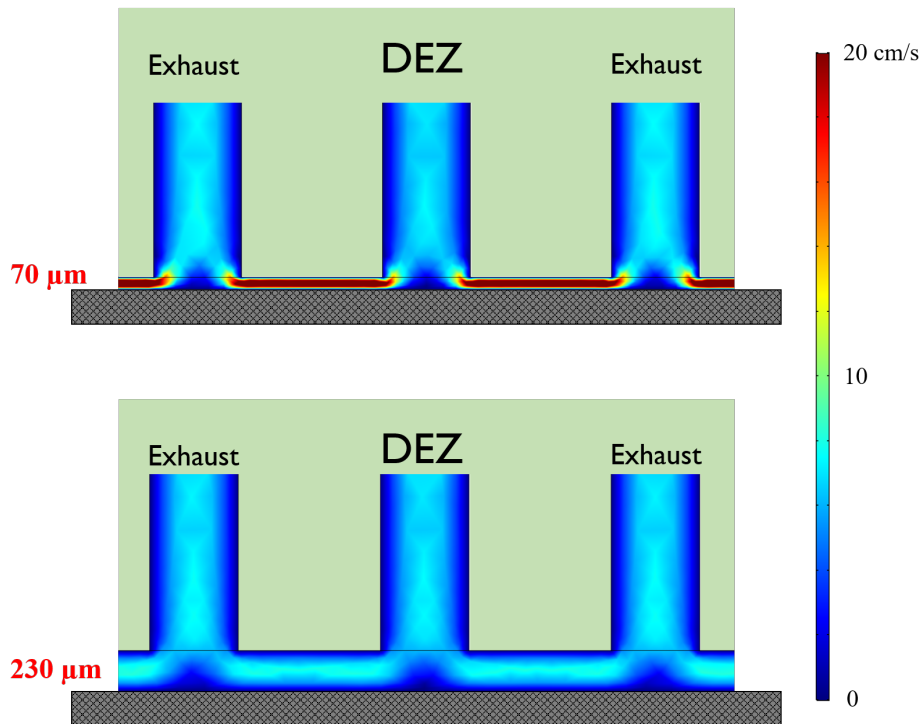


Figure 3.28: The effect of the injector-substrate distance on the gas velocity, illustrated using COMSOL Multiphysics simulation. For this illustration, only one part of the injector is shown.

nm/cycle for a distance in the range of  $[150 \mu\text{m}; 200 \mu\text{m}]$ . Interestingly, a further decrease of the injector-substrate distance reduces the growth rate. This effect can be explained by an increase of the precursor speed when decreasing the gap between the injector and the substrate, as shown in figure 3.28. Our hypothesis is that if the gas speed is too high, especially in the direction parallel to the substrate surface, the adsorption kinetics of the precursor by the substrate is less efficient. As a summary, for our current design of the gas injector, the optimized distance between the injector and the substrate is about  $150\text{-}200 \mu\text{m}$ .

Figure 3.29 shows the X-ray diffraction patterns of ZnO samples deposited with different injector/substrate distances (from  $70 \mu\text{m}$  to  $270 \mu\text{m}$ ). All samples present a growth following the preferential orientation  $[100]$ . For the samples having large injector-substrate gap ( $230 \mu\text{m}$  and  $270 \mu\text{m}$ ), the second dominant reflection  $[002]$  becomes non-negligible. This trend was observed in Figure 3.16, when studying the effect of the DEZ bubbling flow, and in both cases, this means that there exists a CVD component during the film growth. This part was lately published in the following paper: Masse de la Huerta, C.; Nguyen, V. H. et al. *Coatings* **2019**, 9 (1), 5.[88]

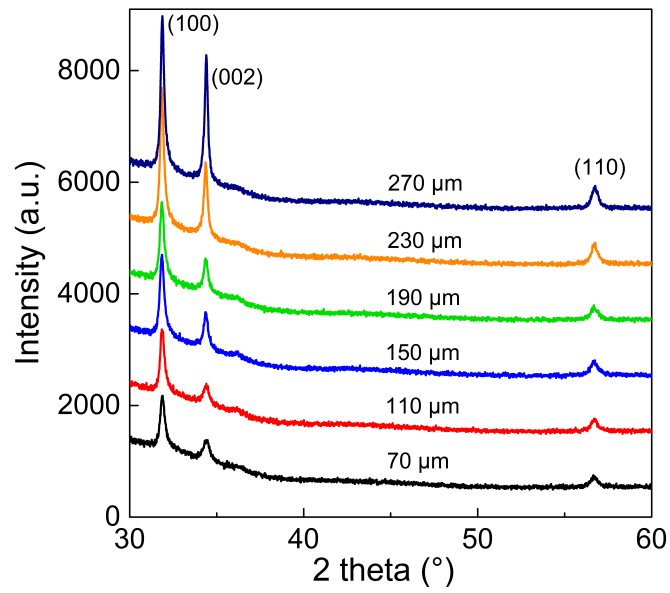


Figure 3.29: X-ray diffraction patterns of ZnO samples deposited with different injector/substrate distances (from 70  $\mu\text{m}$  to 270  $\mu\text{m}$ ).

## 3.2 Optimization of ZnO:Al thin film deposition

The effect of impurity doping of ZnO layers fabricated by AP-SALD has been already investigated by other groups: ZnO:Al by Illiberi et al.[89] (2014) using a circular reactor head and ZnO:Al by Ellinger et al. [90] (2014) using a close proximity SALD injector, which is similar to our injector design. In this part, we discuss in detail the optimization work of ZnO:Al films, the effect of aluminum doping on the physical properties of the films deposited by our close-proximity AP-SALD system.

### 3.2.1 Tuning aluminum content in ZnO:Al films

As described in chapter 2, the aluminum doping in ZnO:Al films was performed by adjusting the mixture between aluminum and zinc precursors, i.e. trimethylaluminum (TMA) and diethylzinc (DEZ), respectively.

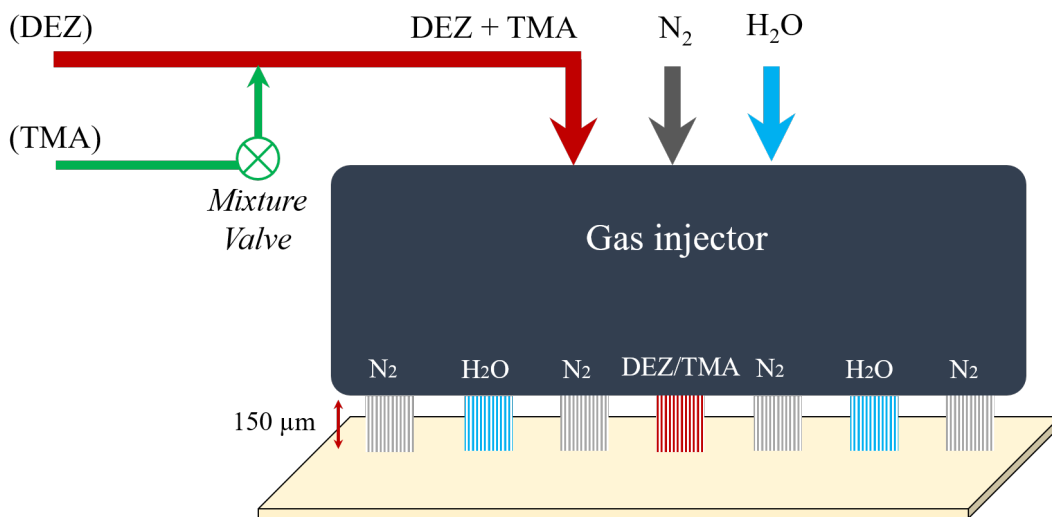


Figure 3.30: Schematic view of the close-proximity AP-SALD system used for ZnO:Al deposition. The Al precursor (TMA) is mixed with the Zn precursor (DEZ) before injecting the mixture onto the substrate.

Figure 3.30 shows a scheme of the close-proximity AP-SALD system used for ZnO:Al deposition, in which TMA is mixed with DEZ through a pneumatic valve before the mixture is injected to the substrate. Indeed, since TMA is very volatile and reactive (compared to DEZ), if the TMA line is permanently exposed to the DEZ line, the deposited ZnO:Al films are overdoped and become completely resistive. In order to avoid the overdoping, the pneumatic valve connecting the TMA and DEZ lines is opened just from time to time during a short duration, as shown in figure 3.31. The Al doping was performed via three steps as follows:

1. Performing Al<sub>2</sub>O<sub>3</sub> depositions until the saturation of TMA.
2. Performing ZnO depositions until the saturation of DEZ lines.
3. Performing TMA pulse cycles to make TMA/DEZ mixture until the saturation of TMA content in DEZ line. The ZnO:Al depositions are now performed as a normal ZnO deposition with the replacement of DEZ line by TMA/DEZ mixture.

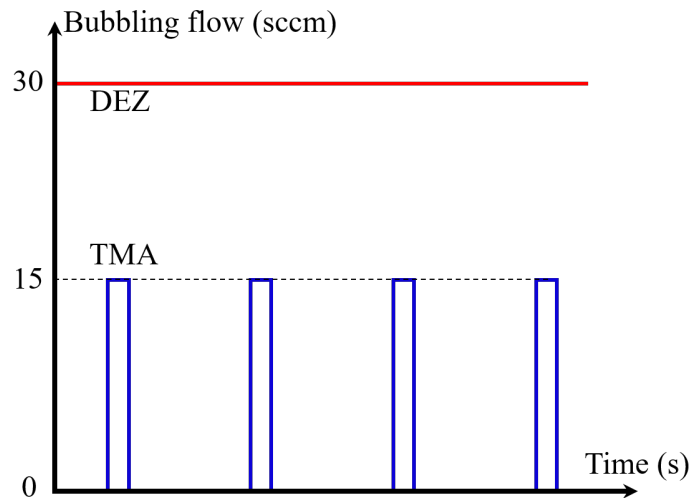


Figure 3.31: Schematic representation of nitrogen bubbling flows through DEZ and TMA bubblers as a function of time.

The first and second steps were separately studied, and actually easier to optimize compared to the third step. Accordingly, the saturation of TMA and DEZ lines can be reached after performing 2000 cycles and 4000 cycles, respectively, resulting in a stable growth per cycle. In order to estimate how long it takes for the system to reach a constant TMA concentration in the TMA/DEZ gas mixture, we performed a series of samples, which have exactly the same deposition parameters (200 °C, 580 cycles, DEZ bubbling and dilution flows: 30/270 sccm, H<sub>2</sub>O bubbling and dilution flows: 150/300 sccm, nitrogen barrier: 900 sccm, substrate velocity: 6 cm/s, TMA bubbling flow: 15 sccm, number of substrate oscillations per TMA pulse: 14, opening time of the mixture valve: 1 s), then we measured the Al content in the deposited films.

Figure 3.32 and Figure 3.33 show the Al content and total transmittance of the ZnO:Al samples obtained by using the same deposition parameters during the saturation period of TMA in TMA/DEZ mixture. The experiments show that about 6400 cycles were needed, i.e. 45 minutes, to achieve a stable Al content of about 1.6 % in the ZnO:Al films. The effect of Al doping in the ZnO:Al samples can be easily visualized via a drop of optical transmittance in

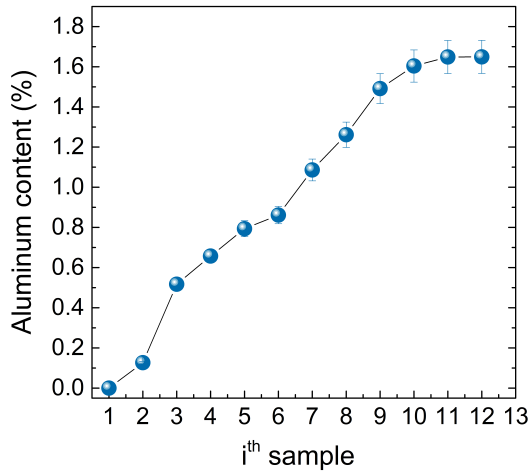


Figure 3.32: The aluminum content estimated by EDS analysis of the samples having the same deposition parameters during the saturation period of TMA in TMA/DEZ mixture. After 12 times of repeating exactly the same deposition parameters, the concentration of TMA in TMA/DEZ mixture is stable.

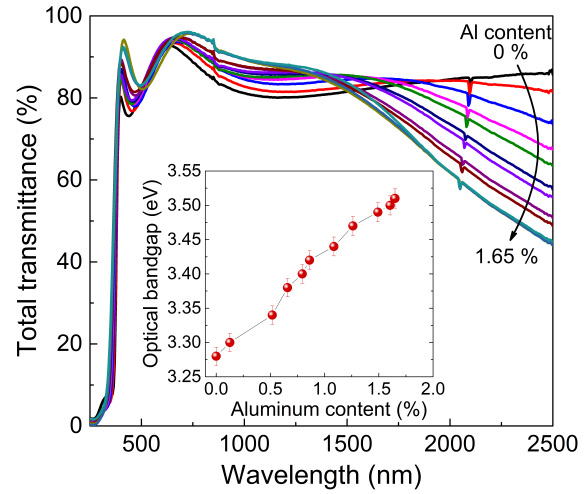


Figure 3.33: Total transmittance with optical bandgap calculated from Tauc plot of the ZnO:Al samples having the same deposition parameters during the saturation period of TMA in TMA/DEZ mixture.

the infrared region due to the plasmonic effect. It follows that the optical bandgap measured by Tauc plot method increases clearly with the Al doping in the ZnO:Al films. This can be explained by the fact that ZnO:Al samples were totally degenerated, i.e. the Fermi level lays above the minimum of the conduction band. Therefore, the increase of the Fermi level, which is directly related to an increase of the Al doping concentration, accompanies the increase of the optical bandgap. This effect will be discussed in details in chapter 4, section 4.1.2.

### Effect of TMA pulse time

In practice, the control of Al doping can be accurately adjusted via two main parameters: the opening duration of the mixture valve (also called TMA pulse time) and the time between two consecutive pulses. Figure 3.34a) shows the effect of TMA pulse time on the Al content ( $\%Al / (\%Al + \%Zn)$ ) measured with EDS, and the resulted carrier concentration in ZnO:Al films. As can be seen, the Al content can be tuned easily from 0.1 % up to 4 % just by increasing the TMA pulse time from 500 ms to 900 ms. As a result, the carrier concentration greatly increases from  $1.5 \times 10^{19} \text{ cm}^{-3}$  up to  $1.9 \times 10^{20} \text{ cm}^{-3}$  for an Al content of 2.5 % then slightly decreases for further increase of Al content in the film. This decrease of the carrier concentration can also be visualized via an increase of the total transmittance in the infrared region for the ZnO:Al sample having 4% of Al content, as shown in 3.34b). The decrease

of the carrier concentration versus increase of Al content can be explained by compensation effects via zinc vacancy formation.[50, 91]

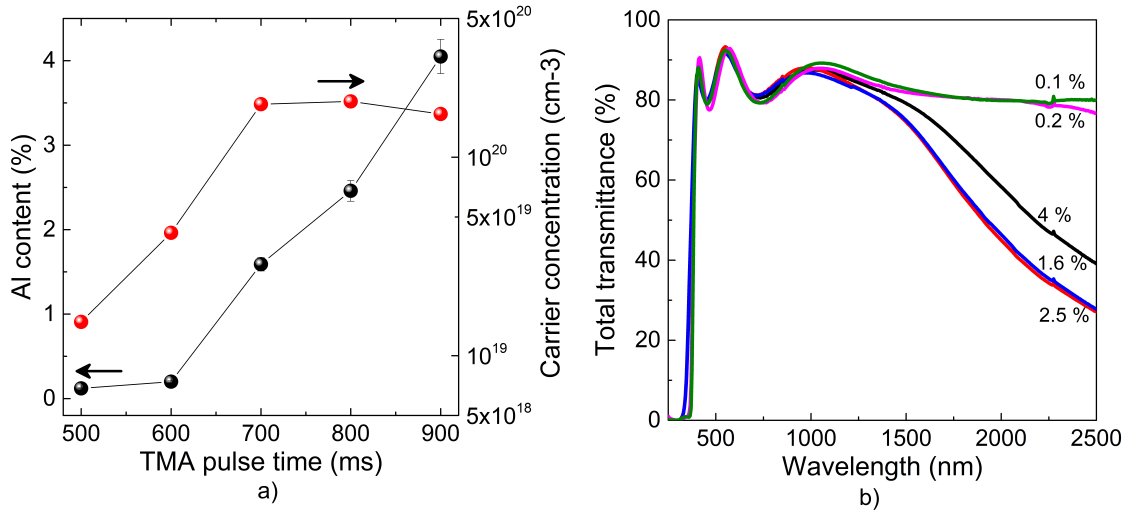


Figure 3.34: a) The Al content (%) estimated by EDX analysis and the resulting carrier concentration versus TMA pulse time used during AP-SALD deposition; b) the total transmittance of ZnO:Al films deposited with different TMA pulse time, varying from 500 ms to 900 ms while the other deposition parameters were fixed.

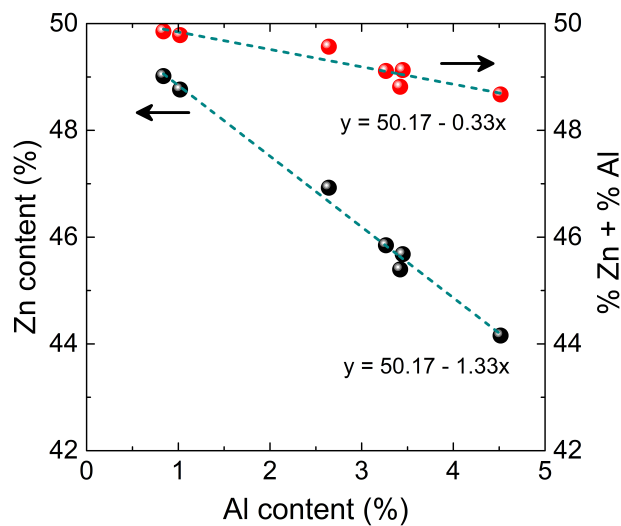


Figure 3.35: Influence of Al content on the Zn content and the total metal content in ZnO:Al films. The data was measured with X-ray micro-analysis technique.

Figure 3.35 shows the effect of the Al doping concentration on Zn content and the total metal content in ZnO:Al films, data measured with X-ray micro-analysis technique. We observed that the Zn content decreases when the Al doping concentration increases, which firstly

should be related to the replacement of the Zn atoms in the ZnO crystallographic lattice by Al atoms. However, the decrease of the total metal content in ZnO:Al films ( $\%Zn + \%Al$ ) can only be explained by the compensation effect when increasing the Al doping concentration, i.e. formation of Zn vacancies. This is totally coherent with the DFT calculation performed by Jannotti & Van de Walle, 2007, in which they showed a decrease of zinc vacancy formation energy when raising the Fermi level, i.e. doping concentration, for the case of oxygen rich atmosphere.[1]

## 3.2.2 Influence of doping on physical properties

### 3.2.2.1 Structural properties

Figure 3.36 and Figure 3.38 show respectively XRD patterns for ZnO:Al films containing different quantities of aluminum and SEM images of the films with percentage of aluminum ( $\%Al/(\%Al+\%Zn)$ ) estimated by EDX analysis. As can be seen, very poorly doped ZnO films ( $< 1\%$ ) show a polycrystalline structure having c-axis [002] as the preferential growth orientation. Then, by increasing the Al doping concentration, the film texture moves from c-axis [002] orientation to [100] orientation as the aluminum quantity in the film increases. When analyzing in detail the positions of the reflections, we observed a shift of the peak (002) towards higher  $2\theta$  ( $^\circ$ ) values. Interestingly, this occurs only for the {002} planes, which have the highest atomic density. According to the Bragg's Law for diffraction condition, the distance between {002} planes should satisfy the following expression:  $\lambda = 2d_{002}\sin\theta$ . Since the ionic radius of  $Al^{3+}$  (53 pm) is smaller than the one of  $Zn^{2+}$  (74 pm),  $d_{002}$  of Zn:Al film is smaller likely due to compressive stress in the lattice caused by the substitution of  $Zn^{2+}$  by smaller  $Al^{3+}$  ions. As a result, the diffraction angle  $2\theta$  was observed to be higher for the case of ZnO:Al films. Moreover, the mean size of the crystallites oriented along [002] direction also decreases for increasing the Al content. Table 3.2 summarizes the variation of (002) peak position and of the mean crystallite size oriented along [002] versus percentage of aluminum in ZnO:Al films.

Now, to explain why the Al incorporation into the ZnO lattice has a strong effect on the growth preferential orientation, we compare the  $Zn^{2+}$  ionic density in the planes (002) and (100). As can be seen in figure 3.37, the  $Zn^{2+}$  density in the (002) plane is 3.6 times higher than the one of the plane (100). This means that it is energetically more favorable to incorporate Al into the less mechanically strained planes, i.e. (100) planes, than into the dense planes (002). The structural modification due to the Al doping can be also visualized via the SEM images along with a cross-section view scheme of different types of morphology, as shown in figure 3.38. The (002) type growth exhibits a round shape grain, viewed from the top, while the (100) type has pyramid-like morphology with elongated grains.

Another important structural parameter that strongly influences on the electrical properties of the ZnO:Al films is the grain size. Obviously, polycrystalline films, such as ZnO or ZnO:Al films, having bigger grains should be more favorable for electron transport, i.e. higher conductivity. However, the ZnO thin film growth on glass or on any amorphous material usually starts with the formation of nano-islands via a nucleation step, then these islands grow to form a continuous film with a certain grain size, which in turn increases with the film thickness.[92]

Figure 3.39 shows AFM images of ZnO:Al films with various thicknesses deposited by

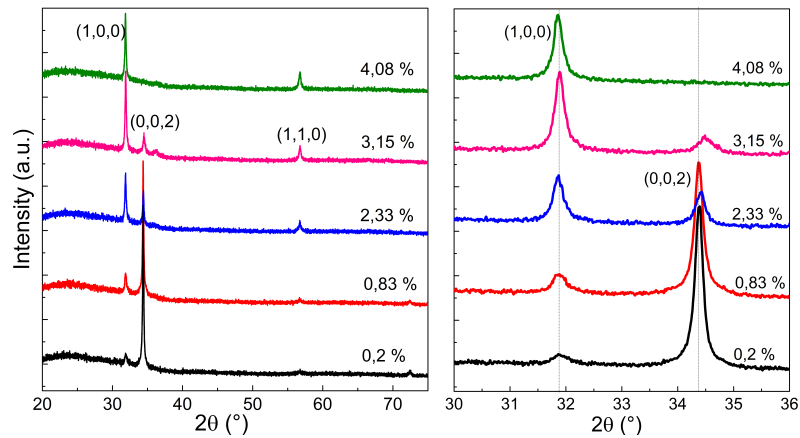


Figure 3.36: X ray diffraction spectra of ZnO:Al samples with different Al doping concentrations. Left: full spectra, right: a zoom on the (100) and (002) reflections.

%Al	(002) reflection position $2\theta$ ( $^{\circ}$ )	Mean crystallite size oriented along (002) (nm)
0.2	34.374	48
0.83	34.375	47
2.33	34.414	42
3.15	34.465	34
4.08	n.a.	n.a

Table 3.2: Variation of (002) peak position and of the mean crystallite size oriented along [002] direction versus percentage of aluminum in ZnO:Al films; for this calculation the value of Scherrer constant was set at 0.9 as a typical value.

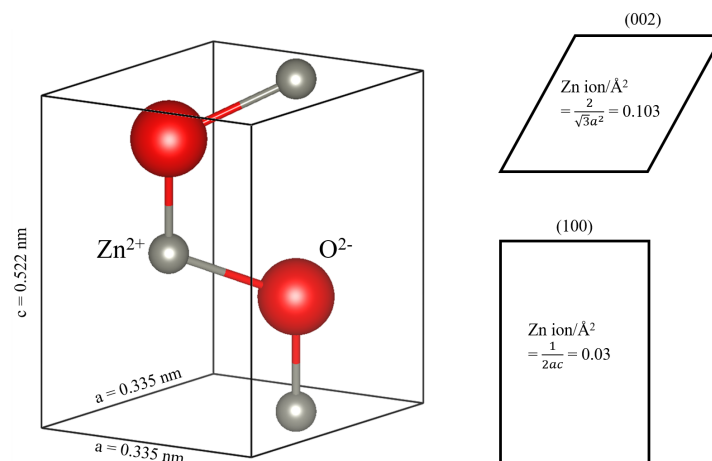


Figure 3.37: ZnO unit cell, as well as (002) and (100) crystallographic planes.

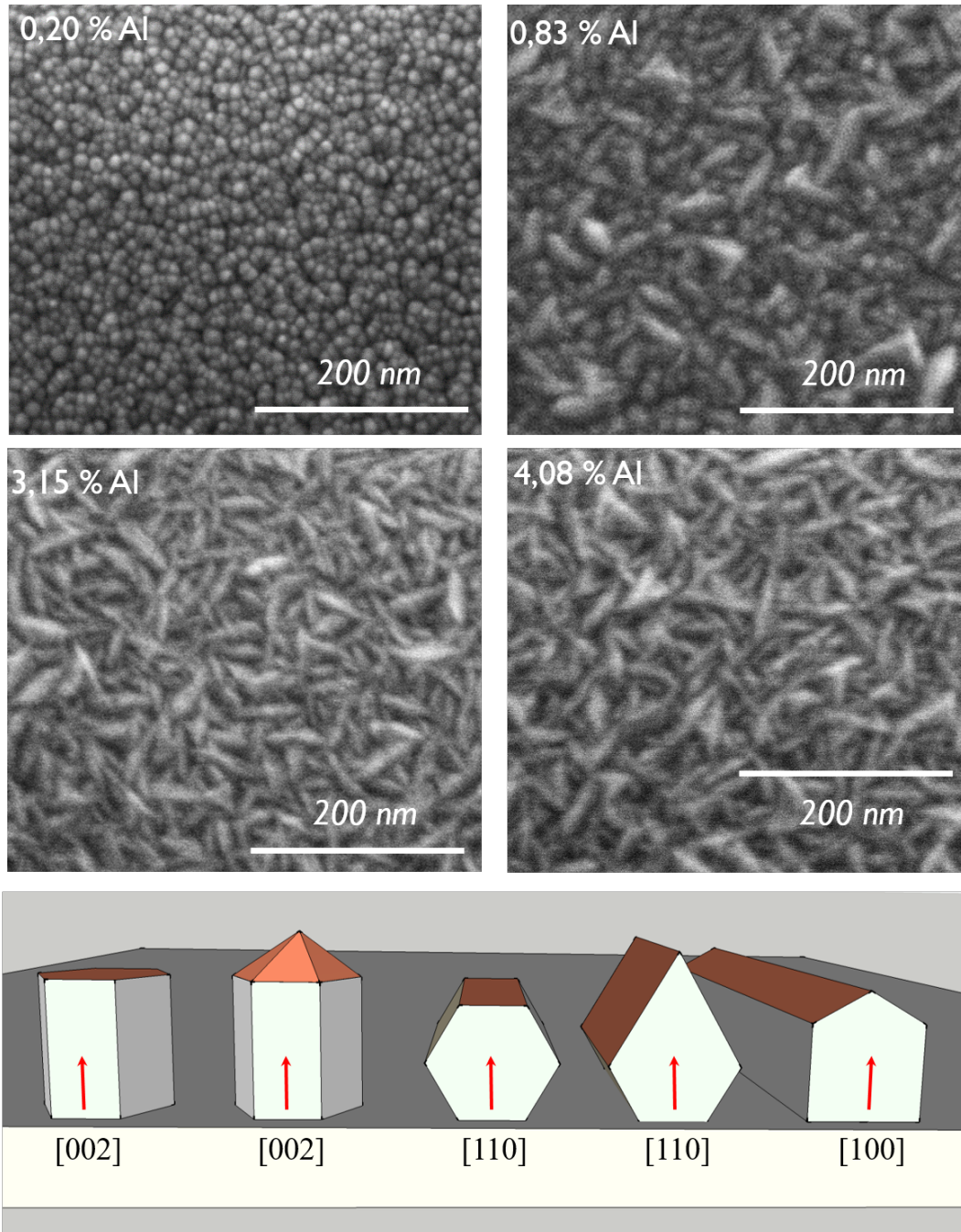


Figure 3.38: SEM images of ZnO:Al samples with different Al doping concentrations, along with a cross-section view scheme of different types of morphology for different crystallographic orientations.

AP-SALD at 200 °C. It can be observed that the thicker films have the bigger grain size. Figure 3.40a) shows that when increasing film thickness from 205 nm to 525 nm, the mean grain size measured with AFM increases significantly, from 46 nm to 69 nm. Since the AFM technique allows only accessing the size of the biggest grains on the top of the films, the mean grain size is actually much lower than the value given by AFM. For calculation in the next chapter, we assume that the mean grain size,  $L$ , can be estimated to be around one half of the grain size measured by AFM, i.e. 20 nm for a 200 nm thick film for example.

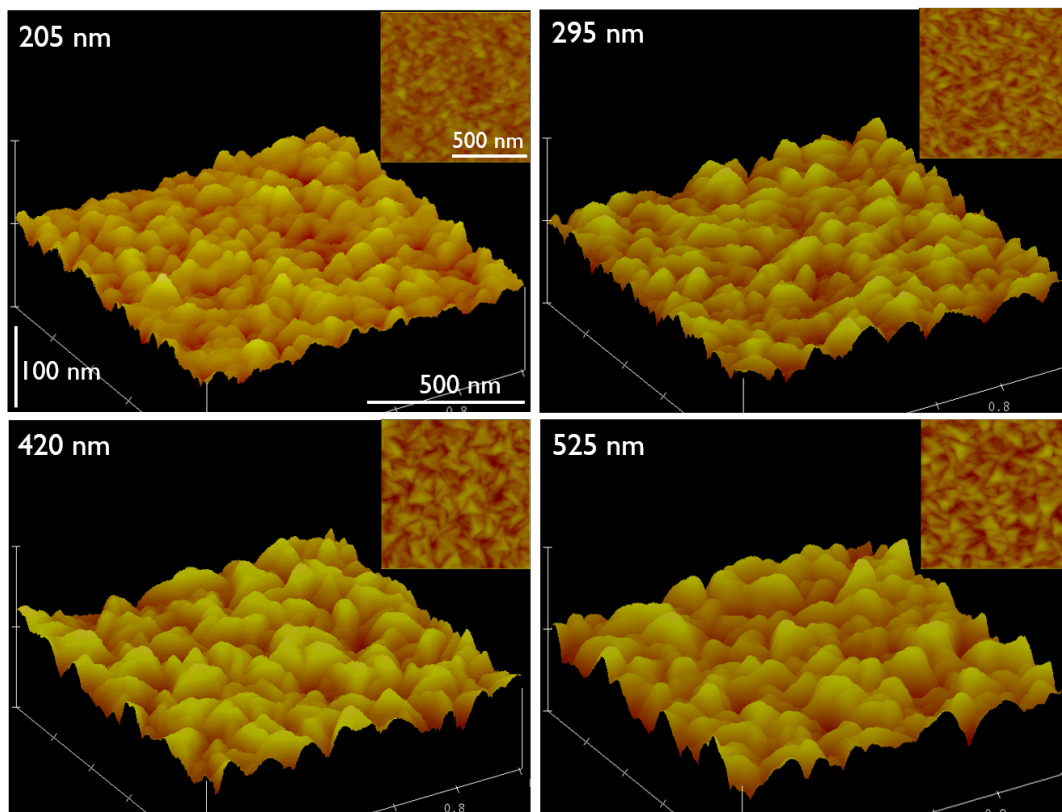


Figure 3.39: AFM images of ZnO:Al films with various thicknesses deposited by AP-SALD at 200 °C. The inset images show corresponding top-view AFM images.

The XRD patterns of the same set of samples shown in Figure 3.40b) illustrate the similar growth orientation for all ZnO:Al films. This is again confirmed by the similar surface morphology studied by SEM imaging, as shown in Figure 3.41a). In addition, Figure 3.41b-d) show respectively dark-field TEM image, high-resolution TEM images of 500nm-thick ZnO:Al film deposited on Silicon substrate at 200 °C. The XRD, SEM and TEM images clearly show that the ZnO:Al films deposited by AP-SALD technique have a good crystalline quality.

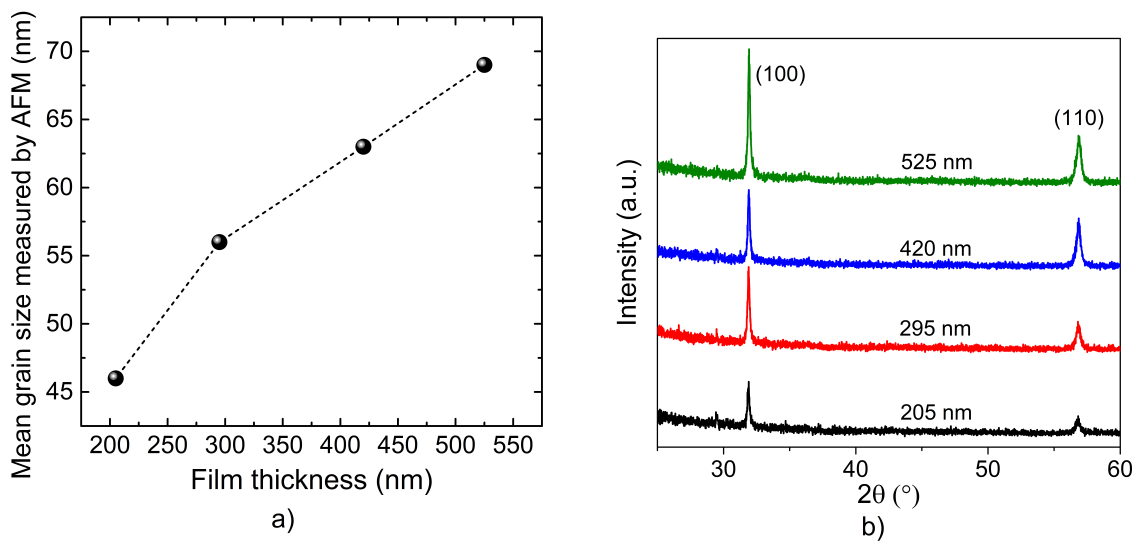


Figure 3.40: a) Mean grain size measured with AFM and b) X-Ray Diffraction patterns of ZnO:Al films with various thicknesses deposited by AP-SALD at 200 °C.

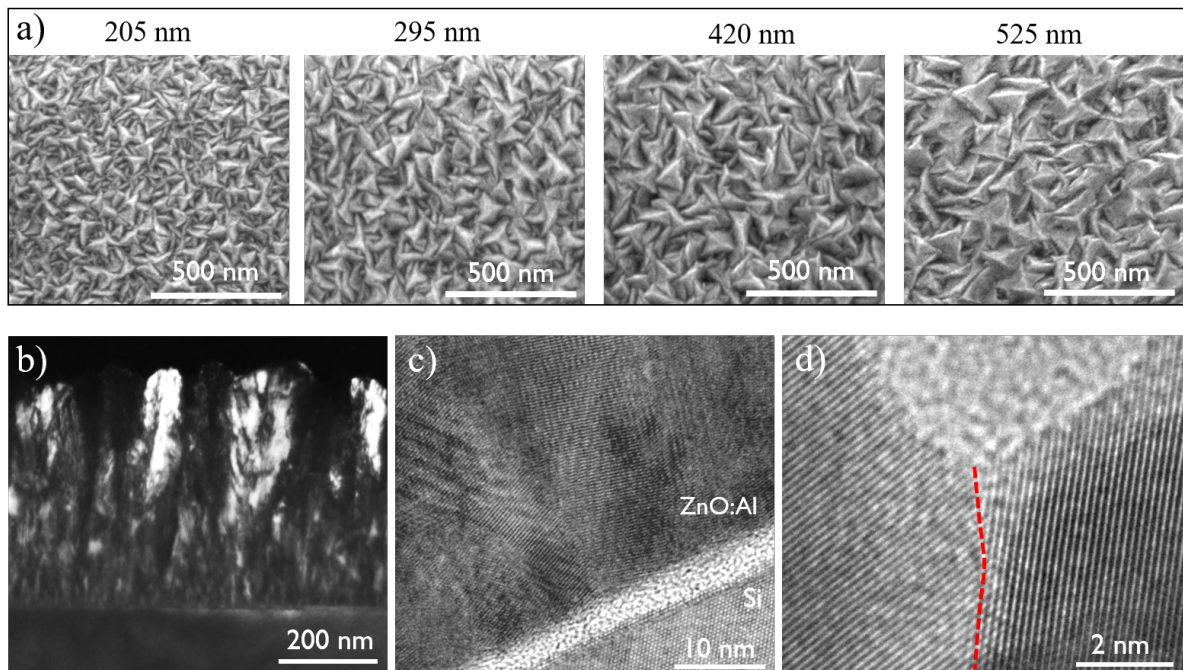


Figure 3.41: a) SEM micrographs of ZnO:Al films with various thicknesses deposited by AP-SALD at 200 °C. b) Dark-field TEM image, c-d) high-resolution TEM images of 500nm-thick ZnO:Al film deposited by AP-SALD on Silicon substrate at 200 °C.

### 3.2.2.2 Electrical properties

Figure 3.42 shows the electrical properties measured with the Hall effect technique of ZnO:Al samples having different Al doping concentration. Accordingly, the sheet resistance drops from  $22\text{ k}\Omega/\text{sq}$  down to  $754\ \Omega/\text{sq}$  when increasing the Al doping concentration from 0.1 % to 4%. This is mainly due to a great improvement of the carrier concentration from  $4 \times 10^{19}\text{ (cm}^{-3}\text{)}$  to  $1.9 \times 10^{20}\text{ (cm}^{-3}\text{)}$ . The mobility starts decreasing at the beginning when increasing the % Al, then it re-increases for larger doping concentration. However, the values of electron mobility still remain modest, which is the main limiting factor to get better conductivity.

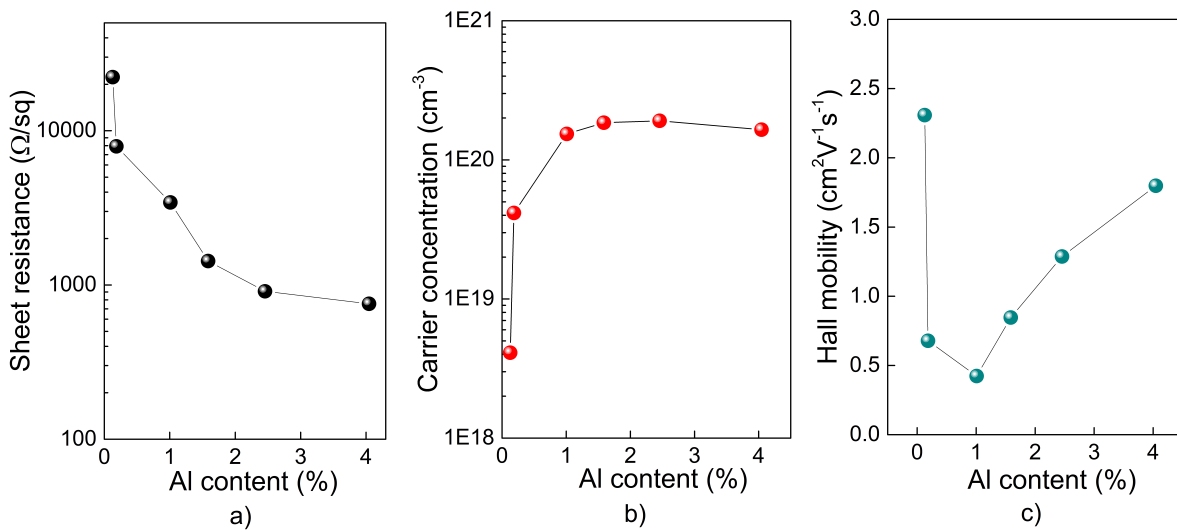


Figure 3.42: a) sheet resistance, b) carrier concentration and c) carrier mobility measured by Hall effect measurement of ZnO:Al samples having different Al doping concentrations. All the films are 185 nm thick.

Table 3.3 shows the electrical properties of as-deposited ZnO:Al films deposited by various methods (MSD, ALD and AP-SALD) in comparison with ITO deposited by MSD. The ITO and ZnO:Al films deposited by MSD and ALD were performed in CEA-INES, while the ZnO:Al film deposited by AP-SALD was performed in LMGP. As can be seen, while the carrier concentrations are rather similar for all samples, a remarkable difference in electron mobility is observed when comparing ZnO:Al films prepared by vacuum-based deposition technique to the film prepared by AP-SALD. Besides, we have shown in the previous section that the films deposited by AP-SALD technique have a good crystalline quality, thus, a low electron mobility might be related to a high electron-trap density at the grain boundaries rather than ingrain scattering. Actually, it is known that the electron mobility in polycrystalline ZnO-based films is crucially affected by the oxidizing atmosphere during deposition.[93–95] Concretely, the oxygen species adsorbed at grain boundaries build a potential barrier for elec-

trons, limiting their mobility from one grain to another. To overcome this difficulty and keep the advantages of fast-deposition, low-temperature and scalable properties of AP-SALD, as well as open-atmosphere deposition techniques in general, the deep comprehension of the carrier transport at grain boundaries, as well as an efficient post-deposition treatment method to recover the conductivity of ZnO:Al films deposited by AP-SALD are highly required.

Material	$P_{O_2}$ [mbar]	Thickness [nm]	Resistivity [ $\Omega cm$ ]	Carrier concentration [ $cm^{-3}$ ]	Carrier mobility [ $cm^2 V^{-1} s^{-1}$ ]
ITO (MSD)	$3 \times 10^{-5}$	92	$8.7 \times 10^{-4}$	$2.2 \times 10^{20}$	33
ZnO:Al (MSD)	$1 \times 10^{-5}$	93	$1.5 \times 10^{-3}$	$2.8 \times 10^{20}$	15
ZnO:Al (MSD)	$2.9 \times 10^{-5}$	284	$1.8 \times 10^{-3}$	$2.7 \times 10^{20}$	13
ZnO:Al (ALD)	1	100	$2.1 \times 10^{-3}$	$2.9 \times 10^{20}$	10
ZnO:Al (AP-SALD)	210	185	$1.4 \times 10^{-2}$	$1.9 \times 10^{20}$	1.8

Table 3.3: The electrical properties of as-deposited ZnO:Al films prepared by different deposition methods (MSD, ALD and AP-SALD) in comparison with ITO prepared by MSD. The oxygen partial pressure during the deposition and the film thickness are also shown. The data related to ITO and to ZnO:Al by MSD was extracted from the work of Carroy et al.[6]

### 3.3 Application of ZnO:Al films deposited by AP-SALD to SHJ solar cells

In literature, ZnO:Al or ZnO:B thin films have been successfully integrated as transparent conductive oxide in silicon heterojunction (SHJ) solar cells, both using sputtering or ALD, as an alternative to ITO.[6, 96–98] Korte et al. have showed an energy conversion efficiency of 19.8 % when using 80 nm ZnO:Al thin films deposited by sputtering as front TCO window.[96] Christmann et al. (EU PVSEC conference, 2016) have used ZnO:Al films deposited by both sputtering and ALD as back contact and showed that the replacement of ITO back contact by ZnO:Al leads to an efficiency gain of 0.45%, i.e. from 22.2 to 22.65 %.[97] Particularly, Carroy et al. in our SHJ group in CEA-INES have demonstrated an energy conversion efficiency of 19.9 % in their SHJ solar cells with ZnO:Al layers deposited with MSD on both sides (compared to 20.4 % for the SHJ cell with ITO as electrodes).[6] The result of this work is summarized in table 3.4. Accordingly, the lower efficiency of the SHJ cells when using ZnO:Al instead of ITO originates from the poorer electrical properties of ZnO:Al as compared to ITO ( $\rho = 1.5 \times 10^{-3} \Omega cm$  for ZnO:Al versus  $\rho = 8.7 \times 10^{-4} \Omega cm$  for ITO, see table 3.3), leading to lower  $FF$  values.

Front/back contact	$V_{OC}$ [mV]	$J_{SC}$ [mA/cm <sup>2</sup> ]	$FF$ [%]	$\eta$ [%]	$R_S$ [ $\Omega/cm^2$ ]
<i>ITO/ITO</i>	718.8	36.4	77.7	20.4	$2.3 \times 10^{-3}$
<i>ITO/ZnO : Al<sub>280nm</sub></i>	720.1	36.3	78.5	20.5	$2.6 \times 10^{-3}$
<i>ZnO : Al/ITO</i>	719.6	36.4	75.2	19.7	$4.4 \times 10^{-3}$
<i>ZnO : Al/ZnO : Al<sub>280nm</sub></i>	720.7	36.3	76.3	19.9	$4.1 \times 10^{-3}$

Table 3.4: IV parameters of SHJ cells with ZnO:Al as transparent electrode(s) (average of 4 cells). Data extracted from the work of Carroy et al. (2015).[6]

In this work, after optimizing the experimental parameters for the deposition of ZnO and ZnO:Al films as discussed in the previous section, we have made the first trials towards the integration of optimized as-deposited films in SHJ solar cells. Since the high performance of SHJ solar cells is achieved thanks to very thin a-Si:H layers (< 20 nm), which allow to greatly passivate the surfaces of the silicon substrate, the TCO deposition has to be soft so that the passivation is maintained after deposition, which is not the case for sputtering, i.e. one of the most popular techniques used in PV industry for TCO deposition. Demarex et al. have indeed shown that plasma luminescence (visible or UV) or electron/particle bombardment during the TCO sputtering can generate a damage of the a-Si:H/c-Si interface passivation.[99] The objectives of this part of the work are thus firstly to study the compatibility of the AP-SALD method with the SHJ technology, and secondly to determine the limiting factor of the

cell performance, therefore, to have a good strategy in the material development.

Figure 3.43 shows the implied open-circuit voltage ( $V_{OC}$ ) measured at 1-sun of a SHJ-like structure before and after ZnO deposition by AP-SALD versus deposition temperature (the implied- $V_{OC}$  is calculated from the excess carrier density generated under 1-sun illumination in open-circuit conditions).[100] An improvement in implied- $V_{OC}$  is observed after ZnO deposition by AP-SALD, which confirms that the AP-SALD technique is totally compatible to the SHJ technology in terms of maintaining the high passivation quality of a-Si:H/c-Si interface.

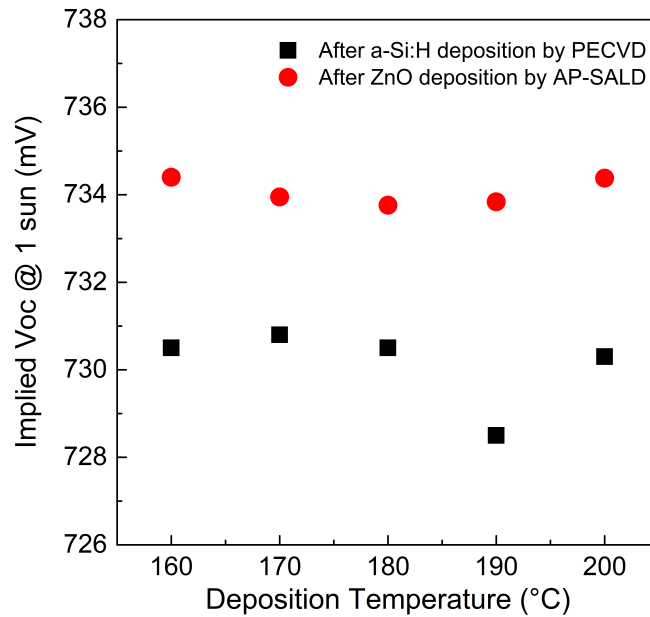


Figure 3.43: Implied open-circuit voltage at 1-sun of a SHJ-like structure before and after ZnO deposition by AP-SALD versus deposition temperature.

Figure 3.44a) and figure 3.44b) respectively show the J-V curves in the dark and under illumination of the SHJ cells with ITO (deposited by MSD) and ZnO:Al (deposited by AP-SALD) as transparent electrodes on both sides. The IV parameters are listed in Table 3.5. As can be seen, all IV characteristics of the SHJ cell with ZnO:Al deposited by AP-SALD are lower compared to the reference cell, with FF dropping the most. This is attributed to a much higher resistivity of as-deposited ZnO:Al films as compared to standard ITO films, which can also be visualized when comparing the dark JV curves as well.

In summary, we have confirmed that AP-SALD is a suitable technique for the deposition of TCOs based on ZnO for application in SHJ cells, as evidenced by the good implied- $V_{OC}$  values obtained after depositing ZnO based layers at 200 °C. Conversely, the performance of the SHJ cell is mainly limited by the modest conductivity of the as-deposited ZnO:Al films prepared by AP-SALD (the same problem occurring when using conventional ALD). Therefore, the

next chapter will be dedicated to the description of a complete study on the limiting factors of the film conductivity, a key point towards further optimization.

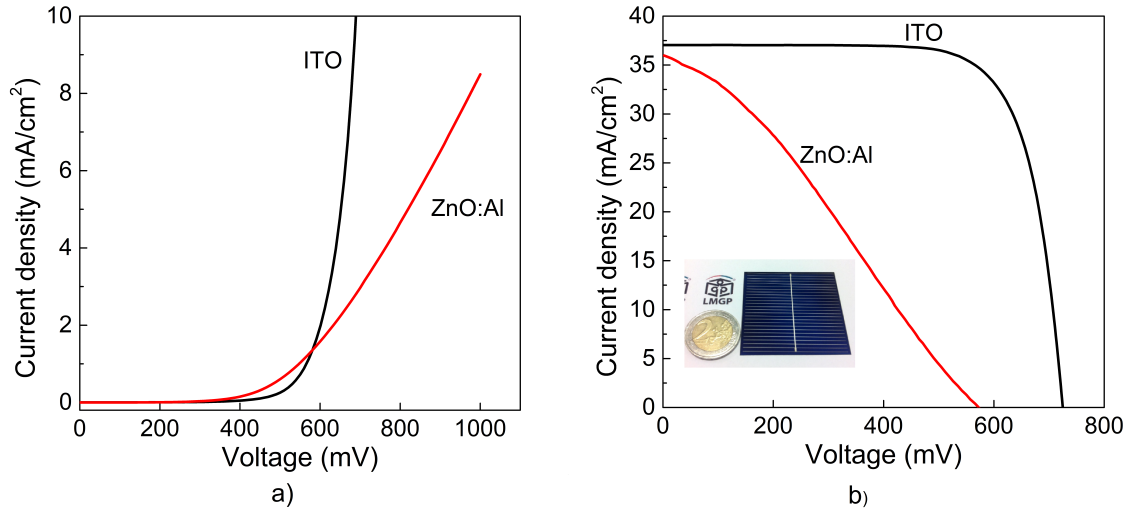


Figure 3.44: J-V curves in the dark (a) and under illumination (b) of SHJ solar cells with ITO (reference cell, size of 14.44 cm<sup>2</sup>) and ZnO:Al as transparent electrodes on both sides, respectively. The results for ZnO:Al were an average of 4 cells of the same size of 24.9 cm<sup>2</sup>.

TCO material	Area [cm <sup>2</sup> ]	V <sub>OC</sub> [mV]	J <sub>SC</sub> [mA/cm <sup>2</sup> ]	FF [%]	η [%]
ITO by MSD	14.44	725	37	74.5	20
ZnO:Al by AP-SALD	24.9	643	36	40.3	9.2

Table 3.5: IV parameters of SHJ cells with ITO deposited by MSD and ZnO:Al deposited by AP-SALD as transparent electrodes on both sides.

### 3.4 Conclusion

In this chapter, the effect of different experimental parameters including the deposition temperature, the gas flows, and the substrate/precursor injector distance on the growth rate, the crystallinity, the electrical/optical properties and the nanostructure of ZnO and ZnO:Al films have been presented.

In summary, we have found an ALD window in the temperature range of [130 °C, 180 °C], which is similar to the values reported in literature.[2] The deposition temperature mainly affects the structural properties of the deposited film, i.e. better crystallinity for higher deposition temperature. The optical bandgap of the ZnO films was also observed to decrease from 3.35 eV to 3.21 eV when the deposition temperature increased from 100 °C to 220 °C, which can be explained thanks to the notion of localized energy states and the band tails in amorphous semiconductor materials.

In the ZnO optimization, we have developed simple physical models, along with using Comsol Multiphysics simulation in order to better understand the effects of the different deposition parameters on the film growth. We have found that in order to obtain high-crystallinity, dense films, the precursors should be supplied sufficiently but, however, below a given flow as well, i.e. > 125 sccm for N<sub>2</sub> bubbling flow through H<sub>2</sub>O, 25-30 sccm for N<sub>2</sub> bubbling flow through DEZ, and a N<sub>2</sub> barrier flow in between [900 sccm, 1200 sccm] (obviously, these values are only valid for our reactor design). In AP-SALD, preventing precursors from mixing is an essential requirement in order to obtain a controllable ALD growth. We have optimized the gap between the gas injector and the substrate and obtained an optimal range of [150 μm, 200 μm]. When studying the effect of the substrate velocity on the growth rate of ZnO, we observed that at very high substrate speeds, the precursors do not have enough time to saturate the substrate surface, resulting in a lower growth rate, while at very low substrate speeds, the diffusion of the precursors through the N<sub>2</sub> barrier may create an CVD-like growth mode, i.e. higher growth rate. Therefore, the optimal values for the substrate speed are in between [5.7 cm/s, 6.4 cm/s], for 30 sccm N<sub>2</sub> bubbling flow through DEZ.

In the case of ZnO:Al films, the Al incorporation into the ZnO lattice has a strong effect on the growth preferential orientation: moving from [002] to [100] when the Al content in the ZnO:Al films increases. The sheet resistance drops from 22 kΩ/sq down to 754 Ω/sq when increasing the Al doping concentration from 0.1 % to 4%. This is mainly due to a large increase in the carrier concentration from  $4 \times 10^{19} \text{ (cm}^{-3}\text{)}$  to  $1.9 \times 10^{20} \text{ (cm}^{-3}\text{)}$ . However, the conductivity of the as-deposited ZnO:Al films is still strongly limited by modest values of mobility ( $\sim 1 - 2 \text{ cm}^2\text{V}^{-1}\text{s}^{-1}$ ).

In the last part of this chapter, we have presented our first result on integrating the optimized as-deposited ZnO:Al films in silicon heterojunction (SHJ) solar cells. We observed

---

that all I-V characteristics of the SHJ cells with ZnO:Al deposited by AP-SALD are lower as compared to the reference cell, with the FF dropping the most. This is mainly attributed to a much higher resistivity of as-deposited ZnO:Al films as compared to standard ITO films. In the next chapter, the study of the limiting factors of the film conductivity is discussed, including the presentation of a new model to describe the conductivity in semiconducting thin films, and a new and efficient post-deposition treatment to enhance the low mobility of as-deposited ZnO:Al films is also discussed.



# Chapter 4

## Carrier transport in ZnO:Al thin film

### Contents

---

<b>4.1</b>	<b>Degeneracy and nonparabolicity in TCOs . . . . .</b>	<b>78</b>
4.1.1	Non-degenerate semiconductors . . . . .	79
4.1.2	Degenerate semiconductors . . . . .	79
<b>4.2</b>	<b>Scattering mechanisms in ZnO:Al . . . . .</b>	<b>81</b>
4.2.1	Phonon - electron scatterings . . . . .	82
4.2.2	Dislocation scattering . . . . .	86
4.2.3	Ionized impurity scattering . . . . .	87
4.2.4	Grain boundary scattering . . . . .	88
<b>4.3</b>	<b>Application of AFTMM model . . . . .</b>	<b>101</b>
4.3.1	Illustration of the AFTMM model in comparison with the analytical model . . . . .	103
4.3.2	Model application to experimental data . . . . .	107
<b>4.4</b>	<b>Effect of UV post-deposition treatment . . . . .</b>	<b>113</b>
4.4.1	Experimental section . . . . .	113
4.4.2	Theoretical model . . . . .	114
4.4.3	Effect of doping concentration . . . . .	116
4.4.4	Effect of temperature during the UV treatment . . . . .	118
4.4.5	Model application to experimental data . . . . .	119
4.4.6	Oxygen readsorption after the UV treatment . . . . .	121
<b>4.5</b>	<b>Conclusion . . . . .</b>	<b>123</b>

---

A deep comprehension of the carrier scattering mechanisms in TCOs is an important step towards low-cost and high-performance TCOs since it provides a guidance on how to optimize the deposition conditions and any eventual post-deposition treatment. This chapter will be dedicated to discuss the different scattering mechanisms limiting electron transport in doped ZnO:Al films, with a main focus put on studying grain boundary scattering. Since ZnO:Al is a degenerate semiconductor, in which the parabolic approximation of the conduction is no longer valid, we will start the discussion by introducing some basic differences between degenerate (e.g. TCOs) and non-degenerate semiconductors.

## 4.1 Degeneracy and nonparabolicity in TCOs

It is widely known that for crystalline structures, electrons obey a Fermi-Dirac distribution. The occupation probability of an electron having a given energy  $E$  measured with respect to the Fermi energy  $E_F$  is:

$$f(E) = \frac{1}{1 + \exp\left(\frac{E - E_F}{k_B T}\right)} \quad (4.1)$$

where  $k_B$  and  $T$  are the Boltzmann constant and temperature, respectively. At 0 K, all states having energy below  $E_F$  are occupied, while states above  $E_F$  are empty. The density of states in the conduction band is given as follows:

$$g(E) = \frac{1}{2\pi^2} \left(\frac{2m_n}{\hbar^2}\right)^{3/2} \sqrt{E - E_C} \quad (4.2)$$

where  $m_n$ ,  $E_C$  are the electron effective mass and the minimum energy level of the conduction band. The density of electrons in the conduction band can be calculated via the integral of the product of  $g(E)$  and  $f(E)$  over the electron energy in the conduction band:

$$n = \int_{E_C}^{\infty} f(E) g(E) dE \quad (4.3)$$

Since electron scattering depends on the electron energy, therefore, both the total electron density ( $\text{cm}^{-3}$ ) and the electron distribution in energy ( $\text{eV}^{-1}\text{cm}^{-3}$ ) are important to study the electron scattering phenomena. In the next sections, we will treat two cases: non-degenerate (undoped ZnO) and degenerate (e.g. ZnO:Al) semiconductors.

### 4.1.1 Non-degenerate semiconductors

For the case of non-degenerate semiconductors, for which the Fermi level is found within the bandgap, the states within the conduction and valence bands overlap only with the tails of the Fermi-Dirac distribution. As a result, the carrier concentration increases significantly when increasing temperature, according to the following equation:

$$n = \frac{1}{2\pi^2} \left( \frac{2m_n}{\hbar^2} \right)^{3/2} \int_{E_C}^{\infty} \frac{\sqrt{E - E_C}}{1 + \exp\left(\frac{E - E_F}{k_B T}\right)} dE \quad (4.4)$$

which is widely used in the simplified version:  $n = N_C \exp\left(\frac{E_F - E_C}{k_B T}\right)$ , where  $N_C = 2 \cdot \left(\frac{m_0 k_B T}{2\pi\hbar^2}\right)^{3/2} \simeq 3.9 \times 10^{18} \text{ cm}^{-3}$  is the effective density of states in the conduction band at 300 K (for undoped ZnO). Therefore, in non-degenerate cases, the electron concentration in the conduction band is lower than this value. Figures 4.1 and 4.2 show respectively the simulation curves of temperature-dependent Fermi-Dirac distribution and temperature-dependent electron density in the conduction band of a non-degenerate ZnO sample having Fermi energy level at 0.1 eV below the minimum of the conduction band, which corresponds to a carrier concentration of  $8 \times 10^{16} \text{ cm}^{-3}$  at 300 K. As shown, the dependency of electron density in the conduction with temperature is very strong in non-degenerate semiconductor, for example increasing from  $7 \times 10^{12}$  at 100 K up to  $3 \times 10^{17}$  at 400 K (Figure 4.2). Another important remark is that most of the conduction electrons in non-degenerate semiconductors, are located close to the minimum of the conduction band, where the shape of the band can be fairly approximated to a parabolic shape. This is not the case where the conduction band fills up, as discussed below.

### 4.1.2 Degenerate semiconductors

In the case of degenerate semiconductors, the high amount of donors fills more than the effective density of states in the conduction band. As a result, the Fermi level is progressively raising, and eventually entering into the conduction band. An example of such degenerate semiconductors are TCOs. The use of eq. 4.3 is still valid, however, the conduction band now overlaps with a much larger part of the Fermi-Dirac distribution, as compared with non-degenerate semiconductors. Figure 4.3 illustrates the temperature-dependence of electron density in the conduction band for temperature varying from 100 K to 400 K (the electron density is about  $1 \times 10^{20} \text{ cm}^{-3}$  in this simulation). As can be seen, an increase of the temperature leads to a larger fraction of the electron distribution towards the high energy range. But, contrary to the previous case, the total carrier density in the conduction band appears to not depend much on temperature.

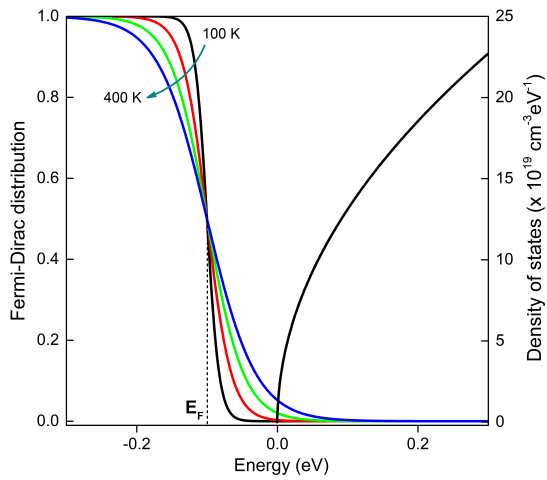


Figure 4.1: Simulation curves of temperature-dependent Fermi-Dirac distribution of a non-degenerate ZnO sample having Fermi level at 0.1 eV below the minimum of the conduction band. The density of states in the conduction band is also presented on the right axis

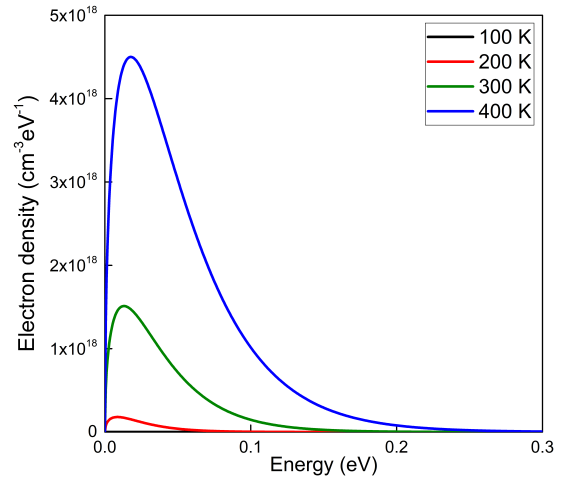


Figure 4.2: Simulation curves of temperature-dependent electron density in the conduction band of a non-degenerate ZnO sample having Fermi energy level at 0.1 eV below the minimum of the conduction band.

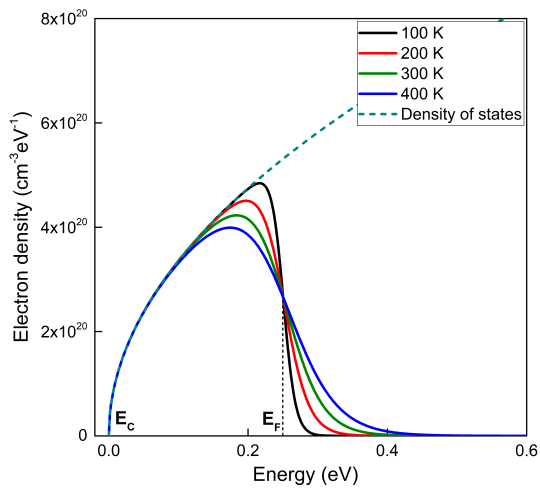


Figure 4.3: Simulation of electron density in the conduction band of a degenerately doped ZnO sample, where the Fermi energy level is found at 0.25 eV above the minimum of the conduction band.

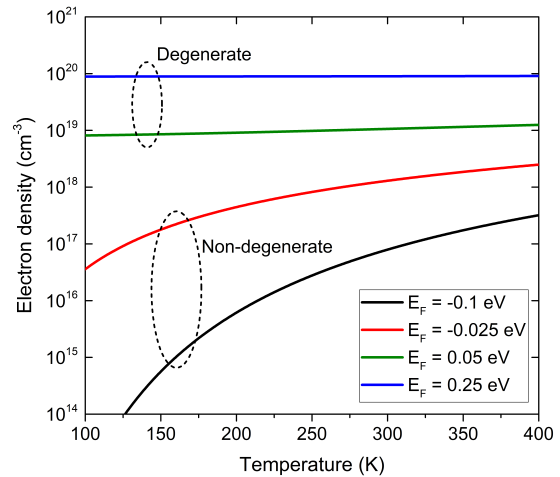


Figure 4.4: Simulation of temperature-dependent electron density of degenerate and non-degenerate ZnO samples. The Fermi energies used in the simulation are measured with respect to the minimum of the conduction band.

To summarize, Figure 4.4 shows the electron density versus temperature for non-degenerate and degenerate semiconductors, in which the Fermi energy level is calculated with respect to the minimum of the conduction band. Accordingly, the non-degenerate cases show a strong increase of electron concentration versus temperature, and this dependence becomes less and less important when the material is degenerately doped. For carrier concentrations of about  $1 \times 10^{20} \text{ cm}^{-3}$  or higher, a constant electron density versus temperature is observed in the conduction band, which can also be considered temperature-independent. Despite this constant electron density, the distribution of electrons in the conduction band remains very useful to understand the electron mobility, since the electron scattering phenomenon also depends on the electron energy distribution.

For highly doped ZnO:Al, the non-parabolic nature of the conduction band should be taken into account. Pisarkiewicz et al. suggested an expression for the effective electron mass as follows:[101]

$$m_n = m_0 \sqrt{1 + 2C \frac{\hbar^2}{m_0} (3\pi^2 n)^{2/3}} \quad (4.5)$$

where  $m_0$ ,  $m_n$  are the effective mass at the bottom of the conduction band and the effective mass at the Fermi level, and C is a constant called nonparabolicity parameter (note that C has the dimension of the inverse of an energy).

## 4.2 Scattering mechanisms in ZnO:Al

In solid-state physics, the carrier mobility in a material characterizes how quickly an carrier can move in the material when applying an electric field. It should be noted that the carriers do not follow a straight path along the electric field direction but they constantly change their direction and velocity due to scattering events. Therefore, the carrier mobility is defined as follows:

$$\mu = \frac{|v_d|}{E} \quad (4.6)$$

where  $|v_d|$  is the average velocity of the carrier, also called drift velocity,  $E$  is the electric field applied. Figure 4.5 shows a scheme of scattering phenomenon of an electron in a n-type material under the effect of an applied electric field. After each scattering event, the electron changes its momentum along a random direction, however, under the effect of electric field, its effective movement after a long enough time follows the opposite direction of the electric field.

In the case of polycrystalline ZnO:Al thin films, the electron mobility is limited by various scattering mechanisms, originated either from the bulk or from grain boundaries. The bulk scattering can be due to electron-phonon interaction, impurities or ingrain crystallographic defects such as dislocations. Back to fundamentals, each scattering mechanism  $i$  generates an average number of scattering events  $n_i^{sc}$  per second, which is inverse of the scattering time  $\bar{\tau}_i$  (average duration between 2 consecutive scattering events, also called relaxation time). By assuming that the scattering mechanisms are independent, the total number of scattering events due to different scattering mechanisms in one second can be summed up, which can also be expressed by using the relaxation time:

$$\frac{1}{\bar{\tau}} = \sum \frac{1}{\bar{\tau}_i} \quad (4.7)$$

Since the drift mobility depends as well on the electron effective mass  $m_n$ , following the equation  $\mu_i = \frac{q}{m_n} \bar{\tau}_i$ , the expression of the total mobility, denoted  $\mu_{total}$ , is expressed:

$$\frac{1}{\mu_{total}} = \sum \frac{1}{\mu_i} \quad (4.8)$$

Eq. 4.8 is known as Matthiessen's rule, and is widely used for studying electron mobility in semiconductors. In single crystalline ZnO where the electron concentration is rather low ( $<1 \times 10^{17} \text{ cm}^{-3}$ ), typical scattering mechanisms are acoustical/optical phonons and piezoelectric mode scatterings. In the case of doped ZnO films with a high electron density up to  $10^{20} \text{ cm}^{-3}$ , the scatterings by impurities and grain boundaries cannot be neglected, usually becoming predominant.

The theoretical description that follows is mainly derived from following documents: "Heavily doped semiconductors" by Victor I. Fistul,[102] "Electronic properties of doped semiconductors" by Shklovskii, B. I. and Efros, A. L.,[103] "Electrical characterization of GaAs materials and devices" by D. C. Look,[104] "Transparent conductive Zinc oxide" by K. Ellmer, A. Klein and B. Rech.[5] Some recent update research articles on the phonon-electron scattering processes applicable for highly doped ZnO cases have also been used.

## 4.2.1 Phonon - electron scatterings

### 4.2.1.1 Optical mode scattering

In a polar semiconductor such as ZnO, the lattice vibrations associated to optical modes (polar-optical phonons) create dipole electric moments which in turn scatters electrons via polar interaction.

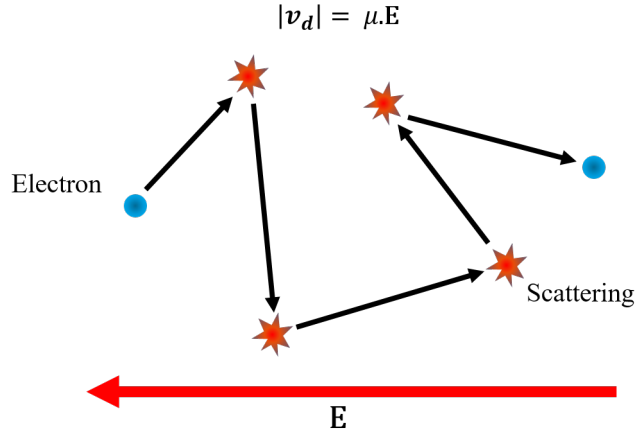


Figure 4.5: Scheme of scattering phenomenon of an electron when an electric field is applied

The optical mode scattering in **non-degenerate** semiconductors has been successfully described by Devlin,[105] through the following expression:

$$\mu_{op} = \frac{q\sqrt{m_e\hbar\omega_0}}{2\left(\frac{1}{\epsilon_\infty} - \frac{1}{\epsilon_s}\right)\omega_0\sqrt{E_H}m_n^{3/2}} \left[ \exp\left(\frac{\hbar\omega_0}{k_B T}\right) - 1 \right] \quad (4.9)$$

where  $E_H$  is the first ionization energy of the hydrogen atom ( $E_H = m_e q^4 / (8\epsilon_0^2 h^2)$ ),  $\epsilon_0$ ,  $\epsilon_\infty$  and  $\epsilon_s$  are the vacuum permittivity, the high frequency and the static dielectric constants (unitless).  $\hbar\omega_0$  is the energy of the longitudinal optical phonon,  $m_e$  and  $m_n$  are the vacuum and effective electron masses.[5]

For **degenerately doped** ZnO:Al, Look and Leedy adapted the Howarth–Sondheimer theory (which is valid for polar semiconductors) to describe the optical mode scattering in their ZnO:Ga films:[50, 106]

$$\mu_{op} = \frac{16\sqrt{2\pi}\epsilon_0\hbar^2\sqrt{k_B T} \left[ \exp\left(\frac{\hbar\omega_0}{k_B T}\right) - 1 \right]}{3q(\hbar\omega_0)m_n^{3/2}(\epsilon_\infty^{-1} - \epsilon_s^{-1})} \cdot F_{ZnO} \cdot \exp\left(\frac{k_B T}{\hbar\omega_0}\right) \quad (4.10)$$

where  $F_{ZnO}$  is an adjustable prefactor depending on the growth condition (see [50, 107]). For non doped ZnO, the longitudinal optical phonon energy is estimated at around 72 meV,[5, 25], while in ZnO:Al, this value was found to vary in the range of [122, 128] meV, according to A. Bikowski and K. Ellmer.[107]

#### 4.2.1.2 Acoustical mode scattering

Under the effect of temperature, the acoustical mode lattice vibrations changes the lattice parameters, which in turn changes locally the bandgap. When electrons move from point to point in the crystal, they are affected by the deformation potential due to the local energetic shift of the band edges. The acoustical mode scattering in non-degenerate semiconductor crystals such as silicon, germanium was successfully described by J. Bardeen and W. Shockley using the deformation potential theory.[5, 108, 109] Accordingly, the acoustical mode mobility is:

$$\mu_{ac} = \frac{2(2\pi)^{\frac{1}{2}} q \hbar^4 c_l}{3E_1^2 (k_B T)^{3/2} m_n^{5/2}} \quad (4.11)$$

where  $E_1$  is the acoustic deformation potential,  $c_l$  the longitudinal elastic constant and  $m_n$  the electron effective mass. This expression is independent of the electron density and only valid within the framework of Boltzmann distribution ( $\exp(E - E_F)/k_B T \gg 1$ , with  $E$  being the electron energy in the conduction band), e.g. the case of non-degenerate semiconductors where the Fermi level is found well below the minimum of the conduction band. In the case of degenerate semiconductors such as highly doped ZnO:Al films, the Fermi-Dirac distribution must be used for calculation. The acoustical mode mobility, which depends on the electron density, is given by:[50, 107, 110]

$$\mu_{ac} = \frac{(\frac{\pi}{3})^{1/3} q \hbar^3 c_l}{E_1^2 n^{1/3} m_n^2 k_B T} \quad (4.12)$$

The longitudinal elastic constant  $c_l$  can be calculated from the elastic constants  $c_{ij}$  ( $c_l = (8c_{11} + 4c_{13} + 3c_{33} + 8c_{44})/15$ ). The deformation potential  $E_1$  is not well known for ZnO, and can be found varying from 1.4 to 31.4 in literature.[5] In this work, we used  $c_l = 140$  GPa,[107] and  $E_1 = 3.8$  eV, as in Look et al.'s work on Ga-doped ZnO.[50] Afterwards, it will be shown that the evaluation of these two parameters is less problematic, since the acoustical mode scattering is less important compared to polar-optical and piezoelectric scatterings.

#### 4.2.1.3 Piezoelectric mode scattering

An acoustic wave propagating in a piezoelectric material such as ZnO is, in general, accompanied by some local electrical disturbances. Piezoelectric scattering was first discussed by Meijer and Polder[111] who described piezoelectric scattering in crystals with zincblende symmetry. 10 years later, Zook developed the model to take account of the anisotropic scattering probability, and the result was applied and valid for CdS.[112] At room temperature

condition, Wagner and Helbig showed that the electron mobility is isotropic in ZnO.[113] For non-degenerate case, the formula for piezoelectric mode scattering is given by:

$$\mu_{pz} = \frac{45\pi (2\pi)^{5/2} \hbar^2 \epsilon_s \epsilon_0}{24 q P_{pz}^2 \sqrt{m_n^3 k_B T}} \quad (4.13)$$

where  $P_{pz}$  is the averaged piezoelectric electro-mechanical coupling coefficient. Recently, Look et al. adapted the previously developed models for the case of degenerately doped ZnO films, the piezoelectric scattering associated mobility being given by:[50]

$$\mu_{pz} = \frac{2 \cdot 3^{1/3} \pi^{2/3} \hbar^3 \epsilon_s \epsilon_0}{P_{pz}^2 q k_B T m_n^2 n^{1/3}} \quad (4.14)$$

where  $P_{pz}$  is the averaged piezoelectric electro-mechanical coupling coefficient. For most semiconductors, this unitless piezoelectric constant is of the order of  $10^{-3}$ , while ZnO exhibits  $P_{pz}$  values of about 0.2 - 0.4. In this work, we have used the value taken from the literature  $P_{pz} = 0.21$ . [110]

#### 4.2.1.4 Comparison of phonon-electron scattering mechanisms

Figure 4.6 and 4.7 illustrate the temperature dependent mobility of ZnO, originating from different phonon-electron scattering mechanisms including acoustical/optical/piezoelectric modes. For this simulation two carrier concentrations were used:  $10^{17} \text{ cm}^{-3}$  to illustrate the non-degenerate case and  $10^{19} \text{ cm}^{-3}$  for the degenerate case. The polar-optical model scattering is observed to become dominant compared to the other modes at temperature as high as 200 K. Conversely, at very low temperature ( $< 100 \text{ K}$ ), the piezoelectric mode scattering is more important. At room temperature (300 K), the non-degenerate and degenerate samples give values of mobility in a similar range, 275 and 320  $\text{cm}^2 \text{V}^{-1} \text{s}^{-1}$ , respectively. These values calculated without taking into account the impurity scattering are comparable to the experimentally value mentioned in the introduction part (200  $\text{cm}^2 \text{V}^{-1} \text{s}^{-1}$ ). It should be noted that the phonon-electron scattering models shown above are valid when assuming that the coefficients  $\hbar\omega_0$ ,  $E_1$ ,  $c_l$  and  $P_{pz}$  are independent of temperature and carrier concentration, which may not be valid for the case of highly doped ZnO. Actually, by adding extrinsic dopants such as  $\text{Al}^{3+}$ , the lattice constants and the electron distributions at the atomic level are modified, therefore, the phonon-electron interactions are not identical as for the case of pure ZnO. In this work, we have assumed that the coefficients used for calculations ( $\hbar\omega_0$ ,  $E_1$ ,  $c_l$  and  $P_{pz}$ ) are approximately similar in ZnO:Al and ZnO.

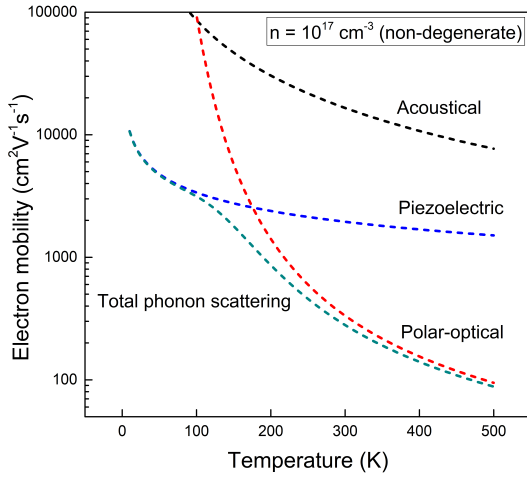


Figure 4.6: Simulated curves of temperature-dependent mobilities induced by acoustical/optical/piezoelectric mode scatterings in non-degenerate ZnO.

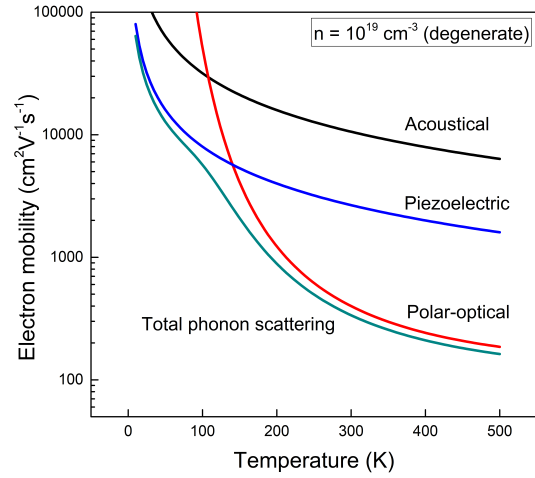


Figure 4.7: Simulated curves of temperature-dependent mobilities induced by acoustical/optical/piezoelectric mode scatterings in degenerate ZnO.

## 4.2.2 Dislocation scattering

In polycrystalline materials, the high concentration of crystallographic defects, especially dislocations, is obviously a factor significantly limiting the electron mobility, and has to be taken into account. We distinguish the dislocation scattering (1D defect), which occurs only inside grains, with the grain boundary scattering, which is actually a 2D-defect scattering. In highly doped ZnO, the dislocations could be more easily formed due to a shift in ionic radius between extrinsic dopant atoms and base lattice atoms. However, this scattering process is rarely used in literature for modeling the electron scattering, possibly due to the lack of data for dislocation densities, which is not at all easy to measure experimentally. Dislocation densities in the order of  $10^{12} \text{ cm}^{-2}$  were reported by L. Sagalowicz et al. when they analyzed their polycrystalline ZnO films deposited by DC magnetron sputtering by using high resolution transmission electron microscopy (HRTEM).[114] Similarly, dislocation densities in the range of  $[1.6 \times 10^{11}; 1.5 \times 10^{12}] \text{ cm}^{-2}$  were estimated for ZnO:Al samples deposited by RF magnetron sputtering.[115] Concerning the modeling of electron mobility limited by dislocation scattering, Look et al. suggested a model applicable to degenerate materials.[116] The model was appropriately applied for the case of lattice-mismatched epitaxy of gallium nitride (GaN) on sapphire substrate ( $\text{Al}_2\text{O}_3$ ). Accordingly, the mobility associated to the dislocation

scattering can be calculated as follows:

$$\mu_{dis} = \frac{4 \cdot 3^{2/3} q c_{dis}^2 n^{2/3}}{\pi^{8/3} \hbar N_{dis}} \left[ 1 + \frac{2 \cdot 3^{1/3} \pi^{8/3} \hbar^2 \epsilon_s n^{1/3}}{q^2 m_n} \right]^{3/2} \quad (4.15)$$

where  $c_{dis}$  is a constant in the order of the lattice parameters, and  $N_{dis}$  denotes the average dislocation density. Equation 4.15 suggests that the dislocation scattering is temperature-independent for degenerate materials such as ZnO:Al films. In this work, the data reported in literature has been used, therefore,  $c_{dis}$  and  $N_{dis}$  were fixed at 0.5 nm and  $10^{12} \text{ cm}^{-2}$ , respectively.[107, 114–116] This assumption is pretty large and needs further work to refine the description of dislocation scattering, since there should be somehow a relationship between the dislocation density and the increase of doping.

### 4.2.3 Ionized impurity scattering

This scattering process describes the interaction of free carriers with the screened Coulomb potential of charged impurities or defects. It was theoretically treated already in 1949 by Conwell and Weisskopf when they studied the temperature-dependent resistivity of germanium semiconductors.[117] The missing part in Conwell and Weisskopf's model was the screening of the Coulomb potential by free charge carriers reducing the Coulomb potential's strength and scattering ability, which was then incorporated into the description of ionized impurity scattering by Brooks and Herring,[118] and by Dingle (1955).[119] Then in 1989, Pisarkiewicz et al. described the ionized impurity scattering in transparent conductive oxide films (for the case of  $\text{SnO}_2$  and  $\text{CdIn}_2\text{O}_4$ ) by taking into account the non-parabolic nature of the conduction band. However, in their expression, they just considered ionized donors, while the compensation effect cannot be neglected in highly doped films such as ZnO:Al. In order to complete the model, Look et al. integrated both the nonparabolicity parameter and the compensation ratio.[50] The carrier mobility associated with ionized impurities can thus be written as follows:

$$\mu_{ii} = \frac{3\epsilon_s^2 h^3}{m_n^2 q^3} \frac{Z_D - K \cdot Z_A}{Z_D^2 + K \cdot Z_A^2} \frac{1}{F_{ii}} \quad (4.16)$$

where  $Z_D$ ,  $Z_A$  refer to the charge of donors and compensating acceptors, respectively. In our case, the main donor is Al, with  $Z_D = 1$ , and the main acceptor is Zn vacancy  $V_{Zn}$  with  $Z_A = 2$ . The compensation ratio K refers to the ratio between the ionized acceptor and donor

concentrations.  $F_{ii}$  denotes the screen function, which depends on the electron density:

$$F_{ii}(\xi_0, \xi_1) = \ln(\xi_0 + 1) \left\{ 1 + \frac{4\xi_1}{\xi_0} \left( 1 - \frac{\xi_1}{8} \right) \right\} - \frac{\xi_0}{\xi_0 + 1} - 2\xi_1 \left( 1 - \frac{5}{16}\xi_1 \right) \quad (4.17)$$

with

$$\xi_0 = (3\pi^2 n)^{1/3} \frac{\epsilon_s \epsilon_0 \hbar^2}{q^2 m_n} \quad (4.18)$$

and

$$\xi_1 = 1 - \frac{m_0}{m_n} \quad (4.19)$$

where  $m_0$ ,  $m_n$  are the effective mass at the bottom of the conduction band and the effective mass at the Fermi level having the formula shown in eq. 4.5.

#### 4.2.4 Grain boundary scattering

While the effect of phonon scattering at grain boundaries on the thermal conductivity of semiconductors has been well discussed,[120] the effect of grain boundaries on the electrical conductivity is still not accurately described for highly doped oxides such as in ZnO:Al. Actually, the charge transport mechanism in the case of non-degenerate semiconductor has been comprehensively described by Seto's model, which is based on thermionic emission,[121] but this model fails to explain the electrical conductivity observed at low temperatures (i.e. below 200 K) for degenerate semiconductors. Indeed, at very low temperatures thermionic emission becomes negligible and thus mobility and conductivity should drop to zero, which is not observed for highly doped semiconductors. In this type of materials, e.g. ZnO:Al, the depletion region at the grain boundaries becomes narrower, while grain boundary potential barrier is often high because of high doping concentration. As a result, field electron emission becomes more favorable compared to thermionic emission. Concerning field electron emission, Stratton (1962) and Simmons (1963) suggested theoretical models for electron tunneling between metal electrodes separated by a thin insulating film.[122, 123] Later on, Seager and Pike (1981) developed a comprehensive model for the tunneling of carriers through grain boundary of degenerately doped GaAs films and showed that thermally assisted tunneling is a dominant carrier transport mechanism.[124] Recently, Sommer et al (2016) adapted the Stratton's model to double Schottky barriers at grain boundaries of ZnO:Al films and also suggested that the field electron emission is the predominant transport process across grain boundaries, as op-

posed to thermionic emission.[125] Due to the impossibility to describe analytically the grain boundary tunneling current with an arbitrary-shaped barrier, the aforementioned models used the Wentzel–Kramers–Brillouin approximation (WKB). But the applicability of this approach to highly doped semiconductor is questionable since the WKB approximation assumes that the potential barrier varies slowly, which is a strong assumption in the case of sharp parabolic potential barrier at the grain boundaries (as detailed in 4.2.4.1). Thus, to date, there is no satisfactory model allowing to describe the contribution of charge tunneling to electron mobility in highly doped semiconductors. In this work, we have fetched inspiration from the approach followed by I.E. Hashem et al. (2013) and K. Mistry et al. (2017) for metal-insulator-metal (MIM) devices to develop a numerical approach by applying the Airy-Function Transfer Matrix Method (AFTMM) to describe more accurately the electron tunneling process through grain boundaries in highly doped semiconductors.[126, 127] Thus, the parabolic potential barrier at the grain boundaries has been modeled by dividing it into several segments, within which the potential is considered as linear. In this way, the wave function in each segment can be computed by using the Airy function.[4] Then, the total tunneling probability from one grain to another has been obtained by multiplying the tunneling probabilities across the different segments. To our knowledge, this is the first time the numerical AFTMM approach is used to calculate the tunneling probability through the grain boundary barriers in semiconductors. In addition, this model can be applied to potential barriers of any shape.

This part will be dedicated to describing in detail our AFTMM model and the analytical model from Seager and Pike, which we have modified in order to extend its applicability to a wider range of doping concentration (hereafter called SPM for Seager-Pike-Modified). We then present the results of applying both models to analyze experimental data measured for ZnO:Al thin films deposited using both physical and chemical techniques, namely, sputtering, ALD and AP-SALD. Finally, in views of the results obtained with our model, we discuss in detail the effect of trap density at the grain boundaries on the electron mobility in ZnO:Al films. This part was lately published in the following paper: V.H. Nguyen et al. *Materials Horizons*, 5 (2018) 715-726.[128]

Figure 4.8 displays the energy band diagram near a grain boundary in the case of highly doped ZnO films. The carriers can cross the grain boundary either by thermionic emission or by tunneling emission. The numbers 1 and 2 refer to two grains separated by a grain boundary;  $E_C$ ,  $E_V$ ,  $E_F$  and  $\Phi_B$  are the bottom of the conduction band (set as reference level), the top of the valence band, the Fermi energy level and the height of the potential barrier, respectively. Note that a downward band bending has been found in some particular cases such as at the surface of undoped single-crystalline  $\text{In}_2\text{O}_3$ ,[43, 129, 130] or at the surface of single-crystalline ZnO treated in hydrogen at 100 K.[131] In our work, we assume that

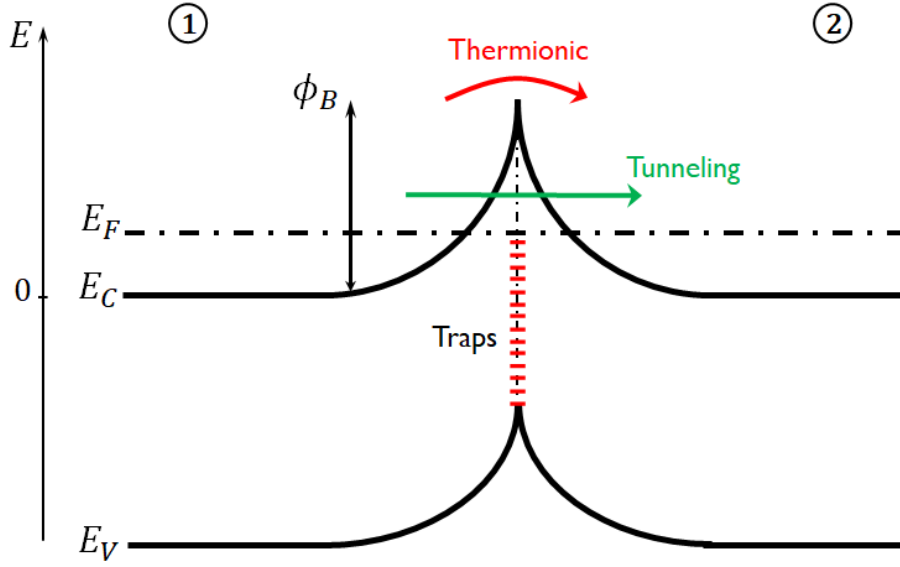


Figure 4.8: Schematic of the band energy at the vicinity of a grain boundary, for the case of n-type degenerate semiconductors such as ZnO:Al films

the upward band bending is generated on both sides of a grain boundary due to the electron trap character of the defects, as widely used when studying n-type polycrystalline TCO films. Since the effective conduction band density of states is in the range of  $10^{18} \text{ cm}^{-3}$ , [5] the doped ZnO films having the carrier concentration higher than  $10^{19} \text{ cm}^{-3}$  should belong to the case of degenerate semiconductors, in which the Fermi level is found in the conduction band. The height of the potential barrier at the grain boundaries  $\Phi_B$  can be calculated by solving Poisson's equation as a first approximation, which leads to two different expressions for  $\Phi_B$ , depending on the trap density in the grain boundaries:

$$\Phi_B = \frac{q^2 N_t^2}{8\epsilon_s \epsilon_0 n}, \quad N_t < nL \quad (4.20)$$

$$\Phi_B = \frac{q^2 L^2 n}{8\epsilon_s \epsilon_0}, \quad N_t > nL \quad (4.21)$$

where  $q$  is the elementary charge,  $\epsilon_0$  and  $\epsilon_s$  are the vacuum permittivity and the static dielectric constant, respectively,  $L$  is the lateral mean grain size,  $n$  is the carrier density in the interior of the grains and  $N_t$  is the trap density at grain boundaries. In the case of a degenerate semiconductor such as ZnO:Al, eq. 4.20 is fulfilled, which means that only part of the grain close to the grain boundary is depleted.

As shown in Figure 4.8, the electrons can pass through the grain boundary either by

thermionic emission or by quantum tunneling phenomenon. It should be mentioned that the pure quantum-tunneling phenomenon refers to the case where the kinetic energy of the incident electron is lower than the height of the potential barrier ( $E < \Phi_B$ ). For the opposite case, where  $E > \Phi_B$ , the phenomenon should be called ‘quantum scattering’. However, in our case, the energies of the incident electrons are distributed over a wide range from the bottom of the conduction band to above of the potential barrier height.[132] For the sake of notation simplicity, in this work we will refer to grain boundary scattering as tunneling emission. The electron mobility due to the tunneling emission contribution,  $\mu_{GB}$ , can be calculated from the tunneling current density as follows:

$$\mu_{GB} = \frac{L}{nq} \left. \frac{dJ}{dV} \right|_{V=0} \quad (4.22)$$

with  $L$  is the average grain size, and  $V$  is the applied voltage on one grain (side 2 in figure 4.8 for example) with respect to the other (side 1). The description of the electron tunneling emission in one-dimensional configuration has been developed by J. G. Simmons[123], C. B. Duke[133] and used by R. Tsu & L. Esaki for their work in resonant tunneling devices.[134] In these works, several assumptions were considered: a) the total energy  $E$  of the tunneling electrons can be written by the sum of the transversal and longitudinal energies  $E_x$  and  $E_{||}$ , respectively, and that these components are independent; b) the tunneling electrons conserve the energy and the transverse component of the momentum (i.e. only transitions in the  $x$ -direction, perpendicular to the grain boundary interface, are considered); c) the parallel wave vector is not altered by the tunneling process. The tunneling current density is thus given as follows:[123, 133, 134]

$$J = \frac{4\pi q m_n}{h^3} \int_0^{\infty} T(E_x) N(E_x) dE_x \quad (4.23)$$

where  $E_x$ ,  $N(E_x)$  and  $T(E_x)$ , respectively, are the component of kinetic energy of an tunneling electron measured perpendicular to the grain boundary plane, the supply function describing the difference in electron distribution at the interface level, and the transmission probability of the tunneling electron. By denoting  $E_{f,i}$  the Fermi level on the  $i$ -side measured relative to the bottom of the conduction band and  $V$  the applied potential on one side with respect to the other, the supply function is given as:

$$N(E_x) = k_B T \cdot \ln \left[ \frac{1 + \exp\left(-\frac{E_x - E_{f,1}}{k_B T}\right)}{1 + \exp\left(-\frac{E_x + qV - E_{f,2}}{k_B T}\right)} \right] \quad (4.24)$$

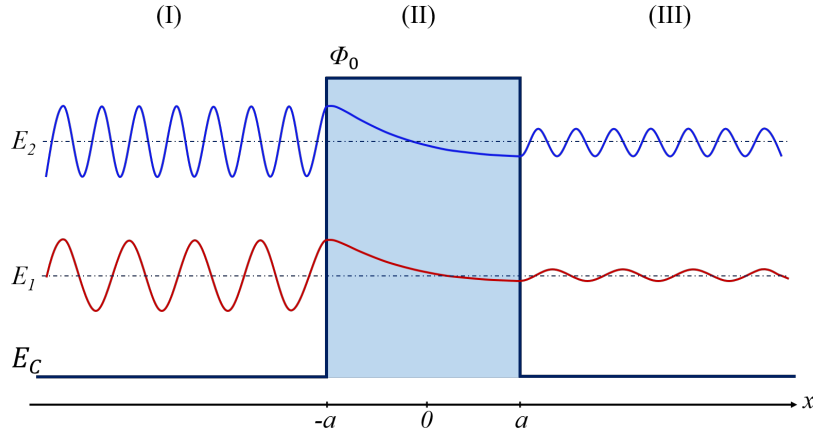


Figure 4.9: Scheme of tunneling through a constant potential barrier, showing a change in wave function of electron before, during and after tunneling through a square potential barrier.  $E_1$ ,  $E_2$  are two electron energy levels in the conduction band ( $E_1 < E_2$ ),  $\phi_0$  represents the potential barrier.

The tunneling transmission probability  $T(E_x)$  is the ratio of the quantum-mechanical current density due to an incident wave in region (1) and a transmitted wave in region (2). With the assumption of plane waves in both regions (1) and (2), the tunneling probability is thus given as:

$$T(E_x) = \left| \frac{\Psi_2(x_2)}{\Psi_1(x_1)} \right|^2 \quad (4.25)$$

with  $\Psi_1(x_1)$  and  $\Psi_2(x_2)$  being, respectively, the wave function on the left side and on the right side, calculated at the turning point  $x_1$  and  $x_2$  (where, the electron kinetic energy  $E$  is equal to the potential energy  $V(x)$ ). Hereafter, two methods to evaluate the tunneling probability of electrons passing through grain boundaries will be described.

#### 4.2.4.1 Analytical approach: SPM model

##### Square barrier shape

Figure 4.9 shows a schematic view of a tunneling process through the simplest potential barrier at grain boundary: square shape. Let us consider the bottom of the conduction band  $E_C$  the reference of electron energy and potential. The potential is described by the following functions:

$$V(x) = 0, \quad \text{when } x < -a \quad (4.26)$$

$$V(x) = \phi_0, \quad \text{when } -a \leq x \leq a \quad (4.27)$$

$$V(x) = 0, \quad \text{when } x > a \quad (4.28)$$

The electron wave functions in these 3 regions can be solved by using the 1D time-independent Schrodinger equation:

$$-\frac{\hbar^2}{2m_n} \frac{\partial^2}{\partial x^2} \Psi(x) + V(x) \Psi(x) = E_x \Psi(x) \quad (4.29)$$

where  $\hbar$  is the reduced Plank constant,  $\Psi(x)$  is the electron wave-function and  $V(x)$  is the potential energy at the grain boundary. Eq. 4.29 has following solutions:

$$\Psi_I(x) = A \exp(ikx) + B \exp(-ikx), \quad \text{when } x < -a \quad (4.30)$$

$$\Psi_{II}(x) = C \exp(-\beta x) + D \exp(\beta x), \quad \text{when } -a \leq x \leq a \quad (4.31)$$

$$\Psi_{III}(x) = F \exp(ikx) + G \exp(-ikx), \quad \text{when } x > a \quad (4.32)$$

where  $k = \sqrt{2m_n E_x} / \hbar$ , and  $\beta = \sqrt{2m_n (\Phi_0 - E_x)} / \hbar$  are wave numbers, A, B, C, D, F and G are constants related to the probability for an electron to be present in the corresponding region. As can be remarked, the solutions in the region (I) and (III) has the plane wave forms, while the wave function in the region (II) is not oscillatory and is in the form of a gradual attenuation. If we consider that only the transmitted wave function exists in the region (III), the tunneling transmission probability can be expressed as follows:

$$T(E_x) = \left| \frac{\Psi_{III}(a)}{\Psi_I(-a)} \right|^2 = \left| \frac{F}{A} \right|^2 \quad (4.33)$$

By using the continuity conditions of wave functions and of their derivatives at the boundaries ( $x = -a$ ,  $x = a$ ), the tunneling probability can be easily solved, and has the following form:

$$T(E_x) = \frac{1}{\cosh^2(2a\beta) + (\gamma/2)^2 \sinh^2(2a\beta)}, \quad \text{with } \gamma = \beta/k - k/\beta \quad (4.34)$$

As can be seen in Figure 4.9, after tunneling, electrons conserve their energy and momentum, but not their wave function module, which is related to the probability of presence. For electrons having energy higher than the barrier,  $\beta$  becomes a complex number and we should

not observe any attenuation of the incident wave, which means that the tunneling probability is equal to 1.

### Arbitrary barrier shape

In general, it is not possible to calculate analytically the tunneling probability if the potential barrier has an arbitrary shape. The most frequently used approximation is the Wentzel–Kramers–Brillouin (WKB) approximation. In the case of constant potential, the solution of the Schrodinger equation can take the form of a simple plane wave:  $\Psi(x) = Ae^{ik(x)}$ , where  $k(x) = \sqrt{2m_n(E_x - V(x))}/\hbar$  is a constant. The WKB approximation assumes that if the potential  $V(x)$  changes slowly with  $x$ , therefore, the wave function solution of the Schrodinger equation can also take the form of simple plane wave:  $\Psi(x) = Ae^{iS(x)}$ , with  $S(x) = \int k(x) dx$ . Replacing this expression in eq. 4.29, we obtain:

$$i\frac{\partial^2}{\partial x^2}S(x) - \left(\frac{\partial S(x)}{\partial x}\right)^2 + (k(x))^2 = 0 \quad (4.35)$$

The wave vector  $k(x)$  is proportional to the square root of the potential  $V(x)$ , which is assumed to be slowly varying. This means that the second derivative of  $S(x)$  is negligible compared to  $(k(x))^2$ , thus we can write:

$$\frac{\partial S(x)}{\partial x} = k(x) \Rightarrow S(x) = \int k(x) dx + Cte \quad (4.36)$$

In the case of tunneling through a grain boundary barrier  $V(x) > E_x$ , the wave function can be expressed as:

$$\Psi(x) = Kexp\left(-\int \sqrt{\frac{2m_n(V(x) - E_x)}{\hbar^2}} dx\right) \quad (4.37)$$

Now, we consider an incoming wave  $\Psi_1$  to the grain boundary barrier  $V(x)$  and a transmitted wave  $\Psi_2$  after passing through the barrier, with two turning points  $x_1$  and  $x_2$  corresponding to the positions where the electron kinetics energy  $E_x$  equal to the potential  $V(x)$ , the tunneling probability is thus given by:

$$T(E_x) = \left|\frac{\Psi_2(x_2)}{\Psi_1(x_1)}\right|^2 = exp\left(-\frac{2}{\hbar} \int_{x_1}^{x_2} \sqrt{2m_n(V(x) - E_x)} dx\right), \quad E < V(x) \quad (4.38)$$

If we approximate the grain boundary barrier as a parabolic solution of Poisson's equation,

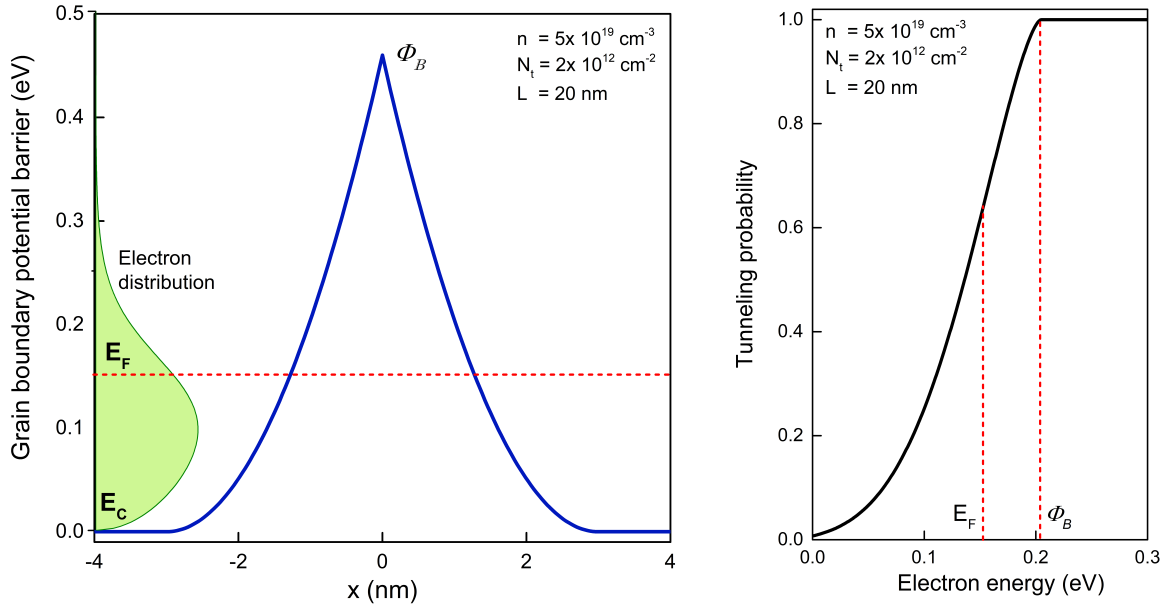


Figure 4.10: Simulation of a grain boundary potential barrier in the case of ZnO:Al along with the electron distribution in the conduction band. Figure 4.11: Simulation of tunneling probability versus electron energy using Seager and Pike's model.

the tunneling probability can be expressed as follows (by using Maple software):

$$T(E_x) = \exp\left(-\frac{2}{\hbar} \sqrt{\frac{\epsilon_0 \epsilon_s}{q^2 n}} \left( \sqrt{\Phi_B} \sqrt{\Phi_B - E_x} - E_x \ln\left(\frac{\sqrt{\Phi_B} + \sqrt{\Phi_B - E_x}}{\sqrt{E_x}}\right) \right)\right), E_x < V(x) \quad (4.39)$$

Figure 4.10 and Figure 4.11 illustrate the simulated curves of grain boundary potential barrier along with the electron distribution in the conduction band and the tunneling probability versus electron energy, respectively. For both figures, the following parameters were used:  $n = 5 \times 10^{19} \text{ cm}^{-3}$ ,  $N_t = 2 \times 10^{12} \text{ cm}^{-2}$ ,  $L = 20 \text{ nm}$ . It can be observed that most of electrons have lower energy than the height of grain boundary potential barrier, leading to an unfavorable thermionic emission. The tunneling probability calculated by using Seager and Pike's model has an abrupt change when the electron energy is equal to the barrier height.

By combining equations 4.22, 4.23, 4.24 and 4.39, we obtain the following equation, which describes the contribution of the grain boundary limiting mobility:

$$\mu_{GB}^{SPM} = \frac{4\pi q m_n L}{h^3 n} \left( \int_0^{\Phi_B} \frac{\exp \left[ -\frac{2}{\hbar} \sqrt{\frac{\epsilon_0 \epsilon_x}{q^2 n}} \left( \sqrt{\Phi_B} \sqrt{\Phi_B - E_x} - E_x \ln \left( \frac{\sqrt{\Phi_B} + \sqrt{\Phi_B - E_x}}{\sqrt{E_x}} \right) \right) \right]}{1 + \exp \left( \frac{E_x - E_f}{k_B T} \right)} dE_x + \int_{\Phi_B}^{\infty} \frac{1}{1 + \exp \left( \frac{E_x - E_f}{k_B T} \right)} dE_x \right) \quad (4.40)$$

The first term in eq. 4.40 refers to the contribution from tunneling emission while the second term is related to the contribution from thermionic emission. This expression was for the first time developed by Seager and Pike.[124] Some minor typos in the equations reported in Seager and Pike's article have been spotted (in their equation (9), the expression of  $E_0$  should have the square root and in their equation (11), there should be a minus sign in the exponent). To simplify, these authors made an approximation considering that  $(\Phi_B - E_F \gg k_B T)$  (i.e. the top of the grain boundary barrier is much above the Fermi energy level) in order to simplify the second integral. While this assumption holds for the case of the low doping level and high trap density at the grain boundary, it prevents the model from being valid in the case where the Fermi level approaches, or is higher than, the top of the grain boundary barrier. In this work, we have used the analytical integral form for the contribution from thermionic emission and have added a numerical evaluation in order to extend the applicability of the model. The modified model is called SPM for Seager–Pike-modified. While the SPM approach is adequate to fit experimental data in the case of GaAs thin films doped with Tellurium in the range  $4 \times 10^{17} - 2 \times 10^{18} \text{ cm}^{-3}$ , [124] the application of the WKB approximation used in this approach is questionable in the case of polycrystalline, highly doped semiconductor thin films. Indeed, to obtain the expression 4.39, we have assumed that the potential varies slowly with  $x$ , which is a strong assumption in the case of sharp parabolic potential barrier, as shown in Figure 4.10. In addition, the WKB approximation does not take into account the reflection at the grain boundary barrier, thus yielding an overestimation of the tunneling probability for the electrons having energy higher than the barrier. Taking into account the aforementioned, we can deduce that the models reported to date are not fully appropriate to describe accurately the grain boundary scattering in the case of polycrystalline degenerate semiconductor films.

#### 4.2.4.2 Airy Function Transfer Matrix Method: a new approach

In order to be able to accurately describe the charge mobility in TCOs and other highly doped systems, new improved models are required. In this part, we describe in detail a new model, based on the application of the numerical Airy-Function Transfer Matrix Method (AFTMM)

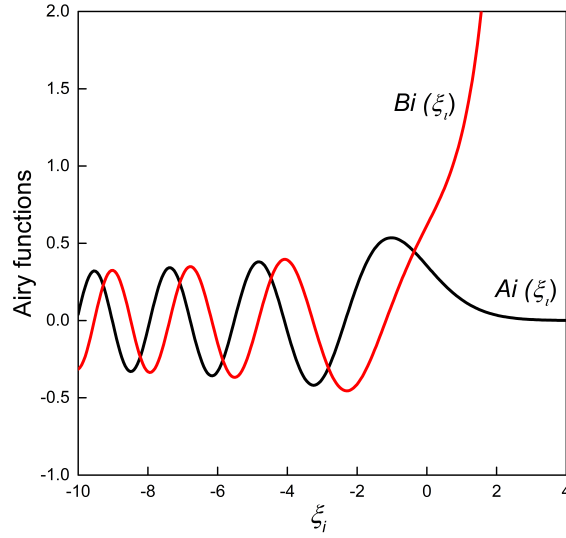


Figure 4.12: Illustration of Airy functions  $Ai$  and  $Bi$  used for calculation of the electron tunneling probability through an arbitrary potential barrier.[4]

approach to calculate the electron tunneling probability passing through a parabolic potential barrier. As mentioned in the previous part, solving analytically the Schrodinger's equation with an arbitrary-shaped barrier is almost impossible. However, the tunneling probability through any potential barrier can be solved if the potential barrier is segmented into several small regions within which the potential is considered constant or linear in each segment (Figure 4.13).[134, 135] The tunneling probability in each segment is then computed and used to get the total transmission probability. In the case of constant potential segments, the accuracy of the resulting tunneling probability strongly depends on the discretization resolution, especially in the case of highly doped polycrystalline semiconductor films with a sharp potential variation at the grain boundaries. Therefore, we have approximated the grain boundary potential having a linear dependency within each segment and then solved the Schrodinger's equation in each segment. The solution can be expressed as a linear combination of Airy functions. The illustration of Airy functions is shown in Figure 4.12.

As shown in figure 4.13, we discretized the grain boundary potential barrier into  $N$  segments with  $N + 1$  equidistant points  $(x_1, x_2 \dots x_i, x_{i+1} \dots x_{N+1})$ , where  $x_1$  and  $x_{N+1}$  correspond to the bottom of the conduction band on each side. The potential  $V(x_1)$  corresponding to each point  $x_i$  follows the parabolic solution of the Poisson's equations. Now, if we consider a polycrystalline highly doped ZnO sample with average grain size of 20 nm, a measurement voltage of 1 V applied over a distance of 1 cm leads to a potential drop of 2  $\mu$ V from one grain to another. Therefore, we assume that the applied polarization does not have any effect on the tunneling probability, as confirmed in the next part.

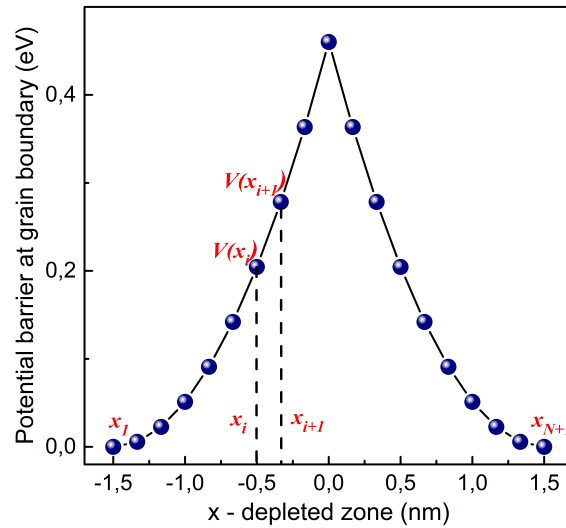


Figure 4.13: A parabolic potential barrier is segmented into  $N$  linear potentials. For this illustration, we used  $n = 2 \times 10^{20} \text{ cm}^{-3}$ ,  $N_t = 6 \times 10^{13} \text{ cm}^{-2}$ ,  $L = 20 \text{ nm}$ .



Figure 4.14: Schematic of the incident, reflected and transmitted electron waves in the conduction band at the  $j^{\text{th}}$  grain boundary.

As shown in 4.2.4.1, the solutions of the 1D time-independent Schrodinger's equation in the interior of the grains, where the potential is zero, have the plane wave forms:

$$\Psi_L(x) = a_L \exp(ik_L x) + b_L \exp(-ik_L x), \quad \text{when } x < x_1 \quad (4.41)$$

$$\Psi_R(x) = a_R \exp(ik_R x) + b_R \exp(-ik_R x), \quad \text{when } x > x_{N+1} \quad (4.42)$$

where  $(\Psi_L, k_L)$  and  $(\Psi_R, k_R)$  are the wave functions and the wave vectors attributed to the left (noted  $L$ ) and right grains (noted  $R$ );  $a_R, b_R, a_L$  and  $b_L$  are constant. We have neglected the applied bias on one side so that we can write the wave vectors as follows:  $k_L = k_R = \sqrt{2m_n E} / \hbar$ . It should be noted that the reflected wave in the right region of the  $j^{\text{th}}$  grain boundary (see Figure 4.14) can be neglected in this calculation because the ratio between the mean grain size and the depletion layer is usually important (20-50 times) in the case of a highly doped semiconductor, which means that the reflected wave due to the  $(j+1)^{\text{th}}$  grain boundary will be scattered by ionized impurities or by the other processes in the grain before reaching and affecting the tunneling phenomenon in the  $j^{\text{th}}$  grain boundary. Therefore, we can suppose that  $b_R = 0$ . Therefore, the objective is to calculate the total tunneling probability, which can be written as follows:  $T = |a_R/a_L|^2$ .

The linear function  $U_i$  of potential in the segment  $(x_i, x_{i+1})$ ,  $2 \leq i \leq N$ , is expressed as:

$$U_i(x) = K_i \cdot (x - x_i), \quad \text{with } K_i = \frac{V(x_{i+1}) - V(x_i)}{x_{i+1} - x_i} \quad (4.43)$$

In order to use the Airy function solution, we need to adjust the 1D time-independent Schrodinger's equation by changing the variable from  $x$  to  $\xi_i$  as follows:[126]

$$\xi_i = \left( \frac{2m_i}{\hbar^2} K_i \right)^{\frac{1}{3}} \left( \frac{V(x_i) - E_x}{K_i} + (x - x_i) \right) \quad (4.44)$$

and the  $x$ -independent derivative:  $\xi'_i = \left( \frac{2m_i}{\hbar^2} K_i \right)^{\frac{1}{3}}$ , where  $m_i$  denotes the electron effective mass in the considered region. In a first approximation, we assume that  $m_i$  is constant when tunneling through the grain boundary barrier and takes the value of the ingrain effective mass  $m_n$ . The 1D time-independent Schrodinger's equation 4.29 in the segment  $(x_i, x_{i+1})$  can thus be written as:

$$\frac{\partial \Psi_i^2}{\partial \xi_i^2} - \xi_i \Psi_i = 0 \quad (4.45)$$

The solution for this type of equation can be expressed as a linear combination of Airy

functions,  $A_i$  and  $B_i$ , which is presented in Figure 4.12:

$$\Psi_i = a_i A_i(\xi_i) + b_i B_i(\xi_i), \quad x_i < x < x_{i+1} \quad (4.46)$$

The similar solution for the wave function in the neighbor segment  $(x_{i-1}, x_i)$  should take the same form, as follows:

$$\Psi_{i-1} = a_{i-1} A_i(\xi_{i-1}) + b_{i-1} B_i(\xi_{i-1}), \quad x_{i-1} < x < x_i \quad (4.47)$$

Now the boundary conditions at the interface between two adjacent segments  $(x_{i-1}, x_i)$  and  $(x_i, x_{i+1})$  require the continuity of the wave functions, as well as its derivative in the position  $x_i$ :

$$a_i A_i(\xi_i) + b_i B_i(\xi_i) = a_{i-1} A_i(\xi_{i-1}) + b_{i-1} B_i(\xi_{i-1}) \quad (4.48)$$

$$a_i A_i'(\xi_i) \xi_i' + b_i B_i'(\xi_i) \xi_i' = a_{i-1} A_i'(\xi_{i-1}) \xi_{i-1}' + b_{i-1} B_i'(\xi_{i-1}) \xi_{i-1}' \quad (4.49)$$

By using the property of the Airy functions:  $A_i(z) B_i'(z) - A_i'(z) B_i(z) = \pi^{-1}$  and then combining the equations 4.48 and 4.49 under the matrix form, we obtain:

$$\begin{bmatrix} a_{i-1} \\ b_{i-1} \end{bmatrix} = T_i \begin{bmatrix} a_i \\ b_i \end{bmatrix} \quad (4.50)$$

Where  $T_i$  is transfer matrix related to the electron tunneling process through the segment  $(x_i, x_{i+1})$  and calculated as follows:

$$T_i = \pi \begin{bmatrix} A_i(\xi_i) B_i'(\xi_{i-1}) - A_i'(\xi_i) B_i(\xi_{i-1}) \frac{\xi_i'}{\xi_{i-1}'} & B_i(\xi_i) B_i'(\xi_{i-1}) - B_i'(\xi_i) B_i(\xi_{i-1}) \frac{\xi_i'}{\xi_{i-1}'} \\ -A_i(\xi_i) A_i'(\xi_{i-1}) + A_i'(\xi_i) A_i(\xi_{i-1}) \frac{\xi_i'}{\xi_{i-1}'} & -B_i(\xi_i) A_i'(\xi_{i-1}) + B_i'(\xi_i) A_i(\xi_{i-1}) \frac{\xi_i'}{\xi_{i-1}'} \end{bmatrix} \quad (4.51)$$

Equation 4.50 is valid only for  $i = [2, \dots, N-1]$ , similarly, the transfer matrices in the segment  $(x_1, x_2)$  and  $(x_N, x_{N+1})$  can be expressed as follows:

$$T_1 = \frac{1}{2} \begin{bmatrix} A_i(\xi_1) + \frac{\xi_1'}{ik_L} A_i'(\xi_1) & B_i(\xi_1) + \frac{\xi_1'}{ik_L} B_i(\xi_1) \\ A_i(\xi_1) - \frac{\xi_1'}{ik_L} A_i'(\xi_1) & B_i(\xi_1) - \frac{\xi_1'}{ik_L} B_i(\xi_1) \end{bmatrix} \quad (4.52)$$

$$T_N = \pi \begin{bmatrix} B_i'(\xi_{N-1}) - \frac{ik_R}{\xi_{N-1}'} B_i(\xi_{N-1}) & B_i'(\xi_{N-1}) + \frac{ik_R}{\xi_{N-1}'} B_i(\xi_{N-1}) \\ -A_i'(\xi_{N-1}) + ik_R A_i(\xi_{N-1}) & -A_i'(\xi_{N-1}) - ik_R A_i(\xi_{N-1}) \end{bmatrix} \quad (4.53)$$

The total tunneling transfer matrix (called  $T_{total}$ ) is calculated by multiplying the transfer matrices in each layer  $(x_i, x_{i+1})$ ,  $1 \leq i \leq N$ , which are already calculated and shown in the equations 4.51, 4.52 and 4.53:

$$T_{total} = \frac{\pi^N}{2} \prod_{i=1}^N T_i = \begin{bmatrix} T_{11} & T_{12} \\ T_{21} & T_{22} \end{bmatrix} \quad (4.54)$$

Finally, with the assumption that no reflection wave exists on the right side (see Figure 4.14), i.e.  $b_R = 0$ , we obtain the total tunneling probability as follows:

$$T_{total} = \left| \frac{a_R}{a_L} \right|^2 = \frac{1}{|T_{11}|^2} \quad (4.55)$$

Concerning the discretization used for the grain boundary barrier, the larger the number of segments the more accurate the calculated result. However, the calculation time will be also longer. Therefore, we fixed a critical value for the number of segments  $S_c$  as follows:

$$\frac{|T_{S_c+1} - T_{S_c}|}{T_{S_c}} \leq 0.0001 \quad (4.56)$$

where  $T_{S_c}$  and  $T_{S_c+1}$  are the tunneling transmission probability of electrons at the Fermi level, calculated with the AFTMM model by using respectively two numbers of segments:  $S_c$  and  $S_c + 1$ . Figure 4.15 shows the tunneling transmission probability and the calculation time as function of the number of segments. When the number of segments varies from 2 to 80, the running time of the model AFTMM to get the value of mobility goes from 0.2 s to 4.5 s. By applying the criteria defined above, the critical value  $S_c$  is determined to be 30, which corresponds to a calculation time of 1.8 s per value. This means that to study the effect of one parameter (temperature, grain size. . .) on the charge transport through grain boundary, it will only take a few minutes. For the remaining of this work, we have fixed the number of segments at this value.

### 4.3 Application of AFTMM model

In this part, we firstly illustrate the main difference between the SPM model and our new AFTMM model, based on the tunneling emission process at grain boundaries. We then apply the AFTMM model to our own experimental data on ZnO:Al thin films prepared by AP-SALD, ALD and DC sputtering, as well as some RF sputtering data extracted from the literature. The parameters used to model the different ZnO:Al samples are shown in Table 4.1:

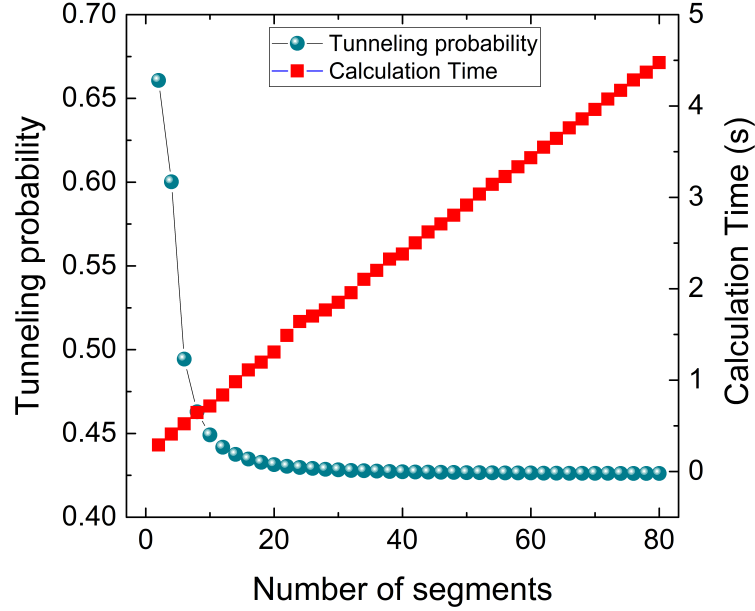


Figure 4.15: Tunneling probability, and associated Matlab running time calculated for electrons at the Fermi level as function of the number of segments used for the discretization of the grain boundary potential barrier. For this evaluation, we used  $n = 2 \times 10^{20} \text{ cm}^{-3}$ ,  $N_t = 6 \times 10^{13} \text{ cm}^{-2}$ ,  $L = 20 \text{ nm}$ .

Parameter [unit]	Values	References
Effective mass $m_0$ [ $kg$ ]	$0.29m_e$	[5]
Nonparabolicity parameter $C$ [ $eV^{-1}$ ]	0.35 – 0.65	[136–138]
Static dielectric constant $\epsilon_s$	8.85	[138]
High-frequency dielectric constant $\epsilon_\infty$	3.66	[138]
Piezoelectric constant $P_\perp$	0.21	[139]
Energy of the longitudinal optical phonon [ $meV$ ]	72.1	[138]
Average longitudinal elastic constant [ $GPa$ ]	200	[5]
Deformation potential $E_{ac}$ [ $eV$ ]	3.8	[5]
Dislocation density $N_{dis}$ [ $cm^{-2}$ ]	$1 \times 10^{12}$	[107, 114, 116]
Compensation ratio $K$	0.1 – 0.15	[50]

Table 4.1: Material parameters of ZnO:Al used for the simulation.

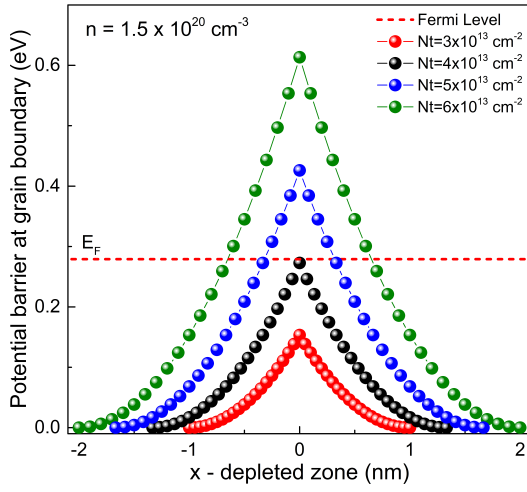


Figure 4.16: Spatial variation of potential barrier plotted for different trap densities in the vicinity of the grain boundary.

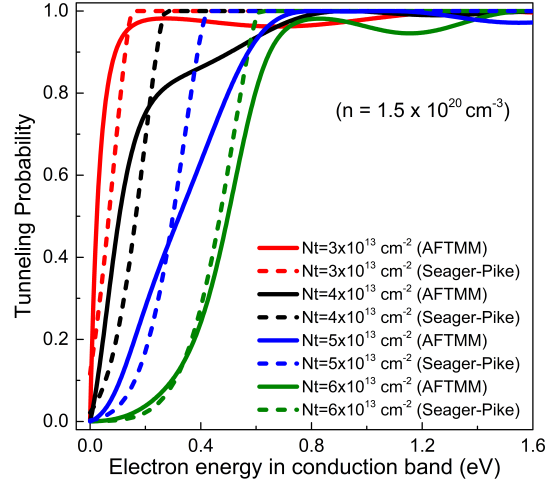


Figure 4.17: The tunneling probability calculated from the Seager Pike modified (SPM) and the AFTMM models.

### 4.3.1 Illustration of the AFTMM model in comparison with the analytical model

As already stated, the carrier transport in polycrystalline materials strongly depends on the trap density at the grain boundaries. Fig. 4.16 and 4.17 illustrate, respectively, the calculated spatial variation of the grain boundary potential barrier for different values of the grain boundary trap density and the resulting tunneling probabilities (calculated by using the AFTMM and the SPM models). Fig. 4.16 shows an important dependence of the relative position between the Fermi level and the barrier height when the trap density at the grain boundary increases from  $3 \times 10^{13}$  to  $6 \times 10^{13} \text{ cm}^{-2}$ . Fig. 4.17 shows an important difference between the tunneling probability calculated with the SPM model using the WKB approach and the one computed with the AFTMM model. Firstly, while the analytical model shows an ideal tunneling probability (i.e. 1) if the electron energy is higher than the potential barrier, the AFTMM model yields a transmission probability lower than 1 for the same energy level. This can be explained by the fact that the WKB approach used for the analytical model neglects the reflection of the incident wave at each interface. The interference between the reflected and the incident waves creates an oscillating behavior of the tunneling probability versus the electron energy, as clearly shown in Fig. 4.17. The difference between the two models becomes more important when the height of the grain boundary barrier is closer to the Fermi level. However, in the situation of a very high potential barrier ( $> 6 \times 10^{13} \text{ cm}^{-2}$  in this case), the difference between the two models is not significant, especially for the low electron energies. The conductivity contribution from the tunneling emission through grain boundaries is evaluated by

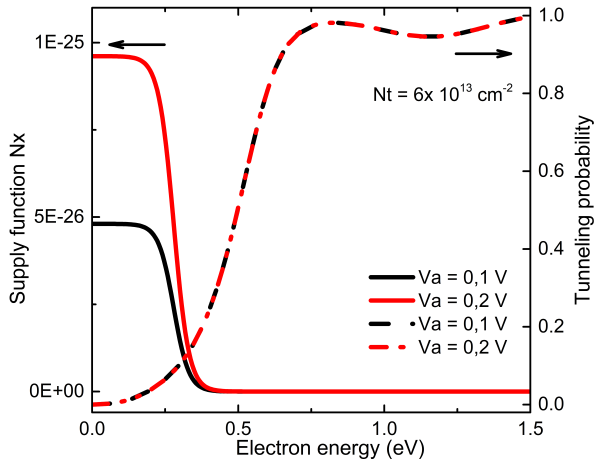


Figure 4.18: Supply function and tunneling probability from the AFTMM model versus electron energy for different applied voltage ( $V_a = 0.1$  V,  $0.2$  V).

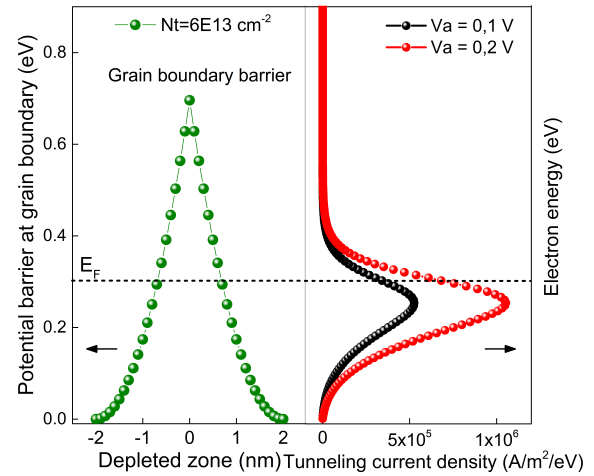


Figure 4.19: Potential barrier at grain boundary (on left) and the associated tunneling current through the barrier as function of electron energy in the conduction band.

computing the derivative of the tunneling current density versus applied voltage  $V_a$ .

Fig. 4.18 shows the supply function (i.e. the difference in electron distribution from one grain to another) and tunneling probability versus the electron energy for two different applied voltages ( $V_a = 0.1$  V and  $0.2$  V over a distance of 1 cm). In the previous part, we have shown that these  $V_a$  values create a voltage drop only on the order of  $\mu\text{V}$  from one grain to another, which is too small to affect the shape of the potential barrier. As can be expected, we observe that the transmission probability remains unchanged, whereas the supply function  $N_x(E_x)$  shows an important variation with  $V_a$ . Also, we note that the population of electrons with energy higher than  $0.45$  eV is negligible, whereas the barrier height is about  $0.6$  eV, therefore making the thermionic emission current very small compared to the tunneling current. The tunneling current density is evaluated by multiplying the supply function and the tunneling probability, as shown in Fig. 4.19. We observe that electrons from a wide energy range, from the minimum of the conduction band up to  $0.15$  eV above the Fermi level, do contribute to the tunneling current, and not only the electrons close to the Fermi level, as often assumed in the literature.[125] Turning to the temperature dependence of the carrier transport, the temperature mainly affects the electron distribution in the conduction band, e.g. the supply function, but not the tunneling probability. Thus, increasing the temperature will widen the electron distribution to a higher energy range, where electrons find a smaller barrier to tunnel through. As a result, the mobility of electrons tunneling through the grain boundary should increase as temperature increases. Thanks to this temperature dependence, this pro-

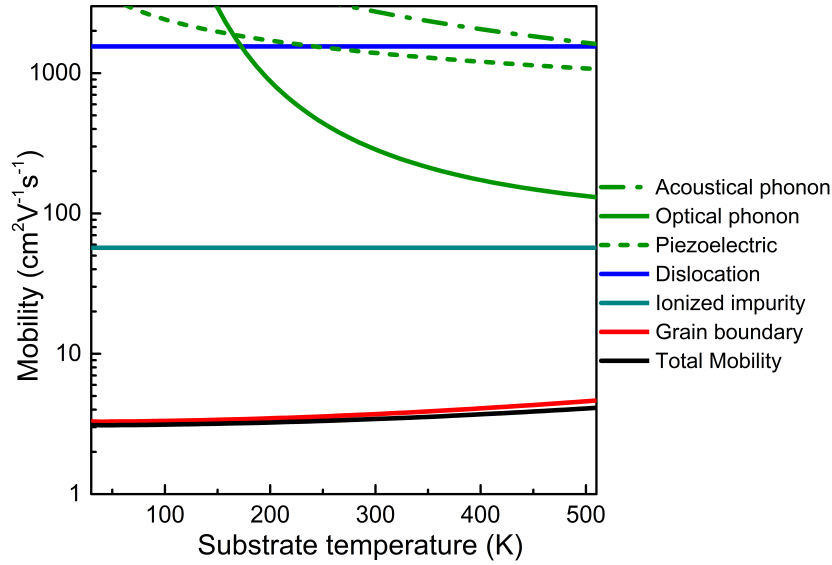


Figure 4.20: Contribution of different scattering mechanisms to the electron mobility, the contribution from grain boundary scattering has been calculated with the AFTMM model. For this illustration, we used  $L = 20 \text{ nm}$ ,  $C = 0.5$ ,  $K = 0.12$ ,  $N_t = 6 \times 10^{13} \text{ cm}^{-2}$ ,  $n = 1.5 \times 10^{20} \text{ cm}^{-3}$ .

cess is often described as thermally assisted tunneling emission. In order to have a complete conductivity model, the other scattering mechanisms (including phonon–electron, dislocation and impurity scatterings) need also to be taken into account. Fig. 4.20 shows an example for a semiconductor with a trap density of  $N_t = 6 \times 10^{13} \text{ cm}^{-2}$  and a carrier concentration of  $n = 1.5 \times 10^{20} \text{ cm}^{-3}$ . When increasing the substrate temperature, the phonon–electron interaction decreases the electron mobility, whereas the scattering by grain boundaries becomes less important. As a result, if an increase of the electron mobility versus temperature is observed, the predominant scattering mechanism is therefore due to grain boundaries.

Fig. 4.21 shows the comparison between the temperature-dependent mobility calculated with the classical Seager–Pike model, the SPM model, and our new AFTMM model. When comparing the two former (analytical) models, we observe that the Seager–Pike model is not applicable for the case of low trap density ( $N_t = 3 \times 10^{13} \text{ cm}^{-2}$ ), where the Fermi level is above the top of the grain boundary barrier. Actually, the thermionic term in their equation was overestimated. By using the analytical expression of the thermionic term as shown in eq. 4.40, the SPM model shows a better approach of temperature-dependent mobility. For higher trap densities ( $N_t > 4 \times 10^{13} \text{ cm}^{-2}$  in this case), the top of the potential barrier becomes higher than the Fermi level, and thus the thermionic term is negligible compared to the tunneling term.

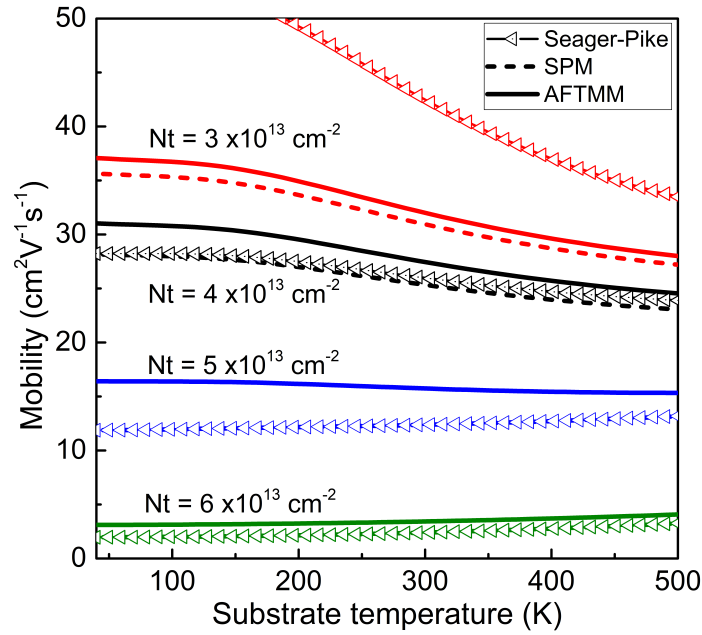


Figure 4.21: Total electron mobility as function of substrate temperature, calculated using three different models: Seager-Pike, SPM and AFTMM with different grain boundary trap densities from  $N_t = 3 \times 10^{13} \text{ cm}^{-2}$  to  $6 \times 10^{13} \text{ cm}^{-2}$ , and the other parameters used for this simulation:  $L = 20 \text{ nm}$ ,  $C = 0.5$ ,  $K = 0.12$ ,  $n = 1.5 \times 10^{20} \text{ cm}^{-3}$ .

As a result, the two models based on the WKB approximation are identical. When comparing the SPM and AFTMM models, we observed that the mobility given by our numerical AFTMM model is higher than that of the analytical model SPM for the same grain boundary trap density  $N_t$ . Indeed, the closer the potential barrier is to the Fermi level, the larger the difference between these two models. Actually, these differences arise from the different assumptions made in these two tunneling transmission models, as discussed above.

Turning to the dependence of mobility with temperature, for low trap densities ( $N_t < 4 \times 10^{13} \text{ cm}^{-2}$ ), the mobility decreases importantly with temperature. This means that the charge transport is mainly dominated by the ionized impurity scattering and by phonon–electron scattering, particularly at higher temperature. However, the trend is still observed for higher trap density ( $N_t = 5 \times 10^{13} \text{ cm}^{-2}$ ), but with a smaller slope. This suggests that the contribution of the grain boundaries starts being competitive with phonon scattering. For higher trap densities ( $N_t \geq 6 \times 10^{13} \text{ cm}^{-2}$ ), the grain boundary scattering becomes the dominating factor in the carrier transport.

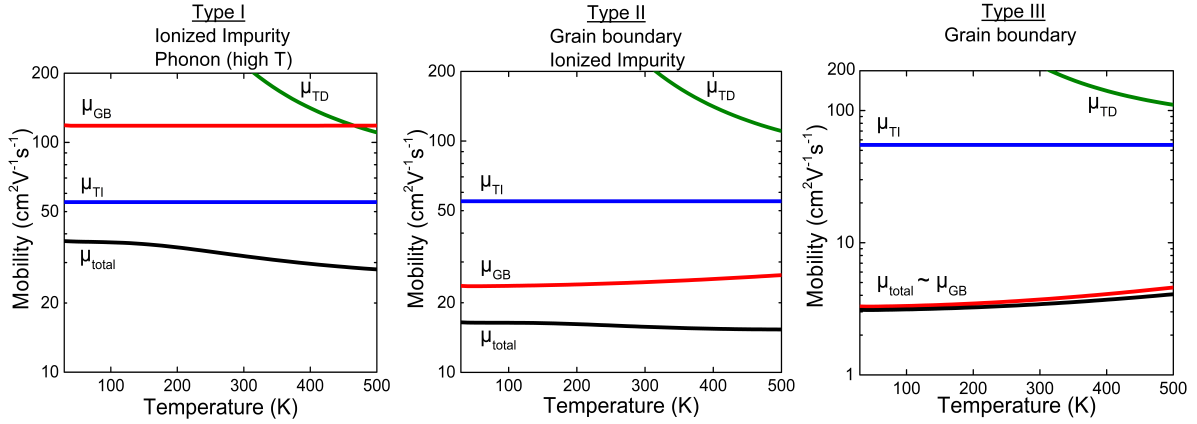


Figure 4.22: Three types of temperature-dependent mobility with corresponding dominant scattering mechanisms in the case of highly doped ZnO.  $\mu_{Ti}$ : temperature independent contributions (ionized impurity and dislocation scattering);  $\mu_{TD}$ : temperature-dependent contributions (acoustical and optical phonons scattering);  $\mu_{GB}$ : grain boundary scattering contribution.

### 4.3.2 Model application to experimental data

Fig. 4.22 shows three different scenarios (type I, II and III) that one may find for the temperature-dependent mobility following Matthiessen's law (eq. 4.8), depending on the predominant scattering processes taking place. There are two types of temperature-dependent scatterings: by the grain boundary and by the phonon-electron interactions. These mechanisms exhibit opposite behavior with temperature. The total mobility is also affected by the temperature-independent processes such as dislocation and ionized impurity scatterings, but these only affect the average value of mobility and not its dependence with temperature. An important conclusion drawn from this observation is that the increase of electron mobility with temperature should be attributed to grain boundary scattering only. Using the considerations above, we have used our AFTMM model to define criteria to establish different regions in which a scattering process will dominate the charge transport in the doped ZnO films. For this purpose, we consider two main scattering mechanisms: grain boundary and ionized impurity scatterings, since they are the two main dominant scattering mechanisms. The criteria are described as follows:

- If  $\mu_{GB} > 2\mu_{ii}$ : the ionized impurity scattering dominates electron transport.
- If  $2\mu_{GB} < \mu_{ii}$ : the grain boundary scattering dominates electron transport.

Fig. 4.23 shows the electron mobility versus carrier concentration for some values of the grain boundary trap density  $N_t$  (from  $1 \times 10^{13} \text{ cm}^{-2}$  to  $7 \times 10^{13} \text{ cm}^{-2}$ ). The variation of carrier mobility versus carrier concentration passes through a maximum value for a constant trap

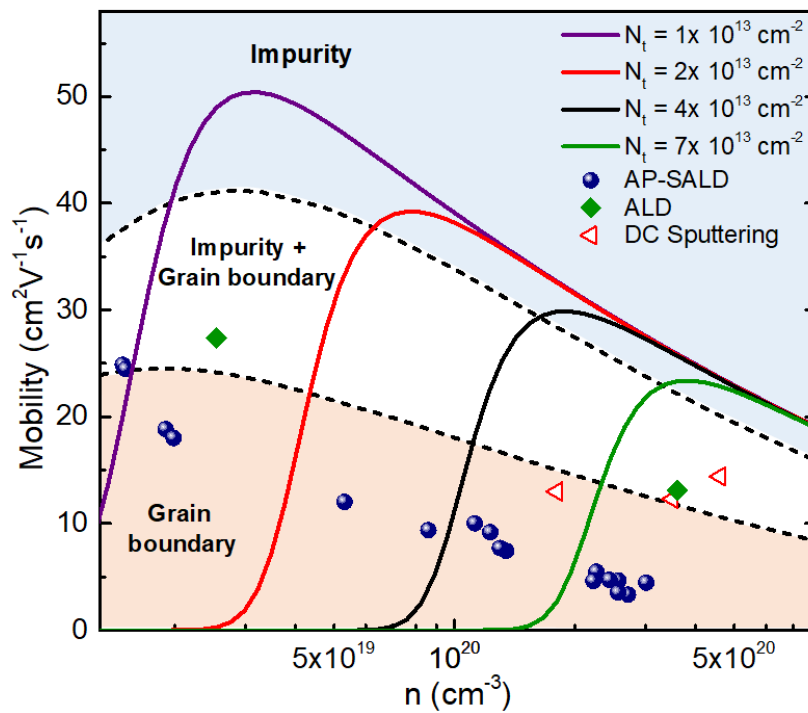


Figure 4.23: Electron mobility as a function of carrier concentration, calculated with the AFTMM model with different grain boundary trap densities ( $L = 20 \text{ nm}$ ,  $C = 0.5$ ,  $K = 0.12$ ). The dotted lines represent the limits of two regions where grain boundaries and ionized impurity scattering dominate the mobility.

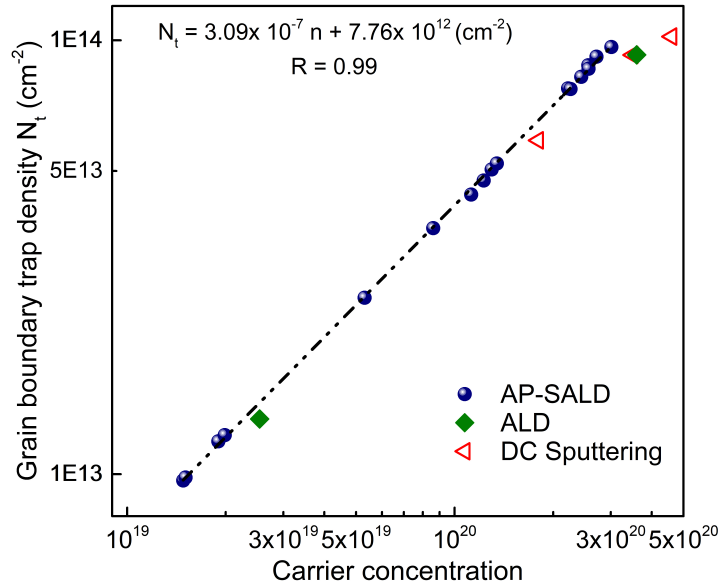


Figure 4.24: The trap density calculated by fitting the temperature-dependent Hall mobility with the model AFTMM as a function of carrier concentration. The samples have a thickness of around 200 nm, grown by AP-SALD at 200 °C (with UV assisted annealing at 200 °C under vacuum as the post-deposition treatment, see section 4.4 below), ALD and DC sputtering.

density  $N_t$ . At first, increasing the carrier concentration reduces the grain boundary potential barrier, leading to a higher mobility because of reduced grain boundary scattering. Then, by further increasing the carrier concentration, an increase of the ionized impurity scattering takes place, leading to a decrease in mobility. For each value of trap density  $N_t$ , we use the criteria defined above to separate three critical regions, namely, impurity, grain boundary, and impurity + grain boundary, where the dominant scattering mechanism is the ionized impurity, the grain boundary and both, respectively. The middle region corresponds to conditions for which both contributions have a comparable value. In addition, the Hall mobility of several ZnO:Al samples deposited on our home-made AP-SALD system is also given. At first, with the atmospheric pressure and under open-air deposition conditions, we find our Hall mobility data in the region dominated by the grain boundary scattering. As mentioned above, this can be explained by the fact that the oxygen atoms adsorbed at the grain boundaries during the fabrication process capture electrons and become negatively charged traps at the grain boundary, reducing the charge transport in the films. Secondly, the mobility keeps decreasing with the carrier concentration from  $1.5 \times 10^{19} \text{ cm}^{-3}$  to  $3 \times 10^{20} \text{ cm}^{-3}$  but does not pass through a maximum, as shown in the case of constant trap density. By scanning the mobility-carrier concentration curve with different trap density  $N_t$  in order to fit our experimental points with the theoretical model AFTMM, we found the fitting values and represent them versus the

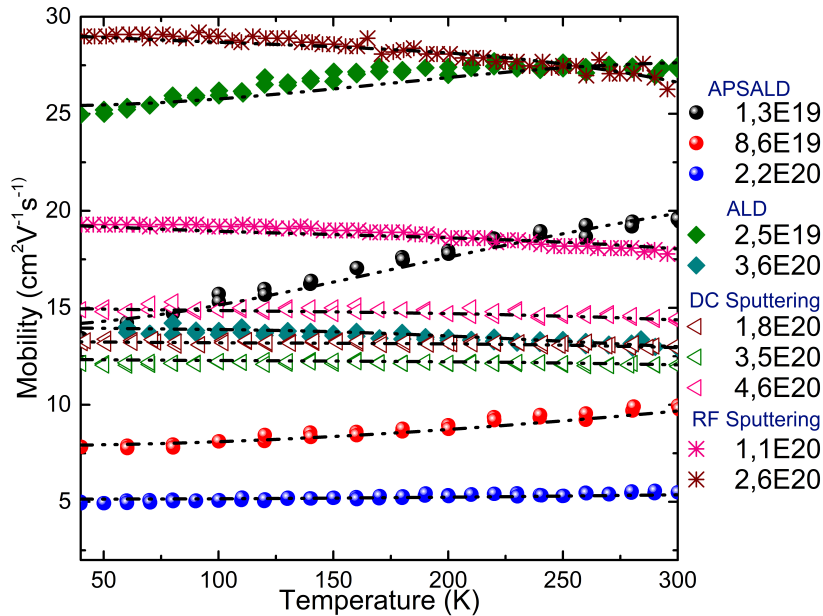


Figure 4.25: Experimental (points) and fitted (dashed lines) mobility as a function of the temperature for the ZnO:Al samples grown at 200 °C by AP-SALD, ALD, and DC sputtering, and two sets of extracted data from the paper of Ellmer and Mientus (samples prepared by RF sputtering).

carrier concentration  $n$  in Fig. 4.24.

Interestingly, a linear relationship is found between  $N_t$  and  $n$ . Actually, the increase of the carrier concentration  $n$  is accompanied by a higher Fermi level which has a consequence of filling more free traps in the grain boundaries. This linear dependence between the grain boundary trap density and the carrier concentration was also found by M. V. Garcia-Cuenca et al. in their work on heavily In-doped polycrystalline CdS films,[140] as well as by N. Sommer et al. in their work on ZnO:Al films.[125] It should be mentioned that the density of grain boundaries depends generally on the fabrication conditions and on the post-deposition treatments performed. In this work, all the AP-SALD samples were subjected to the same postdeposition treatment. A similar linear relationship can be determined for the ZnO:Al samples prepared by other methods, as shown in Fig. 4.24, where we show also some data from samples prepared by ALD and by DC sputtering. The trap density at grain boundaries  $N_t$  of these samples is slightly lower for the same carrier concentration than the value obtained for AP-SALD. This shift can be related to the sample preparation under lower oxygen partial pressure conditions in the case of ALD and DC sputtering, when compared with AP-SALD.

Fig. 4.25 shows both the experimental and simulated Hall mobility versus temperature and the associated fitting parameters using our AFTMM model for the ZnO:Al samples grown at 200 °C by AP-SALD, ALD, and DC sputtering and data extracted from the paper of Ellmer

Method	Input parameters			Extracted parameters ( $N_t/\Phi_B$ )	
	$n_{Hall}$ [ $cm^{-3}$ ]	$C$ [ $eV^{-1}$ ]	$K$	$N_t \times 10^{13}$ [ $cm^{-2}$ ]	$\Phi_B/E_F$ [ $eV$ ]
AP-SALD	$1.3 \times 10^{19}$	0.35	0.10	$0.91 \pm 0.01$	0.16/ 0.04
	$8.6 \times 10^{19}$	0.41	0.11	$3.53 \pm 0.01$	0.37/ 0.15
	$2.2 \times 10^{20}$	0.53	0.13	$7.62 \pm 0.01$	0.67/ 0.29
ALD	$2.5 \times 10^{19}$	0.36	0.10	$1.24 \pm 0.01$	0.16/ 0.07
	$3.6 \times 10^{20}$	0.60	0.14	$8.9 \pm 0.1$	0.56/ 0.40
DC Sputtering	$1.8 \times 10^{20}$	0.50	0.13	$5.7 \pm 0.1$	0.46/ 0.25
	$3.5 \times 10^{20}$	0.60	0.14	$9.0 \pm 0.1$	0.59/ 0.39
	$4.6 \times 10^{20}$	0.65	0.15	$9.9 \pm 0.1$	0.55/ 0.47
RF Sputtering[7]	$1.1 \times 10^{20}$	0.50	0.12	$3.9 \pm 0.1$	0.35/ 0.18
	$2.6 \times 10^{20}$	0.54	0.13	$5.1 \pm 0.1$	0.26/ 0.32

Table 4.2: Parameters used for and extracted from the fits in Fig. 4.25 of the temperature-dependent Hall mobility of selected ZnO:Al films grown by AP-SALD, ALD, and DC sputtering and two samples from the literature.[7] The Fermi level is also represented along the barrier height calculated from the AFTMM model.

and Mientus[7] (samples prepared by RF sputtering). The results of the fits are summarized in Table 4.2, in which we show the experimental data from the Hall Effect measurement, as well as the parameters used for and extracted from the fits. For the fits, we assumed that the electron–phonon scattering is similar for all the samples, while the average grain size was fixed at 20 nm after analyzing experimental data for the AP-SALD films. As shown, our model allows the fitting of the experimental Hall data for the ZnO:Al films with a large variation of carrier concentration, as well as deposition techniques. Note that only the samples grown by AP-SALD and the poorly doped sample grown by ALD show an increasing mobility versus temperature, in contrast with the other samples having a carrier concentration of the same order. According to the criteria defined in Fig. 4.22, this behavior belongs to type III, where the carrier transport is mainly dominated by grain boundary scattering. In addition, the mobility variation is more significant in the case of poorly doped films, where the effect of thermally tunneling emission is the most remarkable. The other samples deposited by ALD and DC sputtering show a decreasing mobility versus temperature, which corresponds to the case of carrier transport dominated by ionized impurity scattering (type I and II in Fig. 4.22). However, the relative variation of mobility versus temperature is more significant in the case of data extracted from the work of Ellmer and Mientus than in our samples, which suggests that the carrier transport in their samples is dominated by ionized impurity scattering and by electron–phonon scattering rather than by grain boundaries. The fitting results shown in Fig. 4.25 are summarized in Table 4.2. The parameters used for fitting are the Hall carrier density  $n_{Hall}$ , which is assumed to be temperature independent, the nonparabolicity param-

eter  $C$  and the compensation ratio  $K$ . Young et al. measured the effective mass  $m_n$  of their ZnO:Al samples deposited by RF sputtering, and estimated that  $m_n$  can vary from 0.3 to 0.48 ( $\times m_e$ ) for carrier concentrations in the range of  $1 \times 10^{20} - 5 \times 10^{20} \text{ cm}^{-3}$ , which correspond to a nonparabolicity parameter varying between 0.3 and 0.7.[136] Look et al. estimated the compensation ratio  $K$  between 0.04 and 0.12 for the case of Gallium doped ZnO films deposited by PLD at 200 °C under a pure argon atmosphere, with a carrier concentration in the range  $8 \times 10^{20} - 1.5 \times 10^{21} \text{ cm}^{-3}$ . [50] In addition, T-Thienprasert et al. used Synchrotron X-ray Absorption Spectroscopy to demonstrate that the compensation effect in the ZnO:Al films becomes more important when the sample deposition is carried out under an oxygen-rich atmosphere.[51] In our work, we studied specimens with carrier concentrations in the range of  $1.3 \times 10^{19} - 4.6 \times 10^{20} \text{ cm}^{-3}$  and assumed that the nonparabolicity  $C$  can vary from 0.3 to 0.65 while the compensation ratio  $K$  can vary between 0.1 and 0.15; such values are associated with the best fits that we obtained. The trap density at the grain boundaries varies from  $9 \times 10^{12} - 9.9 \times 10^{13} \text{ cm}^{-2}$  when the doping level in the ZnO:Al films increases from  $1.3 \times 10^{19} - 4.6 \times 10^{20} \text{ cm}^{-3}$ . However, as already pointed out in Fig. 4.24, the grain boundary trap density also depends on the deposition technique used. For example, two samples have a very similar doping level:  $2.2 \times 10^{20} \text{ cm}^{-3}$  in the case of AP-SALD and  $2.6 \times 10^{20} \text{ cm}^{-3}$  in the case of sputtering, but they show grain boundary trap densities of  $7.62 \times 10^{13} \text{ cm}^{-2}$  and  $5.1 \times 10^{13} \text{ cm}^{-2}$ , respectively. The Fermi level  $E_F$  is also presented along with the potential barrier height  $\Phi_B$  at the grain boundaries, calculated from extracted trap density  $N_t$  and Hall carrier concentration  $n$ . In most of the samples, the potential barrier  $\Phi_B$  is significantly higher than the Fermi level, which confirms again the negligible effect of thermionic emission. It should also be noted that in the sample with the highest mobility value, the Fermi level stays well above the top of the grain boundary potential barrier, which means that the grain boundary scattering has a small impact as compared to the other scattering phenomena. Hence, the observed improvement in mobility in this case should be only related to a reduction of the ionized impurity scattering.

This section was dedicated to the study of the scattering mechanisms limiting carrier transport in undoped ZnO and ZnO:Al films, with a focus on the grain boundary scattering. We have found that the charge transport in the films deposited by our AP-SALD system is totally dominated by the grain boundary scattering, with a high grain boundary trap density estimated from the fits with the experimental data using the new AFTMM model. In the following part, we will present an efficient method to reduce the grain boundary trap density, thus remarkably enhancing the electron mobility in the undoped ZnO and ZnO:Al films deposited by AP-SALD.

## 4.4 Effect of UV post-deposition treatment

Many researchers have suggested ways of reducing the electron trap density at the grain boundary, such as by performing post-deposition annealing at high temperatures ( $\geq 400$  °C), either in vacuum[95, 141] or in a hydrogen-rich atmospheres,[52, 142, 143] which are not cost-effective methods. Another possibility would be to benefit from the known interaction between UV light and ZnO to desorb trapped oxygen on the surface and at the grain boundaries. In 1959, Barry and Stone [93] used heavy oxygen ( $^{18}\text{O}$ ) to study the oxygen exchange with ZnO at different temperatures. In 1996, Zhang[144] also studied the adsorption and photo-desorption of oxygen on the surface and crystallite interfaces of sputtered ZnO films by performing a UV treatment in different atmospheres. Recently, Hagendorfer et al. reported a decrease of 4 orders of magnitude in resistance on their AZO films prepared by aqueous solution after a UV radiation exposure.[145] However, although the effect of UV light on highly doped polycrystalline ZnO thin films was observed a few decades ago, a comprehensive study of the relationship between the UV light treatment and the conductivity of the films is still missing. In this work, we use low-temperature ( $< 220$  °C) UV assisted annealing under vacuum to decrease the electron trap density at the grain boundaries of ZnO and ZnO:Al films deposited by AP-SALD. We begin by developing a theoretical model of carrier transport in the polycrystalline ZnO based films to interpret the *in-situ* measurements of the electrical conductivity during the UV treatment. The model provides a quick and simple way of extracting the trap density at the grain boundaries, which is a critical parameter directly affecting the electrical properties of the films and usually very difficult to estimate. The effect of the UV assisted annealing of ZnO films with different doping levels and thicknesses, as well as the oxygen desorption rate versus annealing temperature is then discussed. In the last part of this work, we show that UV treated films quickly reabsorb oxygen if exposed to the atmosphere at high temperatures (200 °C). Finally, we demonstrate that such oxygen readsorption can be blocked thanks to a very thin alumina ( $\text{Al}_2\text{O}_3$ ) barrier layer. The result shown in this section was lately published in the following paper: Nguyen, V. H. et al. *ACS Applied Nano Materials*, **2018**, 1 (12), 6922–6931.[146]

### 4.4.1 Experimental section

All samples used in this study were deposited on borosilicate glass substrates with our AP-SALD system. The substrate temperature was maintained at 200 °C. The samples oscillated under the injector at a distance of 150  $\mu\text{m}$  and with a speed of 6.5 cm/s. The bubbling and dilution flows were respectively 30 and 270 sccm for DEZ, 150 and 300 sccm for  $\text{H}_2\text{O}$ ; the  $\text{N}_2$  flow was fixed at 1000 sccm. TMA was injected into the DEZ line with a frequency of 1

TMA pulse per 56 DEZ-H<sub>2</sub>O cycles. The post-deposition treatments applied to the AP-SALD deposited samples were carried out under vacuum (0.03 mbar) at various temperatures ranging between room temperature and 220 °C. During the treatments, the samples were subjected to UV light illumination for 120 mins (wavelength: 365 nm, light output power: 245 μW/cm<sup>2</sup>, distance between sample and light source: 15 cm).

The photoluminescence measurement has been carried out with a continuous laser excitation at 266 nm (1.2 mW, Crylas FQCW 266-10). The emission from the ZnO and ZnO:Al samples was collected by an optic fiber located close to the samples, dispersed by a spectrometer (iHR Triax 320 Jobin-Yvon) and detected by a liquid-nitrogen cooled Si CCD detector.

#### 4.4.2 Theoretical model

In the previous section, we have demonstrated that the scattering by grain boundaries is the predominant mechanism in polycrystalline ZnO films prepared in the open atmosphere such as the case of AP-SALD. Therefore, as a first approximation, we can write  $\mu_{total} = \mu_{GB}$ . In this part, both analytical (SPM) and numerical (AFTMM) models will be used to study the effect of a UV treatment on the variation of the grain boundary trap density  $N_t$  and the potential barrier  $\Phi_B$ . According to the work of Barry and Stone,[93] the oxygen adsorption kinetics by ZnO films follows the Roginski-Zeldovich equation:

$$Q(t) = \frac{1}{b} \left\{ \ln \left( t + \frac{1}{ab} \right) + \ln(ab) \right\} \quad (4.57)$$

where Q refers to the amount of oxygen adsorbed by ZnO at time t; while a and b are constants relating, respectively, to the initial adsorption rate and the rate of change of the activation energy with the adsorption coverage.

Here, we applied this theory to the opposite case: oxygen desorption during UV illumination. Figure 4.26 presents a schematic illustration of the oxygen desorption mechanisms at the grain boundaries of ZnO:Al thin films, in which  $E_F$ ,  $E_C$  and  $E_V$  refer respectively to the Fermi level, the minimum of the conduction level and the top of the valence band. During UV irradiation photo-generated holes will be driven by the electric field nearby the grain boundary to the interface where negatively charged adsorbed oxygen atoms are neutralized. If this desorption process occurs close to the surface of the film, the oxygen can be easily pumped away. Conversely, if it occurs in the bulk, the released oxygen molecules need to diffuse to the surface to be pumped away. Therefore, the oxygen desorption process can be accelerated by increasing the sample temperature. As described, the UV light is the driving force to decrease the grain boundary trap density. Since our samples were prepared at 200 °C, we assume that annealing at temperatures of about 200 °C does not affect the structural properties of the

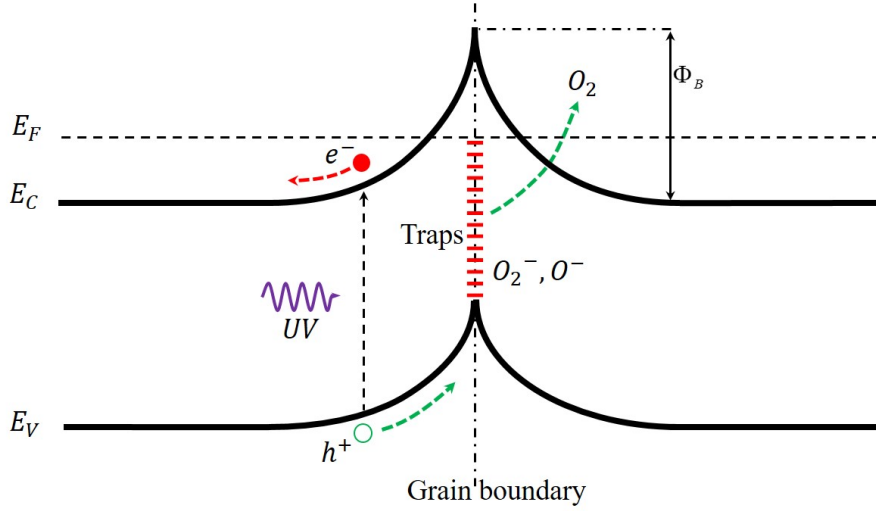


Figure 4.26: Schematic image of the oxygen desorption mechanisms at grain boundaries of ZnO:Al.  $E_F$ ,  $E_C$  and  $E_V$  refer respectively to the Fermi level, the minimum of the conduction level and the top of the valence band.

films, therefore grain size and grain boundary surfaces remain constant. It follows that the total quantity of adsorbed oxygen species at the grain boundaries is considered to be proportional to the grain boundary trap density  $N_t$  ( $\text{cm}^{-2}$ ). Hence, at a time  $t$  after turning the UV lamp on, the trap density can be expressed as follows:

$$N_t(t) = N_{t_0} \left[ 1 - A \cdot \ln \left( 1 + \frac{t}{t_0} \right) \right] \quad (4.58)$$

where  $N_{t_0}$  refers to the initial value of trap density at grain boundaries,  $A$  denotes the initial desorption rate and  $t_0$  is the time constant related to the desorption kinetics. In doped ZnO films, the carrier concentration is usually high ( $10^{19} - 10^{21} \text{ cm}^{-3}$ ), and as a first approximation, we assume that the number of electrons released from grain boundaries does not affect the ingrain carrier concentration (i.e.  $N_t \ll nL$ , here  $L$  is the mean grain size). Moreover, Drude's model, which is generally accepted for TCO thin films, shows that the carrier mobility is inversely proportional to the resistivity. Therefore, the relative resistivity variation of the film treated under UV illumination can be expressed as follows:

$$R(t) = \frac{\rho(t)}{\rho(t_0)} = \frac{\mu(\Phi_{B_0})}{\mu(\Phi_B(t))} \quad (4.59)$$

where  $\Phi_{B_0} = q^2 N_{t_0}^2 / (8\epsilon_s \epsilon_0 n)$  is the grain boundary potential barrier at the initial time  $t_0$ . By combining eq. 4.20 and eq. 4.58, we obtain the expression of the grain boundary potential

barrier at the time  $t$ :

$$\Phi_B(t) = \frac{q^2 N_t^2 \left[ 1 - A \ln \left( 1 + \frac{t}{t_0} \right) \right]^2}{8 \epsilon_s \epsilon_0 n} \quad (4.60)$$

By fitting the experimental data with eq. 4.59 using the Seager-Pike-Modified (SPM) or the new AFTMM models, the trap density at the grain boundaries  $N_t(t)$  and its variation with time, as well as the constants  $A$  and  $t_0$ , can be evaluated. In the next part, the influence of different parameters such as the substrate temperature during the UV treatment and the doping concentration on physical properties of undoped and Al-doped ZnO films are discussed.

### 4.4.3 Effect of doping concentration

Figure 4.27 shows the sheet resistance, Hall carrier concentration and mobility of undoped and doped ZnO samples, before and after UV treatment (at 200 °C under vacuum for 2 h) versus Al dopant concentration. The inset images show the corresponding variations of the conductance, carrier concentration and mobility before and after the UV treatment, respectively. As shown in the figure, the undoped ZnO sample exhibits an improvement of carrier concentration up to 3.5 times after the UV treatment, while the doped ZnO samples have a slightly lower improvement ( $\sim 1.25$  times). This can be explained by the fact that as-deposited undoped ZnO films have a low carrier concentration ( $\sim 4 \times 10^{18} \text{ cm}^{-3}$ ), and thus the additional electrons released from grain boundaries exert a more important contribution than in the case of ZnO:Al, for which the ingrain carrier concentration is already very high ( $> 10^{20} \text{ cm}^{-3}$ ). As for carrier mobility, it increases greatly for the samples with low doping ( $\leq 1\%$  Al), reaching  $25 \text{ cm}^2 \text{ V}^{-1} \text{ s}^{-1}$  for the undoped samples. Conversely, for 1% Al doped film, the mobility only reaches  $7.1 \text{ cm}^2 \text{ V}^{-1} \text{ s}^{-1}$ . This is so since by increasing the doping concentration in ZnO:Al films, both the trap density at the grain boundaries and the impurity scattering become more important.[125, 128]

Thus, the results show that the improvement in the electrical conductivity mainly originates from the increase in carrier mobility rather than in carrier concentration, which validates our initial assumption. As stated in the previous section, the grain boundary scattering is still the predominant limiting factor for mobility in undoped ZnO and ZnO:Al films prepared by open-air techniques such as AP-SALD. However, the upper limit for carrier mobility improvement via the UV treatment is fixed by the impurity scattering. This is another reason why in undoped ZnO films, a larger conductivity improvement is observed as compared to ZnO:Al. In our case, the UV treatment leads to a resistivity drop from  $6.1 \times 10^{-2} \text{ } \Omega \text{ cm}$  to a minimum resistivity value of  $2.9 \times 10^{-3} \text{ } \Omega \text{ cm}$  for the as-deposited ZnO:Al samples with a doping concentration

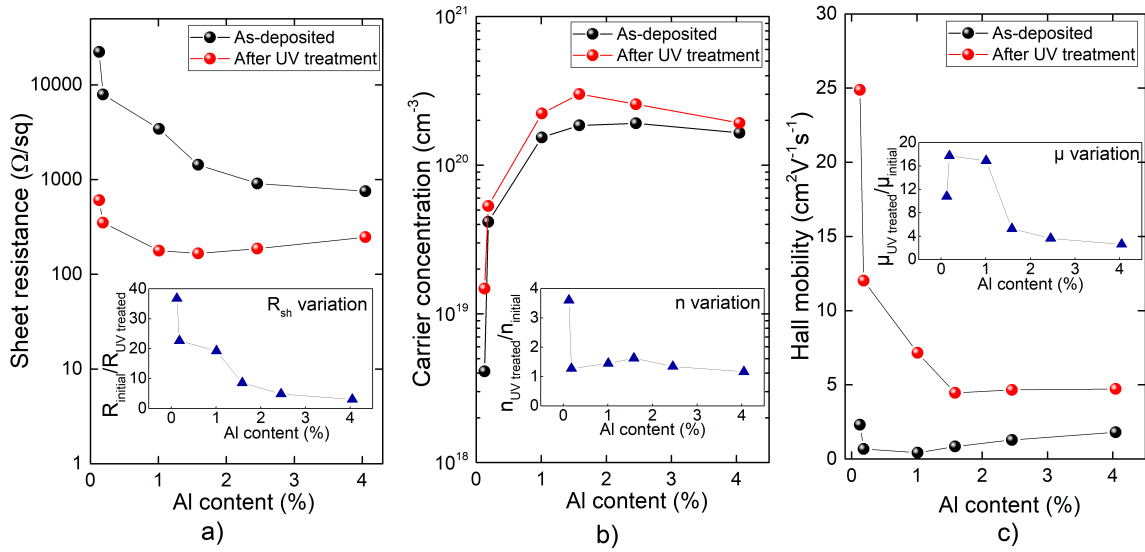


Figure 4.27: Electrical properties of ZnO films deposited by AP-SALD with different Al doping levels before and after the UV treatment at 200 °C under vacuum: a) sheet resistance, b) Hall carrier concentration, c) Hall carrier mobility. The insets show the variations of the conductance, carrier concentration and mobility before and after the UV treatment, respectively. All the films are 185 nm thick.

of 1.6 % Al, which is similar to the value obtained when using conventional ALD ( $3.2 \times 10^{-3} \Omega cm$  achieved at 1.9 % Al).[147]

As shown by the data reported in Figure 4.27, the effect of 365 nm UV light on the electrical properties of the ZnO:Al films strongly depends on their doping concentration. From the light-matter interaction point of view, the absorption coefficient of ZnO:Al films at 365 nm depends upon the doping concentration. Indeed, a shift in the optical bandgap from 3.28 eV for undoped ZnO sample to 3.44 eV for 1.26% Al-doped ZnO sample was observed, as expected from the Burstein-Moss effect, while the UV light used for treatment has an energy of 3.4 eV. The total transmittance of undoped and doped ZnO samples is shown in Figure 4.28a, with a zoom in the UV range. The transparency at 365 nm of the 1.26 % Al doped ZnO sample is rather large ( $T \sim 45 \%$ ), while the values of the 0.52 % Al doped ZnO and undoped ZnO samples are respectively 22 % and 10 %. Also, the doping effect can be observed from photoluminescence spectra (measured at 20 K using an excitation energy of 4.66 eV), as shown in Figure 4.28b. In the case of the ZnO:Al samples, just one part of the exciton emission peaks is located below the 365 nm threshold level (3.4 eV), while the peak of ZnO is totally located below this energy, explaining the high absorption coefficient of undoped ZnO, and therefore the enhanced effect of the UV treatment.

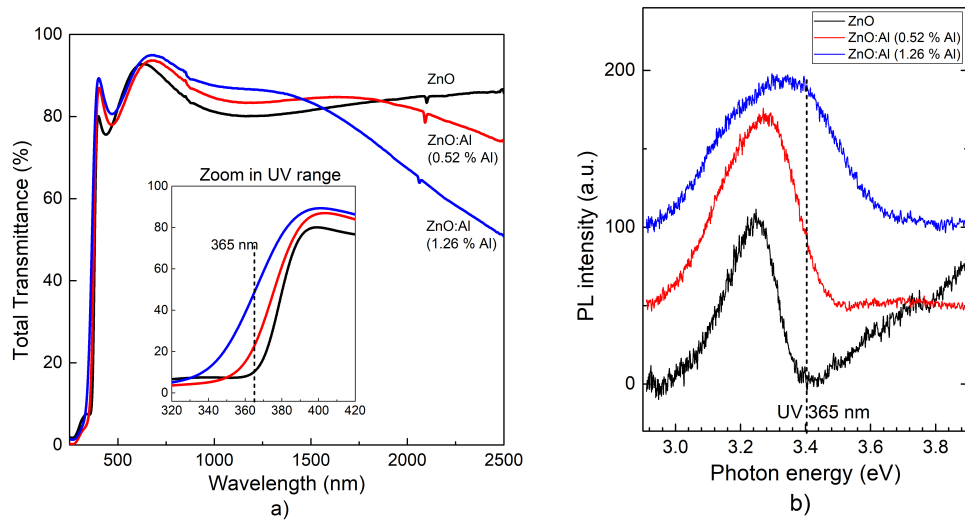


Figure 4.28: a) Total transmittance of ZnO:Al films with different doping concentrations, the inset image zooms into the UV range of [320 nm, 420 nm] and b) The photoluminescence spectrum around 365 nm of ZnO and ZnO:Al with different doping levels, the emissions were recorded at 20 K using an excitation energy of 4.66 eV.

#### 4.4.4 Effect of temperature during the UV treatment

Figure 4.29 shows the influence of the substrate temperature during the UV treatment on the electrical properties of undoped ZnO and ZnO:Al films. As can be seen, higher conductivity values are obtained when using a higher substrate temperature. As for the RT experiments, the effect is more considerable in the case of undoped ZnO than doped ZnO samples in the whole temperature range used, due to the difference in absorption coefficient, as explained in the previous section. Here, we confirm again the small variation of the carrier concentration for degenerately Al-doped ZnO samples ( $n > 10^{20} \text{ cm}^{-3}$ ), while a significant improvement of carrier concentration for undoped ZnO sample is observed since the amount of electrons released from grain boundaries under the UV treatment is comparable to the initial doping level. Conversely, the impact of the treatment temperature on the carrier mobility is very remarkable. When the treatment temperature increases from 25 °C to 220 °C, the electron mobility dramatically increases from  $0.45 \text{ cm}^2\text{V}^{-1}\text{s}^{-1}$  up to  $21.2 \text{ cm}^2\text{V}^{-1}\text{s}^{-1}$  for undoped ZnO sample, and from  $3 \text{ cm}^2\text{V}^{-1}\text{s}^{-1}$  to  $5.78 \text{ cm}^2\text{V}^{-1}\text{s}^{-1}$  for heavily doped ZnO sample. For the low temperature range used (25 °C – 220 °C), no change in the film morphology or crystallinity is observed. Therefore, the increase of the electron mobility versus the UV treatment temperature can only be explained by a decrease of oxygen traps at the grain boundaries. In literature, the oxygen diffusion in undoped ZnO and ZnO:Al has been studied at high temperatures (900 °C – 1000 °C) by means of the gas-solid isotope exchange method using the isotope  $^{18}\text{O}$

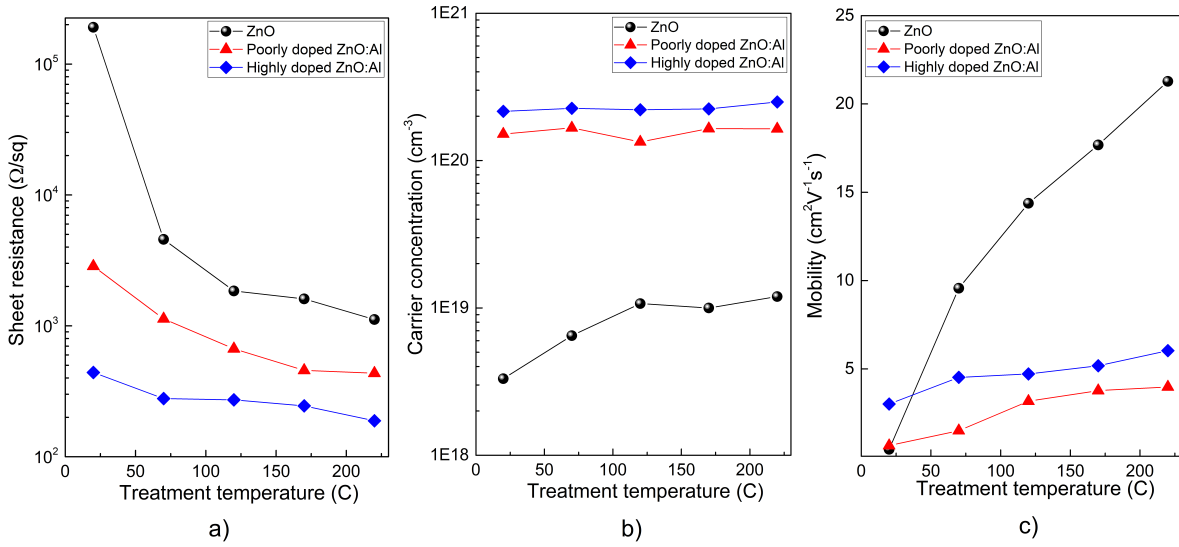


Figure 4.29: Influence of the substrate temperature during UV treatment on the electric properties of undoped and doped ZnO films; a) sheet resistance, b) Hall carrier concentration and c) Hall carrier mobility as a function of substrate temperature. All the films have the same thickness of 220 nm.

as oxygen tracer.[148, 149] Accordingly, it was found that oxygen grain boundary diffusion is 3 to 4 orders of magnitude greater than oxygen volume diffusion in both pure and doped ZnO. In the case of thin ZnO films with a very high density of grain boundaries, the oxygen diffusion via grain boundaries is assumed to be very significant. Without UV illumination, the annealing temperature required for a significant improvement of the conductivity is often higher than 400 °C, as reported in literature.[95, 141] In our case, a low temperature (< 220 °C) combined with the UV treatment under mild vacuum already leads to a remarkable improvement in conductivity, which provides the possibility to use soft substrates, such as plastic or paper.

#### 4.4.5 Model application to experimental data

Figure 4.30 shows the relative variation of resistance during the UV treatment at 70 °C under vacuum (0.03 bar) for undoped ZnO and ZnO:Al samples, along with the fitting curves shown in solid red lines thanks to eq. 4.59. A very good agreement between experimental data and modeling is observed. Table 4.3 summarizes the parameters extracted from the fits of the experimental curves using the two models described in the theory part. Interestingly, the two models provide similar results. As shown, the initial trap density  $N_{t_0}$  increases from  $6.9 - 7.2 \times 10^{12}$  ( $\text{cm}^{-2}$ ) for undoped ZnO sample up to  $6.7 - 6.9 \times 10^{13}$  ( $\text{cm}^{-2}$ ) for the 1.6 % Al doped

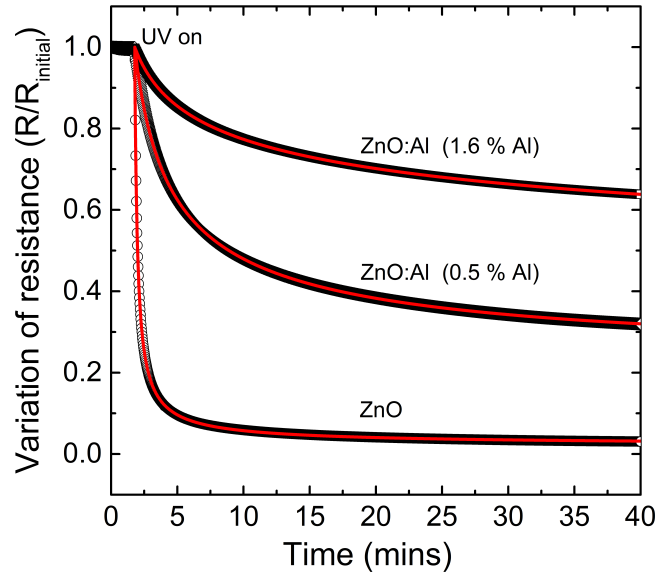


Figure 4.30: The variation of resistance ( $R/R_{\text{initial}}$ ) during UV treatment under vacuum for undoped ZnO and two ZnO:Al samples. The substrate temperature was maintained at 70 °C. A high fitting quality of experimental data with the two presented models is observed, as shown by the solid red lines.

ZnO sample, which corresponds to a carrier concentration of  $2.05 \times 10^{20} \text{ cm}^{-3}$ . This result is completely coherent with the result shown in the previous section, in which the temperature-dependent Hall data (for a temperature range 30 K - 300 K ) was fitted with the new AFTMM model, resulting in a grain boundary trap density of  $7.62 \times 10^{13} (\text{cm}^{-2})$  for ZnO:Al sample with a doping concentration of  $2.1 \times 10^{20} (\text{cm}^{-3})$ . Thus, the *in-situ* UV treatment method described in this work provides an easy means to calculate the grain boundary trap density that is simpler and much faster than temperature-dependent Hall measurements, which usually require a fairly complex set-up.

Concerning the two parameters related to the desorption kinetics, we observe that when the doping concentration increases, the parameter  $A$  related to the initial desorption rate significantly decreases while the time constant  $t_0$  increases. This means that the desorption process is faster in the case of undoped ZnO compared to the cases of ZnO:Al samples. The first reason for this observation is that undoped ZnO has a stronger ability to absorb the 365 nm UV light than ZnO:Al samples, as discussed in Section 4.4.3. Secondly, undoped ZnO has a larger depletion layer at grain boundaries as compared to highly doped ZnO:Al samples, which have a much higher electron concentration, and therefore, a thinner depletion layer at the grain boundaries. Consequently, it is more difficult for an oxygen atom released from the undoped ZnO grain boundaries to recapture back an electron (in the conduction band next to the grain

Sample	Extracted parameters from the fits by using:	$N_{t_0} (cm^{-2})$	$A (\times 10^{-2})$	$t_0 (s)$
ZnO	SPM model	$(7.2 \pm 0.2) \times 10^{12}$	$8.4 \pm 0.1$	$13.0 \pm 0.1$
	AFTMM model	$(6.9 \pm 0.2) \times 10^{12}$	$9.8 \pm 0.1$	$14.0 \pm 0.1$
ZnO:Al (0.5 %)	SPM model	$(5.4 \pm 0.2) \times 10^{13}$	$5.2 \pm 0.1$	$95.1 \pm 0.4$
	AFTMM model	$(5.4 \pm 0.2) \times 10^{13}$	$5.6 \pm 0.1$	$92.1 \pm 0.5$
ZnO:Al (1.6 %)	SPM model	$(6.7 \pm 0.2) \times 10^{13}$	$1.6 \pm 0.1$	$102 \pm 1$
	AFTMM model	$(6.9 \pm 0.2) \times 10^{13}$	$1.6 \pm 0.1$	$106 \pm 1$

Table 4.3: Results of fitting the experimental curves shown in Figure 4.30 with the SPM and AFTMM models.  $N_{t_0}$  denotes the initial grain boundary trap density,  $A$  and  $t_0$  are two constants related to the initial desorption rate and the time constant of the desorption kinetics, respectively.

boundary) than in the case of highly doped ZnO:Al samples. While both models AFTMM and SPM provide similar results for the ZnO samples prepared by AP-SALD, the AFTMM method is more powerful and can be applied for a wider range of doping concentrations, as well as for systems in which the potential barrier has a complex shape, which is not the case for the SPM model.

Concerning the reliability of the fit parameters, while the parameters related to desorption kinetics ( $A$  and  $t_0$ ) can be easily fitted with a small error, the grain boundary trap density depends on the error of the Hall carrier concentration. Actually, what generates the time-dependent evolution of the conductivity during the UV treatment is the variation with time of the grain boundary potential barrier  $\Phi_B(t)$ , as described in eq. 4.60. And because  $\Phi_B(t)$  is directly proportional to  $N_{t_0}^2/n$ , the evaluation of  $N_{t_0}$  cannot be independent of the Hall carrier concentration. The errors of values shown in Table 4.3 correspond to a 5% variation of the Hall carrier concentration.

#### 4.4.6 Oxygen readsorption after the UV treatment

In order to obtain an efficient improvement of the conductivity via the UV treatment discussed here, three key factors are required: a) appropriate UV light absorption to create electron-hole pairs, b) moderate temperatures ( $\sim 200$  °C) to increase the oxygen diffusion from the film bulk to the sample surface, and c) a vacuum chamber to pump the released oxygen molecules out. In the case of the samples treated with all the three listed factors, the conductivity improvement obtained is stable in the open-air at room temperature up to several months. Actually, the oxygen readsorption requires an activation energy  $E_{activation} > k_B T_{ambient}$ , leading to a very slow oxygen adsorption rate by the treated film at room temperature. However, if a treated sample is heated up in the open air, its conductivity decreases gradually due to oxygen

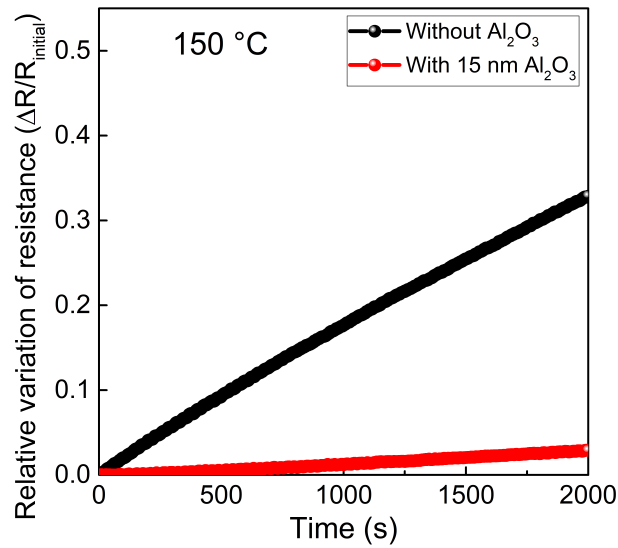


Figure 4.31: The relative variation of resistance ( $\Delta R/R_{\text{initial}}$ ) of two 200 nm thick ZnO:Al samples, with and without 15 nm of  $\text{Al}_2\text{O}_3$  protection layer, as a function of time when the samples were maintained at 150 °C in the open air.

readsorption. Therefore, an efficient gas diffusion barrier layer is required to prevent oxygen readsorption. Aluminum oxide ( $\text{Al}_2\text{O}_3$ ) films deposited by ALD have demonstrated to act as an excellent gas diffusion barrier for organic light emitting devices (OLEDs) thanks to their pinhole-free characteristic.[150–152] In this work, an  $\text{Al}_2\text{O}_3$  protection layer can be prepared in open-air, low temperature conditions with our AP-SALD system. Figure 4.31 compares the relative variation of resistance of two UV-treated ZnO:Al samples (under vacuum, at 200 °C), with and without protection layer, when the samples were maintained at 150 °C in open air. As a result, we observe a clear stability improvement of the film conductivity with a 15 nm  $\text{Al}_2\text{O}_3$  layer deposited at 60 °C by AP-SALD.

The effect of UV illumination of ZnO films deposited in oxidizing atmospheres, and its dependence with temperature, can indeed be used to design improved UV or oxygen sensors. Figure 4.32 illustrates the conductivity behavior of a 25 nm – thick ZnO sample versus time when it is alternatively exposed to the 365 nm UV light. This very thin ZnO film was fabricated at 200 °C by AP-SALD, and had an as-deposited sheet resistance of about 1 M $\Omega$ /sq. During this experiment, the sample was maintained at 130 °C (shown at the top of Figure 4.32) and at 200 °C (shown at the bottom of Figure 4.32).

When the UV was switched on, the film resistance decreased by a factor close to 3 within the first 10 seconds in both cases. However, when the UV was turned off, the time to recover the initial resistance was significantly different. Consequently, the time it takes to perform 5 on/off UV cycles in the case of 130 °C is approximately 10 times longer than in the case of 200

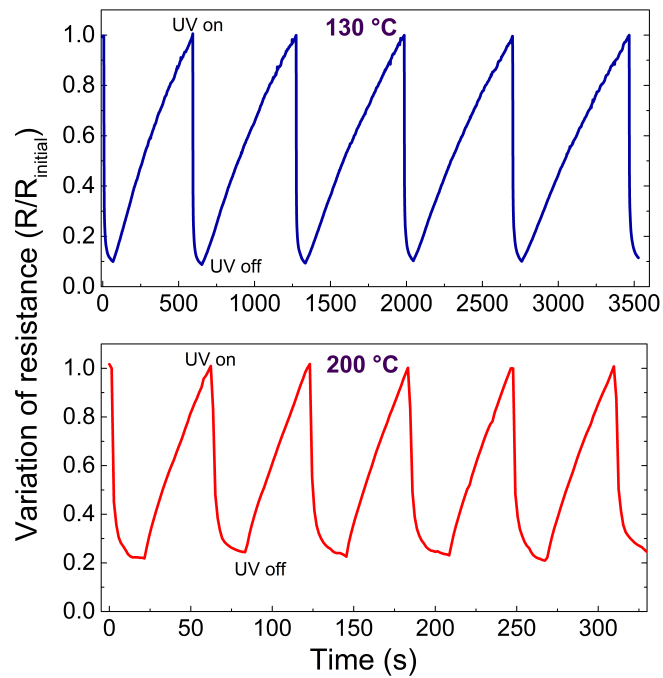


Figure 4.32: The variation of resistance ( $R/R_{\text{initial}}$ ) of 25 nm - thick ZnO sample as a function of time when alternatively illuminating the samples with the 365 nm UV light. The samples were maintained at 130 °C and 200 °C, respectively, in the open air.

°C. This can be explained by the fact that the oxygen readsorption kinetics at 200 °C is much faster than at 130 °C, which is totally coherent with what was discussed in Section 4.4.4. This interesting effect could be for instance used to fabricate a simple transparent UV or oxygen sensor by deposition a thin ZnO layer ( $\sim 25$  nm) by AP-SALD on a transparent heater based on ITO or silver nanowire networks, which can be used as a transparent heater thanks to the Joule effect.[153]

## 4.5 Conclusion

In summary, we have presented a complete, comprehensible numerical model by using the Airy Function Transfer-Matrix Method (AFTMM) to describe the charge transport phenomena at the grain boundaries in polycrystalline ZnO:Al films. The key to this new approach is the discretization of the grain boundary potential into linear segments, which allows an accurate calculation of the electron tunneling probability. The comparison of our model with a modified analytical model from Seager and Pike is discussed. Studying theoretically the dependence of carrier mobility on carrier concentration, we formulated criteria to determine the predominant scattering mechanisms in ZnO:Al films, in which its applicability is independent

of the deposition method used.

By analyzing Hall mobility data, we found that the carrier transport in the samples prepared by AP-SALD is dominated by the grain boundary scattering, while in the case of samples prepared by ALD and DC sputtering, both grain boundaries and ionized impurity scattering are dominant. A high fitting quality of our AFTMM model to the temperature-dependent Hall mobility data over a large range of carrier concentration in the ZnO:Al films prepared by different techniques has been demonstrated. The trap density at the grain boundaries extracted from the fits showed a linear relationship with the carrier concentration in the ZnO:Al samples deposited by AP-SALD. Accordingly, the electron trap density at the grain boundaries for ZnO:Al samples (carrier concentration of  $2.2 \times 10^{20} \text{ cm}^{-3}$ ) prepared by AP-SALD was estimated to be about  $7.6 \times 10^{13} \text{ cm}^{-2}$ , which is significantly higher compared to  $5.1 \times 10^{13} \text{ cm}^{-2}$  for the case of ZnO:Al sample deposited by RF sputtering, which has a similar carrier concentration ( $2.6 \times 10^{20} \text{ cm}^{-3}$ ).

According to the results found in the first part of this chapter, the conductivity of the films deposited by our AP-SALD system is totally dominated by grain boundary scattering. In the second part of this chapter, we have presented an efficient and simple method to improve the carrier mobility, thus the conductivity, of as-deposited ZnO and ZnO:Al thin films. It consists in the UV assisted treatment of the films at low temperatures ( $\leq 220 \text{ }^\circ\text{C}$ ) and under mild vacuum. The physical mechanism behind it is that the UV-generated holes neutralize the adsorbed oxygen species at the grain boundaries, thus releasing the oxygen molecules that can then diffuse from within the film to the film surface, to be finally pumped away under vacuum. As a result, for the samples treated at  $200 \text{ }^\circ\text{C}$ , the carrier mobility increased greatly from below  $1 \text{ cm}^2\text{V}^{-1}\text{s}^{-1}$  up to  $25 \text{ cm}^2\text{V}^{-1}\text{s}^{-1}$  for the undoped ZnO case and to  $7.1 \text{ cm}^2\text{V}^{-1}\text{s}^{-1}$  for 1% doped ZnO:Al sample. This corresponds to a resistivity drop from  $6.1 \times 10^{-2} \text{ }\Omega\text{cm}$  for the as-deposited ZnO:Al sample to a minimum resistivity of  $2.9 \times 10^{-3} \text{ }\Omega\text{cm}$  (for a doping concentration of 1.6 % Al), which is similar to the values obtained for conventional ALD. Additionally, we have used the AFTMM model to fit the experimental data obtained from the UV *in situ* time-dependent conductivity measurements. The results of the fitting have shown an estimation of the grain boundary trap density of about  $7 \times 10^{12} \text{ cm}^{-2}$  for undoped ZnO sample, and  $6.8 \times 10^{13} \text{ cm}^{-2}$  for the ZnO:Al sample with a doping concentration of  $2.05 \times 10^{20} \text{ cm}^{-3}$ . The grain boundary trap density extracted from this work is rather similar to the result extracted from analyzing the temperature-dependent Hall data of equivalent films, as shown above. Also, we have showed that the stability of the conductivity of the films when exposed to the open-air at high temperature can be drastically enhanced by encapsulating the treated samples with a thin conformal  $\text{Al}_2\text{O}_3$  deposited by AP-SALD.

The deep comprehension of the carrier scattering mechanisms in ZnO:Al films (or more

general in TCOs) is an important step towards low-cost and high-performance materials since it provides guidance on how to optimize the deposition conditions, and how to choose appropriate post-deposition techniques.



# Chapter 5

## Metal oxide/AgNW composites: high performance flexible TCMs

### Contents

---

<b>5.1</b>	<b>Thin conformal ZnO coating as a protective layer for AgNWs . . . . .</b>	<b>128</b>
5.1.1	Experimental section . . . . .	129
5.1.2	Effect of ZnO coating on adhesion and transparency of AgNW networks . . . . .	130
5.1.3	Effect of the ZnO coating on the electrical and thermal stability of AgNW networks . . . . .	133
5.1.4	Rationalization of the effect of the ZnO coating on the stability of AgNW networks . . . . .	136
5.1.5	Evaluation of the performance of transparent heaters based on ZnO coated AgNWs . . . . .	139
<b>5.2</b>	<b>ZnO:Al/AgNW nanocomposites . . . . .</b>	<b>141</b>
5.2.1	Model of two parallel resistances . . . . .	143
5.2.2	Model considering the presence of local percolating AgNW clusters below the network percolation threshold . . . . .	145
<b>5.3</b>	<b>Quantitative assessment of the effects of the ZnO coating on AgNW networks . . . . .</b>	<b>154</b>
<b>5.4</b>	<b>Conclusion . . . . .</b>	<b>156</b>

---

In this chapter, the development of high-performance TCMs based on AgNW networks and ZnO/ZnO:Al thin films will be discussed. Firstly, we study the effect of a thin conformal ZnO coating deposited by our AP-SALD system on the electrical and thermal stabilities of the AgNW networks. Then, for the sake of improving both the stability and the conductivity, a composite based on ZnO:Al thin film and AgNW (hereafter called ZnO:Al/AgNW nanocomposite) will be presented, including both theoretical and experimental studies of the electrical properties of the nanocomposite.

## 5.1 Thin conformal ZnO coating as a protective layer for AgNWs

Metallic nanowire networks and specially those composed of silver nanowires (AgNWs) have attracted much attention in the past few years.[154–156] By virtue of their excellent electrical and optical properties (10-20  $\Omega/sq$  sheet resistance and about 90 % transmittance in the visible range) and their mechanical flexibility, silver nanowire networks are considered as promising candidates for flexible optoelectronic applications. Another clear advantage of TE based on AgNW is the possibility to establish simple large-scale fabrication through solution processing[157] and a lower price than indium tin oxide (ITO), which is so far considered as the most standard and efficient transparent conducting oxide.[14] It has even been shown that by further optimizing the deposition and post-deposition conditions, and the aspect ratio (length/diameter) of the nanowires, the resulting networks can surpass the electrical-optical properties of (ITO).[158] AgNW networks have been investigated or even efficiently integrated into devices such as transparent heaters,[159, 160] solar cells,[161] or touch screens.[162] Despite these attractive potentialities, the integration of AgNW based TE in real devices is not yet widely considered in industrial devices due namely to their potential thermal and electrical instabilities,[163, 164] as well as low adhesion and aging issues.[155] For instance, while an electrical welding or thermal annealing is beneficial for reducing junction resistance (between adjacent AgNWs) thanks to local sintering, it is also known that reaching too high a temperature leads to spheroidization of the AgNWs. This causes the loss of the percolating nature of the network, thus eventually leading to an infinite electrical resistance.[164] Left unprotected, AgNW networks would undergo local oxidation and/or melt, which adversely affects the conductivity of AgNW films. While the morphological instability of bulk silver occurs at temperatures higher than 960 °C, degradation induced by thermal annealing can occur at much lower temperature (i.e. < 300 °C) due to the high surface-to-volume ratio in nanowires. The idea of preparing composite electrodes by coating metallic

nanowires with a very thin oxide layer has already been considered in literature[165] as a possible remedy to such instabilities. Some researchers have used titanium dioxide ( $\text{TiO}_2$ ) coatings,[166, 167] as well as ZnO or ZnO:Al.[168, 169] Clearly, the shell used has shown encouraging results in terms of stability enhancement. However, in order for such composite electrodes to remain attractive in terms of cost and simple processing, the oxide layer should be deposited by low-cost, vacuum-free scalable approaches, among which AP-SALD is a promising technique.

In the first part of this chapter, we focus on the use of AP-SALD to deposit ZnO coatings on AgNWs based TE, and the thorough investigation of the effects of the ZnO coating thickness on the properties of AgNW networks in terms of electrical and thermal stabilities. The results shown in Section 5.1 were lately published in the following paper: A. Khan, V. H. Nguyen, D. Muñoz-Rojas, S. Aghazadehchors, C. Jiménez, N. D. Nguyen, D. Bellet, ACS Appl. Mater. Interfaces **2018**, 10, 19208 (two first authors contributed equally).[170] Similarly, the stability of copper nanowires (CuNWs) in ambient conditions was also greatly enhanced by using a thin  $\text{Al}_2\text{O}_3$  coating deposited by AP-SALD, the results were then published in the following paper: C. Celle, A. Cabos, T. Fontecave, B. Laguitton, A. Benayad, L. Guettaz, Nathalie Pélissier, V. H. Nguyen, D. Bellet, D. Muñoz-Rojas, J.-P. Simonato, Nanotechnology **2018**, 29, 085701.[171] However, in the next parts, only results related to AgNWs will be discussed.

### 5.1.1 Experimental section

#### Deposition of AgNW networks

AgNW suspensions in isopropanol were purchased from Seashell technology, USA. The average length of AgNWs was 32  $\mu\text{m}$  while their average diameter was 130 nm. The as-received suspensions, with initial concentration of 10 mg/ml, were diluted to various concentrations and then deposited on Corning glass (C1737-S111) substrates using spin coating at room temperature. The substrates were cleaned through a sonication in acetone, then rinsed in isopropanol, then washed with distilled water and finally dried with  $\text{N}_2$  gas before AgNW deposition. Deposition parameters (nanowires solution concentration, rotating speed of the spin coater and dispensing rate) and post-deposition thermal annealing parameters (temperature and duration) were optimized to obtain highly transparent (~90 % transmittance) and highly conductive (~10  $\Omega/\text{sq}$  sheet resistance) AgNW networks. The best electrical-optical properties of AgNW networks were obtained by spin-coating 1 ml of suspension (0.5 mg/ml, in two stages of 0.5 ml each with a 20 s pause between them, allowing the surface to dry) over 2.5 cm x 2.5 cm corning glass substrates at ambient atmospheric conditions using a spin-coater with rotation of 1500 rpm. The optimal post-deposition thermal annealing (250 °C for 30 minutes) step is

necessary to desorb the organic residues and to decrease the electrical resistance of the junctions between adjacent AgNWs.[164] A second set of samples was deposited for performing isothermal annealing tests and to test the electrical stability using different voltage ramps. In this case, the diameter of NWs was around 90 nm and the lengths could vary from 10 to 20  $\mu\text{m}$ . The initial suspension was diluted to 0.2 g/L prior to deposition. An airbrush infinity CR was used to spray NWs on Corning glass substrates. During deposition, a  $\text{N}_2$  flow at 3 bar was used, and the airbrush scanned the substrate in the X-Y direction for 15 cycles. The substrates were kept at 90 °C during the deposition. The as-deposited samples were annealed at 230 °C for 1 h to minimize the electrical resistance and ensure intimate junction between adjacent AgNWs.

### Thermal and electrical stability studies

The stability of AgNW networks was assessed through *in situ* measurement of the network electrical resistance during either thermal or voltage ramps by using a two-probe setup with a Keithley 2400 sourcemeter. Thermal stability was studied by subjecting the AgNW networks to thermal ramps from room temperature to 500 °C at a rate of 2 °C/min. Isothermal test at 320 °C for 1 hour were also performed. The electrical stability of the networks was measured in two ways. In the first constant voltage ramp at a rate of 0.1 volt/min, were applied up to specimen failure (i.e. when the electrical resistance diverged) to samples coated with different ZnO thicknesses (the networks used were fabricated using the AgNWs with an average diameter of 130 nm). In the second, equivalent networks made using the AgNWs with average diameter of 90 nm were coated with 25 nm of ZnO and different voltage ramps were applied, namely, 0.05, 0.075 and 0.1 V/min. To assess the use of these AgNW networks as transparent heater, different voltages were applied while the temperature of the samples was measured *in situ* using a thin resistance temperature detector (RTD) embedded in a 120  $\mu\text{m}$  thick PET layer, therefore limiting thermal inertia. The RTD was placed in thermal contact with the sample, below the substrate (details on the setup have been reported previously).[153, 158]

#### 5.1.2 Effect of ZnO coating on adhesion and transparency of AgNW networks

A SEM image of the bare AgNWs annealed at 250 °C for 30 minutes is shown in Figure 5.1a), where effective sintering of the wires at the junctions is clearly visible. A coated AgNW network with a 30 nm thick ZnO coating deposited with AP-SALD is shown in the SEM image in Figure 5.1b). The distinct morphology of the ZnO coating can be observed both on the nanowires and the glass surface. As shown in the figures, the surface of the bare nanowires

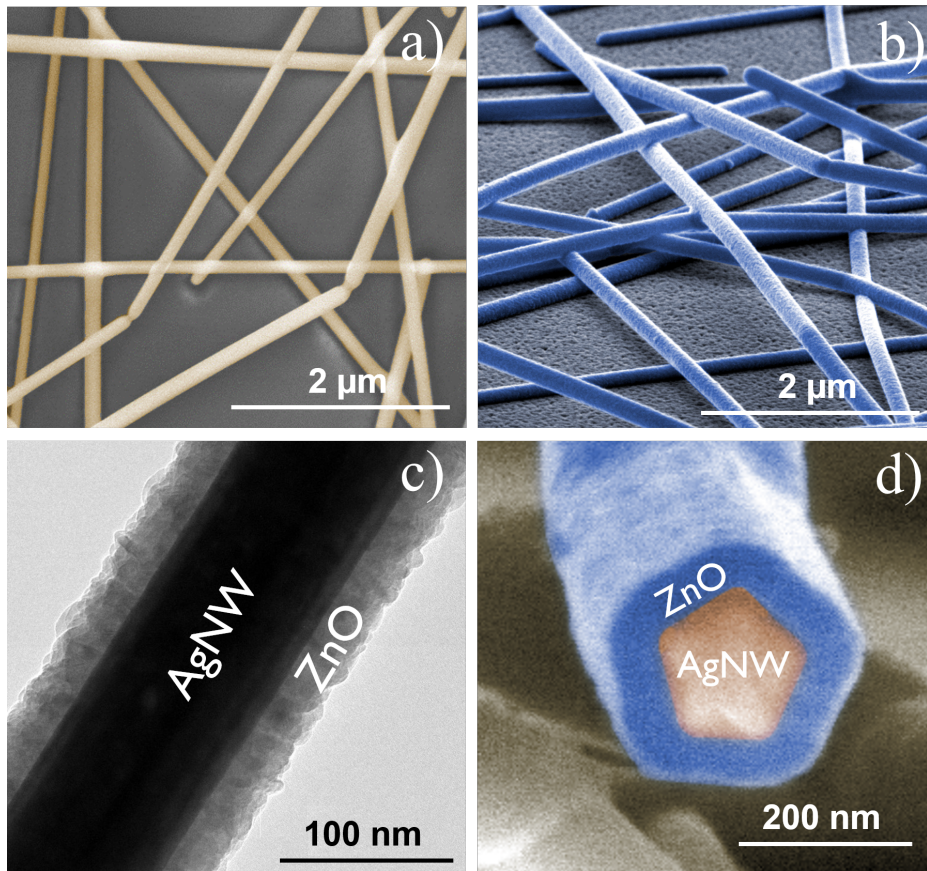


Figure 5.1: (a) Scanning electron microscopy (SEM) image of the AgNW network deposited by spin coating and annealed at 250 °C for 30 minutes to sinter the junctions, (b) SEM image of AgNW networks coated with 30 nm of ZnO deposited with AP-SALD. (c) Transmission electron microscopy (TEM) image of a 30 nm thick ZnO coated AgNW, (d) Back scattered SEM image of a coated AgNW (allowing to highlight the elemental contrast) showing the usual fivefold symmetry twinning of AgNWs surrounded by a uniform 30 nm thick ZnO layer.

appears smooth while that of ZnO-coated AgNWs shows the typical granular morphology of ZnO coatings deposited by AP-SALD.

A transmission electron microscopy (TEM) image of a 30 nm coating of ZnO on a AgNW is shown in Figure 5.1c). Such coating appears very conformal: this point is crucial since this is a prerequisite for an efficient protection against any instability. Figure 5.1d) shows a back scattered SEM image of a ZnO coated AgNW which enables to highlight the elemental contrast: the usual fivefold symmetry twinning of AgNWs is well seen, as well as the surrounding uniform ZnO layer. Again the conformal and continuous aspect of the coating appears in a very clear way in this image. Before focusing on the effects of ZnO coating on electrical and thermal stability of AgNW networks, we first consider the effects on both the network

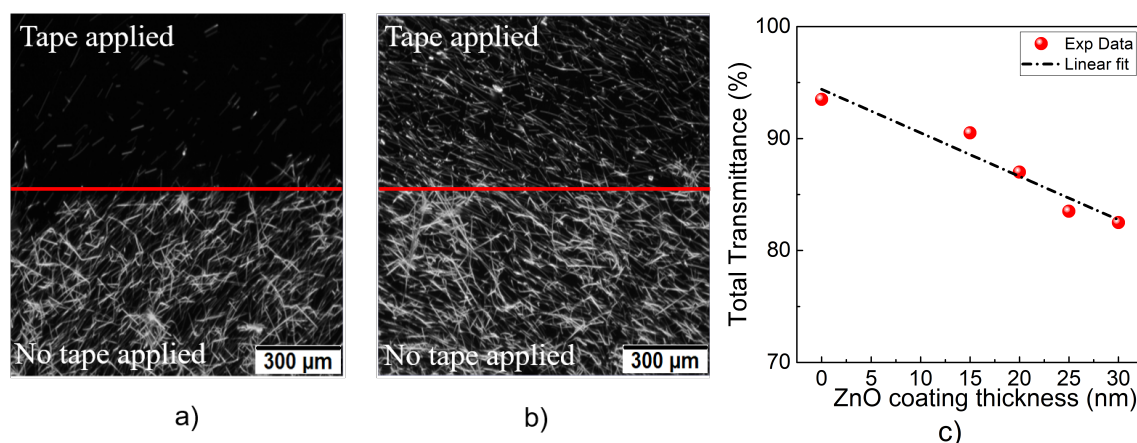


Figure 5.2: (a-b) Optical microscope images of the bare and the AgNW network coated by a thin layer (30 nm) of ZnO, respectively, showing the effect of the scotch tape test. The upper (lower) half is the region where tape was (not) applied; (c) Transmittance of AgNW networks at 550 nm (after subtraction of the glass substrate transmittance) versus the ZnO coating thickness deposited by AP-SALD. Increase in thickness of the ZnO coating results in a linear decrease of the transmittance.

adhesion and optical transparency. It is known that low adhesion of AgNW networks to the substrate can be one of the drawbacks of these materials when used as TE: even a gentle rub can remove nanowires from the substrate. The influence of the AP-SALD ZnO coating on the adherence of AgNW network on the glass substrate was thus investigated. To do so, a scotch tape test was applied to both the bare and the coated networks to qualitatively compare their adhesion strength to the substrates.

Figure 5.2a) and 5.2b) show the optical microscope images of the bare and the ZnO coated AgNWs networks at the edge of the locations where the tape was applied. The upper parts in the figures correspond to the areas in which the scotch tape test was applied, while the lower parts correspond to areas outside the tested zone. Figure 5.2a) corresponds to the bare AgNWs, while Figure 5.2b) corresponds to the ZnO coated AgNWs. It can be clearly seen from Figure 5.2a) that for bare AgNW networks most of the nanowires are removed, showing the very low adhesion of the bare AgNWs to the substrate. Conversely, Figure 5.2b) shows that for coated networks numerous nanowires remained on the substrate, thereby showing a clear improvement in AgNWs adhesion to the substrate. The low resistance of the networks was also maintained after the tape test, while for uncoated networks the resistance after the tape test was 3 orders of magnitude higher ( $k\Omega$ ).

The effect of the ZnO coating on electrode transparency was also evaluated. Figure 5.2c) reports the influence of the ZnO coating thickness on the optical transparency (measured for a wavelength of 550 nm) of coated AgNW networks. Note the network transmittance is mea-

sured after subtracting the substrate contribution, as explained in Lagrange's et al. article.[158] In a first approximation a linear decrease of optical transparency from 93.5 % to 82.5 % can be observed (as expected for a linear expansion of an exponential function close to unity). For an optimized integration of coated AgNW network a compromise should be considered, depending on the application targeted. Indeed, as seen below, a thicker ZnO coating is associated to a more efficient thermal and electrical stability but at the expenses of optical transparency. This slight decrease of optical transparency is nevertheless still acceptable for many applications. Finally it is worth noting that the electrical resistance of the AgNW network remains similar, within experimental incertitude, before and after ZnO coating.

### 5.1.3 Effect of the ZnO coating on the electrical and thermal stability of AgNW networks

For all considered applications, both electrical and thermal instabilities of AgNW networks can be a key issue for their efficient integration into real devices, since this could drastically reduce the lifetime of the TE and thus of the associated device. The effect of a ZnO coating on the electrical and thermal stabilities of the AgNW networks has been evaluated as a function of the thickness of the ZnO coating. In this regard, there is no universal definition of metallic network stability. In the present work, we define the stability of an AgNW network (during either thermal or voltage ramps) as a domain of variation of voltage or temperature where the change of network resistance is reversible. Inversely the instability can be observed when the electrical resistance suddenly increases during a ramp from few tens of Ohms to more than  $10^4 \Omega$ . We first consider thermal stability and then the electrical stability. Similar AgNW networks were spin-coated on Corning glass substrates, then ZnO coatings of various thicknesses were deposited by AP-SALD. The initial electrical resistance of each specimen was similar with an average value of  $12.1 \Omega$  and a standard deviation of  $2.1 \Omega$  regardless the ZnO layer thickness. The stability of AgNW networks to high temperatures was investigated during thermal ramps from room temperature to  $500 \text{ }^\circ\text{C}$  at a heating rate of  $2 \text{ }^\circ\text{C}/\text{min}$ .

Figure 5.3a) shows that in all cases AgNW networks exhibit a slight linear increase of resistance with temperature, which is related to the electron-phonon interaction. For bare AgNW networks and those coated with a thin ZnO layer, this linear dependence is then followed by a very sharp increase of the electrical resistance. This last feature stems from a non-reversible phenomenon which leads to the spheroidization of the AgNWs (the driving force being the total surface energy reduction). This morphological instability is called the Plateau-Rayleigh instability and has been already well described in the case of metallic nanowires.[158, 164] The spheroidization is at the origin of the loss of the electrical percolating nature of the net-

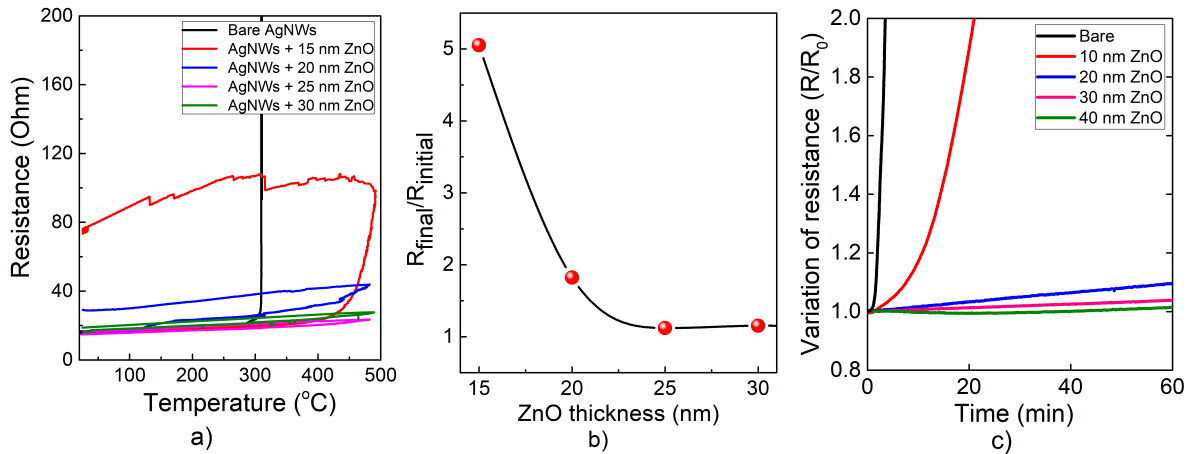


Figure 5.3: a) Variation of electrical resistance ( $R/R_0$ ) of bare and ZnO coated AgNW networks measured during thermal ramps from room temperature to 500 °C with a heating/cooling rate of 2 °C/min. (b) Ratio between final and initial resistances of AgNW networks, respectively, after and before the thermal ramp up to 500 °C. Increasing the thickness of the ZnO coating increases the thermal stability, and thus the electrical resistance reversibility. (c) Relative variation of resistance of bare and ZnO coated AgNW networks measured at constant temperature of 320 °C versus time.

work, which can then be observed through the sharp divergence in electrical resistance for some specimens. Figure 5.3a) clearly shows that by increasing the thickness the ZnO coating, higher temperatures can be achieved before the instability is observed. For instance, a bare AgNW network deteriorates at 315 °C while the AgNW network coated with ZnO of at least 25 nm can sustain temperatures up to 500 °C while showing finite electrical resistance. In particular, networks coated with only 15 nm show a resistance that is 5 times the original one after undergoing the thermal ramp. With 20 nm of ZnO coating, the increase of resistance goes down to 1.8 times the original value. Finally, for 25 nm and thicker coatings, the final resistance after the thermal ramp is only 1.1 times higher than the initial value. The effect of the thickness of the ZnO coating appears quite evident in terms of resistance reversibility. In order to assess the network thermal stability by another method, the resistance of the networks was measured versus time at constant temperature (320 °C). This feature can be observed in Figure 5.3c), where the variation of electrical resistance  $R/R_0$  is plotted against time during an annealing at 320 °C for specimens associated to several ZnO coating thicknesses. Clearly, increasing the thickness of the ZnO coating enhances the stability of the network. A ZnO layer with thickness of 20–30 nm appears sufficient to maintain a constant electrical resistance. In a similar approach, we subjected the networks to electrical stress to study their electrical stability.

Figure 5.4a) reports the variation of the electrical resistance of bare and coated (different

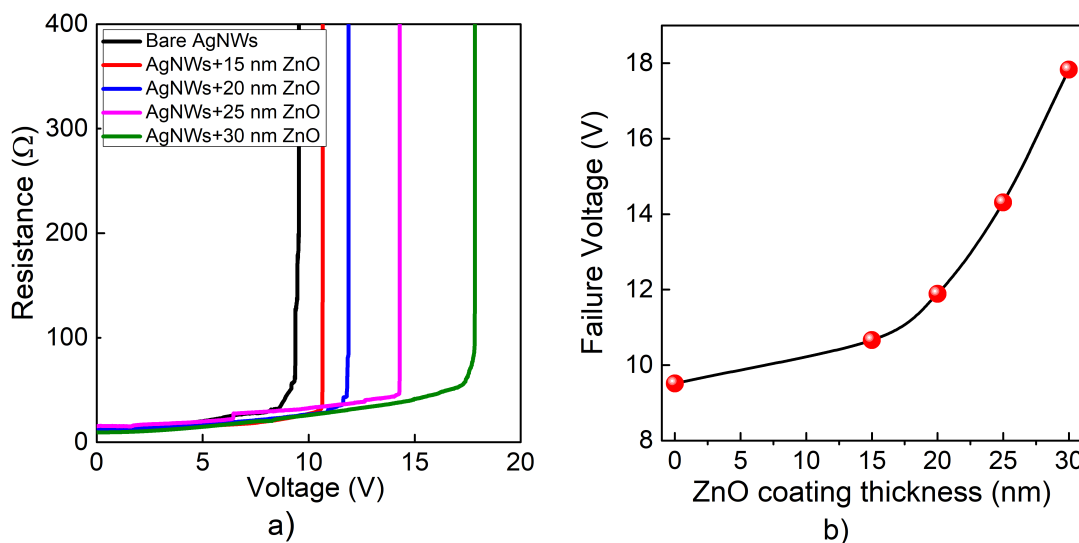


Figure 5.4: (a) Variation of electrical resistance for bare and ZnO coated AgNW networks subjected to voltage ramps of 0.1 V/min. The bare AgNW network shows failure at around 9 V, while the stability of ZnO coated AgNW networks increases with increasing ZnO coating thickness reaching up to 18 V for 30 nm of ZnO coating. (b) Failure voltage limit dependence versus ZnO coating thickness. A clear, nonlinear increase of the failure voltage versus ZnO layer thickness is observed (the line is a guide to the eye).

thicknesses) AgNW networks versus applied voltage during a voltage ramp of 0.1 V/min. In all cases a slight increase of the electrical resistance versus voltage is observed at low voltage. The origin of such a resistance increase is the Joule effect: when an electric current flows through the network the temperature of the latter rises and so does the electrical resistance, due to the electron-phonon interactions. This evolution is reversible, at least when low voltages are considered. For larger voltages, the network can exhibit an electrical failure which is associated with a sudden and non-reversible increase of the electrical resistance. The resistance curves obtained during the *in situ* electrical measurements displayed in Figure 5.4a) again show that increasing the thickness of the ZnO coating allows to reach higher voltages before failure takes place. This is similar to what has been observed above when considering the thermal stability. While bare networks show failure at around 9 volts, the stability of ZnO coated networks reaches up to 18 V for 30 nm of ZnO coating, which corresponds to a 100% increase of the associated voltage failure. Figure 5.4b) shows the voltage failure dependence versus ZnO thickness. This clearly shows that the ZnO coating enhances efficiently the electrical stability of AgNW networks. As in the case of the thermal stability enhancement provided by the coating, the electrical stability enhancement does not show a linear relationship with ZnO thickness.

In a recent work by M. Lagrange,[153] a physical model estimating the link between the

average electrical current density  $\langle j \rangle$  and the voltage  $V$  applied between two opposite electrodes separated by a distance  $W$  was reported. The relation can be written as follows:  $\langle j \rangle = 2V/(\pi\rho W)$  where  $\rho$  is the electrical resistivity of an AgNW. Therefore, from the voltage values observed in Figure 5.4, one can deduce that the current density at failure varies between  $1.6 \times 10^{10}$  A/m<sup>2</sup> for non-coated AgNW and  $3.2 \times 10^{10}$  A/m<sup>2</sup> for AgNW coated with ZnO. Such values of electrical current density are associated at the network level where enough AgNW have undergone a failure. These values at the network level can be compared with the one observed by Stahlmecke et al.,  $35 \times 10^{10}$  A/m<sup>2</sup>, for which void formation within an individual AgNW was clearly observed due to electromigration.[172] The fact that the current density associated with the network failure is lower than the one observed by Stahlmecke et al. might indicate that the AgNW associated with smaller diameters degrade first, or areas of the networks with the lower-than-average nanowire density.

#### 5.1.4 Rationalization of the effect of the ZnO coating on the stability of AgNW networks

The origin of the nanowire Plateau-Rayleigh instability has already been reported several times, both for metallic nanowires and as well for other types of nanowires.[173] The main driving force at the origin of such instability is the reduction in total surface energy. Figure 5.5a) shows a simple schematic representation of a junction between two AgNWs. When subjected to a thermal annealing or a voltage ramp (the Joule effect increasing the temperature of the network), the junction undergoes a morphological evolution which aims at decreasing its total surface energy. The consequence is local sintering, and therefore the junction resistance is lowered, as well as the network electrical resistance. Figure 5.5b) and 5.5c) illustrate such morphological changes at different stages of the treatment: the first one leads to the minimum electrical resistance (local sintering) of the junction while the second one is associated to the onset of network degradation (with local junction breakage probably at the hottest points of the AgNW network). An example of actual morphological instability is presented in Figure 5.5d), which shows a SEM picture of a AgNW network subjected to an electrical load or to a thermal annealing close to the failure limit (before a complete spheroidization). All these morphological modifications are possible provided atomic surface diffusion can take place. But such atomic diffusion can be hindered by an oxide coating. This is the reason, for instance, why sintering of metallic powder is operated in a reductive atmosphere (often with presence of hydrogen)[174, 175], to prevent the formation of surface oxide layer that would prevent the sintering. A thin interfacial SiO<sub>2</sub> layer is also known to weaken the thermal diffusion of metallic boron or arsenic into silicon.[176, 177] Figure 5.5e) exhibits a schematic represen-

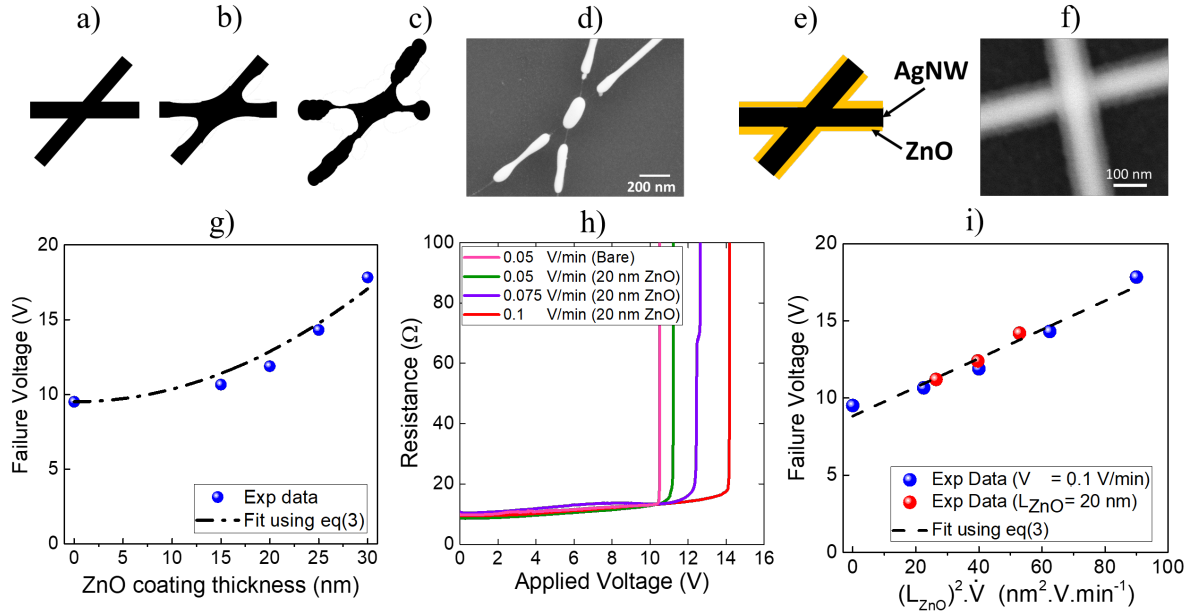


Figure 5.5: Schematic representation of a junction between two adjacent AgNWs for a) as-deposited junction, while b) shows a local sintering and c) the beginning of the deterioration of the junction that will eventually (if the thermal or electrical load continues) lead to the deterioration of the network. d) SEM image of a junction within a AgNW network after thermal or electrical load just before the failure point. e) A very thin and conformal ZnO coating (of thickness  $L_{ZnO}$ ) over a junction is schematically represented. f) SEM image of an intact junction coated with ZnO. g) Dependence of the experimental failure voltage versus the ZnO coating thickness, measured during a voltage ramp, as well as the calculated values using eq. 5.3, showing a good agreement (the rate of voltage increase,  $\dot{V}$ , is 0.1 V/min). h) Resistance versus voltage for voltage ramps with different  $\dot{V}$  values for ZnO coated samples (25 nm in all cases). i) Dependence of the experimental network failure voltage versus the product of  $\dot{V}$  and  $(L_{ZnO})^2$ , as well as the theoretical values from eq. 5.3, again showing a good agreement.

tation of the coated nanowires studied here (Fig 5.1c) and 5.1d)) while Figure 5.5f) shows a SEM image of a AgNW coated with 25 nm ZnO. Based on the above arguments dealing with atomic surface diffusion, a simple way to estimate the effects of the ZnO coating on the AgNW network stability can be considered in terms of failure time  $t^{fail}$ . Let us consider the electrical stability and the effect on it of a ZnO coating (of a certain thickness  $L_{ZnO}$ ) as reported in Figure 5.4. The failure time  $t^{fail}$  will be directly associated to a failure voltage  $V^{fail}$  during a voltage ramp through:  $V^{fail} = \dot{V} \cdot t^{fail}$  where  $\dot{V}$  is the voltage increase ramp.

While the thermal failure of AgNWs is associated to AgNW morphological changes caused only by the Plateau-Rayleigh instability, for electrical failure both electromigration and/or local heating can cause deterioration (very probably locally within the network close to resis-

tive junctions between adjacent AgNWs). These two physical mechanisms are as well controlled by surface diffusion for the low AgNW diameter involved here (130 nm). For coated nanowires, atomic surface diffusion is partially delayed because silver atoms should first diffuse through the thin oxide layer before the deterioration of the junction can start occurring. Since the ZnO coating induces an increase of the failure time (see Figure 5.4b)), then  $t^{fail}$  dependence with ZnO coating thickness ( $L_{ZnO}$ ) can be written as follows:

$$t^{fail}_{coated\ AgNW}(L_{ZnO}) = t^{fail}_{bare\ AgNW} + \Delta t^{fail}(L_{ZnO}) \quad (5.1)$$

where  $t^{fail}_{bare\ AgNW}$  and  $t^{fail}_{coated\ AgNW}$  are the failure time (for which the AgNW network electrical resistance is diverging) for bare AgNW and ZnO coated AgNW networks, respectively. As shown schematically in Figure 5.5,  $t^{fail}_{bare\ AgNW}$  can be associated to the time (or voltage during a voltage ramp) required for Ag atoms to undergo enough displacement enabling the morphological instability of bare AgNW. When an AgNW is coated with a thin oxide layer, the additional diffusion of Ag atoms through the thin oxide layer induces a delay, noted  $\Delta t^{fail}(L_{ZnO})$ . By using the basic diffusion laws in first approximation, the latter is directly dependent on the oxide layer thickness  $L_{ZnO}$  through:

$$L_{ZnO} = \sqrt{2 \cdot D \cdot \Delta t^{fail}(L_{ZnO})} \quad (5.2)$$

where  $D$  is the diffusion coefficient of Ag atoms through the oxide barrier. Therefore this simple model would lead to a voltage failure versus ZnO coating thickness  $L_{ZnO}$  given by:

$$V^{fail}_{coated\ AgNW}(L_{ZnO}) = V^{fail}_{bare\ AgNW} + \frac{\dot{V} L_{ZnO}^2}{2D} \quad (5.3)$$

where  $\dot{V}$  is the voltage rate associated to the voltage ramp (equal to 0.1 V/min). Figure 5.5g) reports the same experimental data as already presented in Figure 5.4b) along with a fit using eq.5.3. Despite the simplicity of the model, the agreement appears very good between the model and experimental data. The only unknown parameter in eq.5.3 is the diffusion coefficient  $D$  of silver atoms through ZnO oxide. The fit presented in Figure 5.5g) yields a  $D$  value of  $7.4 \times 10^{-16} \text{ cm}^2/\text{s}$ . The comparison between this  $D$  value and the ones reported in literature is not trivial since the diffusion coefficient depends drastically on: i/ the structural properties of the oxide (presence of defects such as grain boundaries or voids) which themselves depend on the growth experimental conditions, and ii/ temperature since diffusion is a thermally activated process. The diffusion coefficient of Ag atoms in ZnO,  $D$ , has a very low value since Ag ion has a low solubility limit in ZnO at equilibrium. This stems from the different valence states of Ag ion and Zn as well as from the larger Ag ionic radius when compared with Zn. Sakaguchi et al. investigated the diffusion of Ag in polycrystalline ZnO in the temperature range 700-

900 °C. They found a Ag diffusion coefficient in ZnO equal to  $7.4 \times 10^{-13} \text{ cm}^2/\text{s}$  at 900 °C. For a lower temperature range, McBrayer et al. studied metal diffusion in SiO<sub>2</sub> oxide layers and reported a Ag diffusion coefficient  $D$  equal to  $10^{-15} \text{ cm}^2/\text{s}$  at 221 °C, which is typically the measured temperature associated to the AgNW network failure. These  $D$  values from the literature are thus in agreement with the value obtained from our model 5.3 (see Figure 5.5g)). According to our model, the failure voltage should also be affected by the value of  $\dot{V}$ , i.e. the rate at which the voltage is increased. Thus, in order to further test the validity of the model, we also performed voltage ramps using different  $\dot{V}$  values on networks coated with 25 nm of ZnO. As shown in Figure 5.5h), a steep increase in resistance at about 11 V is observed when using a  $\dot{V}$  of 0.05 V/min. For faster voltage ramps, the failure voltage increased from 12 V for a  $\dot{V}$  of 0.075 V/min to over 14 V for  $\dot{V}$  of 0.1 V/min. Figure 5.5i) shows the failure voltage versus the product  $\dot{V}L_{\text{ZnO}}^2$ , with data both from constant voltage ramps with different ZnO thicknesses (Figure 5.4a)) and from voltage ramps with different rates (Figure 5.5h)). Again, the agreement appears very good between the model and experimental data, so if one takes into account that the networks used in both cases (Figure 5.4a) and Figure 5.5h)) were fabricated using AgNWs with different diameter and lengths, and with different deposition methods (spin-coating vs. spray-coating), respectively, as detailed above.

### 5.1.5 Evaluation of the performance of transparent heaters based on ZnO coated AgNWs

One key characteristic of AgNW networks when used for transparent heater applications is their electrical non-reversibility after applying voltage ramps or voltage plateaus. To assess the reversibility of the electrical resistance of bare and ZnO coated AgNW networks, voltage plateaus were applied at 1, 3, 5, 7, 5, 3 and 1 V with a duration of 45 minutes each. Figure 5.6a) shows an *in situ* measurement of electrical resistance of the studied AgNW networks. The bare AgNW network clearly shows a continuous degradation especially for the largest voltage plateau (7 V) with a continuous observed increase of the resistance with time. Conversely, a ZnO coated network (25 nm thick) became reversible and stable under the same conditions. Another way of demonstrating these effects is to plot the measured electrical resistance versus temperature. As shown in Figure 5.6b), the ZnO coating has clear positive effects on the reversibility of the electrical resistance when compared with the bare network. Interestingly, Figure 5.6b) shows that AgNW networks, if well protected against morphological instability, can not only be used as transparent heaters but as well as a transparent temperature sensors.

Thanks to the positive effects of the ZnO coating, which increases the voltage failure limits, the heating capability of AgNW network can be enhanced. One such example is shown

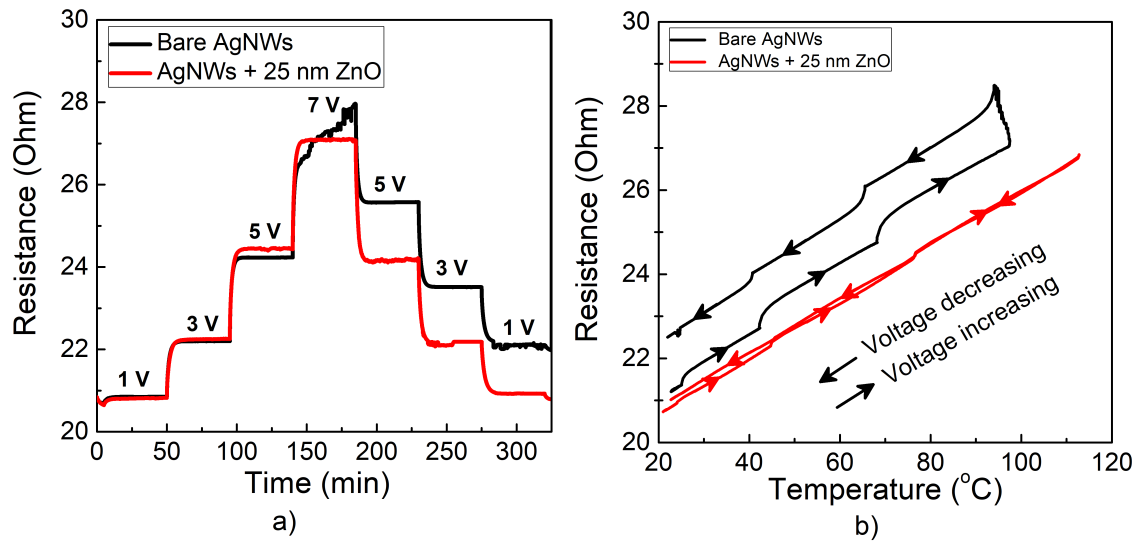


Figure 5.6: (a) Electrical resistance of AgNW networks measured versus time during voltage plateaus of 1, 3, 5 and 7 V applied to the bare and ZnO coated networks. Each plateau was 45 minutes long, and the whole series then reversed. (b) Dependence of electrical resistance versus temperature measured during voltage plateaus of 1-3-5-7-5-3-1 V for both bare and ZnO coated (25 nm) networks. A much better stability is observed for the ZnO coated network.

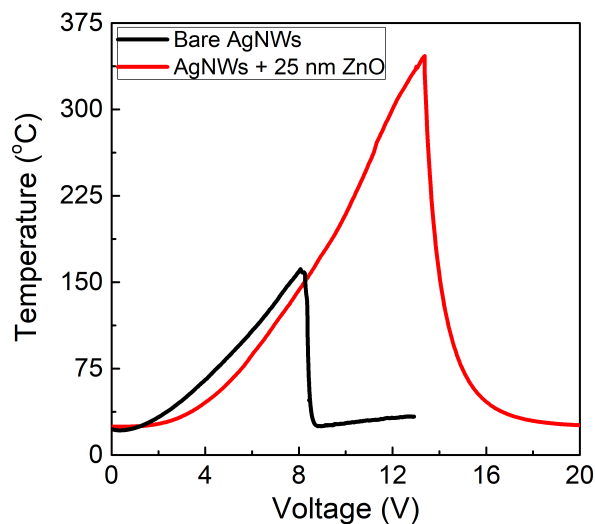


Figure 5.7: Measured temperature versus voltage during a voltage ramp of 0.1 V/min for bare and coated AgNW networks, the latter being associated to a 25 nm thick ZnO coating. The bare AgNW network exhibits an electrical failure at about 8 volts while the coated AgNW network can undergo a voltage up to 14 volts and can therefore remain a transparent heater at much higher temperature.

in Figure 5.7, where for a voltage ramp of 0.1 V/min the bare AgNW network degraded at around 8 V and the corresponding maximum temperature measured was 150 °C. Conversely, the network protected by a 25 nm thick ZnO coating degraded at around 14 V and the related corresponding maximum temperature was 350 °C (an increase of a 133%). The maximum temperature limit can therefore be drastically enhanced thanks to the ZnO coating over the AgNWs since atomic surface diffusion can be partially delayed.

## 5.2 ZnO:Al/AgNW nanocomposites

As seen in the previous section, bare AgNW networks suffer from thermal and electrical instabilities, requiring an effective and conformal protective layer. We have also seen in Chapter 4 that ZnO:Al films deposited by AP-SALD are still relatively resistive ( $\rho \sim 3 \times 10^{-3} \Omega cm$ ) as compared to the conventional TCM, i.e. ITO ( $\rho \sim 10^{-4} \Omega cm$ ), or to FTO ( $\rho \sim 3 \times 10^{-4} \Omega cm$ ) developed by Rey et al. in our laboratory.[178] Additionally, bare AgNW networks are not continuous in matter, therefore, they cannot act as an effective collection layer in photovoltaic applications (because of gaps between nanowires) nor as an effective injection layer (for LED applications), or an antireflective window (in silicon based solar cell for example). In order to overcome the instability and discontinuity drawbacks of AgNW networks, as well as the modest conductivity of ZnO:Al thin films prepared by AP-SALD, we have explored the idea of fabricating a high-performance TCM based on ZnO:Al thin film and AgNW network, hereafter called ZnO:Al/AgNW nanocomposites, in which a thin ZnO:Al layer ( $\sim 100 \text{ nm} - 150 \text{ nm}$ ) is deposited on the top of the AgNW network. The results obtained are presented in this section.

Figure 5.8 shows SEM images of a bare AgNW network (left) and a ZnO:Al/AgNW nanocomposite (right, with 100 nm thick ZnO:Al film deposited on the AgNW network) under the electron beam. The charge effect in the case of bare AgNWs can be clearly observed, but not for ZnO:Al/AgNW nanocomposite. Charging of the bare AgNW sample takes place in the open area of the AgNW mesh resulting in an electron beam induced potential contrast. The electrons accumulated at the free space between nanowires cannot be collected by the AgNW network since the bottom glass substrate is insulator, while by depositing 100 nm thick ZnO:Al thin films on top of the network, the electron collection is clearly more efficient. This visualization is actually rather similar to the case of a solar cell, in which the photogenerated charges in the bottom active layers need to be collected by the TCMs.

ZnO:Al/AgNW nanocomposites have been already considered by a few groups,[179–181] in whose works, the optical and electrical performances of the nanocomposite have been reported. According to our knowledge, the electrical properties of the bare AgNW network have

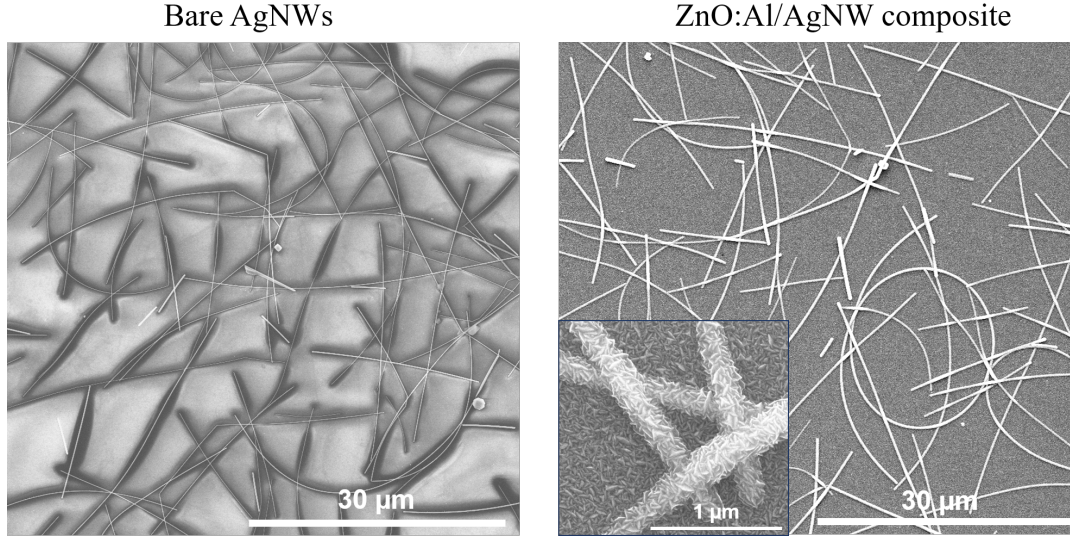


Figure 5.8: SEM images of a bare AgNW network (left) and a ZnO:Al/AgNW nanocomposite (right, with 100 nm thick ZnO:Al film) under electron beam having an acceleration voltage of 10 kV. The charge effect in the gaps between AgNWs can be clearly observed in the case of bare AgNWs. The inset image on the right illustrates the similar ZnO:Al morphology obtained on glass and on AgNWs.

been rather well investigated in the literature, while the conductivity of a nanocomposites such as ZnO:Al/AgNWs has not been studied yet. The study presented here consists of fabricating and studying networks of AgNWs of different density, and to investigate its physical properties either as bare AgNWs on a glass substrate, or when coated by a thin ZnO:Al layer. The role of the AgNW network density will be considered as a main parameter.

The electrical conductivity of a AgNW network originates from the percolation phenomenon. The percolation theory states that rather close to the percolation threshold (i.e. when the network density  $n$  ( $m^{-2}$ ), defined as the number of AgNWs per unit area, is just above the critical density  $n_C$ ), the electrical resistivity of the network,  $\rho$ , is proportional to  $(n - n_C)^{-\gamma}$  for which  $\gamma$  is found to be in the range [1.23, 1.43], and often considered equal to 1.29 or 4/3.[182] Therefore, if the network electrical resistance is noted  $R(n)$ , we can write:

$$R(n) \sim \rho_{AgNW} (n - n_C)^{-\gamma} \quad (5.4)$$

where  $\rho_{AgNW}$  refers to the electrical resistivity of one single AgNW, which can be calculated from the resistivity of bulk silver,  $\rho_{bulk}^{Ag}$ , the nanowire diameter,  $D_{NW}$ , and the bulk silver mean free path,  $\Lambda$ , as follows:[158, 183]

$$\rho_{AgNW} = \rho_{bulk}^{Ag} \left( 1 + \frac{\Lambda}{2D_{NW}} \right) \quad (5.5)$$

The expression for  $R(n)$  has been successfully used for instance by Lagrange et al.[158] and by Langley et al.[184] with  $\gamma = 4/3$  or  $= 1.29$ , respectively (in this work, we considered that  $\gamma = 1.29$ ). In order to avoid any confusion,  $n$ , which was used to denote the electron concentration in the ZnO:Al films, will be replaced from now by the areal mass density  $amd$  ( $mg/m^{-2}$ ) (defined as the AgNW density  $n$  times the average mass of one single AgNW).

### 5.2.1 Model of two parallel resistances

The first model considered here uses this percolation theory for, on one side, the AgNW network on the insulating bare glass, and on the other side for a AgNW network with a ZnO:Al thin layer. In this case, we can in a first approximation consider that the AgNW network and the ZnO:Al layer are two resistances in parallel. For this model, we assume that:

1. The AgNW network density ( $amd$ ) is constant over the whole sample, which means that there is no spatial distribution of  $amd$
2. There is no contribution of the AgNW network to the total conductivity of the nanocomposite if the  $amd$  is lower than  $amd_C$

Therefore, if  $amd \leq amd_C$ ,  $R_{nanocomposite} = R_{ZnO:Al}$ , and if  $amd > amd_C$ , we can then write:

$$R_{AgNW} = K\rho_{AgNW} (amd - amd_C)^{-\gamma} \quad (5.6)$$

$$R_{nanocomposite} = \left[ \frac{1}{K\rho_{AgNW} (amd - amd_C)^{-\gamma}} + \frac{1}{R_{ZnO:Al}} \right]^{-1} \quad (5.7)$$

where  $K$  is a parameter (which contains the specimen size and shape),  $R_{ZnO:Al}$ ,  $R_{AgNW}$  and  $R_{nanocomposite}$  refer to the resistances of a standalone ZnO:Al thin film, the bare AgNW network and the ZnO:Al/AgNW nanocomposite, respectively. Eq. 5.6 and eq. 5.7 are only valid if  $amd > amd_C$ . Conversely, if  $amd < amd_C$ , i.e. the bare AgNW network is not percolating, the resistance of the bare AgNW network is considered, in this first model, as infinite. Therefore, thanks to these two equations, one can fit the experimental data, respectively for bare AgNW networks and for ZnO:Al/AgNW nanocomposites with only one fitting parameter:  $K$ . Both experimental and fit curves are reported on Figure 5.9.

The agreement between both curves appear rather good knowing that the used model is very simple and only one fitting parameter,  $K$ , has been considered. The value of  $K$  used for the fits is:  $7.88 \times 10^{10}$ . The main disagreement appears for an  $amd$  lower but close to  $amd_C$ , which is quite normal since the simple model used here does only consider an electrical contribution from AgNW when the latter form a percolating network.

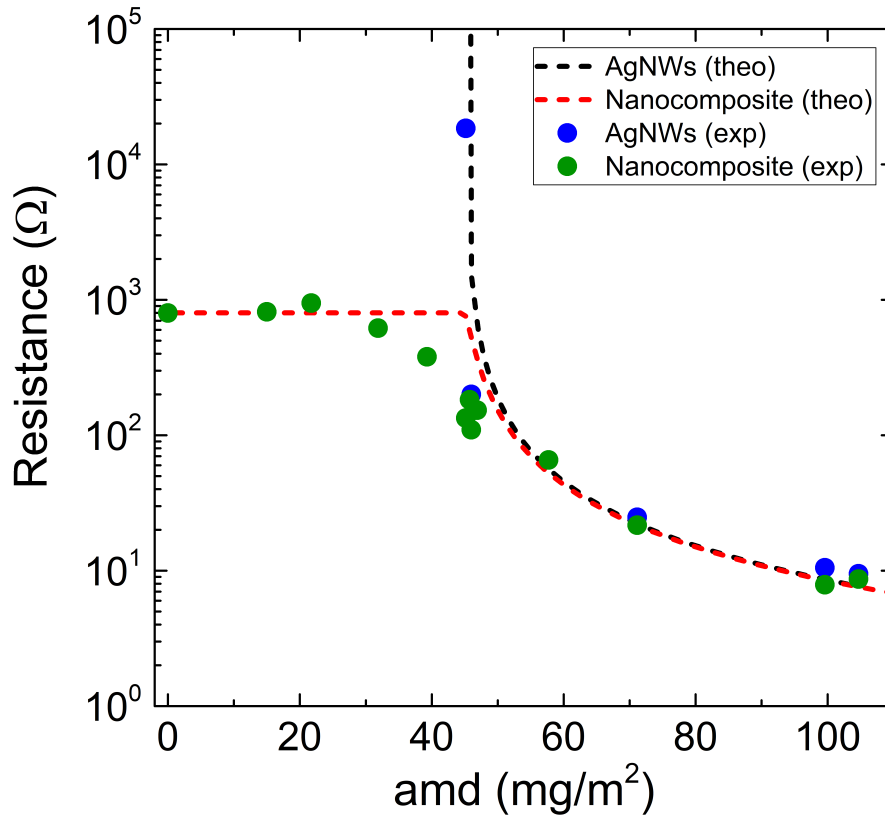


Figure 5.9: Experimental electrical resistance of AgNW network measured during this work versus areal mass density ( $amd$ ) for a network deposited on glass (blue symbols) and for a 100 nm thick ZnO:Al layer grown by AP-SALD deposited above a similar AgNW network (green symbols). The resistance of 100 nm thick ZnO:Al film on glass was 800  $\Omega$ . The fitting curves use eq. 5.6 and eq. 5.7 for the AgNW deposited on glass (black dashed curve) and for the AgNW/AZO nanocomposite (red dashed curve), respectively.

As shown in Figure 5.9, in the case of the bare AgNW networks, the sheet resistance is not measurable until the network becomes percolating, which occurs around an  $amd$  value of  $45 \text{ mg/m}^2$ . This value of  $amd_C$  is to be compared with the theoretical expression. It has been shown for a long time already, thanks to Monte Carlo simulations, that the critical density  $n_C$  associated to the stick percolation occurrence is equal to  $5.64/L_{NW}^2$ , where  $L_{NW}$  is the stick length, and then here AgNW length.[185] The associated  $amd_C$  can be written as follows:

$$amd_C = n_C d^{Ag} \frac{\pi D_{NW}^2}{4} L_{NW} \quad (5.8)$$

where  $d^{Ag}$  is the silver density and  $D_{NW}$  the average diameter of AgNWs. By using the following values:  $D_{NW} = 79 \text{ nm}$ ,  $L_{NW} = 7 \text{ }\mu\text{m}$  and  $d^{Ag} = 10.5 \times 10^3 \text{ kg/m}^3$ , eq. 5.8 leads to a theoretical value of  $42.6 \text{ mg/m}^2$  which is very close to the experimental one ( $45 \text{ mg/m}^2$ ).

### 5.2.2 Model considering the presence of local percolating AgNW clusters below the network percolation threshold

In the previous model, we assumed that the  $amd$  of the AgNW network was constant over the whole surface of the sample, which is actually not valid in practice due to several error sources, either from imperfect deposition system or from the intrinsic statistic properties of the random network itself. Accordingly, the average  $amd$  of the sample could be known by controlling the quantity of AgNWs deposited on the whole sample, however, what cannot be controlled is the  $amd$  at a certain position on the substrate, which is actually a random variable in statistics. As a first approximation, we assume that there is a normal distribution of  $amd$ , with two parameters: the average value of  $amd$  (called  $\overline{amd}$ ) and the standard deviation (called  $\sigma_{amd}$ ). Figure 5.10a) illustrates the probability density (called  $pdf^{\overline{amd}}$ ) and the cumulative probability (called  $cdf^{\overline{amd}}$ ) as a function of  $amd$  (for this simulation,  $\overline{amd} = 45$ ,  $\sigma_{amd} = 8 \text{ mg/m}^2$  were used). These functions  $pdf^{\overline{amd}}$  and  $cdf^{\overline{amd}}$  are associated to a normal distribution of  $amd$  with an average value,  $\overline{amd}$ , and a standard deviation,  $\sigma_{amd}$ . As an example, if we consider a large enough number of small areas on the sample, there will be 79 % of those areas having an  $amd$  in the range of  $[35, 55] \text{ (mg/m}^2\text{)}$ . Figure 5.10b) shows an optical microscope image of a AgNW network deposited on glass by spin-coating. This illustrates a non-negligible spatial distribution of the  $amd$  over the large area of the sample, which confirms our assumption above.

Figure 5.11 illustrates the variation of the numbers of clusters having an  $amd > amd_C = 45 \text{ (mg/m}^2\text{)}$  when increasing the average network density from 35 to 45 ( $\text{mg/m}^2$ ) ( $\sigma_{amd}$  was fixed at  $8 \text{ mg/m}^2$  for this illustration). This simulation was performed by attributing randomly an arbitrary network density  $amd$ , which follows a normal distribution with  $\overline{amd} = 45$ ,  $\sigma_{amd} = 8$

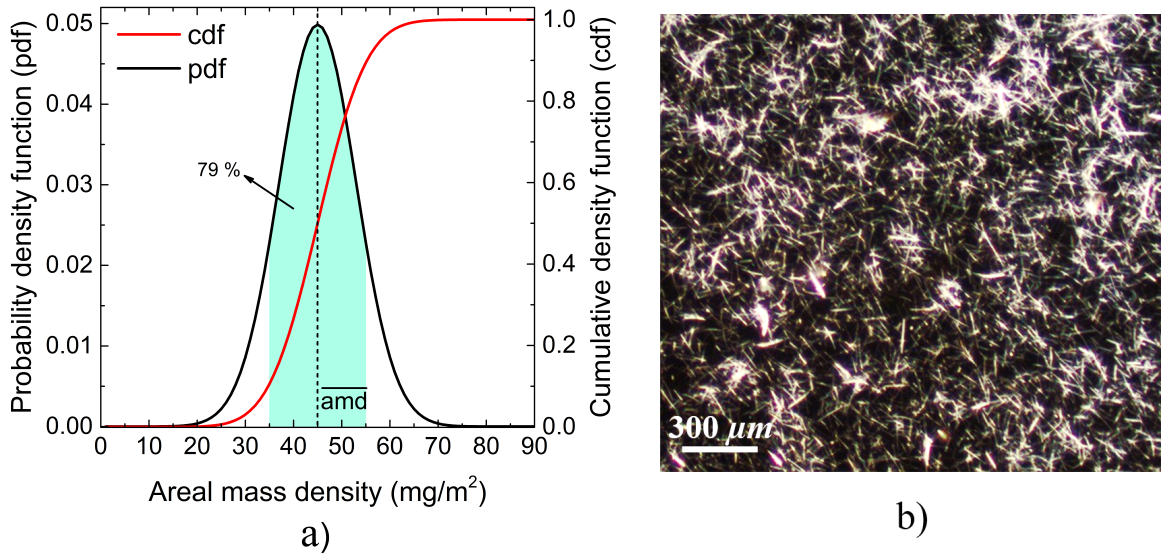


Figure 5.10: a) Illustration of the probability density function (denoted  $pdf^{\overline{amd}}$ , left axis) and the cumulative density function (denoted  $cdf^{\overline{amd}}$ , right axis) as a function of areal mass density ( $amd$ ), the shaded area corresponds to a probability of 79 % of obtaining an  $amd$  in between  $[35, 55]$  ( $\text{mg}/\text{m}^2$ ) (for this **simulation**,  $\overline{amd} = 45$ ,  $\sigma_{amd} = 8$  were used); b) Optical microscope image of a AgNW network deposited on glass by spin-coating (image credit to A. Khan).

$\text{mg}/\text{m}^2$ , to an array of  $m \times m$  small squares of a large square sample (size of  $10 \times 10 \text{ cm}^2$ ). We can clearly observe in Figure 5.11 that even for  $\overline{amd}$  below  $amd_C$ , some percolating clusters can already be formed.

As can be seen, the cluster size is not a constant and the shapes of clusters are pretty complex. As a first approximation, we assume that the nanocomposite is equivalent to a very simple model, as shown in Figure 5.12. Accordingly,  $R_{ZnO:Al}^s$  is a resistance related to the fraction of the ZnO:Al film covering the non-percolating AgNW network (black area in Figure 5.11),  $R_{ZnO:Al}^p$  is a resistance related to the fraction of the ZnO:Al film covering the percolating clusters, which is in parallel with the  $R_{clusters}^p$  (the total resistance of the clusters, bright area in Figure 5.11). In the present case, we have:  $R_{ZnO:Al}^s + R_{ZnO:Al}^p = R_{ZnO:Al} = 800 \Omega$ .

Figure 5.13 shows the density of percolation probability as a function of  $amd$  for the case of a sample having an average  $\overline{amd} = 35$ , and the percolation threshold  $amd_C = 45$ . The probability to have percolating clusters, i.e. a local area on the surface having an  $amd$  greater than  $amd_C$ , is actually equal to the red shaded area in Figure 5.13, and calculated as:  $(1 - cdf^{\overline{amd}}(amd_C))$ . Therefore, the number of percolating clusters is directly proportional to  $(1 - cdf^{\overline{amd}}(amd_C))$ . On the other hand, because the percolating clusters do not have the same  $amd$ , but again, distributed from  $amd_C$  to  $\infty$ , we assume that all these clusters have an

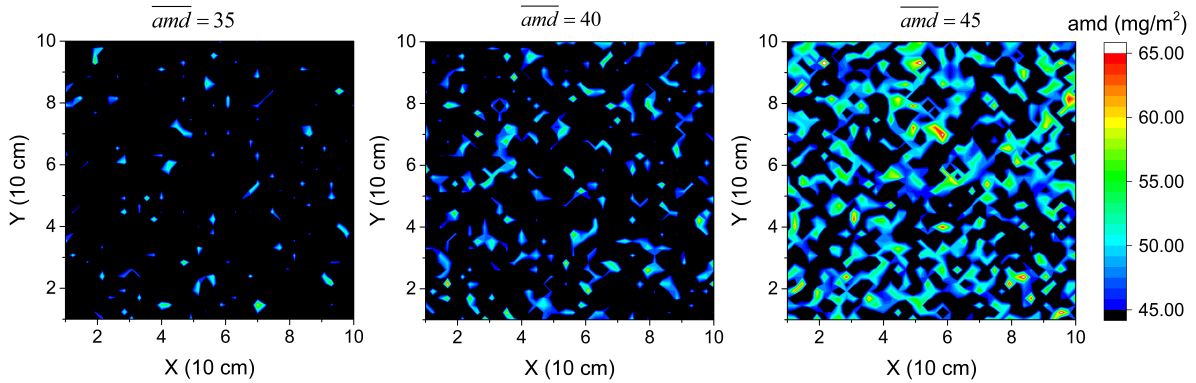


Figure 5.11: Illustration of the numbers of clusters having an  $amd > amd_C$  when increasing the average network density  $\overline{amd}$  from 35 to 45 ( $\text{mg}/\text{m}^2$ ) ( $\sigma_{amd}$  was fixed at  $8 \text{ mg}/\text{m}^2$  for this **simulation**). Black regions refer to the non-percolating part of the network, bright regions refer to the percolating clusters.

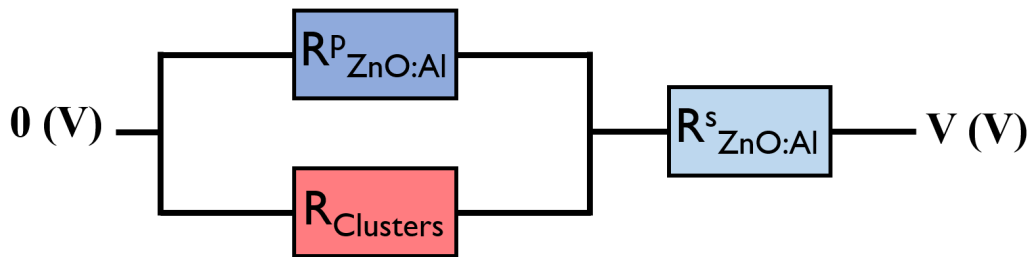


Figure 5.12: A simple equivalent electrical circuit of the ZnO:Al/AgNW nanocomposite.  $R^s_{\text{ZnO:Al}}$  is a resistance related to the fraction of the ZnO:Al film covering the non-percolating AgNW network (the black part in Figure 5.11),  $R^p_{\text{ZnO:Al}}$  is a resistance related to the fraction of the ZnO:Al film covering the percolating clusters, which is in parallel with the  $R^p_{\text{clusters}}$  (the total resistance of the clusters).

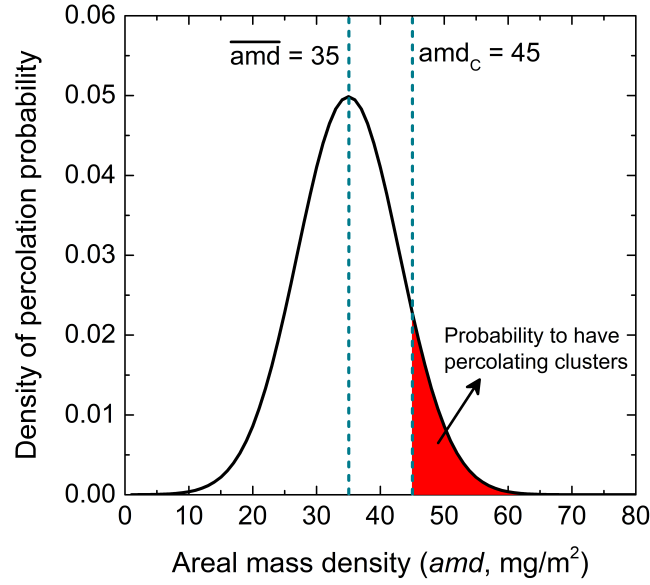


Figure 5.13: Density of percolation probability (*pdf*) as a function of *amd* for the case of a sample having an average  $\overline{amd} = 35$ , and the percolation threshold  $amd_C = 45$ . The surface of the red shaded area refers to the probability of having percolating clusters, and can be calculated as  $(1 - cdf^{\overline{amd}}(amd_C))$ .

equivalent *amd* equal to  $\alpha \cdot amd_C$ , with  $\alpha$  is a fitting parameter and slightly greater than 1. Therefore, the resistance of one percolating cluster can be expressed as follows:

$$R_{cluster} = K\rho_{AgNW} (\alpha \cdot amd_C - amd_C)^{-\gamma} \quad (5.9)$$

According to the simple equivalent electrical circuit of the ZnO:Al/AgNW nanocomposite shown in Figure 5.12, the resistance of the nanocomposite for the case of  $\overline{amd} \leq amd_C$  is expressed by:

$$R_{nanocomposite}^{\overline{amd} \leq amd_C}(\overline{amd} \leq amd_C) = R_{ZnO:Al} cdf^{\overline{amd}} + [1 - cdf^{\overline{amd}}] \frac{R_{cluster} R_{ZnO:Al}}{R_{cluster} + R_{ZnO:Al}} \quad (5.10)$$

For the case of  $\overline{amd} > amd_C$ , all percolating clusters forms a complete percolating network, which is considered as a resistance in parallel with the ZnO:Al thin film. The resistance of a standalone percolating AgNW network is given as follows:

$$R_{AgNW_s}(\overline{amd}) = K\rho_{AgNW} (\overline{amd} - amd_C)^{-\gamma} \quad (5.11)$$

One can note that this formula diverges at  $\overline{amd} = amd_C$ , and then the AgNWs could not

contribute to the electrical resistance of the specimen. For the sake of continuity between the two regimes when  $\overline{amd} = amd_C$ , we added the contribution of the local percolating clusters to the classical percolation term valid for  $\overline{amd} > amd_C$ , a contribution that we call the critical resistance:

$$\frac{1}{R_{nanocomposite}^{\overline{amd} \leq amd_C}(\overline{amd} = amd_C)} = \frac{1}{R_{ZnO:Al}} + \frac{1}{R_{critical}} + \frac{1}{R_{nanocomposite}^{\overline{amd} > amd_C}(\overline{amd} = amd_C)} \quad (5.12)$$

where

$$R_{nanocomposite}^{\overline{amd} \leq amd_C}(\overline{amd} = amd_C) = \frac{1}{2} \left( R_{ZnO:Al} + \frac{R_{cluster} R_{ZnO:Al}}{R_{cluster} + R_{ZnO:Al}} \right) \quad (5.13)$$

and  $R_{nanocomposite}^{\overline{amd} > amd_C}(\overline{amd} = amd_C) = \infty$ . Thus, the critical resistance can be expressed by:

$$R_{critical} = \left[ \frac{1}{\frac{1}{2} \left( R_{ZnO:Al} + \frac{R_{cluster} R_{ZnO:Al}}{R_{cluster} + R_{ZnO:Al}} \right)} - \frac{1}{R_{ZnO:Al}} \right]^{-1} \quad (5.14)$$

Finally, when  $\overline{amd} > amd_C$ , the formula for the nanocomposite resistance is given as follows:

$$R_{nanocomposite}^{\overline{amd} > amd_C}(\overline{amd} > amd_C) = \left[ \frac{1}{K \rho_{AgNW} (\overline{amd} - amd_C)^{-\gamma}} + \frac{1}{R_{critical}} + \frac{1}{R_{ZnO:Al}} \right]^{-1} \quad (5.15)$$

### Analysis of fitting parameters

Table 5.1 shows the parameters used for the simulation study, as well as the fitting parameters used for analyzing and understanding the experimental data. Figure 5.14a) and 5.14b) show the effect of two parameters  $R_{ZnO:Al}$  and  $K$  on the resistance of the ZnO:Al/AgNW nanocomposite, respectively. As can be seen, the ZnO:Al resistance affects only the resistance of the nanocomposite at relatively low AgNW network densities ( $\ll amd_C$ ), while the parameter  $K$ , which is directly proportional to the resistance of the AgNW network, determines the resistance of the nanocomposite at high AgNW network densities ( $\gg amd_C$ ). It is possible to consider extreme values of  $amd/amd_C$  (i.e. very low or very large compared to unity) for which either ZnO:Al or the AgNW network dominates the conductivity, these parameters ( $R_{ZnO:Al}$  and  $K$ ) can be easily found. Indeed, the critical and difficult region to model and understand is when the AgNW network density tends to  $amd_C$ , for which the eval-

Symbol	Description	Value [unity]	Reference
$d^{Ag}$	Mass density of Ag	$10.5 \times 10^3 [kg/m^3]$	<a href="http://wikipedia.org">wikipedia.org</a>
$\rho_{bulk}^{Ag}$	Resistivity of bulk Ag	$1.59 \times 10^{-8} [\Omega m]$	<a href="http://wikipedia.org">wikipedia.org</a>
$D_{NW}$	Average diameter of AgNWs	79 [nm]	Our data
$L_{NW}$	Average length of AgNWs	7 [ $\mu m$ ]	Our data
$\Lambda$	Electron mean free path in Ag	53 [nm]	[186]
$\gamma$	Conductivity exponent in percolation theory	1.29 [unitless]	[182]
$R_{ZnO:Al}$	Resistance of $2.5 \times 2.5 \text{ cm}^2$ ZnO:Al	800 [ $\Omega$ ]	Our data
$amd_C$	Threshold of percolating regime	30 – 50 [ $mg/m^2$ ]	Fitting parameter
$\overline{\sigma_{amd}}$	Standard deviation in the case $amd$ has a normal distribution	1 – 8 [ $mg/m^2$ ]	Fitting parameter
$K$	A constant related to the shape and the geometry of the AgNW network	$[mg^\gamma m^{-(2\gamma+1)}]$	Fitting parameter
$\alpha$	A coefficient related to the average density of percolating clusters	1.0 – 1.3 [unitless]	Fitting parameter

Table 5.1: Parameters used for the simulation of the resistance of ZnO:Al/AgNW nanocomposites.

uation of  $\alpha$  and  $\overline{\sigma_{amd}}$  becomes important. Figure 5.15a) and 5.15b) show the effect of two parameters  $\alpha$  and  $\overline{\sigma_{amd}}$  on the resistance of the ZnO:Al/AgNW nanocomposite, respectively. The parameter  $\alpha$  is directly related to the conductivity of the percolating clusters via eq. 5.9:  $R_{cluster} = K\rho_{AgNW}(\alpha \cdot amd_C - amd_C)^{-1.29}$ . As shown in Figure 5.15a), the resistance of the nanocomposite decreases when increasing  $\alpha$  from 1.001 to 1.2, for  $\overline{amd}$  close to  $amd_C$ . As described in the presentation of the model, the parameter  $\overline{\sigma_{amd}}$  determines how much the AgNW network density is distributed around an average value,  $\overline{amd}$ , which means that it is related to the number of the percolating clusters. As can be seen in the figure, this parameter mainly affects the conductivity of the nanocomposite at  $\overline{amd} < amd_C$ .

After carefully analyzing the effect of different parameters on the conductivity of the ZnO:Al/AgNW nanocomposite, we have applied the cluster model to our experimental data. Figure 5.16 shows the fitting results using eq. 5.10 and eq. 5.15.  $\overline{\sigma_{amd}} = 5$ ,  $\alpha = 1.2$  and  $K = 9.5 \times 10^{10}$  were used. We observe that the experimental data related to the bare AgNW networks deposited on glass can be relatively well fitted using a percolating threshold of

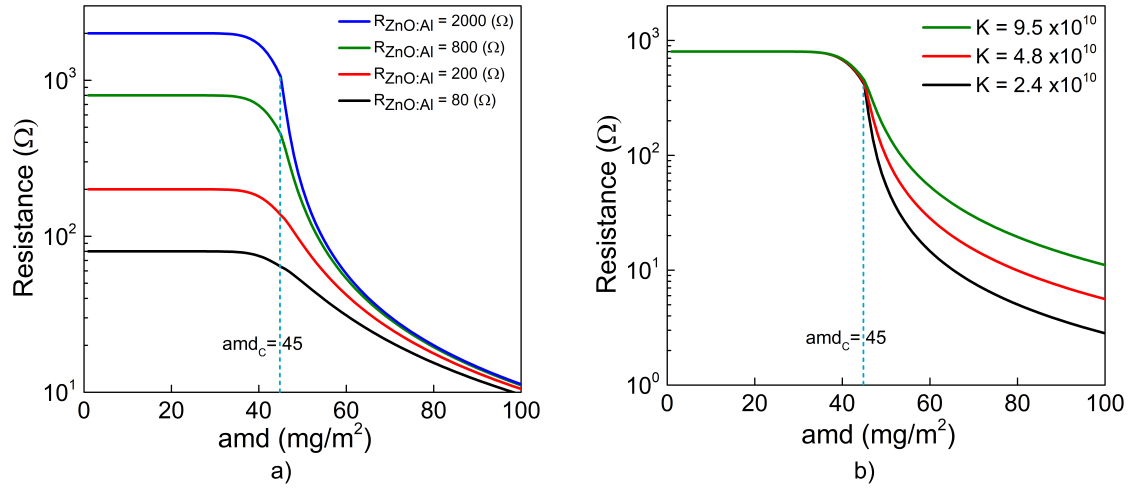


Figure 5.14: Effect of a)  $R_{ZnO:Al}$  and b)  $K$  on the resistance of the nanocomposites. These **simulation** results were obtained by using  $amd_C = 45$ ,  $\sigma_{amd} = 5$ ,  $\alpha = 1.2$  for both figures, then  $K = 9.5 \times 10^{10}$  for a) and  $R_{ZnO:Al} = 800$  for b).

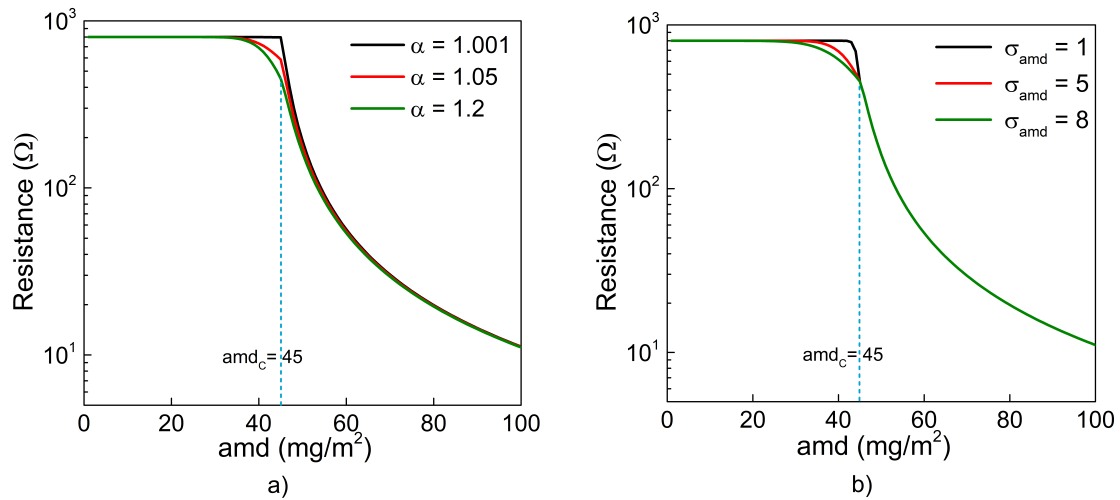


Figure 5.15: Effect of a)  $\alpha$  and b)  $\sigma_{amd}$  on the resistance of the nanocomposites. These **simulation** results were obtained by using  $amd_C = 45$ ,  $K = 9.5 \times 10^{10}$ ,  $R_{ZnO:Al} = 800$  for both figures, then  $\sigma_{amd} = 5$  for a) and  $\alpha = 1.2$  for b).

$amd_C = 45 \text{ mg/m}^2$ , however, using this  $amd_C$  value for the ZnO:Al/AgNW nanocomposite does not lead to a good agreement with the developed model. If a lower value of  $amd_C$  is used for fitting the experimental data of the nanocomposite ( $amd_C = 39 \text{ mg/m}^2$ ), the agreement between experimental and fitting curves appears rather good.

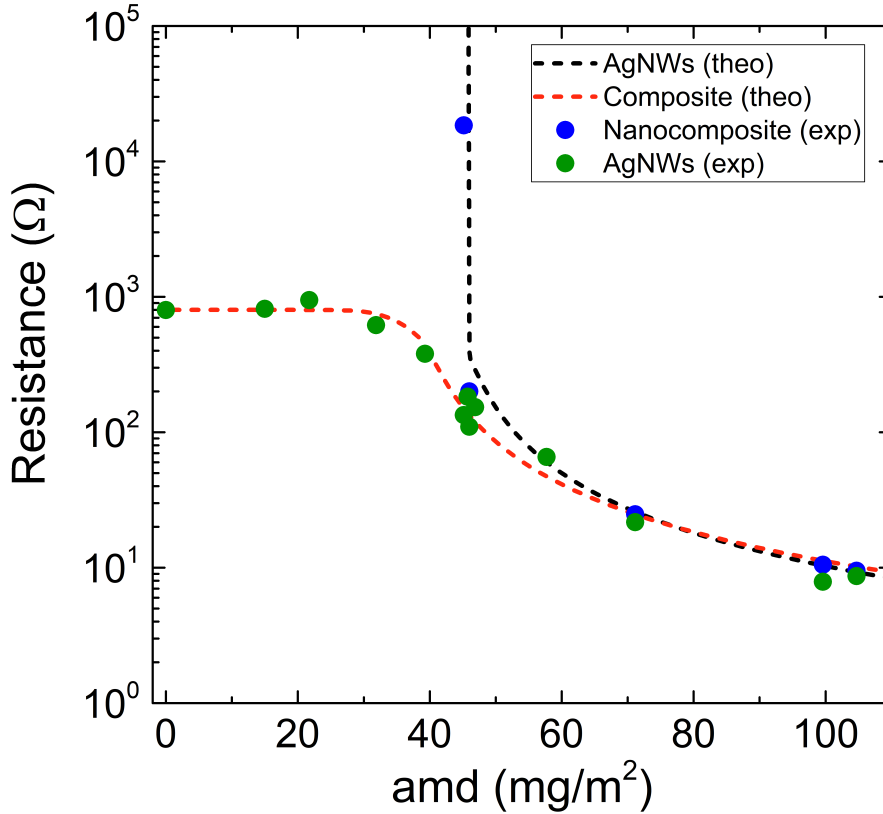


Figure 5.16: Experimental electrical resistance of AgNW network measured during this work versus areal mass density ( $amd$ ) for a network deposited on glass (blue symbols) and for a 100 nm thick ZnO:Al layer grown by AP-SALD deposited above a similar AgNW network (green symbols). The resistance of 100 nm thick ZnO:Al film on glass was  $800 \Omega$ . The fitting curves use eq. 5.10 and eq. 5.15 for the AgNW deposited on glass (black dashed curve,  $\overline{amd}_C = 45$ ) and for the AgNW/AZO nanocomposite (red dashed curve,  $\overline{amd}_C = 39$ ).  $\sigma_{\overline{amd}} = 5$ ,  $\alpha = 1.2$  and  $K = 9.5 \times 10^{10}$  were used.

Indeed, the two presented models were developed by assuming that the AgNW network is a 2-D system and that there is no interaction between the ZnO:Al film and the AgNW network. In reality, the AgNWs are sprayed on top of each other, and form actually a 3-D system if the network density is rather important. In such a configuration, depositing a thin ZnO:Al layer on top of the AgNWs can significantly improve the contact between AgNWs, or in other words, the ZnO:Al thin films help to stick better the individual AgNWs together. To conclude

with this part of the study, one can find a good agreement between the experimental electrical resistance of both bare and ZnO/Al coated AgNWs thanks to a simple physical model. Such a model can help designing a ZnO:Al/AgNW nanocomposite thanks to the calculation of its electrical resistance. The optimization of the ZnO:Al/AgNW nanocomposite for transparent electrode application should include its optical properties. Figure 5.17a) shows the variation of the sheet resistance and the total transmittance of a 110 nm thick ZnO:Al/AgNW nanocomposite as a function of the spray coating cycle, i.e. AgNW network density. Accordingly, the sheet resistance of the nanocomposite decreases from 1000 to 4  $\Omega/sq$  upon increasing of the network density. However, the transmittance of the nanocomposite decreases from close to 90 % to 79 %. Figure 5.17b) shows the diffuse transmittance of the same set of samples. As can be seen, the diffuse transmittance of the ZnO:Al/AgNW nanocomposite increases with the network density. In the laboratory, a protocol is being developed to obtain more reliable and accurate values of the haze factor of TCM based on AgNWs, however the increasing trend observed is clear. This is actually very interesting in photovoltaic applications in which the diffuse light can increase the light absorption, thus, the photogenerated current in the devices. In summary, the samples having a sheet resistance of about 7  $\Omega/sq$  and a total transmittance  $\sim$  83 % have a great potential for photovoltaic applications thanks to their high optical-electrical performance, their enhanced electrical and thermal stability thanks to the ZnO:Al thin layer, as well as their potential for applications in flexible devices.

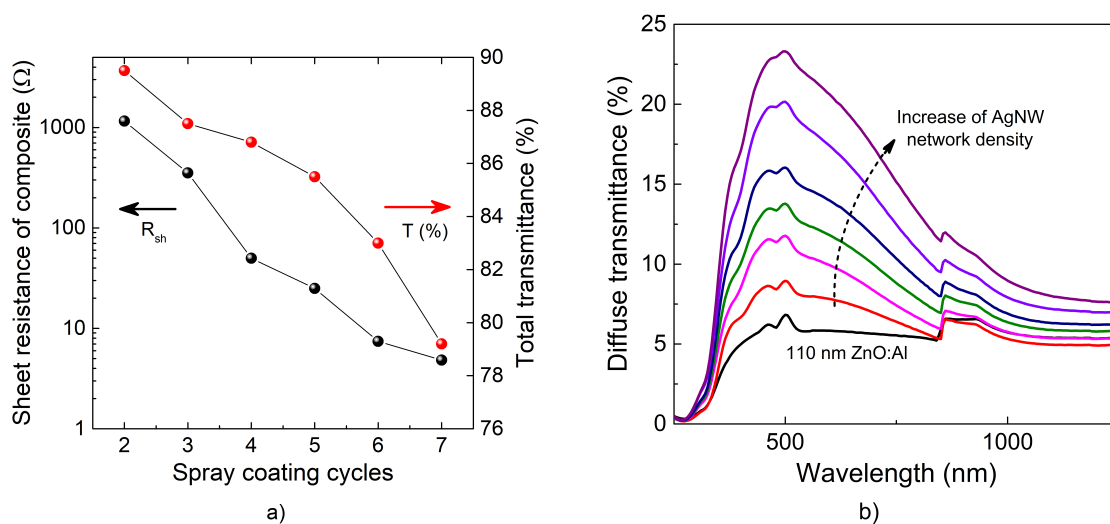


Figure 5.17: a) Variation of the sheet resistance and the total transmittance of a 110 nm thick ZnO:Al/AgNW nanocomposite as a function of the spray coating cycle, i.e. AgNW network density; b) the dependence of the diffuse transmittance of the ZnO:Al/AgNW nanocomposite on the AgNW network density.

### 5.3 Quantitative assessment of the effects of the ZnO coating on AgNW networks

We have shown earlier in this chapter that the coating of AgNWs by a very thin and conformal ZnO layer leads to a clear enhancement of the electrical stability of AgNW networks. This enhancement is at the expense of a slight decrease of the optical transparency of the coated AgNW network. The question which arises is whether one can: i/ assess in a quantitative way the effects of a thin coating on the main properties of the network through a more generalized figure of merit (FoM) and ii/ if we can estimate the dependence of the ZnO layer thickness, noted  $t_{ZnO}$ , on this FoM value?

So far, the most frequently used FoM is the one proposed by Haacke in 1976,[187] for which the FoM is defined by  $T_r^{10}/R_{sh}$ , where  $T_r$  is the optical transparency and  $R_{sh}$  the sheet resistance of the AgNW network. Obviously, this FoM does not consider the electrical stability of the network while such a stability is crucial for an efficient integration with industrial devices. Indeed instabilities of AgNW networks can reveal to be dramatic.[163] One simple and physical way to build a new FoM that considers not only the optical and electrical properties but also the electrical stability is to consider that the maximal electrical power that a AgNW network can sustain before failure. This power,  $P_{failure}$ , can be written as:  $P_{failure} = V_{failure}^2/R$ , where  $V_{failure}$  is associated to the voltage failure for which the electrical resistance  $R$  starts diverging. Since for a square and rather dense AgNW network,  $R_{sh}$  and  $R$  are experimentally very close to each other,[158] a simple and physical way to consider a more general FoM is to consider:  $T_r^{10}V_{failure}^2/R_{sh}$ . However, since  $P_{failure}$  is proportional to the specimen size, one could consider instead:

$$FoM_{stability} = \frac{T_r^{10}}{R_{sh}} P_{failure} = \frac{T_r^{10} V_{failure}^2}{R_{sh}^2} \quad (5.16)$$

As shown by Figure 5.2c), the ZnO coating slightly decreases the optical transmittance, while  $R_{sh}$  remains constant. This corresponds to the following equation:

$$T_r^{coated} = T_r^{bare} \exp(-a \cdot t_{ZnO}) \quad (5.17)$$

where  $T_r^{coated}$  and  $T_r^{bare}$  are the optical transparency of the coated and bare networks, respectively. The value of  $a$ , deduced from Figure 5.2c), is equal to  $3.5 \times 10^{-3} \text{ nm}^{-1}$  when  $t_{ZnO}$  is expressed in nm.

As shown by Figure 5.4b),  $V_{failure}$  increases with the ZnO thickness, and the dependence

was shown to be:

$$V_{failure}^{coated} = V_{failure}^{bare} (1 + b \cdot t_{ZnO}^2) \quad (5.18)$$

where  $V_{failure}^{coated}$  and  $V_{failure}^{bare}$  are the failure voltage of the coated and bare networks. The value of  $b$ , deduced from Figure 5.4b), is equal to  $8.4 \times 10^{-4} \text{ nm}^{-2}$ .

Therefore, the new FoM can be written as a function of the ZnO layer thickness, as follows:

$$FoM_{stability}^{coated} = FoM_{stability}^{bare} [\exp(-a \cdot t_{ZnO})]^{10} (1 + b \cdot t_{ZnO}^2)^2 \quad (5.19)$$

The ratio of FoM, the coated network's FoM divided by the bare network's FoM, can be calculated from eq. 5.19 and is plotted in Figure 5.18. The ratio decreases initially since the  $V_{failure}$  increases very slowly with small values of  $t_{ZnO}$ . This decrease of FoM is of 17.5% for  $t_{ZnO}$  close to 12 nm. However for  $t_{ZnO}$  around 26 nm the FoM value is then identical to the initial one and then increases up to much larger values, reaching a value of 2.67 for  $t_{ZnO} = 100$  nm, showing the interest of coating AgNW networks for enhanced performances.

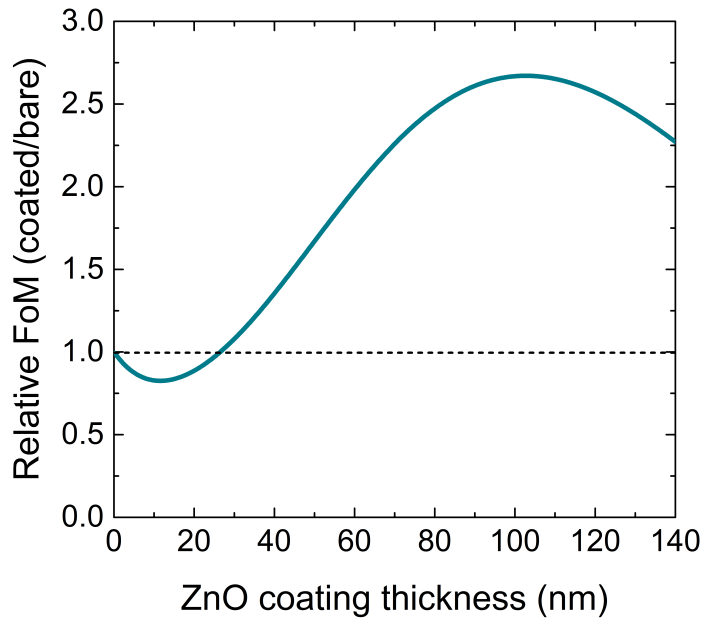


Figure 5.18: The ratio of FoM, the coated network's FoM divided by the bare network's FoM, as a function of ZnO coating thickness.

It is worth noticing that the real optimal  $t_{ZnO}$  value will depend on the intended applications. For flexible transparent electrode applications, the ZnO thickness layer should not be too thick to avoid any brittleness of the ZnO layer. When the AgNW network is required to play a role, such as carrier collector (for solar cells) or carrier injector (for OLEDs), the limitation

will stem from the transport of the electrical carriers through the ZnO layer. For a non-flexible transparent heater, the optimal ZnO layer thickness would be around 100 nm, at least as long as the optical transparency corresponds to the application need, since in such case, the AgNW network transparency would be about 70%. In conclusion, the proposed analysis described above can be used for a quantitative assessment for the optimal integration of a coated AgNW network within a device, knowing that the approach will be application-dependent. Finally, the new FoM can also be generalized and applied for any type of metal oxide coating with assumption that the resistance of the bare AgNW network and the coated one should remain similar.

## 5.4 Conclusion

In summary, ZnO thin layers of different thicknesses were deposited on AgNW networks by AP-SALD and the effects on the main physical properties of the networks were studied. It is shown that the ZnO coatings drastically improve adhesion as well as thermal and electrical stabilities of AgNW networks, with only a small decrease in optical transparency. The stability improvement observed is directly related to the thickness of the ZnO coating, i.e. the thicker the ZnO coating layer, the better the thermal and electrical stabilities of the network. However, ZnO-coated AgNW networks are slightly less transparent when the ZnO coating thickness is increased and thus a compromise in terms of ZnO thickness should be determined depending on the targeted application. The coated AgNW networks were evaluated as transparent heaters, proving to be much more stable than bare networks and thus reaching temperatures as high as 350 °C during a voltage ramp. In particular, the electrical failure voltage (and associated temperature) increased from 8 V (150 °C) to 14 V (350 °C) for bare and coated AgNWs, respectively, which represents a 133% increase in achievable temperature. Thanks to a simple model, we have shown that the origin of the stability enhancement can be associated with hindered atomic diffusion on the surface of the AgNWs because it is partially delayed due to the low diffusion of Ag atoms through the ZnO coating, thus preventing junction deterioration.

To overcome the instability of bare AgNW networks and to improve the electrical conductivity of ZnO:Al film deposited by AP-SALD, we have explored the idea of fabricating a high-performance TCM based on ZnO:Al thin film and AgNW network, namely ZnO:Al/AgNW nanocomposites, in which a thin ZnO:Al layer (~ 100 nm - 150 nm) is deposited on the top of the AgNW network. As a result, nanocomposite samples having a sheet resistance of about 7  $\Omega/sq$  and a total transmittance ~ 83 % were obtained. To better understand the electrical properties of the nanocomposites, we have developed two simple physical models: i) the first one assumes that the nanocomposite is actually equivalent to the resistance of the ZnO:Al

thin film if the AgNW network is not percolating, conversely, it is two resistances ( $R_{ZnO:Al}$  and  $R_{AgNWs}$ ) in parallel if the AgNW network is percolating, ii) the second model takes into account the contribution of local percolating clusters to the conductivity of the nanocomposites, even under the network percolation threshold. Although these physical models are rather simplistic, the agreement with data appears rather good.

In the last part of this chapter, we have proposed a new way to calculate the figure of merit (FoM) of the coated AgNW network by taking into account not only the optical and electrical properties but also the electrical stability. The proposed analysis can be used for a quantitative assessment for the optimal integration of a coated AgNW network within a device, knowing that the approach will be application-dependent.



# Bibliography

- [1] Anderson Janotti and Chris G Van de Walle. Fundamentals of zinc oxide as a semiconductor. *Reports on Progress in Physics*, 72(12):126501, December 2009. [xiii](#), [8](#), [9](#), [63](#)
- [2] Moataz Bellah M. Mousa, Christopher J. Oldham, Jesse S. Jur, and Gregory N. Parsons. Effect of temperature and gas velocity on growth per cycle during Al<sub>2</sub>O<sub>3</sub> and ZnO atomic layer deposition at atmospheric pressure. *Journal of Vacuum Science & Technology A: Vacuum, Surfaces, and Films*, 30(1):01A155, January 2012. [xv](#), [38](#), [39](#), [74](#)
- [3] Hynek Biederman. *Plasma polymer films*. World Scientific, 2004. [xv](#), [40](#), [41](#)
- [4] National Institute of Standards and Technology. *NIST handbook of mathematical functions*. Cambridge University Press, Cambridge New York Melbourne, 2010. OCLC: 837238676. [xix](#), [89](#), [97](#)
- [5] Klaus Ellmer, Andreas Klein, and Bernd Rech, editors. *Transparent conductive zinc oxide: basics and applications in thin film solar cells*. Number 104 in Springer Series in Materials Science. Springer, Berlin, 2008. [xxv](#), [5](#), [7](#), [9](#), [10](#), [82](#), [83](#), [84](#), [90](#), [102](#)
- [6] P Carroy, D Muñoz, F Ozanne, A Valla, P Mur, and G Rodriguez. Analysis of different front and back TCO on heterojunction solar cells. *Proc. 31st Eur. Photovolt. Sol. Energy Conf*, pages 359–364, 2015. [xxv](#), [xxvi](#), [70](#), [71](#)
- [7] Klaus Ellmer and Rainald Mientus. Carrier transport in polycrystalline transparent conductive oxides: A comparative study of zinc oxide and indium oxide. *Thin Solid Films*, 516(14):4620–4627, May 2008. [xxvi](#), [111](#)
- [8] D. S. Ginley, H. Hosono, and D.C. Paine. *Handbook of Transparent Conductors*. Springer, September 2010. [3](#)

- [9] K. L. Chopra, S. Major, and D. K. Pandya. Transparent conductors - A status review. *Thin solid films*, 102(1):1–46, 1983. [3](#)
- [10] Jean Rousset, Edgardo Saucedo, and Daniel Lincot. Extrinsic Doping of Electrodeposited Zinc Oxide Films by Chlorine for Transparent Conductive Oxide Applications. *Chemistry of Materials*, 21(3):534–540, February 2009. [3](#)
- [11] Wenxi Guo, Zijie Xu, Fayin Zhang, Shuyao Xie, Hongyao Xu, and Xiang Yang Liu. Recent Development of Transparent Conducting Oxide - Free Flexible Thin Film Solar Cells. *Advanced Functional Materials*, 26(48):8855–8884, December 2016. [3](#)
- [12] David S. Hecht, Liangbing Hu, and Glen Irvin. Emerging Transparent Electrodes Based on Thin Films of Carbon Nanotubes, Graphene, and Metallic Nanostructures. *Advanced Materials*, 23(13):1482–1513, April 2011.
- [13] Tadatsugu Minami. Transparent conducting oxide semiconductors for transparent electrodes. *Semiconductor Science and Technology*, 20(4):S35–S44, April 2005. [3](#)
- [14] Klaus Ellmer. Past achievements and future challenges in the development of optically transparent electrodes. *Nature Photonics*, 6(12):809–817, November 2012. [3](#), [128](#)
- [15] Tadatsugu Minami. Present status of transparent conducting oxide thin-film development for Indium-Tin-Oxide (ITO) substitutes. *Thin Solid Films*, 516(17):5822–5828, July 2008. [3](#), [10](#)
- [16] K. Ellmer, F. Kudella, R. Mientus, R. Schieck, and S. Fiechter. Influence of discharge parameters on the layer properties of reactive magnetron sputtered ZnO:Al films. *Thin Solid Films*, 247(1):15–23, July 1994. [3](#)
- [17] Akio Suzuki, Tatsuhiko Matsushita, Takanori Aoki, Yoshitaka Yoneyama, and Masahiro Okuda. Pulsed laser deposition of transparent conducting indium tin oxide films in magnetic field perpendicular to plume. *Japanese Journal of Applied Physics*, 40(4B):L401, 2001. [3](#)
- [18] Tadatsugu Minami, Shingo Suzuki, and Toshihiro Miyata. Electrical Conduction Mechanism of Highly Transparent and Conductive ZnO Thin Films. *MRS Proceedings*, 666:F1.3, 2001. [3](#)
- [19] T. S. Suntola and J. Antson, 1977, US Pat., 4,058,430. [4](#), [24](#)
- [20] T. S. Suntola, A. J. Pakkala and S. G. Lindfors, 1983, US Pat., 4,389,973. [4](#)

- [21] David Muñoz-Rojas and Judith MacManus-Driscoll. Spatial atmospheric atomic layer deposition: a new laboratory and industrial tool for low-cost photovoltaics. *Mater. Horiz.*, 1(3):314–320, 2014. [4](#)
- [22] Andrea Illiberi, R Scherpenborg, Y Wu, F Roozeboom, and P Poodt. Spatial Atmospheric Atomic Layer Deposition of  $\text{Al}_x\text{Zn}_{1-x}\text{O}$ . *ACS applied materials & interfaces*, 5(24):13124–8, December 2013.
- [23] Paul Poodt, David C. Cameron, Eric Dickey, Steven M. George, Vladimir Kuznetsov, Gregory N. Parsons, Fred Roozeboom, Ganesh Sundaram, and Ad Vermeer. Spatial atomic layer deposition: A route towards further industrialization of atomic layer deposition. *Journal of Vacuum Science & Technology A: Vacuum, Surfaces, and Films*, 30(1):010802, 2012. [25](#)
- [24] Xavier Moya and David Muñoz-Rojas. *Materials for sustainable energy applications: conversion, storage, transmission and consumption*. Singapore, 2016. OCLC: 957651903. [4](#)
- [25] Ü. Özgür, Ya. I. Alivov, C. Liu, A. Teke, M. A. Reshchikov, S. Doğan, V. Avrutin, S.-J. Cho, and H. Morkoç. A comprehensive review of ZnO materials and devices. *Journal of Applied Physics*, 98(4):041301, August 2005. [5](#), [7](#), [83](#)
- [26] C. Klingshirn. ZnO: From basics towards applications. *physica status solidi (b)*, 244(9):3027–3073, September 2007.
- [27] Zhou Li, Rusen Yang, Min Yu, Fan Bai, Cheng Li, and Zhong Lin Wang. Cellular Level Biocompatibility and Biosafety of ZnO Nanowires. *The Journal of Physical Chemistry C*, 112(51):20114–20117, December 2008. [5](#)
- [28] J.-H. Lim, C.-K. Kang, K.-K. Kim, I.-K. Park, D.-K. Hwang, and S.-J. Park. UV Electroluminescence Emission from ZnO Light-Emitting Diodes Grown by High-Temperature Radiofrequency Sputtering. *Advanced Materials*, 18(20):2720–2724, October 2006. [5](#)
- [29] Byeong-Yun Oh, Min-Chang Jeong, Tae-Hyoung Moon, Woong Lee, Jae-Min Myoung, Jeoung-Yeon Hwang, and Dae-Shik Seo. Transparent conductive Al-doped ZnO films for liquid crystal displays. *Journal of Applied Physics*, 99(12):124505, June 2006. [5](#)
- [30] F Decremps, J Zhang, and R. C Liebermann. New phase boundary and high-pressure thermoelasticity of ZnO. *Europhysics Letters (EPL)*, 51(3):268–274, August 2000. [5](#)

- [31] E. A. Secco. Decomposition of Zinc Oxide. *Canadian Journal of Chemistry*, 38(4):596–601, April 1960. 5
- [32] S. Moller and R. Palumbo. Solar thermal decomposition kinetics of ZnO in the temperature range 1950–2400k. *Chemical Engineering Science*, 56(15):4505–4515, August 2001. 5
- [33] Katsumi Maeda, Mitsuru Sato, Ikuo Niikura, and Tsuguo Fukuda. Growth of 2 inch ZnO bulk single crystal by the hydrothermal method. *Semiconductor Science and Technology*, 20(4):S49–S54, April 2005. 6, 12
- [34] Wenwen Lin, Dagui Chen, Jiye Zhang, Zhang Lin, Jiakui Huang, Wei Li, Yonghao Wang, and Feng Huang. Hydrothermal Growth of ZnO Single Crystals with High Carrier Mobility. *Crystal Growth & Design*, 9(10):4378–4383, October 2009. 6
- [35] D.C. Look, D.C. Reynolds, J.R. Sizelove, R.L. Jones, C.W. Litton, G. Cantwell, and W.C. Harsch. Electrical properties of bulk ZnO. *Solid State Communications*, 105(6):399–401, February 1998. 6, 12
- [36] Masami Hirose, Yoshio Furuya, and Ikumaro Kubo. Growth of ZnO Single crystal from ZnBr<sub>2</sub>. *Japanese Journal of Applied Physics*, 9(6):726–727, June 1970. 6
- [37] Y. Segawa, A. Ohtomo, M. Kawasaki, H. Koinuma, Z. K. Tang, P. Yu, and G. K. L. Wong. Growth of ZnO Thin Film by Laser MBE: Lasing of Exciton at Room Temperature. *physica status solidi (b)*, 202(2):669–672, August 1997. 6
- [38] Akihiro Hachigo, Hideaki Nakahata, Kenjiro Higaki, Satoshi Fujii, and Shinichi Shikata. Heteroepitaxial growth of ZnO films on diamond (111) plane by magnetron sputtering. *Applied Physics Letters*, 65(20):2556–2558, November 1994. 6
- [39] M. A. L. Johnson, Shizuo Fujita, W. H. Rowland, W. C. Hughes, J. W. Cook, and J. F. Schetzina. MBE growth and properties of ZnO on sapphire and SiC substrates. *JEM*, 25(5):855–862, May 1996. 6
- [40] Wen-Ching Shih and Mu-Shiang Wu. Growth of ZnO films on GaAs substrates with a SiO<sub>2</sub> buffer layer by RF planar magnetron sputtering for surface acoustic wave applications. 137(3-4):319–325, 1994. 6
- [41] Fumiyasu Oba, Shigeto R. Nishitani, Seiji Isotani, Hirohiko Adachi, and Isao Tanaka. Energetics of native defects in ZnO. *Journal of Applied Physics*, 90(2):824–828, July 2001. 7

- [42] M. D. McCluskey and S. J. Jokela. Defects in ZnO. *Journal of Applied Physics*, 106(7):071101, October 2009. [9](#)
- [43] P. D. C. King and T. D. Veal. Conductivity in transparent oxide semiconductors. *Journal of Physics: Condensed Matter*, 23(33):334214, 2011. [7](#), [9](#), [89](#)
- [44] Anderson Janotti and Chris G. Van de Walle. Native point defects in ZnO. *Physical Review B*, 76(16), October 2007. [8](#)
- [45] Yong-Sung Kim and C. H. Park. Rich Variety of Defects in ZnO via an Attractive Interaction between O Vacancies and Zn Interstitials: Origin of n-Type Doping. *Physical Review Letters*, 102(8), February 2009. [9](#)
- [46] D. C. Look, G. C. Farlow, Pakpoom Reunchan, Sukit Limpijumnong, S. B. Zhang, and K. Nordlund. Evidence for Native-Defect Donors in n-Type ZnO. *Physical Review Letters*, 95(22), November 2005. [9](#)
- [47] F. Tuomisto, V. Ranki, K. Saarinen, and D C. Look. Evidence of the Zn Vacancy Acting as the Dominant Acceptor in n-Type ZnO. *Physical Review Letters*, 91(20), November 2003. [10](#)
- [48] F. Tuomisto, K. Saarinen, D. C. Look, and G. C. Farlow. Introduction and recovery of point defects in electron irradiated ZnO. *Physical Review B*, 72(8), August 2005. [10](#)
- [49] Holger von Wenckstern, Swen Weinhold, Gisela Biehne, Rainer Pickenhain, Heidemarie Schmidt, Holger Hochmuth, and Marius Grundmann. Donor Levels in ZnO. In *Advances in Solid State Physics*, Advances in Solid State Physics, pages 263–274. Springer, Berlin, Heidelberg. [10](#)
- [50] D. C. Look, K. D. Leedy, L. Vines, B. G. Svensson, A. Zubiaga, F. Tuomisto, D. R. Dutt, and L. J. Brillson. Self-compensation in semiconductors: The Zn vacancy in Ga-doped ZnO. *Physical Review B*, 84(11), September 2011. [11](#), [62](#), [83](#), [84](#), [85](#), [87](#), [102](#), [112](#)
- [51] J. T-Thienprasert, S. Rujirawat, W. Klysubun, J. N. Duenow, T. J. Coutts, S. B. Zhang, D. C. Look, and S. Limpijumnong. Compensation in Al-Doped ZnO by Al-Related Acceptor Complexes: Synchrotron X-Ray Absorption Spectroscopy and Theory. *Physical Review Letters*, 110(5), January 2013. [11](#), [112](#)
- [52] Byeong-Yun Oh, Min-Chang Jeong, Doo-Soo Kim, Woong Lee, and Jae-Min Myoung. Post-annealing of Al-doped ZnO films in hydrogen atmosphere. *Journal of Crystal Growth*, 281(2-4):475–480, August 2005. [12](#), [113](#)

- [53] Hideaki Agura, Hirokazu Okinaka, Shigeyasu Hoki, Takanori Aoki, Akio Suzuki, Tatsuhiko Matsushita, and Masahiro Okuda. Low-resistive and transparent AZO films prepared by PLD in magnetic field. *Electrical Engineering in Japan*, 151(2):40–45, April 2005. [12](#)
- [54] O Kluth, B Rech, L Houben, S Wieder, G Schope, C Beneking, H Wagner, A Löffl, and H. W Schock. Texture etched ZnO:Al coated glass substrates for silicon based thin film solar cells. *Thin Solid Films*, 351(1):247–253, August 1999. [12](#)
- [55] G. Luka, L. Wachnicki, B.S. Witkowski, T.A. Krajewski, R. Jakiela, E. Guziewicz, and M. Godlewski. The uniformity of Al distribution in aluminum-doped zinc oxide films grown by atomic layer deposition. *Materials Science and Engineering: B*, 176(3):237–241, February 2011. [12](#)
- [56] Andrea Illiberi, R Scherpenborg, Y Wu, F Roozeboom, and P Poodt. Spatial Atmospheric Atomic Layer Deposition of  $\text{Al}_x\text{Zn}_{1-x}\text{O}$ . *ACS applied materials & interfaces*, 5(24):13124–8, December 2013. [12](#)
- [57] Peter Würfel and Uli Würfel. *Physics of Solar Cells: From Basic Principles to Advanced Concepts*. John Wiley & Sons, March 2009. [16](#)
- [58] William Shockley and Hans J. Queisser. Detailed Balance Limit of Efficiency of pn Junction Solar Cells. *Journal of Applied Physics*, 32(3):510–519, March 1961. [18](#)
- [59] D. M. Chapin, C. S. Fuller, and G. L. Pearson. A New Silicon p-n Junction Photocell for Converting Solar Radiation into Electrical Power. *Journal of Applied Physics*, 25(5):676–677, May 1954. [19](#)
- [60] Stefaan De Wolf, Antoine Descoeurdes, Zachary C. Holman, and Christophe Ballif. High-efficiency Silicon Heterojunction Solar Cells: A Review. *green*, 2(1), January 2012. [19](#)
- [61] K. Masuko, M. Shigematsu, T. Hashiguchi, D. Fujishima, M. Kai, N. Yoshimura, T. Yamaguchi, Y. Ichihashi, T. Mishima, N. Matsubara, T. Yamanishi, T. Takahama, M. Taguchi, E. Maruyama, and S. Okamoto. Achievement of More Than 25 % Conversion Efficiency With Crystalline Silicon Heterojunction Solar Cell. *IEEE Journal of Photovoltaics*, 4(6):1433–1435, November 2014. [19](#)
- [62] Daisuke Adachi, Jose Luis Hernandez, and Kenji Yamamoto. Impact of carrier recombination on fill factor for large area heterojunction crystalline silicon solar cell with 25.1% efficiency. *Applied Physics Letters*, 107(23):233506, December 2015. [19](#)

- [63] Kunta Yoshikawa, Hayato Kawasaki, Wataru Yoshida, Toru Irie, Katsunori Konishi, Kunihiro Nakano, Toshihiko Uto, Daisuke Adachi, Masanori Kanematsu, Hisashi Uzu, and Kenji Yamamoto. Silicon heterojunction solar cell with interdigitated back contacts for a photoconversion efficiency over 26%. *Nature Energy*, 2(5):17032, May 2017. [19](#)
- [64] Martin A. Green, Yoshihiro Hishikawa, Wilhelm Warta, Ewan D. Dunlop, Dean H. Levi, Jochen Hohl-Ebinger, and Anita W. H. Ho-Baillie. Solar cell efficiency tables - version 50. *Progress in Photovoltaics: Research and Applications*, 25(7):668–676, July 2017. [19](#)
- [65] Chapter 1 Overview of Chemical Vapour Deposition. In Anthony C. Jones and Michael L. Hitchman, editors, *Chemical Vapour Deposition: Precursors, Processes and Applications*, pages 1–36. The Royal Society of Chemistry, 2009. [23](#)
- [66] David H. Levy, Diane Freeman, Shelby F. Nelson, Peter J. Cowdery-Corvan, and Lyn M. Irving. Stable ZnO thin film transistors by fast open air atomic layer deposition. *Applied Physics Letters*, 92(19):192101, May 2008. [25](#)
- [67] David H. Levy. Process for atomic layer deposition. *U.S. Patent No. 7413982.*, August 2008. [25](#)
- [68] David Muñoz-Rojas, Viet Huong Nguyen, César Masse de la Huerta, Sara Aghazadehchors, Carmen Jiménez, and Daniel Bellet. Spatial Atomic Layer Deposition (SALD), an emerging tool for energy materials. Application to new-generation photovoltaic devices and transparent conductive materials. *Comptes Rendus Physique*, 18(7):391–400, September 2017. [25](#), [26](#)
- [69] P. Ryan Fitzpatrick, Zachary M. Gibbs, and Steven M. George. Evaluating operating conditions for continuous atmospheric atomic layer deposition using a multiple slit gas source head. *Journal of Vacuum Science & Technology A: Vacuum, Surfaces, and Films*, 30(1):01A136, December 2012.
- [70] Rong Chen, Ji-Long Lin, Wen-Jie He, Chen-Long Duan, Qi Peng, Xiao-Lei Wang, and Bin Shan. Spatial atomic layer deposition of ZnO/TiO<sub>2</sub> nanolaminates. *Journal of Vacuum Science & Technology A: Vacuum, Surfaces, and Films*, 34(5):051502, September 2016.
- [71] Viet Huong Nguyen, João Resende, Carmen Jiménez, Jean-Luc Deschanvres, Perrine Carroy, Delfina Muñoz, Daniel Bellet, and David Muñoz-Rojas. Deposition of ZnO based thin films by atmospheric pressure spatial atomic layer deposition for application

- in solar cells. *Journal of Renewable and Sustainable Energy*, 9(2):021203, March 2017. 26
- [72] Alexander S. Yersak, Yung C. Lee, Joseph A. Spencer, and Markus D. Groner. Atmospheric pressure spatial atomic layer deposition web coating with in situ monitoring of film thickness. *Journal of Vacuum Science & Technology A: Vacuum, Surfaces, and Films*, 32(1):01A130, December 2014. 26
- [73] L. J. van der PAUW. A method of measuring specific resistivity and Hall effect of discs of arbitrary shape. 13(1):1–9, 1958. 29
- [74] B. T. Khuri Yakub, G. S. Kino, and P. Galle. Studies of the optimum conditions for growth of rf sputtered ZnO films. *Journal of Applied Physics*, 46(8):3266–3272, August 1975. 36
- [75] H.H. Quon and D.P. Malanka. Chemical vapour deposition of epitaxial ZnO films. *Materials Research Bulletin*, 10(5):349–354, May 1975. 36
- [76] David H. Levy, Shelby F. Nelson, and Diane Freeman. Oxide Electronics by Spatial Atomic Layer Deposition. *Journal of Display Technology*, 5(12):484–494, December 2009. 36
- [77] A Illiberi, F Roozeboom, and P Poodt. Spatial atomic layer deposition of zinc oxide thin films. *ACS applied materials & interfaces*, 4(1):268–72, January 2012.
- [78] Andrea Illiberi, Robert Scherpenborg, Mirjam Theelen, Paul Poodt, and Fred Roozeboom. On the environmental stability of ZnO thin films by spatial atomic layer deposition. *Journal of Vacuum Science & Technology A: Vacuum, Surfaces, and Films*, 31(6):061504, August 2013.
- [79] Andrea Illiberi, R Scherpenborg, Y Wu, F Roozeboom, and P Poodt. Spatial Atmospheric Atomic Layer Deposition of  $\text{Al}_x\text{Zn}_{1-x}\text{O}$ . *ACS applied materials & interfaces*, 5(24):13124–8, December 2013.
- [80] Carolyn R. Ellinger and Shelby F. Nelson. Selective Area Spatial Atomic Layer Deposition of ZnO,  $\text{Al}_2\text{O}_3$ , and Aluminum Doped ZnO Using Poly(vinyl pyrrolidone). *Chemistry of Materials*, 26(4):1514–1522, February 2014.
- [81] A. Illiberi, R. Scherpenborg, F. Roozeboom, and P. Poodt. Atmospheric Spatial Atomic Layer Deposition of In Doped ZnO. *ECS Journal of Solid State Science and Technology*, 3(5):P111–P114, March 2014. 36

- [82] J. Tauc and A. Menth. States in the gap. *Journal of Non-Crystalline Solids*, 8:569–585, 1972. [40](#)
- [83] P. W. Anderson. Absence of Diffusion in Certain Random Lattices. *Phys. Rev.*, 109(5):1492–1505, March 1958. [40](#)
- [84] A. R. Zanatta and I. Chambouleyron. Absorption edge, band tails, and disorder of amorphous semiconductors. *Physical Review B*, 53(7):3833–3836, February 1996.
- [85] Kaien Xu, Manwen Yao, Jianwen Chen, Pei Zou, Yong Peng, Fei Li, and Xi Yao. Effect of crystallization on the band structure and photoelectric property of SrTiO<sub>3</sub> sol-gel derived thin film. *Journal of Alloys and Compounds*, 653:7–13, December 2015. [40](#)
- [86] R Swanepoel. Determination of the thickness and optical constants of amorphous silicon. *Journal of Physics E: Scientific Instruments*, 16(12):1214–1222, December 1983. [43](#)
- [87] Tommi Kaariainen, David Cameron, Marja-Leena Kaariainen, and Arthur Sherman. *Atomic layer deposition: principles, characteristics, and nanotechnology applications*. Scrivener [u.a.], Salem, 2. ed edition, 2013. [46](#)
- [88] César Masse de la Huerta, Viet Huong Nguyen, Jean-Marc Dedulle, Daniel Bellet, Carmen Jiménez, and David Muñoz-Rojas. Influence of the Geometric Parameters on the Deposition Mode in Spatial Atomic Layer Deposition: A Novel Approach to Area-Selective Deposition. *Coatings*, 9(1):5, January 2019. [57](#)
- [89] a. Illiberi, R. Scherpenborg, F. Roozeboom, and P. Poodt. Atmospheric Spatial Atomic Layer Deposition of In-Doped ZnO. *ECS Journal of Solid State Science and Technology*, 3(5):P111–P114, March 2014. [59](#)
- [90] Carolyn R. Ellinger and Shelby F. Nelson. Selective Area Spatial Atomic Layer Deposition of ZnO, Al<sub>2</sub>O<sub>3</sub>, and Aluminum-Doped ZnO Using Poly(vinyl pyrrolidone). *Chemistry of Materials*, 26(4):1514–1522, February 2014. [59](#)
- [91] G. Luka, T. A. Krajewski, B. S. Witkowski, G. Wisz, I. S. Virt, E. Guziewicz, and M. Godlewski. Aluminum-doped zinc oxide films grown by atomic layer deposition for transparent electrode applications. *Journal of Materials Science: Materials in Electronics*, 22(12):1810–1815, December 2011. [62](#)

- [92] Manh-Hung Chu, Liang Tian, Ahmad Chaker, Evgenii Skopin, Valentina Cantelli, Toufik Ouled, Raphaël Boichot, Alexandre Crisci, Sabine Lay, Marie-Ingrid Richard, Olivier Thomas, Jean-Luc Deschanvres, Hubert Renevier, Dillon Fong, and Gianluca Ciatto. Evaluation of Alternative Atomistic Models for the Incipient Growth of ZnO by Atomic Layer Deposition. *Journal of Electronic Materials*, 46(6):3512–3517, June 2017. [64](#)
- [93] T. I. Barry and F. S. Stone. The reactions of oxygen at dark and irradiated zinc oxide surfaces. *Proc. R. Soc. Lond. A*, 255(1280):124–144, March 1960. [69](#), [113](#), [114](#)
- [94] J.F. Chang and M.H. Hon. The effect of deposition temperature on the properties of Al-doped zinc oxide thin films. pages 79–86, 2001.
- [95] Mingwei Zhu, Hui Huang, Jun Gong, Chao Sun, and Xin Jiang. Role of oxygen desorption during vacuum annealing in the improvement of electrical properties of aluminum doped zinc oxide films synthesized by sol gel method. *Journal of Applied Physics*, 102(4):043106, August 2007. [69](#), [113](#), [119](#)
- [96] L. Korte, E. Conrad, H. Angermann, R. Stangl, and M. Schmidt. Advances in a-Si:H/c-Si heterojunction solar cell fabrication and characterization. *Solar Energy Materials and Solar Cells*, 93(6-7):905–910, June 2009. [71](#)
- [97] G. Christmann. Silicon heterojunction solar cells using aluminum doped zinc oxide as back contact: sputtering and ALD, June 2016. [71](#)
- [98] Henriette A. Gatz, Dibyashree Koushik, Jatin K. Rath, Wilhelmus M.M. Kessels, and Ruud E.I. Schropp. Atomic Layer Deposited ZnO: B As Transparent Conductive Oxide for Increased Short Circuit Current Density in Silicon Heterojunction Solar Cells. *Energy Procedia*, 92:624–632, August 2016. [71](#)
- [99] Benedicte Demaurex, Stefaan De Wolf, Antoine Descoedres, Zachary Charles Holman, and Christophe Ballif. Damage at hydrogenated amorphous/crystalline silicon interfaces by indium tin oxide overlayer sputtering. *Applied Physics Letters*, 101(17):171604, October 2012. [71](#)
- [100] R. A. Sinton, A. Cuevas, and M. Stuckings. Quasi-steady-state photoconductance, a new method for solar cell material and device characterization. In *Conference Record of the Twenty Fifth IEEE Photovoltaic Specialists Conference - 1996*, pages 457–460, May 1996. [72](#)

- [101] T. Pisarkiewicz, K. Zakrzewska, and E. Leja. Scattering of charge carriers in transparent and conducting thin oxide films with a non-parabolic conduction band. *Thin Solid Films*, 174:217–223, July 1989. [81](#)
- [102] Victor I Fistul. *Heavily doped semiconductors*. Springer Science & Business Media, 2012. [82](#)
- [103] Boris Isaakovich Shklovskii and Alex L Efros. *Electronic properties of doped semiconductors*, volume 45. Springer Science & Business Media, 2013. [82](#)
- [104] D. C. Look. *Electrical Characterization of GaAs Materials and Devices*. Wiley, 1989. [82](#)
- [105] S. S Devlin, M. Aven, and J. S. Prener. *Physics and chemistry of II-VI Compounds*, volume 549-609. Wiley, New York, 1967. [83](#)
- [106] D. J. Howarth and E. H. Sondheimer. The theory of electronic conduction in polar semiconductors. In *Proceedings of the Royal Society of London A: Mathematical, Physical and Engineering Sciences*, volume 219, pages 53–74. The Royal Society, 1953. [83](#)
- [107] Andre Bikowski and Klaus Ellmer. Analytical model of electron transport in polycrystalline, degenerately doped ZnO films. *Journal of Applied Physics*, 116(14):143704, October 2014. [83](#), [84](#), [87](#), [102](#)
- [108] J. Bardeen and W. Shockley. Deformation Potentials and Mobilities in Non-Polar Crystals. *Physical Review*, 80(1):72–80, October 1950. [84](#)
- [109] Zhigang Shuai, Linjun Wang, and Chenchen Song. Deformation Potential Theory. In *Theory of Charge Transport in Carbon Electronic Materials*, SpringerBriefs in Molecular Science, pages 67–88. Springer, Berlin, Heidelberg, 2012. [84](#)
- [110] D. L. Rode. *Semiconductors and Semimetals*, volume 10. Elsevier, January 1975. [84](#), [85](#)
- [111] H. J. G. Meijer and D. Polder. Note on polar scattering of conduction electrons in regular crystals. *Physica*, 19:255–264, 1953. [84](#)
- [112] J. David Zook. Piezoelectric Scattering in Semiconductors. *Physical Review*, 136(3A):A869–A878, November 1964. [84](#)
- [113] P. Wagner and R. Helbig. The Hall effect and the anisotropy of the mobility of the electrons in ZnO. Technical report, August 1977. [85](#)

- [114] Laurent Sagalowicz and Glen R. Fox. Planar defects in ZnO thin films deposited on optical fibers and flat substrates. *Journal of Materials Research*, 14(05):1876–1885, May 1999. [86](#), [87](#), [102](#)
- [115] Andre Bikowski and Klaus Ellmer. A comparative study of electronic and structural properties of polycrystalline and epitaxial magnetron-sputtered ZnO:Al and Zn<sub>1-x</sub>Mg<sub>x</sub>O:Al Films - Origin of the grain barrier traps. *Journal of Applied Physics*, 114(6):063709, August 2013. [86](#)
- [116] David C. Look, C. E. Stutz, Richard J. Molnar, K. Saarinen, and Z. Liliental-Weber. Dislocation-independent mobility in lattice-mismatched epitaxy: application to GaN. *Solid state communications*, 117(10):571–575, 2001. [86](#), [87](#), [102](#)
- [117] E. Conwell and V. F. Weisskopf. Theory of Impurity Scattering in Semiconductors. *Physical Review*, 77(3):388–390, February 1950. [87](#)
- [118] Harvey Brooks. Theory of the Electrical Properties of Germanium and Silicon. *Advances in Electronics and Electron Physics*, 7:85–182, January 1955. [87](#)
- [119] R. B. Dingle. Scattering of electrons and holes by charged donors and acceptors in semiconductors. *The London, Edinburgh, and Dublin Philosophical Magazine and Journal of Science*, 46(379):831–840, August 1955. [87](#)
- [120] Hyun-Sik Kim, Stephen D. Kang, Yinglu Tang, Riley Hanus, and G. Jeffrey Snyder. Dislocation strain as the mechanism of phonon scattering at grain boundaries. *Materials Horizons*, 3(3):234–240, 2016. [88](#)
- [121] John Y. W. Seto. The electrical properties of polycrystalline silicon films. *Journal of Applied Physics*, 46(12):5247–5254, December 1975. [88](#)
- [122] R. Stratton. Volt-current characteristics for tunneling through insulating films. *Journal of Physics and Chemistry of Solids*, 23(9):1177–1190, 1962. [88](#)
- [123] John G. Simmons. Generalized Formula for the Electric Tunnel Effect between Similar Electrodes Separated by a Thin Insulating Film. *Journal of Applied Physics*, 34(6):1793–1803, June 1963. [88](#), [91](#)
- [124] C. H. Seager and G. E. Pike. Electron tunneling through GaAs grain boundaries. *Applied Physics Letters*, 40(6):471–474, March 1982. [88](#), [96](#)

- [125] Nicolas Sommer, Jurgen Hupkes, and Uwe Rau. Field Emission at Grain Boundaries: Modeling the Conductivity in Highly Doped Polycrystalline Semiconductors. *Phys. Rev. Applied*, 5(2):024009, February 2016. [89](#), [104](#), [110](#), [116](#)
- [126] Islam E. Hashem, Nadia H. Rafat, and Ezzeldin A. Soliman. Theoretical Study of Metal-Insulator-Metal Tunneling Diode Figures of Merit. *IEEE Journal of Quantum Electronics*, 49(1):72–79, January 2013. [89](#), [99](#)
- [127] Kissan Mistry, Mustafa Yavuz, and Kevin P. Musselman. Simulated electron affinity tuning in metal-insulator-metal (MIM) diodes. *Journal of Applied Physics*, 121(18):184504, May 2017. [89](#)
- [128] Viet Huong Nguyen, Ulrich Gottlieb, Anthony Valla, Delfina Muñoz, Daniel Bellet, and David Muñoz-Rojas. Electron tunneling through grain boundaries in transparent conductive oxides and implications for electrical conductivity: the case of ZnO:Al thin films. *Materials Horizons*, 5(4):715–726, 2018. [89](#), [116](#)
- [129] P. D. C. King, T. D. Veal, D. J. Payne, A. Bourlange, R. G. Egdell, and C. F. McConville. Surface Electron Accumulation and the Charge Neutrality Level in In<sub>2</sub>O<sub>3</sub>. *Phys. Rev. Lett.*, 101(11):116808, September 2008. [89](#)
- [130] P. D. C. King, T. D. Veal, F. Fuchs, Ch. Y. Wang, D. J. Payne, A. Bourlange, H. Zhang, G. R. Bell, V. Cimalla, O. Ambacher, R. G. Egdell, F. Bechstedt, and C. F. McConville. Band gap, electronic structure, and surface electron accumulation of cubic and rhombohedral In<sub>2</sub>O<sub>3</sub>. *Phys. Rev. B*, 79(20):205211, May 2009. [89](#)
- [131] H. Moormann, D. Kohl, and G. Heiland. Work function and band bending on clean cleaved zinc oxide surfaces. *Surface Science*, 80:261–264, February 1979. [89](#)
- [132] Liang S.-D. *Quantum Tunneling And Field Electron Emission Theories*. World Scientific, November 2013. [91](#)
- [133] C. B. Duke. *Tunneling in Solids*. Academic Press, 1969. [91](#)
- [134] R. Tsu and L. Esaki. Tunneling in a finite superlattice. *Applied Physics Letters*, 22(11):562–564, June 1973. [91](#), [97](#)
- [135] Yuji Ando and Tomohiro Itoh. Calculation of transmission tunneling current across arbitrary potential barriers. *Journal of Applied Physics*, 61(4):1497–1502, February 1987. [97](#)

- [136] D. L. Young, T. J. Coutts, V. I. Kaydanov, A. S. Gilmore, and W. P. Mulligan. Direct measurement of density-of-states effective mass and scattering parameter in transparent conducting oxides using second-order transport phenomena. *Journal of Vacuum Science & Technology A: Vacuum, Surfaces, and Films*, 18(6):2978–2985, November 2000. [102](#), [112](#)
- [137] W M Kim, I H Kim, J H Ko, B Cheong, T S Lee, K S Lee, D Kim, and T-Y Seong. Density-of-state effective mass and non-parabolicity parameter of impurity doped ZnO thin films. *Journal of Physics D: Applied Physics*, 41(19):195409, October 2008.
- [138] V. Romanyuk, N. Dmitruk, V. Karpyna, G. Lashkarev, V. Popovych, M. Dranchuk, R. Pietruszka, M. Godlewski, G. Dovbeshko, I. Timofeeva, O. Kondratenko, M. Taborska, and A. Ievtushenko. Optical and Electrical Properties of Highly Doped ZnO:Al Films Deposited by Atomic Layer Deposition on Si Substrates in Visible and Near Infrared Region. *Acta Physica Polonica A*, 129(1a):A–36–A–40, January 2016. [102](#)
- [139] Xiaocheng Yang, Chunchuan Xu, and N. C. Giles. Intrinsic electron mobilities in CdSe, CdS, ZnO, and ZnS and their use in analysis of temperature-dependent Hall measurements. *Journal of Applied Physics*, 104(7):073727, 2008. [102](#)
- [140] M. V. Garcia-Cuenca, J. L. Morenza, and J. Esteve. Electron tunneling in heavily In doped polycrystalline CdS films. *Journal of Applied Physics*, 56(6):1738–1743, September 1984. [110](#)
- [141] F. Ruske, M. Roczen, K. Lee, M. Wimmer, S. Gall, J. Hupkes, D. Hrunski, and B. Rech. Improved electrical transport in Al-doped zinc oxide by thermal treatment. *Journal of Applied Physics*, 107(1):013708, January 2010. [113](#), [119](#)
- [142] Hao Tong, Zhonghua Deng, Zhuguang Liu, Changgang Huang, Jiquan Huang, Hai Lan, Chong Wang, and Yongge Cao. Effects of post-annealing on structural, optical and electrical properties of Al-doped ZnO thin films. *Applied Surface Science*, 257(11):4906–4911, March 2011. [113](#)
- [143] D. Gaspar, L. Pereira, K. Gehrke, B. Galler, E. Fortunato, and R. Martins. High mobility hydrogenated zinc oxide thin films. *Solar Energy Materials and Solar Cells*, 163:255–262, April 2017. [113](#)
- [144] D. H. Zhang. Adsorption and photodesorption of oxygen on the surface and crystallite interfaces of sputtered ZnO films. *Materials Chemistry and Physics*, 45(3):248–252, 1996. [113](#)

- [145] Harald Hagendorfer, Karla Lienau, Shiro Nishiwaki, Carolin M. Fella, Lukas Kranz, Alexander R. Uhl, Dominik Jaeger, Li Luo, Christina Gretener, Stephan Buecheler, Yaroslav E. Romanyuk, and Ayodhya N. Tiwari. Highly Transparent and Conductive ZnO: Al Thin Films from a Low Temperature Aqueous Solution Approach. *Advanced Materials*, 26(4):632–636, January 2014. [113](#)
- [146] Viet Huong Nguyen, Daniel Bellet, Bruno Masenelli, and David Muñoz-Rojas. Increasing the Electron Mobility of ZnO-Based Transparent Conductive Films Deposited by Open-Air Methods for Enhanced Sensing Performance. *ACS Applied Nano Materials*, 1(12):6922–6931, December 2018. [113](#)
- [147] Do-Joong Lee, Hyun-Mi Kim, Jang-Yeon Kwon, Hyoji Choi, Soo-Hyun Kim, and Ki-Bum Kim. Structural and Electrical Properties of Atomic Layer Deposited Al-Doped ZnO Films. *Adv. Funct. Mater.*, 21(3):448–455, February 2011. [117](#)
- [148] Harry L. Tuller. ZnO Grain Boundaries: Electrical Activity and Diffusion. *Journal of Electroceramics*, 4(1):33–40, December 1999. [119](#)
- [149] Antonio Claret Soares Sabioni, Marcelo Jose Ferreira Ramos, and Wilmar Barbosa Ferraz. Oxygen Diffusion in Pure and Doped ZnO. *Materials Research*, 6(2):6, 2003. [119](#)
- [150] M. D. Groner, F. H. Fabreguette, J. W. Elam, and S. M. George. Low-Temperature Al<sub>2</sub>O<sub>3</sub> Atomic Layer Deposition. *Chemistry of Materials*, 16(4):639–645, February 2004. [122](#)
- [151] Arrelaine A Dameron, Stephen D Davidson, Beau B Burton, Peter F Carcia, R Scott McLean, and Steven M George. Gas Diffusion Barriers on Polymers Using Multilayers Fabricated by Al<sub>2</sub>O<sub>3</sub> and Rapid SiO<sub>2</sub> Atomic Layer Deposition. page 8.
- [152] Tony Maindron, Jean-Yves Simon, Emilie Viasnoff, and Dominique Lafond. Stability of 8-hydroxyquinoline aluminum films encapsulated by a single Al<sub>2</sub>O<sub>3</sub> barrier deposited by low temperature atomic layer deposition. *Thin Solid Films*, 520(23):6876–6881, September 2012. [122](#)
- [153] M Lagrange, T Sannicolo, D Muñoz-Rojas, B Guillo Lohan, A Khan, M Anikin, C Jiménez, F Bruckert, Y Bréchet, and D Bellet. Understanding the mechanisms leading to failure in metallic nanowire-based transparent heaters, and solution for stability enhancement. *Nanotechnology*, 28(5):055709, February 2017. [123](#), [130](#), [135](#)

- [154] Sukanta De, Thomas M. Higgins, Philip E. Lyons, Evelyn M. Doherty, Peter N. Nirmalraj, Werner J. Blau, John J. Boland, and Jonathan N. Coleman. Silver Nanowire Networks as Flexible, Transparent, Conducting Films: Extremely High DC to Optical Conductivity Ratios. *ACS Nano*, 3(7):1767–1774, July 2009. [128](#)
- [155] Chuan Fei Guo and Zhifeng Ren. Flexible transparent conductors based on metal nanowire networks. *Materials Today*, 18(3):143–154, April 2015. [128](#)
- [156] Linxiang He and Sie Chin Tjong. Nanostructured transparent conductive films: Fabrication, characterization and applications. *Materials Science and Engineering: R: Reports*, 109:1–101, November 2016. [128](#)
- [157] Daniel Bellet, Melanie Lagrange, Thomas Sannicolo, Sara Aghazadehchors, Viet Huong Nguyen, Daniel P. Langley, David Muñoz-Rojas, Carmen Jiménez, Yves Bréchet, and Ngoc Duy Nguyen. Transparent Electrodes Based on Silver Nanowire Networks: From Physical Considerations towards Device Integration. *Materials*, 10(6):570, May 2017. [128](#)
- [158] M. Lagrange, D. P. Langley, G. Giusti, C. Jiménez, Y. Bréchet, and D. Bellet. Optimization of silver nanowire-based transparent electrodes: effects of density, size and thermal annealing. *Nanoscale*, 7(41):17410–17423, 2015. [128](#), [130](#), [133](#), [142](#), [143](#), [154](#)
- [159] Caroline Celle, Celine Mayousse, Eleonore Moreau, Henda Basti, Alexandre Carella, and Jean-Pierre Simonato. Highly flexible transparent film heaters based on random networks of silver nanowires. *Nano Research*, 5(6):427–433, June 2012. [128](#)
- [160] Daniel Langley, Gael Giusti, Celine Mayousse, Caroline Celle, Daniel Bellet, and Jean-Pierre Simonato. Flexible transparent conductive materials based on silver nanowire networks: a review. *Nanotechnology*, 24(45):452001, 2013. [128](#)
- [161] Fei Guo, Xiangdong Zhu, Karen Forberich, Johannes Krantz, Tobias Stubhan, Michael Salinas, Marcus Halik, Stefanie Spallek, Benjamin Butz, Erdmann Spiecker, Tayebbeh Ameri, Ning Li, Peter Kubis, Dirk M. Guldi, Gebhard J. Matt, and Christoph J. Brabec. ITO-Free and Fully Solution-Processed Semitransparent Organic Solar Cells with High Fill Factors. *Advanced Energy Materials*, 3(8):1062–1067. [128](#)
- [162] Dong-Hwan Kim, Youngmin Kim, and Jong-Woong Kim. Transparent and flexible film for shielding electromagnetic interference. *Materials & Design*, 89:703–707, January 2016. [128](#)

- [163] Hadi Hosseinzadeh Khaligh and Irene A Goldthorpe. Failure of silver nanowire transparent electrodes under current flow. *Nanoscale Research Letters*, 8(1):235, 2013. [128](#), [154](#)
- [164] D. P. Langley, M. Lagrange, G. Giusti, C. Jiménez, Y. Bréchet, N. D. Nguyen, and D. Bellet. Metallic nanowire networks: effects of thermal annealing on electrical resistance. *Nanoscale*, 6(22):13535–13543, 2014. [128](#), [130](#), [133](#)
- [165] Frederik S. F. Morgenstern, Dinesh Kabra, Sylvain Massip, Thomas J. K. Brenner, Philip E. Lyons, Jonathan N. Coleman, and Richard H. Friend. Ag-nanowire films coated with ZnO nanoparticles as a transparent electrode for solar cells. *Applied Physics Letters*, 99(18):183307, October 2011. [129](#)
- [166] Rui Zhu, Choong-Heui Chung, Kitty C. Cha, Wenbing Yang, Yue Bing Zheng, Huanping Zhou, Tze-Bin Song, Chun-Chao Chen, Paul S. Weiss, Gang Li, and Yang Yang. Fused Silver Nanowires with Metal Oxide Nanoparticles and Organic Polymers for Highly Transparent Conductors. *ACS Nano*, 5(12):9877–9882, December 2011. [129](#)
- [167] Tze-Bin Song, You Seung Rim, Fengmin Liu, Brion Bob, Shenglin Ye, Yao-Tsung Hsieh, and Yang Yang. Highly Robust Silver Nanowire Network for Transparent Electrode. *ACS Applied Materials & Interfaces*, 7(44):24601–24607, November 2015. [129](#)
- [168] Areum Kim, Yulim Won, Kyoohye Woo, Chul-Hong Kim, and Jooho Moon. Highly Transparent Low Resistance ZnO/Ag Nanowire/ZnO Composite Electrode for Thin Film Solar Cells. *ACS Nano*, 7(2):1081–1091, February 2013. [129](#)
- [169] Anh-Tuan Pham, Xuan-Quang Nguyen, Duc-Huy Tran, Vu Ngoc Phan, Thanh-Tung Duong, and Duy-Cuong Nguyen. Enhancement of the electrical properties of silver nanowire transparent conductive electrodes by atomic layer deposition coating with zinc oxide. *Nanotechnology*, 27(33):335202, August 2016. [129](#)
- [170] Afzal Khan, Viet Huong Nguyen, David Muñoz-Rojas, Sara Aghazadehchors, Carmen Jiménez, Ngoc Duy Nguyen, and Daniel Bellet. Stability Enhancement of Silver Nanowire Networks with Conformal ZnO Coatings Deposited by Atmospheric Pressure Spatial Atomic Layer Deposition. *ACS Applied Materials & Interfaces*, 10(22):19208–19217, June 2018. [129](#)
- [171] Caroline Celle, Anthony Cabos, Thomas Fontecave, Bruno Laguitton, Anass Benayad, Laure Guettaz, Nathalie Pelissier, Viet Huong Nguyen, Daniel Bellet, David Muñoz-Rojas, and Jean-Pierre Simonato. Oxidation of copper nanowire based transparent

- electrodes in ambient conditions and their stabilization by encapsulation: application to transparent film heaters. *Nanotechnology*, 29(8):085701, February 2018. [129](#)
- [172] B. Stahlmecke, F.-J. Meyer zu Heringdorf, L. I. Chelaru, M. Horn-von Hoegen, G. Dumpich, and K. R. Roos. Electromigration in self-organized single-crystalline silver nanowires. *Applied Physics Letters*, 88(5):053122, January 2006. [136](#)
- [173] Zhaoguo Xue, Mingkun Xu, Yaolong Zhao, Jimmy Wang, Xiaofan Jiang, Linwei Yu, Junzhan Wang, Jun Xu, Yi Shi, Kunji Chen, and Pere Roca i Cabarrocas. Engineering island-chain silicon nanowires via a droplet mediated Plateau-Rayleigh transformation. *Nature Communications*, 7:12836, September 2016. [136](#)
- [174] A. Vagnon, O. Lame, D. Bouvard, M. Di Michiel, D. Bellet, and G. Kapelski. Deformation of steel powder compacts during sintering: Correlation between macroscopic measurement and in situ microtomography analysis. *Acta Materialia*, 54(2):513–522, January 2006. [136](#)
- [175] A. Vagnon, J.P. Riviere, J.M. Missiaen, D. Bellet, M. Di Michiel, C. Josserond, and D. Bouvard. 3d statistical analysis of a copper powder sintering observed in situ by synchrotron microtomography. *Acta Materialia*, 56(5):1084–1093, March 2008. [136](#)
- [176] Shotaro Takeuchi, Ngoc D. Nguyen, Frederik E. Leys, Roger Loo, Thierry Conard, Wilfried Vandervorst, and Matty Caymax. Vapor Phase Doping with N-type Dopant into Silicon by Atmospheric Pressure Chemical Vapor Deposition. *ECS Trans.*, 16(10):495–502, March 2008. [136](#)
- [177] N. D. Nguyen, E. Rosseel, S. Takeuchi, J. L. Everaert, R. Loo, J. Goossens, A. Moussa, T. Clarysse, M. Caymax, and W. Vandervorst. Vapor phase doping and sub-melt laser anneal for the fabrication of Si-based ultra-shallow junctions in sub-32 nm CMOS technology. In *2009 International Semiconductor Device Research Symposium*, pages 1–2, December 2009. [136](#)
- [178] G. Rey, C. TERNON, M. Modreanu, X. Mescot, V. Consonni, and D. Bellet. Electron scattering mechanisms in fluorine-doped SnO<sub>2</sub> thin films. *Journal of Applied Physics*, 114(18):183713, November 2013. [141](#)
- [179] Manuela Gobelt, Ralf Keding, Sebastian W. Schmitt, Bjorn Hoffmann, Sara Jackle, Michael Latzel, Vuk V. Radmilovic, Velimir R. Radmilovic, Erdmann Spiecker, and Silke Christiansen. Encapsulation of silver nanowire networks by atomic layer deposition for indium-free transparent electrodes. *Nano Energy*, 16:196–206, September 2015. [141](#)

- [180] Kirill Zilberberg, Felix Gasse, Richie Pagui, Andreas Polywka, Andreas Behrendt, Sara Trost, Ralf Heiderhoff, Patrick Gornn, and Thomas Riedl. Highly Robust Indium-Free Transparent Conductive Electrodes Based on Composites of Silver Nanowires and Conductive Metal Oxides. *Advanced Functional Materials*, 24(12):1671–1678, March 2014.
- [181] Qijin Huang, Wenfeng Shen, Xingzhong Fang, Guofei Chen, Ye Yang, Jinhua Huang, Ruiqin Tan, and Weijie Song. Highly Thermostable, Flexible, Transparent, and Conductive Films on Polyimide Substrate with an AZO/AgNW/AZO Structure. *ACS Applied Materials & Interfaces*, 7(7):4299–4305, February 2015. [141](#)
- [182] Milan Zezelj and Igor Stankovic. From percolating to dense random stick networks: Conductivity model investigation. *Physical Review B*, 86(13), October 2012. arXiv: 1206.0939. [142](#), [150](#)
- [183] Aveek Bid, Achyut Bora, and A. K. Raychaudhuri. Temperature dependence of the resistance of metallic nanowires of diameter greater than 15 nm : Applicability of Bloch-Gruneisen theorem. *Physical Review B*, 74(3), July 2006. [142](#)
- [184] Daniel P. Langley, Mélanie Lagrange, Ngoc Duy Nguyen, and Daniel Bellet. Percolation in networks of 1-dimensional objects: comparison between Monte Carlo simulations and experimental observations. *Nanoscale Horizons*, 3(5):545–550, 2018. [143](#)
- [185] Jiantong Li and Shi-Li Zhang. Finite-size scaling in stick percolation. *Phys. Rev. E*, 80(4):040104, October 2009. [145](#)
- [186] Daniel Gall. Electron mean free path in elemental metals. *Journal of Applied Physics*, 119(8):085101, February 2016. [150](#)
- [187] G. Haacke. New figure of merit for transparent conductors. *Journal of Applied Physics*, 47(9):4086–4089, September 1976. [154](#)

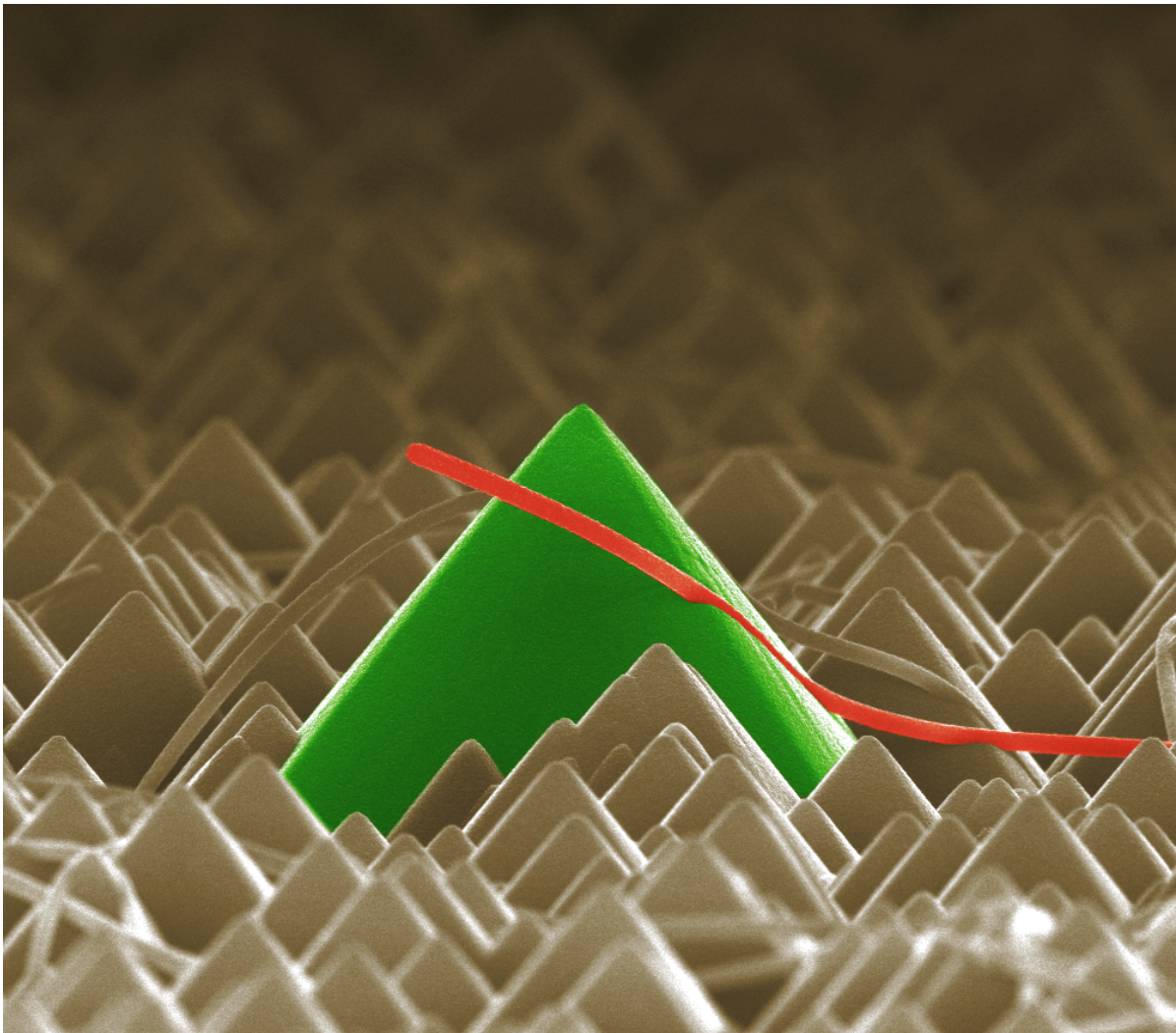


## List of related publications

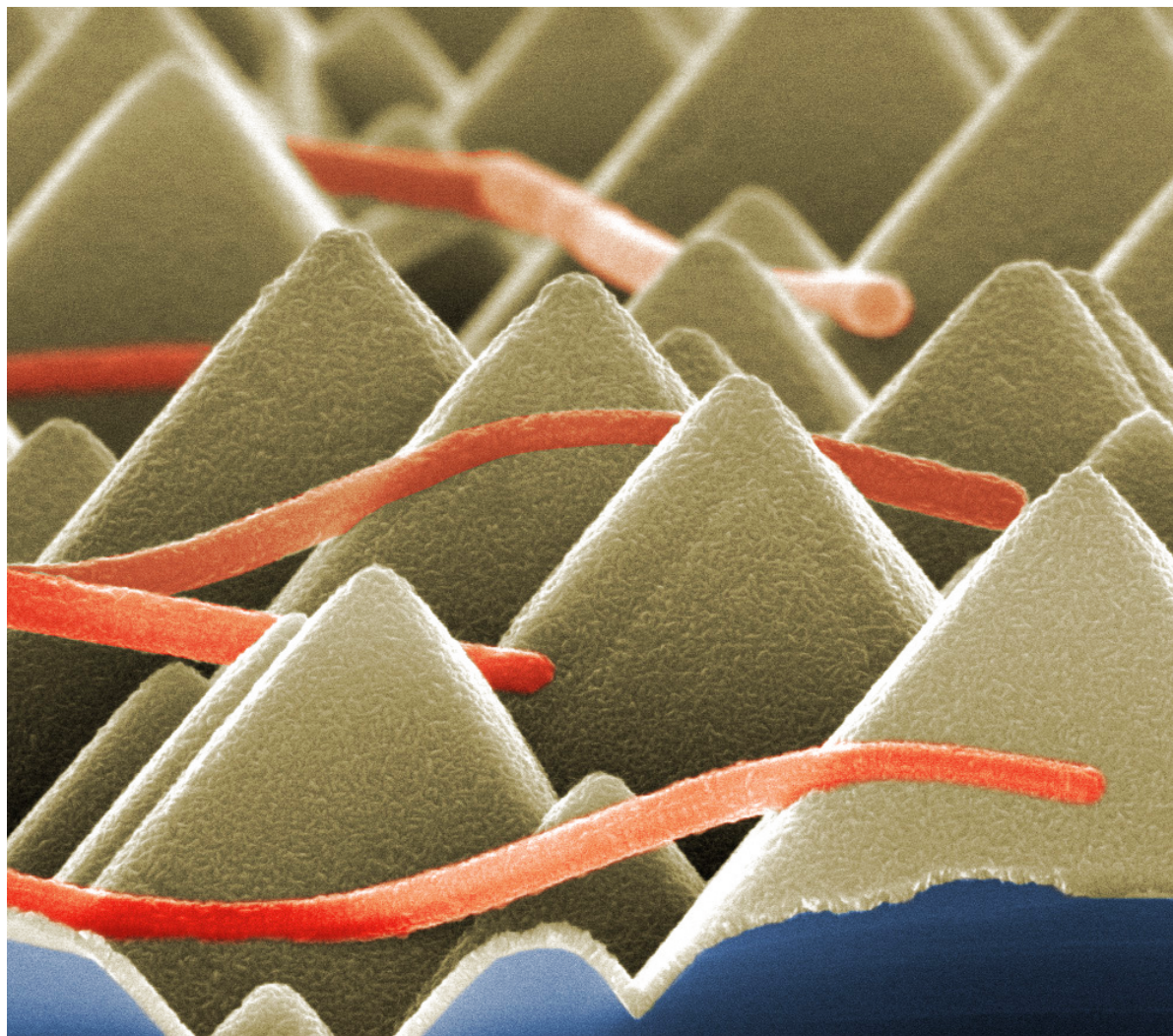
1. [Nguyen, V. H.](#); Resende, J.; Jiménez, C.; Deschanvres, J.-L.; Carroy, P.; Muñoz, D.; Bellet, D.; Muñoz-Rojas, D. Deposition of ZnO Based Thin Films by Atmospheric Pressure Spatial Atomic Layer Deposition for Application in Solar Cells. *J. Renew. Sustain. Energy* **2017**, 9 (2), 021203.
2. [Nguyen, V. H.](#); Gottlieb, U.; Valla, A.; Munoz, D.; Bellet, D.; Muñoz-Rojas, D. Electron Tunneling through Grain Boundaries in Transparent Conductive Oxides and Implications for Electrical Conductivity: The Case of ZnO:Al Thin Films. *Materials Horizons*. **2018**, 5 (4), 715–726.
3. [Nguyen, V. H.](#); Bellet, D.; Masenelli, B.; Muñoz-Rojas, D. Increasing the Electron Mobility of ZnO-Based Transparent Conductive Films Deposited by Open-Air Methods for Enhanced Sensing Performance. *ACS Applied Nano Materials* **2018**, 1 (12), 6922–6931
4. Khan, A.; [Nguyen, V. H.](#); Muñoz-Rojas, D.; Aghazadehchors, S.; Jiménez, C.; Nguyen, N. D.; Bellet, D. Stability Enhancement of Silver Nanowire Networks with Conformal ZnO Coatings Deposited by Atmospheric Pressure Spatial Atomic Layer Deposition. *ACS Appl. Mater. Interfaces* **2018**, 10 (22), 19208–19217.
5. Muñoz-Rojas, D.; [Nguyen, V. H.](#); Masse de la Huerta, C.; Aghazadehchors, S.; Jiménez, C.; Bellet, D. Spatial Atomic Layer Deposition (SALD), an Emerging Tool for Energy Materials. Application to New-Generation Photovoltaic Devices and Transparent Conductive Materials. *Comptes Rendus Phys.* **2017**, 18 (7), 391–400.
6. H. Alshehri, A.; Mistry, K.; [Nguyen, V. H.](#); H. Ibrahim, K.; Muñoz-Rojas, D.; Yavuz, M.; P. Musselman, K. Quantum-Tunneling Metal-Insulator-Metal Diodes Made by Rapid Atmospheric Pressure Chemical Vapor Deposition. *Advanced Functional Materials*. **2018**, 0 (0), 1805533
7. Bellet, D.; Lagrange, M.; Sannicolo, T.; Aghazadehchors, S.; [Nguyen, V. H.](#); Langley, D. P.; Muñoz-Rojas, D.; Jiménez, C.; Bréchet, Y.; Nguyen, N. D. Transparent Electrodes

- Based on Silver Nanowire Networks: From Physical Considerations towards Device Integration. *Materials* **2017**, 10 (6), 570.
8. Celle, C.; Cabos, A.; Fontecave, T.; Laguitton, B.; Benayad, A.; Guettaz, L.; Nathalie Pélissier; [Nguyen, V. H.](#); Bellet, D.; Muñoz-Rojas, D.; et al. Oxidation of Copper Nanowire Based Transparent Electrodes in Ambient Conditions and Their Stabilization by Encapsulation: Application to Transparent Film Heaters. *Nanotechnology* **2018**, 29 (8), 085701.
  9. Liu, H.; [Nguyen, V. H.](#); Roussel, H.; Chaix-Pluchery, O.; Gélard, I.; Rapenne, L.; Deschanvres, J.-L.; Jiménez, C.; Muñoz-Rojas, D. The Role of Humidity in Tuning the Texture and Electrical Properties of Cu<sub>2</sub>O Thin Films Deposited via Aerosol Assisted MOCVD. *Advanced Materials Interfaces*. **2018**, 0 (0), 1801364
  10. Masse de la Huerta, C; [Nguyen, V. H.](#); Dedulle, J-M.; Bellet, D.; Jiménez, C.; Muñoz-Rojas, D. Influence of the Geometric Parameters on the Deposition Mode in Spatial Atomic Layer Deposition: A Novel Approach to Area-Selective Deposition. *Coatings* **2019**, 9 (1), 5

# Nanoart



This SEM image was taken in 11/2017 by a SEM FEG QUANTA 250 at LMGP when we tried to make a composite transparent electrode based on AgNW network and ZnO:Al thin film. The image shows the cross-section view (tilt angle of  $3^\circ$ ) of such a nanocomposite deposited on a textured silicon substrate with pyramid-like surface morphology. Width of image:  $12\ \mu\text{m}$ , diameter of uncoated nanowire:  $50\ \text{nm}$ , ZnO:Al thickness:  $75\ \text{nm}$ .



This SEM image shows a cross-section view (tilt angle of  $3^\circ$ ) of a ZnO:Al/AgNW nanocomposite electrode deposited on a textured silicon substrate with pyramid-like surface morphology. Diameter of uncoated nanowire: 50 nm, ZnO:Al thickness: 75 nm.

